Optimization of layered bifunctional catalytic systems for one-step synthesis of dimethyl ether

zur Erlangung des akademischen Grades einer

Doktorin der Ingenieurwissenschaften (Dr.-Ing.)

von der KIT-Fakultät für Chemieingenieurwesen und Verfahrenstechnik des Karlsruher Instituts für Technologie (KIT)

genehmigte

DISSERTATION

von

Giulia Baracchini

aus Genua (Italien)

Tag der mündlichen Prüfung: 03/07/2020
Erstgutachter: Prof. Dr.-Ing. Roland Dittmeyer
Zweitgutachter: Prof. Dr. Wilhelm Schwieger

Act as though everything depended on you;
Pray as though everything depended on God.

St. Ignatius of Loyola

Al Nonno Piero

Some passages, figures and tables in this dissertation have already been published in similar form in the following published sources:

G. Baracchini, A. G. F. Machoke, M. Klumpp, R. Wen, P. Arnold W. Schwieger and R. Dittmeyer, Structured catalysts for the direct synthesis of dimethyl ether from synthesis gas: a comparison of core@shell versus hybrid catalyst configuration, *Catal. Today*, **2020**, 342, 46 - 58

G. Baracchini, M. Klumpp, P. Arnold and R. Dittmeyer, Direct synthesis of Dimethyl Ether: a simulation study on the influence of the catalyst configuration, *Chem. Eng. J.*, **2020**, 396, 125 - 155

Zusammenfassung

Die Direktsynthese von Dimethylether (DME) aus Synthesegas (STD) über Methanol (MeOH) als Zwischenprodukt ist ein vielversprechender Prozess zur Umsetzung des Power-to-X Konzepts, bei dem der erneuerbare Strom über Wasserstoff in synthetischen Kraftstoffen oder Chemikalien gespeichert wird. Die Verschiebung des thermodynamischen Gleichgewichts der Methanolsynthese und damit die Erzielung eines hohen CO-Umsatzgrades sowie einer hohen DME-Selektivität sind entscheidende Aspekte für diesen Prozess, dessen effiziente Umsetzung zu einem großen Teil von der jeweiligen Katalysatorkonfiguration abhängt. Im Rahmen dieser Arbeit wurden mehrere Katalysatorkonfigurationen, die durch die Kombination von $CuO/ZnO/Al_2O_3$ (CZA) mit Zeolith H-ZSM-5 (Z) für die Methanolsynthese bzw. deren Dehydratisierung erhalten wurden, verglichen, wobei Modellierungs-, Synthese- und Charakterisierungswerkzeuge in Verbindung gebracht wurden. Es wurden Hybridpartikel mit einer Nachbarschaft der beiden Katalysatoren sowohl im Mikrometerbereich (mittlere Nähe, CZA+Z) als auch im Submikrometerbereich (große Nähe, CZA&Z) sowie strukturierte Kern@Schale Partikel (CZA@Z) in einem Festbettreaktor (PBR) untersucht. Darüber hinaus wurden dementsprechende planare (beschichtete) Konfigurationen, nämlich die hybriden Schichtsysteme mit mittlerer (CZA#Z) und größer Nähe (CZA&/Z) sowie ein strukturiertes Doppelschichtsystem (CZA//Z) in einem Mikrokanalreaktor (μ-CR) untersucht.

Die Modellierung von Reaktion und Stofftransport in diesen Katalysatoren wurde mit einem 3D-Poren-Netzwerkmodell (3D-CPNM) durchgeführt, das geeignet ist den polykristallinen anisotropen Zeolithen zu beschreiben. Dazu wurden sowohl Strukturparameter aus der Charakterisierung zur Beschreibung des Stofftransports als auch die Kinetik der Reaktionen implementiert. Die Leistung für die STD-Reaktion in Abhängigkeit des CZA/Zeolith-Verhältnisses bei jedem dieser Katalysatoren sowie als Funktion der Betriebsparameter wurde untersucht.
Alle Katalysatoren wurden ausgehend von der Flammsprühpyrolyse (FSP) und der hydrothermalen Synthese für das CZA bzw. den Zeolith hersynthetisiert. Anschließend wurden die partikelförmigen Katalysatoren durch entweder gleichzeitige Pelletierung (CZA+Z) oder Sprühtrocknung (CZA&Z) und zweistufige hydrothermale Synthese (*in-situ seeding* und *secondary growth*) (CZA@Z) präpariert; die entsprechenden Schichtstrukturen (CZA&/Z, CZA#Z und CZA//Z) wurden durch Siebdruck in Mikrokanäle eingebracht.
Die Katalysatoren wurden charakterisiert, um die physikalisch-chemischen Eigenschaften und die Aktivität des einzelnen CZA sowie der kombinierten Konfigurationen für die STD-Reaktion zu bestimmen. Dabei konnten zusätzliche Informationen über den Einfluss der Synthese auf die endgültigen Katalysatoren, die bei der Modellierung nicht berücksichtigt werden konnten, beobachtet und experimentell ausgewertet werden.

Ausgehend von den Ergebnissen der Modellierung, Synthese und Charakterisierung konnte festgestellt werden, welche und warum bestimmte Katalysatorkonfigurationen für die Durchführung der STD-Reaktion besonders geeignet sind: das Hybridpartikelsystem mittlerer Nähe CZA+Z und die strukturierte Doppelschicht CZA//Z wurden als die vielversprechendsten Katalysatorkonfigurationen in Bezug auf CO-Umsatz und DME-Selektivität für die Anwendung im Festbettreaktor bzw. im beschichteten Mikroreaktor identifiziert.

Abstract

The direct synthesis of dimethyl ether (DME) from synthesis gas (STD) via methanol (MeOH) as an intermediate is a promising option for implementation of the Power-to-X concept, involving the storage of renewable electrical energy via hydrogen or synthesis gas in synthetic fuels or chemicals. The STD reaction shifts the equilibrium conversion dictated by thermodynamics to higher values compared to methanol synthesis alone at given conditions. Notwithstanding, proper catalyst materials and a suitable configuration have to be found that would support high CO-conversion as well as high DME-selectivity. In this work, different catalyst configurations obtained by combining $CuO/ZnO/Al_2O_3$ (CZA) for MeOH synthesis with zeolite H-ZSM-5 (Z) for its dehydration are investigated bringing into connection modelling, synthesis and characterization tools. In this way, hybrid particles with proximity of the two catalysts in both the micrometer-scale (medium proximity, CZA+Z) and the sub-micrometer-scale (close proximity, CZA&Z) as well as structured core@shell particles (CZA@Z) were investigated in a packed-bed-reactor (PBR). Moreover, their planar (coated) counterparts, namely the hybrid layered systems with medium (CZA#Z) and close proximity (CZA&/Z) and a structured double layer system (CZA//Z) were investigated in a wall-coated micro-channel-reactor (μ-CR).

The modelling of reaction and diffusion inside the catalysts was based on a 3D-crystal- lite pore network model (3D-CPNM), able to describe e.g. the polycrystalline anisotropic zeolite. Moreover, structural parameters obtained from the characterization, a description of the mass transport and the kinetics of the reactions were implemented. The performance of these catalyst systems in the STD reaction was studied focusing on the influence of the CZA/Z ratio and the operational parameters (temperature, *F/W*, feed composition).
All the catalysts were synthesized starting from flame spray pyrolysis (FSP) and hydrothermal synthesis for the CZA and the zeolite, respectively. Afterwards, the preparation of the catalyst configurations was achieved by using simultaneous pelletization (CZA+Z), spray drying (CZA&Z) and a two-step hydrothermal synthesis (*in-situ* seeding followed by secondary growth) (CZA@Z) for the particulate systems; the planar counterparts (CZA&/Z, CZA#Z and CZA//Z) were brought into the micro-channels by screen printing.
The catalysts were characterized in order to determine the physico-chemical properties and the activity of CZA only as well as of the combined configurations for the STD reaction. In doing this, additional information about the influence of the synthesis procedure on the final catalyst, which could not be taken into account during the modelling, could be observed and experimentally evaluated.

Combining the results coming from modelling, synthesis and characterization, it was possible to conclude which and why certain catalyst configurations are better suitable for performing the STD reaction: the hybrid particulate system of medium proximity CZA+Z and the structured double layer CZA//Z were

identified as the most promising catalyst configurations in terms of CO-conversion and DME-selectivity for application in the PBR and μ-CR, respectively.

Contents

1 Motivation . . . **1**
1.1 Objectives of the Dissertation . . . 3

2 State of the Art . . . **5**
2.1 Methanol Synthesis . . . 5
2.1.1 The $CuO/ZnO/Al_2O_3$ catalyst for the STM reaction . . . 5
2.2 Flame Spray Pyrolysis as a Technique for CZA Synthesis . . . 8
2.3 Direct Synthesis of DME . . . 9
2.3.1 Catalyst configuration and composition . . . 9
2.3.2 Activity and stability of bifunctional STD catalyst systems . . . 10
2.3.3 Byproduct formation . . . 12
2.3.4 Mechanism and kinetics of one-stage DME synthesis . . . 12
2.4 Coating Techniques . . . 13
2.4.1 Slurry preparation . . . 13
2.4.2 Slurry deposition . . . 14
2.4.3 Other coating techniques . . . 15
2.5 Screen Printing . . . 16
2.5.1 Rheology . . . 16
2.5.2 Paste formulation . . . 20

3 Modelling . . . **21**
3.1 Model development . . . 21
3.1.1 The catalysts . . . 21
3.1.2 Diffusion . . . 25
3.1.3 Reaction kinetics . . . 26
3.1.4 Reactor modelling . . . 26
3.1.5 Implementation of the model in MatLab® . . . 27
3.2 Results & discussion . . . 29
3.2.1 Influence of the relative amounts of the two catalysts . . . 29
3.2.2 Influence of catalyst configuration and its composition . . . 30
3.2.3 Influence of reaction temperature . . . 36
3.2.4 Influence of *F/W* . . . 39
3.2.5 Influence of feed composition . . . 40
3.3 Summary . . . 41

4 Synthesis . . . **43**
4.1 Materials and equipment . . . 43
4.2 FSP-CZA . . . 43

4.2.1 Semi-continuous collection of the nanopowder . . . 45
4.3 Particulate catalyst configurations . . . 47
4.3.1 Hybrid particulate catalyst of medium proximity (CZA+Z) . . . 48
4.3.2 Hybrid particulate catalyst of close proximity (CZA&Z) . . . 48
4.3.3 Structured core@shell particulate catalyst (CZA@Z) . . . 49
4.4 Planar catalyst configurations . . . 53
4.4.1 Preliminary investigations . . . 54
4.5 Summary . . . 55

5 Characterization . . . 57
5.1 Methods . . . 57
5.2 FSP-CZA: physico-chemical characterization . . . 59
5.2.1 Influence of the collection system . . . 59
5.2.2 Influence of the solvent . . . 61
5.2.3 Further characterization of the FSP-CZA . . . 64
5.2.4 Influence of the calcination . . . 65
5.2.5 Agglomerated SD-CZA . . . 67
5.3 FSP-CZA: reaction tests . . . 68
5.4 Particulate catalyst configurations: physico-chemical characterization . . . 70
5.4.1 Hybrid particulate catalyst of medium proximity (CZA+Z) . . . 70
5.4.2 Hybrid particulate catalyst of close proximity (CZA&Z) . . . 70
5.4.3 Structured core@shell particulate catalyst (CZA@Z) . . . 72
5.5 Particulate catalyst configurations: reaction tests . . . 75
5.5.1 Hybrid particulate catalyst of medium proximity (CZA+Z) . . . 76
5.5.2 Structured core@shell particulate catalyst (CZA@Z) . . . 77
5.6 Planar catalyst configurations: rheology of the pastes . . . 78
5.6.1 Hybrid planar catalyst of medium proximity (CZA#Z) . . . 78
5.6.2 Structured planar double layer catalyst system (CZA//Z) . . . 80
5.7 Planar catalyst configurations: structural characterization . . . 83
5.7.1 Calcination of the coated foils . . . 83
5.7.2 Hybrid planar catalyst of medium proximity (CZA#Z) . . . 85
5.7.3 CZA planar catalyst system . . . 87
5.7.4 Structured planar double layer catalyst system (CZA//Z) . . . 89
5.8 Planar catalyst configurations: reaction tests . . . 90
5.8.1 Hybrid planar catalyst of medium proximity (CZA#Z) . . . 90
5.8.2 CZA planar system . . . 92
5.8.3 Structured planar double layer catalyst (CZA//Z) . . . 93
5.9 Kinetic study of the STM reaction . . . 95
5.9.1 Further modelling results . . . 96
5.10 Summary . . . 97

6 CO_2 activation for MeOH synthesis . . . 101
6.1 State of the Art . . . 101
6.1.1 Catalysts for CO_2-to-MeOH reaction . . . 101
6.2 Synthesis . . . 104

6.3 Characterization . . . 105
6.3.1 ZrO_2: physico-chemical characterization . . . 105
6.3.2 CZZ catalysts: physico-chemical characterization . . . 107
6.3.3 CZZ catalysts: reaction tests in the CO_2-to-MeOH reaction . . . 110
6.4 Summary . . . 112

7 Conclusion & Outlook . . . 115

List of Abbreviations and Symbols . . . 119

List of Figures . . . 123

List of Tables . . . 129

Bibliography . . . 131

A Supplementary Figures and Tables . . . 147

1 Motivation

It is generally accepted that anthropogenic emissions of greenhouse gases are responsible for global warming and the consequent climate change occurring on our planet [1, 2]. In order to limit its otherwise unavoidable effects, in 2015, by the Paris Agreement, the member states of the United Nations committed themselves to limiting the temperature rise to well below 2 °C compared to pre-industrial levels [3]. In their special so called "1.5 °C report", in 2018 the Intergovernmental Panel on Climate Change stated that the maximum increase in global temperature should rather be kept at 1.5 °C above pre-industrial levels at most to avoid drastic climate-related consequences to, e.g., health, food security, water supply, and economic growth [4]. As outlined by the United Nations, in the European Union the emission in the transport sector even increased by 19.27 % from 1990 until 2017 [5]. Therefore, it is of crucial importance to replace the conventional fossil sources in the production of fuels, that is why the European Commission defined the target to reach at least a share of 10 % of transport fuels from renewable sources by 2020 and 14 % in 2030 according to the 2009 [6] and 2018 [7] renewable energy directives, respectively. However, in 2050 as the latest, net-zero CO_2 emissions should be reached in order to meet the 1.5 °C target [3].

As renewable power will be the most obvious energy source in a defossilized future energy system by 2050, the straight-forward fuel will be renewable power itself, i.e., e-mobility. However, for certain transport sectors such as heavy duty transportation and long-distance aviation, the high energy density of hydrocarbon fuels will also be needed in the future. Therefore, it is urgent to produce synthetic hydrocarbon fuels by innovative approaches, e.g., following the so-called Power-to-X (P2X) concept, which involves the storage of electrical energy in chemical bonds, typically using water and CO_2 as H- and C-sources, respectively (see schematic representation in Figure 1.1) [8, 9]. The final product can be gaseous or liquid hydrocarbons or oxygenates (methane, Fischer-Tropsch products, alcohols, ethers). These concepts permit the replacement of fuels or chemicals currently produced from fossil energy and allow the continued use of the existing infrastructure for storage, distribution and application. If the

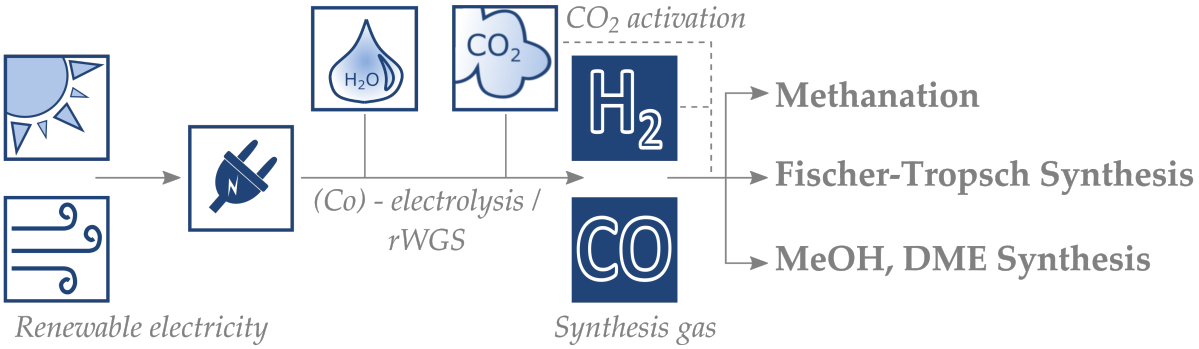


Figure 1.1: Scheme of the Power-to-X concept.

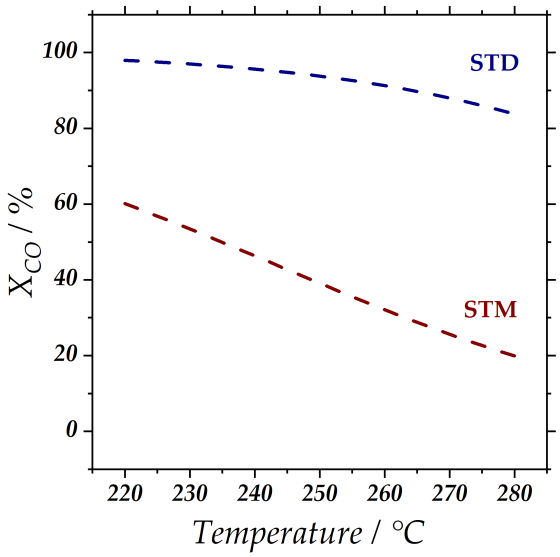


Figure 1.2: CO-conversion (X_{CO}) at the thermodynamic equilibrium for synthesis gas to methanol (STM) and direct synthesis of DME (STD).

CO_2 stems from the atmosphere and the energy needed for its conversion into fuels in the Power-to-X process is *CO_2-free*, a closed CO_2-cycle is established [10, 11].

Against this background, dimethyl ether (DME) synthesized from CO_2 and renewable hydrogen is of great interest, as it can be used as a fuel, either directly in compression-ignition engines, or after further processing into a substitute for fossil-based gasoline (DME-to-Gasoline). In addition, DME is a valuable feedstock for the chemical industry (e.g. DME-to-Olefin) [12, 13, 14]. In the conventional process, DME is produced from synthesis gas (CO/H_2) in two separate steps: first, the synthesis gas is converted over a Cu-based catalyst into methanol (synthesis gas to methanol (STM), Equations 1.1 - 1.3), which is then dehydrated in a second step to DME over a solid acid catalyst, such as γ-Al_2O_3 or zeolites (methanol to DME (MTD), Equation 1.4). In doing this, the thermodynamics limits the CO-conversion (X_{CO}) in the STM reaction under the typical operating conditions (p = 30 - 50 bar; T = 200 - 260 °C) to rather small values, which makes energy-intensive recycling of the unreacted synthesis gas after the first step necessary.

$$CO + 2\,H_2 \rightleftharpoons CH_3OH \qquad \Delta H^{\circ}_{298\,\mathrm{K}} = -90.7\,\mathrm{kJ\,mol^{-1}} \tag{1.1}$$

$$CO_2 + 3\,H_2 \rightleftharpoons CH_3OH + H_2O \qquad \Delta H^{\circ}_{298\,\mathrm{K}} = -49.8\,\mathrm{kJ\,mol^{-1}} \tag{1.2}$$

$$CO + H_2O \rightleftharpoons CO_2 + H_2 \qquad \Delta H^{\circ}_{298\,\mathrm{K}} = -40.9\,\mathrm{kJ\,mol^{-1}} \tag{1.3}$$

$$2\,CH_3OH \rightleftharpoons CH_3OCH_3 + H_2O \qquad \Delta H^{\circ}_{298\,\mathrm{K}} = -23.4\,\mathrm{kJ\,mol^{-1}} \tag{1.4}$$

In the context of decentralized Power-to-Fuel concepts, small scale, as simple as possible and highly efficient (i.e. high per-pass yield to the desired product) processes and plants are required. Here, the combination of the STM with the methanol (MeOH) dehydration in one single stage is very promising (one-stage synthesis gas to DME (STD)): by directly converting the MeOH to DME via the subsequent reaction (Equation 1.4), the equilibrium of the STM-reaction is shifted to the products and, thus, hig-

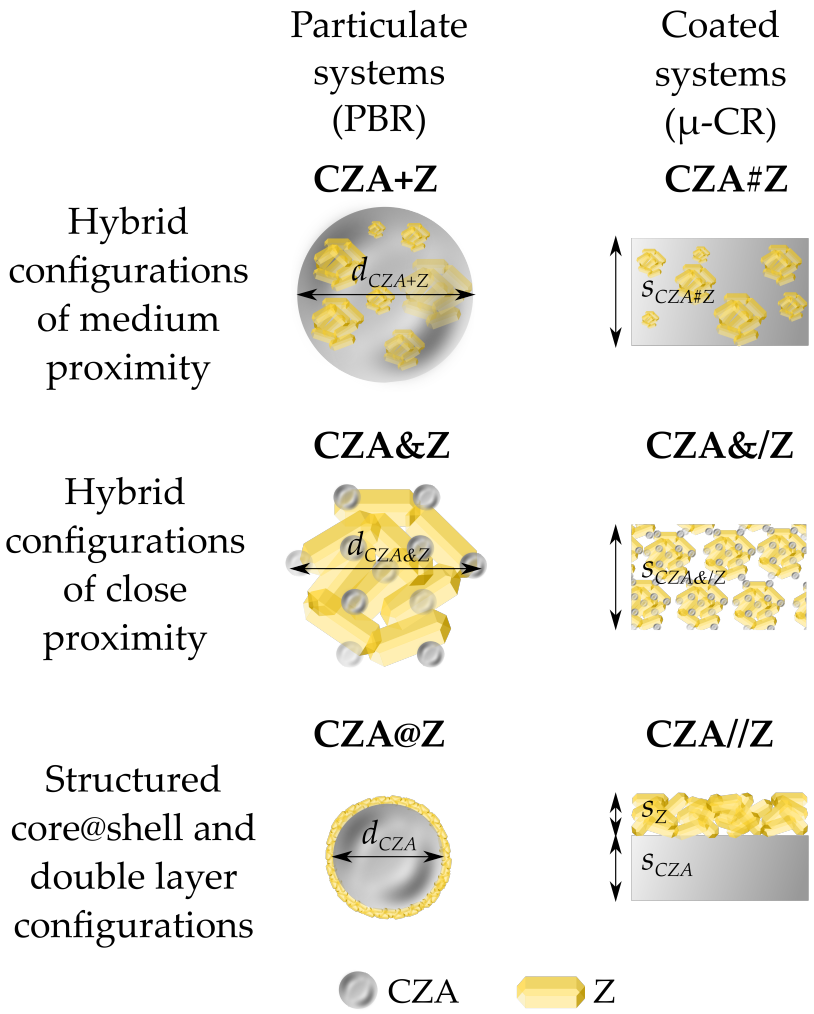


Figure 1.3: Illustration of the catalyst configurations investigated in the frame of this thesis.

her X_{CO} can be achieved. In addition to the increase of per-pass X_{CO}, enhancing the DME-selectivity (S_{DME}) can further contribute to the compactness of the plant. Both, X_{CO} and S_{DME}, can be optimized by choosing the proper catalyst materials and their arrangement.

1.1 Objectives of the Dissertation

In the frame of the P2X concept described above, this work aims at bringing into connection modelling, synthesis and characterization tools applied to different catalyst configurations for the STD reaction. The catalyst systems considered and investigated were obtained by combining the $Cu/ZnO/Al_2O_3$ (CZA) and zeolite H-ZSM-5 (Z) for the STM and the MTD reactions, respectively.

These configurations cover both, particulate and planar (coated) configurations operated in a packed-bed-reactor (PBR) and a micro-channel-reactor (μ-CR), respectively. Figure 1.3 illustrates all the catalyst configurations considered, their nomenclature and application: first, hybrid particulate and planar systems with the two catalysts either arranged at the micrometer-scale (medium proximity: CZA+Z and CZA#Z) or the sub-micrometer-scale (close proximity: CZA&Z and CZA&/Z); second, structured catalysts with a dedicated ordering of the two individual catalysts, namely the spherical core@shell particu-

late system (CZA@Z) as well as its planar counterpart (CZA//Z).

The challenge of the **modelling** is the capability to foresee how the catalytic systems together with the synthesis parameters influence both X_{CO} and product distribution; the challenge of the **synthesis** is the preparation of the catalysts, which should be reproducible and compliant to the concepts pursued and the corresponding assumptions in the modelling; challenge of the **characterization** is the accomplishment of the parameters to be implemented in the modelling as well as the validation of the theoretical study and of the succesful synthesis. Figure 1.4 schematically represents the knowledge-based approach which is the background of this study.

The structure of this dissertation can be briefly summarized as follows: chapter 2 gives the theoretical background and the state of the art concerning catalysis and reaction engineering in the STD process; the modelling of the catalyst configurations for the STD reaction in both PBR and μ-CR is presented in chapter 3; the synthesis procedure of the catalysts is described in chapter 4; the characterization of the materials synthesized, with respect to the physico-chemical properties and the activity shown in the reactors, is outlined in chapter 5. CO_2 activation for the MeOH synthesis is considered separately in chapter 6. Finally, in chapter 7 the principal outcomes and findings of this work are summarized and an outlook to future studies is given.

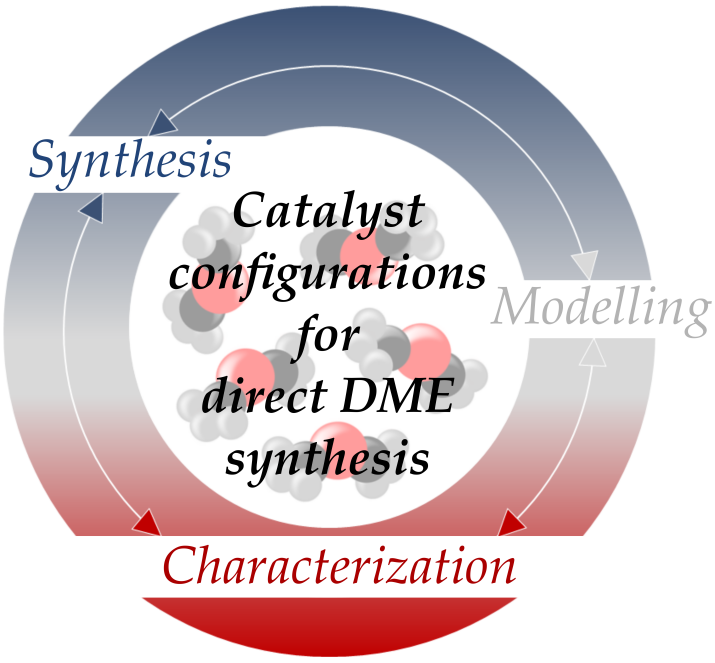


Figure 1.4: Knowledge-based circular work flow pursued in this thesis.

This work was supported by the German Research Foundation (DFG) via its priority program 1570 *Porous Media with Defined Pore Structure in Process Engineering - Modelling, Application, Synthesis*; (Grant No. DI 696/9-3 and SCHW 478/23-3) and by the Vector Foundation (CO_2*mpactDME*).

2 State of the Art

In the following a state of the art regarding the scientific response to the challenges relative to the decentralized STD process, with focus on the methods used in the frame of this work, is given. The catalysis in the STM process is presented in section 2.1; the possibility of preparing a CZA-catalyst via flame spray pyrolysis (FSP) is demonstrated in section 2.2. Section 2.3 deals with the catalysis, in particular the potential of hybrid or bifunctional catalysts with a dedicated configuration, and with the modelling of the STD process. Finally, several coating techniques as well as a detailed description of the screen printing are presented in sections 2.4 and 2.5, respectively.

2.1 Methanol Synthesis

With a global annual consumption of $85 \cdot 10^6$ t in 2016, MeOH is one of the most important commodities in chemical manufacturing [15]. The MeOH production from synthesis gas on industrial scale started in 1923 at *BASF* with the *high temperature process*: a Cr/Zr-based catalyst was operated at p = 300 bar and T = 300 - 400 °C, even if Cu-based materials, more active but more sensitive to the presence of poisons (above all sulphur), were already known [15]. From the 1950s on, a higher purity of the synthesis gas could be achieved and Cu-based catalysts could be used in the *low temperature process*, operated at $30\,\text{bar} \leq p \leq 120\,\text{bar}$ and $200\,°\text{C} \leq T \leq 300\,°\text{C}$: both better selectivity and economy of the process were fulfilled [15, 16, 17]. From the 1970s onwards, the optimization of the MeOH production was focused on the reactor concept, and several fixed-bed-reactors were developed (e.g. the boiling water reactor (*ICI*) and the water-cooled reactor and the gas-cooled-reactor (*Lurgi*)). Due to the low equilibrium conversion of the reaction system (see also Figure 1.2), the target of process optimization was to improve the cooling of the reaction mixture along the catalytic bed in order to obtain higher conversion. In general, the plant consists of three sections: *(i)* the synthesis gas generation (containing up to 10 vol.% CO_2), *(ii)* the MeOH synthesis and *(iii)* the MeOH distillation. A recycling of the unreacted synthesis gas is necessary in large scale plants [15, 16].
Beside Cu, the application of noble metals, such as Pd and Au, has come into question, and the activity of these systems has been proved since the 1920s [17, 18, 19, 20]. Recently, Gentzen et al. reported the activity of a Pd-based catalyst combined with γ-Al_2O_3 for the STD reaction by feeding CO-rich gas [18]; Xu et al. investigated a $Pd/ZnO/Al_2O_3$ catalyst for the MeOH synthesis from a CO_2-rich gas [19]; gold supported over several oxides was studied by Sakurai and Haruta, concluding that the highest yield to MeOH is obtained on a $Au/ZnO/TiO_2$ catalyst [20]. However, noble metals have not been industrially used as catalysts for the STM so far [17].

2.1.1 The $CuO/ZnO/Al_2O_3$ catalyst for the STM reaction

Due to the tendency of pure copper towards sintering, the metal should be supported on other oxides [17]. Even if $Cu/ZnO/Al_2O_3$ (CZA) catalysts have been industrially used for decades, finding out

why this combination is the best as well as which mechanism is taking place on these catalysts has been subject to a scientific diatribe [16, 17]. In this way, the evolution within the STM catalysis was somehow opposite compared to theory: the industrial solution came before its rational demonstration through scientific studies. First, the role of the ZnO, which can catalyse the STM reaction alone, and its coupling with the metallic Cu have been investigated; second, the advantage in using Al_2O_3 as a third component instead of other inert oxides, such as Cr_2O_3, TiO_2, Ga_2O_3 and ZrO_2, has been proven [17].

In general, the CZA catalyst is prepared by co-precipitation, starting from a Cu-rich molar solution. In the open literature criteria for the optimization of the synthesis are reported, e.g. by finding the most proper metal molar ratio and precipitation conditions (temperature, pH, aging time) [16]. Beside the wet syntheses, flame combustion methods are also reported in literature (see section 2.2) [17]. Even if CZA catalysts have been prepared for decades by several companies [16], such as the European *Clariant*, *Johnson Matthey* and *Haldor Topsøe* as well as the Japanese *Mitsubishi Gas* (e.g. patents [21, 22]), in the last years, many studies have been published with respect to the co-precipitation method and its possible improvement [23, 24, 25]. Behrens et al. compared the precipitation synthesis of commercial CZA catalysts starting from nitrate- and formate-solutions [23]. The authors could optimize the synthesis with nitrates as precursors and confirmed the advantage of the industrial preparation procedure: controlling both pH and temperature hinders the sequential precipitation of CuO and ZnO, and a more homogeneous metal distribution within the particle is achieved [23]. Moreover, when the same operation is applied to the formate solution, the resulting CZA catalyst presents an even higher Cu surface area and higher activity for the STM reaction, concluding that the formate route could be subject to further optimization [23]. The addition of a surfactant in the solution to be precipitated was investigated by Chu et al., who compared blank CZA (without any addition of surfactant) to CZA catalysts prepared from solutions containing different amounts of surfactant; the authors demonstrated a promising performance of the catalyst when adding tetraethylammonium hydroxide during the co-precipitation [24].

The mechanism of the STM reaction has been subject to several studies, in order to find out which is the main MeOH source, either CO and/or CO_2, the rate determining step, and the active sites on the CZA surface [17]. In the 1990s, it could be proved, mostly by isotope studies, that the main C-source is CO_2, even if the catalyst is able to convert CO through a parallel, but slower, route [17]. In the same years, kinetic models were proposed, either considering both CO_2- and CO-hydrogenation [26], or CO_2 as the main and sole source [27]; in both cases, one single kind of active site on the catalyst surface was considered [26, 27]. A better understanding of the commercial CZA catalysts, provided e.g. in many contributions of the research groups of Behrens and Schlögl (see Refs. [28, 29]), allowed the development of kinetic equations for the STM taking into account the presence of different types of active sites on the catalytic surface, as in the study of Seidel et al. (see also section 2.3.4) [30].
Further studies were focused on the intermediates produced during CO- and CO_2-hydrogenation: in general, it is accepted that the former takes place through the formyl ($HCO^\star$) route, and the latter though the formate ($HCOO^\star$) route [31, 32, 33]. In particular, the CO-hydrogenation steps can be summarized as $CO^\star \rightarrow HCO^\star \rightarrow CH_2O^\star \rightarrow CH_3O^\star \rightarrow CH_3OH^\star$ [33, 34]. Yang et al. proposed a third path, which starts either from CO or CO_2, through the formation of the carboxyl group ($COOH^\star$) [31], even if this is not in accordance with what was reported by Kunkes et al., who referred the carboxyl-route to the

r-WGS only and not to the CO_2-hydrogenation mechanism [32]. Regarding the rate determining steps of CO- and CO_2-hydrogenation, these have been identified in the hydrogenation of the formyl group to CH_2O^* and in the hydrogenation of the formic acid ($HCOOH^*$) to $CH_3O_2^*$, respectively [33, 34].
It is important to recall that the mechanism and the kinetics of a reaction system depend on the catalyst and its physico-chemical properties. In literature, beside the studies about the STM kinetics, the structure of industrial CZAs was investigated, so that the requirements for the synthesis of a proper catalyst for the STM are available starting from several contributions [28, 29, 34, 35]. In general, the advantage due to synergy between the Cu and ZnO is well reported [28, 34, 35]; furthermore, Al_2O_3 acts as a structural promoter [29]. As reported in the work of Behrens et al., the final CZA should have a Cu molar content higher than 50 % [28]. Even if the Cu alone catalyses the STM reaction, the presence of ZnO is crucial, as the oxide allows to disperse the copper phase to increase its surface area [28]. Combining experimental and theoretical results, Behrens et al. proved that the stepped Cu[211] surface, stabilized by bulk defects, is more active compared to the flat Cu[111], due to the lower energy barrier for the formation of intermediates during both CO- and CO_2-hydrogenation [28]. The authors reported that Cu nanoparticles in the form of spheres intrinsically contain steps and that this shape should be a target during the synthesis of the CZA [28]. The presence of defects in a commercial CZA catalyst was statistically analysed by Kasatkin et al., who found a correspondence between the amount of non-equilibrium structures (defects and lattice strain) within Cu and a better activity [36]. However, the metallic Cu is not the sole active site during the STM as the ZnO does not act as sole spacer among the Cu particles [28, 34, 35, 36]. Under reaction conditions, the interaction between Cu and ZnO as well as the substitution with Zn in the Cu lattice (alloy) allow the partial coverage of the Cu surface with ZnO_x, with a consequently higher activity (the energy barrier for intermediate formation decreases) [28, 35]. The important role of ZnO in the reaction mechanism was investigated by Studt et al.: at reaction conditions (at least 5 vol.% CO_2 in the feed) the presence of ZnO decreases the energy barrier of formate (intermediate in the CO_2-to-MeOH reaction) hydrogenation to the final product; on the contrary, formate acts as a poison on sole Cu, as its further hydrogenation is kinetically hindered with consequent blockage of the active sites for CO-hydrogenation [34]. Beside this, the authors confirmed by $^{13}CO_2$ isotope labelling experiments that MeOH is formed mainly from CO_2 during the STM reaction [34].
According to Kasatkin et al., Al_2O_3 is present in the CZA material either as a segregated structure or as mixed-oxide particles; the authors observed mainly amorphous Al_2O_3 agglomerates mixed with Zn and Cu and, rarely, crystallized Al-rich structures, attributed most likely to zinc aluminate, $ZnAl_2O_4$, rather than to pure cubic Al_2O_3 [36]. Behrens et al. synthesized different CZA catalysts via co-precipitation, according to a commercial recipe, changing the amount of Al_2O_3 and maintaining the molar ratio Cu/Zn = 70/30; the authors concluded that the formation of the less active aurichalcite, $(Cu,Zn)_5(OH)_6(CO_3)_2$, and hydrotalcite, $(Cu,Zn)_xAl_{1-x}(OH)_2(CO_3)_{x/2} \cdot m\ H_2O$ phases is hindered at an Al-concentration of approximatively 3 - 4 mol.-%, favouring the desired zinc malachite phase, $(Cu,Zn)_2(CO_3)(OH)_2$, able to increase the Cu-dispersion, and allowing a better performance at STM reaction conditions in terms of Y_{MeOH} [29]. A higher amount of the promoter favours the formation of the hydrotalcite phase, namely the incorporation of Zn^{2+} in the Al-phase, with consequent lower availability of Cu^{2+} to be incorporated into the zinc malachite. The formation of this phase takes place during the crystallization of the coprecipitate, as also reported in the study of Günter et al. [29, 37].

2.2 Flame Spray Pyrolysis as a Technique for CZA Synthesis

Flame synthesis techniques are currently used for preparation of CZA catalysts (e.g. Ref. [38, 39]). Flame spray pyrolysis (FSP) belongs to the flame aerosol technology, which consists in the formation of fine particles from gases in a flame and are distinguished by particle growth within short time (one second) at high process temperatures [40]. In general, the precursor containing the metal source and the solvent is injected in the burner, and the solvent evaporates due to the high temperature of the flame. The resulting vapour is pyrolysed forming clusters that quickly grow to nanosized particles by nucleation and/or surface reactions; the aerosol stream leaves the high-temperature zone and is cooled down in the low-temperature sector, where the product is collected. The particle grow mostly through either coagulation (weak physical forces among the primary particles) or fusion/coalescence (strong chemical forces holding together the primary particles). This is the so-called *gas-to-particle* conversion, through which it is possible to obtain nanoparticles homogeneous in size. Otherwise, the so-called *droplet-to-particle* conversion takes place: part of the precursor decomposes thermally, part precipitates from the sprayed droplet, leading to densification and sintering; the final product is large, solid or hollow particles [40].
The product is collected by glass fibre filters, bag-house filters, electrostatic precipitators or cyclone separators. The properties of the product are influenced by the precursor, the residence time and the process temperature [40, 41].

A big advantage of FSP is the usage of only one step to synthesize nanopowder from a precursor, while the conventional wet-phase methods include many steps of filtering and washing to achieve the separation of the product from the liquid phase. The FSP procedure can make the whole process more efficient and, if the proper raw materials are used, still not expensive [42]. Nitrate salts are common metal precursors, as they easily dissolve in cheap solvents (like alcohols), even if their low volatility could lead to the formation of bigger and hollow particles according to the *droplet-to-particle* mechanism. By using proper solvents, instead of e.g. alcohols, this challenge can be overcome. Increasing the boiling point and the enthalpy of combustion of the solvent and/or directly adding carboxylic acid can promote the formation of carboxylates in the solution, which are more volatile than the starting nitrate salts [41]. The pyrolysis of such precursor solutions takes place via the *gas-to-particle* mechanism, obtaining more homogeneous nanoparticles [41].
Focusing on the aimed synthesis of this work, namely the CZA catalyst, the *droplet-to-particle* mechanism is reported to take place when starting from Al- and Zn- nitrates, while it has not been observed in the case of Cu-nitrate so far [41]. When Al-nitrates are dissolved in ethanol (EtOH) and pyrolysed to Al_2O_3, the observation of the *droplet-to-particle* mechanism came as a surprise; Strobel and Pratsinis state that only substituting EtOH with a proper mixture of organic components, the *gas-to-particle* mechanism takes place and void-free nanoparticles homogeneous in size can be obtained [41]. During the pyrolysis of the Zn-nitrate solved in EtOH via the *droplet-to-particle* route, the dissociation of ZnO, to Zn and O_2 takes place in the gas phase at temperatures above 1700 °C, namely in the high temperature zone; afterwards, when the temperature decreases, solid ZnO recombines. Therefore, the formation of ZnO can be described with an indirect *gas-to-particle* mechanism [41].
In the open literature, the synthesis of CuO via FSP is reported for applications in catalysis as well as in electrochemistry [38, 43]. Chiang et al. have studied the influence on the CuO particle size during

FSP synthesis using nitrate salts as metal source and deionized water as solvent, claiming that the size can be tailored by adjusting the precursor concentration and the residence time in the high temperature zone [43]. Applying these considerations to this work, where the residence times could not be changed (see section 4.2), only the conclusions about the precursor concentration are noteworthy: increasing the molarity from 0.02 up to 1.4 M, an increase of the product particle size should be expected [43]. The same research group discussed the formation of hollow particles when starting from copper nitrate in the mixture H_2O/EtOH = 90/10 (in vol.-%); no voids were visible increasing the pyrolysis temperature [44]. In a further study, Ce/Cu-based catalysts for the WGS reaction were successfully synthesized via FSP starting from organic metal precursors dissolved in water [45].
In summary, the FSP production of CuO starting from copper nitrates does not show the challenges reported for Al_2O_3 and ZnO oxides, as hollow-free well dispersed CuO nanoparticles were prepared starting from EtOH/H_2O mixtures as solvent, which have a lower combustion enthalpy than pure organic solutions. A proper solvent should be found for the successful synthesis of homogeneous nanosized ZnO and Al_2O_3.

2.3 Direct Synthesis of DME

2.3.1 Catalyst configuration and composition

In the STD process, the choice of a proper arrangement of the catalysts influences both the X_{CO} as well as the product distribution. The proximity of the two individual catalytic species involved can be used as a criterion for their classification: in general, the simplest combination of two different catalysts is a *(i)* physical mixture of particles or pellets on the reactor level (hybrid catalyst bed) [38, 46, 47]. Bringing the active sites for the two reactions closer together by using a *(ii)* physical mixture on the pellet level could be even more beneficial, as the probability for the intermediate (MeOH) to leave the reactor without getting dehydrated to DME decreases [48, 49, 50, 51, 52, 53, 54, 55, 56]. This hybrid system on the pellet level *(ii)* can be prepared by mixing the dried STM- and MTD-catalysts [49, 50, 55] or by preparing a suspension of the two catalysts followed by its filtering, washing, drying and calcination before pelletizing (e.g., pressing into tablets and crushing into the desired size fraction) [52, 56]. In this catalyst configuration, the arrangement of the two catalysts within the pellet cannot be precisely controlled during the preparation of the system. However, it could be achieved, in principle, with tailored synthesis procedures: *(iii)* bifunctional catalysts with a desired arrangement of the two catalysts within the particle being enforced during the synthesis allow for a predefined arrangement, e.g., by synthesizing at least one catalyst in the presence of the other. Thereby, it is possible to control the structure of the bifunctional catalyst and, eventually, achieve a hierarchical arrangement. One example of such a bifunctional, structured catalyst is the STM-catalyst@MTD-catalyst core@shell system, which has been reported to be very promising for enhancing especially S_{DME} [57, 58, 59, 60, 61, 62]. In a core@shell system, the MeOH formed in the core stands a good chance to be converted to DME in the shell, as it has to diffuse through the MTD catalyst shell on its way out of the particle. Further procedures for preparation of bifunctional catalysts for STD with intimate proximity of the two constituents enforced by the preparation principle for STD are reported in literature, such as co-precipitation of the STM catalyst in a MTD-catalyst-containing suspension [63, 54] or the simultaneous co-precipitation, resp. self-assembly of the metallic and acidic functionalities [51].

2.3.2 Activity and stability of bifunctional STD catalyst systems

Even if close proximity of the active sites of the two catalysts should be beneficial for the STD process, in literature this intimate contact has been identified to cause a change of the catalyst connected to deactivation. Martínez et al. studied type *(ii)* hybrid STM-catalyst/zeolite systems and the changes they undergo in several contributions [64, 65, 66, 67], which are comprehensively summarized by Dadgar et al. [46]. It is proposed that the solid-state ion exchange (Cu^{2+} and, eventually, Zn^{2+} vs. protons of the zeolite), the deactivation of the Cu-sites by extra framework aluminum (EFAl), and the promotion of copper sintering by terminal hydroxyl groups or by the water being formed during the STD reaction can cause drastic changes of the STM resp. MTD catalyst activity and stability. Moreover, it was shown that type *(i)* physical mixtures ($\omega_{STM}/\omega_{MTD}$ = 2) do not accelerate deactivation of the STM-catalyst caused by interactions between the two catalysts within an observed period of 50 h TOS [65]. In order to overcome the deactivating interaction between STM and MTD catalysts, García-Trenco and Martínez confined the STM catalyst within the pores of a SBA-15 silica support before mixing it with the zeolite ($\omega_{STM}/\omega_{MTD}$ = 2) to obtain a type *(i)* physical mixture and type *(ii)* hybrid pellets, respectively. Using this approach, both catalyst systems showed retarded deactivation compared to a physical mixture of unsupported CZA and zeolite within 25 h TOS [49]. Dagdar et al. investigated the effects of MeOH dehydration on STM (i.e., on the Cu-based catalyst performance) on the type *(i)* physical mixtures CZA/ZSM-5 ($\omega_{STM}/\omega_{MTD}$ = 8/1) and CZA/γ-Al_2O_3 ($\omega_{STM}/\omega_{MTD}$ = 1/4) [46]. From the results obtained the authors concluded that, independently of the type of dehydration catalyst used, and even though there should be a thermodynamic benefit, in long term the MeOH synthesis kinetics is negatively affected by combining the STM and MTD reactions. The authors attributed these findings to the higher partial pressure of water during the STD reaction in comparison to the sole STM reaction. However, no deactivation was observed within 72 h TOS [46].

Ramos et al. compared the performance of the STD reaction on different type *(i)* physical mixtures ($\omega_{STM}/\omega_{MTD}$ = 1/1) for various acidic catalysts, concluding that the most efficient system is CZA/H-ZSM-5. By changing the ratio $\omega_{STM}/\omega_{MTD}$ of this combination in the range between 1 and 4, the authors observed a comparable activity and concluded that at these conditions the overall STD reaction is limited by the STM-step [47]. Similar studies were carried out by Peláez et al., who investigated the STD process using type *(i)* physical mixture CZA/γ-Al_2O_3 and reported $\omega_{STM}/\omega_{MTD}$ = 12.33 as the most efficient mass ratio of the two catalysts with respect to X_{CO} and Y_{DME} [68].

In literature, the hybrid system on pellet level *(ii)* has been investigated focusing on the influence of the preparation method (dry vs. wet mixing) and of the $\omega_{STM}/\omega_{MTD}$ ratio [49, 50, 64]. In this context, Cai et al. observed an increase in activity and a comparable product distribution when changing the $\omega_{STM}/\omega_{MTD}$ ratio of the hybrid pellets made via dry mixing from 1/2 up to 5/3. No information about the deactivation of the catalyst is given in the accordant paper [50]. Ereña et al. claimed that hybrid pellets prepared via wet mixing of CZA/NaH-ZSM-5 and CZA/γ-Al_2O_3 with $\omega_{STM}/\omega_{MTD}$ equal to 4 and 2, respectively, perform well in terms of X_{CO} and S_{DME} in STD [52]. The same authors observed the production of paraffins and a deactivation of the CZA/γ-Al_2O_3 system within 50 h TOS assigned to the deposition of coke [69]. Gentzen et al. prepared a type *(ii)* hybrid CZA/γ-Al_2O_3 pelletized system via wet mixing with $\omega_{STM}/\omega_{MTD}$ = 1, which showed deactivation within 115 h TOS as signified by lower X_{CO}, but constant S_{DME} [56]. García-Trenco et al. showed that for $\omega_{STM}/\omega_{MTD}$ = 6 and 3, in general, hybrid type *(ii)* pellets made via dry mixing perform better than via wet mixing. X_{CO} and S_{DME} decreased

with increasing $\omega_{STM}/\omega_{MTD}$ ratio, which was not the case for the physical mixture *(i)*, able to perform close to the thermodynamic equilibrium up to $\omega_{STM}/\omega_{MTD}$ = 9 [64].

Bifunctional catalysts reported in literature obtained from special syntheses rather than from mixing according to *(iii)* have been most often synthesized via the co-precipitation method, and, in some cases, their performance was compared with that of the type *(i)* physical mixture [51, 54, 63]. Ahmad et al. report a similar activity of a bifunctional catalyst made via oxalate co-precipitation with respect to the *(i)* physical mixture [63]. Jeong et al. synthetized and investigated bifunctional CZA/γ-Al_2O_3 catalysts prepared via co-precipitation of the STM catalyst in a γ-Al_2O_3 containing slurry with $\omega_{STM}/\omega_{MTD}$ in the range of 1 - 7, observing the best performance in terms of STD reaction rate for $\omega_{STM}/\omega_{MTD}$ = 1.75 with no deactivation within 20 h TOS [54]. A one-pot synthesis of CuO precipitation during γ-Al_2O_3 self-assembly was carried out by Jiang et al. showing a constant activity of the bifunctional catalyst for TOS > 15 h [51].

Several studies show the advantage of bifunctional core@shell catalysts in the STD reaction: prepared via different routes, higher S_{DME} and higher X_{CO} were found in comparison to either type *(ii)* hybrid particles of the same individual catalysts with $\omega_{STM}/\omega_{MTD}$ = 10 [57] resp. $\omega_{STM}/\omega_{MTD}$ = 5 [58] or type *(i)* hybrid catalyst bed with $\omega_{STM}/\omega_{MTD}$ = 10 [59]. However, except for the work of Phienluphon et al., where correspondence between the compositions of the core@shell catalyst and the hybrid particles was found, in the mentioned studies the $\omega_{STM}/\omega_{MTD}$ of the hybrid particle reference system did not match the composition of the accordant core@shell system, making it difficult to draw robust conclusions from the results presented. CZA-core@MFI-zeolite-shell catalysts (shell thickness: 3.9 µm, ω_{MTD} = 7.6 %) prepared by Yang et al. showed lower X_{CO} than the bare core catalyst. However, the core@shell catalysts exhibited higher S_{DME} than the physical mixture ($\omega_{STM}/\omega_{MTD}$ = 10) [57]. Wang et al. hydrothermally synthesized a CZA-core@amorphous-SiO_2/Al_2O_3-shell catalyst and reported for the sample with 10 µm shell thickness likewise higher conversion than the physical mixtures ($\omega_{STM}/\omega_{MTD}$ = 10) [59]. Nie et al. prepared core@shell catalysts with a zeolite-core enwrapped by a Cu-based shell showing higher X_{CO} as compared to the bare MeOH synthesis reference catalyst [62]. Here, the authors attributed the beneficial effect of this configuration to the maximization of the contact between MeOH synthesis sites and MeOH dehydration sites. Nevertheless, deactivation was observed in the first hours of the STD reaction and ascribed to potential interaction between the two catalyst constituents [62]. In [60], Pinkaew et al. prepared a Cr/ZnO-core@SAPO 46-shell catalysts ($\omega_{STM}/\omega_{MTD}$ = 20) which showed higher conversion and higher S_{DME} compared to hybrid pellets of $\omega_{STM}/\omega_{MTD}$ = 10. Phienluphon et al. reported the synthesis of a CZA-core@SAPO 11-shell ($\omega_{STM}/\omega_{MTD}$ = 5) via a physical coating method showing higher X_{CO} and S_{DME} in the STD reaction as compared to the accordant type *(ii)* hybrid pellets [58]. In the latter contribution, the authors explicitly mention that the core@shell catalyst configuration protects the core catalyst from the harsh reaction environments [58]. Building on this, Sánchez-Contador et al. recently reported the preparation of a Cu-based-core@SAPO-11-shell catalysts also applying the physical coating method with $\omega_{STM}/\omega_{MTD}$ = 2/1, 1/1 and 1/2 and found higher X_{CO} and S_{DME} as compared to the accordant type *(ii)* hybrid pellet reference catalysts [61]. It is noteworthy that setting the proper ratio for physical mixtures and, in most of the cases, for hybrid particles is feasible, but cannot be freely controlled for a core@shell system due to the synthesis procedure. In addition, with the shell thickness (decreasing $\omega_{STM}/\omega_{MTD}$) the corresponding diffusion path length within the shell increases which could result in mass transport limitations.

2.3.3 Byproduct formation

During the STD process, the formation of by-products (i.e. hydrocarbons (HC)) might become an issue when the acidity of the dehydration catalyst is sufficiently strong and the reaction temperature is high enough. In general, these reactions should be avoided during the STD process, whereas they are crucial for the so-called Methanol-to-Gasoline and Methanol-to-Olefin processes, which are operated at least at 290 °C, in order to increase the selectivity towards the hydrocarbons [70, 71, 72]. The STD process is efficiently operated in the temperature range of 250 - 280 °C [68, 73]. Using type *(ii)* hybrid catalyst pellets for the STD reaction at p = 30 bar and feeding a mixture of H_2/CO = 4/1, Aguayo et al. detected hydrocarbon formation already at 250 °C [70]. The authors proposed that, due to the high pressure of the system, the formation of paraffins occurs directly from the syngas and is catalysed by the metallic sites. This was proven by feeding a mixture of MeOH and DME at the same conditions without any hydrocarbon formation [70]. Ereña et al. operated the STD reaction feeding a gas mixture of $H_2/CO/CO_2$ = 3/1.5/1. The production of hydrocarbons increased when increasing the temperature from 175 °C up to 350 °C (S_{HC} = 0 % up to 275 °C) [73]. Ahmad et al. ran the STD reaction at 40 bar and 250 °C, feeding the gas mixture H_2/CO = 1/1 and found a selectivity S_{HC} = 1 - 7 %, depending on the preparation route of the catalyst [63]. Cai et al. observed a dependency of the S_{HC} on zeolite particle size and *GHSV*: at p = 20 bar and T = 260 °C a maximum of S_{HC} = 2 % was detected for the largest zeolite particle size and smallest *GHSV* investigated [74]. Jeong et al. operated the STD reaction at p = 35 bar and T = 270 °C with a synthesis gas feed of H_2/CO = 2/1. After changing the CZA/γ-Al_2O_3 ratio from 1 to 7, the formation of HC (mainly methane) was observed with S_{HC} between 2.4 - 4.6 % [54].

2.3.4 Mechanism and kinetics of one-stage DME synthesis

In open literature, modelling of the individual stages, namely the STM and MTD and, in some cases, also the STD process are discussed. Mainly, these works comprise kinetic studies, some also coupled with a reactor modelling, based on CZA catalyst and either γ-Al_2O_3 or zeolites for the two stages, respectively, and aim to identify the optimal operating conditions of the processes [26, 27, 30, 68, 70, 75, 76, 77, 78, 79]. Concerning the STM process, thermodynamic and kinetic studies as well as investigations on the internal mass transport at the reaction conditions considered can be found in Refs. [26, 27, 30, 80, 81]. The mechanism and the kinetics of the STM have been discussed for decades, and different reaction rate laws have been proposed such as in the works of Graaf et al., Vanden Bussche and Froment, as well as in the more recent work of Seidel et al., to name but a few [26, 27, 30]. The earlier works of Graaf et al. and of Vanden Bussche and Froment assumed only one single type of active sites [26, 27], while Seidel et al. considered three different kinds of catalytically active sites: the ones responsible for the activation of hydrogen, oxidized sites for CO-hydrogenation and the reduced sites for CO_2-hydrogenation (see also section 2.1.1) [30]. For the second stage (MTD), Bercic and Levec investigated the influence of mass transport and kinetics over γ-Al_2O_3, while Tavan et al. compared the performance of γ-Al_2O_3 and H-ZSM-5 [75, 76]. Regarding the STD, Hadipour and Sohrabi reported a model of a fixed-bed-microreactor under dynamic conditions over a physical mixture of CZA and γ-Al_2O_3 [77], Lu et al. proposed a mechanism and kinetics for the STD in a fluidized-bed reactor for the CZA/H-ZSM-5 system [78]. In a recent contribution Peláez et al. simulated the STD process via 2D multi-scale modelling of a multi-tubular fixed bed reactor [79]. In general, the side-reactions (production of hydrocarbons) are not considered in

the studies on the mechanism mentioned above [68, 77, 82], while the research groups of Ordóñez and Bilbao proposed a kinetic model of the STD process also taking the inhibition by water [68] as well as the co-production of hydrocarbons into account [70]. In most of the works mentioned, the processes were studied on commercial catalysts and, for the STD in particular, either the view was limited to a physical mixture of the two catalysts on reactor level or the influence of the particular catalyst configuration was not considered at all [26, 75, 76, 77]. However, this is a crucial parameter in the STD process, as the two catalysts can be arranged in close proximity following various concepts (see section 2.3.1) with consequently completely different structural parameters and transport properties.

In summary, several studies in literature have discussed the potential of bifunctional catalyst systems in the direct STD reaction based on different preparation principles and configurations of the catalyst(s). In addition, based on literature, deactivation effects must be considered when Cu-based MeOH synthesis catalysts are in close proximity to an acidic dehydration catalyst. Therefore, experimentally determined reaction performance data alone might be misleading when comparing different catalyst configurations. Furthermore, the production of side-products (hydrocarbons) during the STD process has been reported at certain conditions by experimental works, which is why some authors included these side reactions in the modelling of the STD kinetics. In order to quantify the effect of a certain catalyst configuration, in this thesis, on the basis of the experimental results, theoretic tools are used to evaluate the bare effect of the catalyst configuration (medium resp. close proximity in hybrid systems and structured bifunctional catalysts; particulate and planar (coated) systems) and composition independent of the aforementioned potential catalyst modification and deactivation caused by the material interactions and without the influence of possible side reactions.

2.4 Coating Techniques

In the open literature plenty of techniques are reported for coating different kinds of layers (e.g. (photo)-catalytic, photovoltaic, electrode materials) on various substrates. In general, they can be divided into methods during which the preparation of a slurry and the coating process are separate and during which the precursor (also named target) of the material to be coated is directly applied to the substrate. In the former category the slurry can be first prepared e.g. via wash-coating, sol-gel or hybrid methods and then coated via dip-, spray-, spin- coating as well as inkjet and screen printing; sputtering, electric beam evaporation, pulsed laser deposition, chemical vapour deposition belong to the latter class of coating techniques [83, 84, 85]. In the following, these techniques applied to catalysis are described.
In general, regardless the coating method used, the substrate needs a pre-treatment, in order to enhance the adhesion with the layer. For this either thermal, up to 1000 °C, or chemical treatments, with nitrates or acids, can be used to obtain a cleaned and rough surface. Similarly, once the deposition of the slurry took place, the coated substrate should be dried and calcined to remove the solvent and the binder components [84].

2.4.1 Slurry preparation

One of the most common slurry based procedures is *wash-coating*, which is also used in industrial scale [83, 86, 87]. It consists of preparing a slurry, containing the catalyst particles homogeneously disper-

sed in the solvent (in general water) and, when an adjustment of the viscosity is necessary, a binder (e.g. hydroxy ethyl cellulose, polyvinyl alcohol). After drying and calcination of the catalytic layer, this can be further wet-impregnated, using metal nitrates, as reported in literature for PdZn, Cu/Al_2O_3 and Cr/Al_2O_3 systems [88, 89]. The *sol-gel* procedure consists of the preparation of a colloidal dispersion containing the precursor of the material to be deposited. Composition, viscosity, pH of the gel as well as ageing time, necessary for gelation of the sol, influence strongly the thickness of the layer, its porosity and the presence of cracks. In literature different metal oxides, such as Al_2O_3, ZrO_2, TiO_2, have been coated via sol-gel. Furthermore, the technique is suitable for coating foams and, in general, highly porous substrates [83, 84, 90, 91, 92]. Besides, hybrid methods between wash-coating and sol-gel can be applied,when the catalyst itself is dispersed in the sol and acts as a binder, participating in the chemical and textural properties of the final layer; higher thickness is in general achieved [84].

2.4.2 Slurry deposition

The easiest way for coating of a slurry is doing it manually by using a pipette. This approach does not require specific equipment but the resulting layer is usually not homogeneous with respect to the thickness. However, this method is reported in literature and could be used for a preliminary study [83, 89]. Commonly, the deposition of the slurry on the substrate occurs by *dip-coating*: the substrate is immersed in the slurry, which is then removed where the coating is not required. Other techniques include *spray-coating*, which requires different properties of the slurry with respect to viscosity, and *spin-coating*, which consists of applying the slurry on the rotating substrate. By spin-coating, the final layer thickness is depending on features of the slurry, such as its viscosity and concentration, on the dispense volume and on the spinning speed [93].
Via *inkjet printing* droplets of a fluid, the ink, are first generated in a nozzle, then deposited on the substrate with the desired pattern, and finally dried, obtaining a layer thickness of few µm. When the fluid contains colourants, an image is created; however, this technique is not limited to graphic design; in the last decades its interest grew for application in printed electronics, ceramic component manufacture and medical applications [94]. The principle of inkjet printing is dispensing and precisely positioning a small volume of fluid (1 - 100 pL) on a substrate with a wide variety of printing patterns. The technique consists of *(i)* generation of the ink droplet to be printed; *(ii)* positioning of the droplets on the substrate; *(iii)* drying of the printed ink for solid layer formation [94, 95, 96]. Once a stable and homogeneous ink, containing the solid nanoparticles to be printed, the solvent and stabilizers, has been prepared, the drop generation takes place either continuously or with a drop-on-demand procedure. In the former, the ink droplets are supplied continuously and upon leaving the nozzle they are deflected by voltage plates; in the latter, the ink droplets are ejected only when required by the system [96]. The size of the droplets is in the range of 10 - 150 µm, in general around 100 µm in case of drop-on-demand and 20 - 50 µm in case of continuous printing, respectively [94]. The positioning of the droplet on the substrate can be achieved either manually, or controlled via a a computer, allowing a variety of printing patterns. The drying process can strongly influence the properties of the final layer through the so called coffee-ring phenomenon, during which the solidification of the different components of the fluid does not occur at the same time, resulting in an uneven layer [94]. The advantage of inkjet printing compared to spin-coating is the presence of the layer only where desired. Therefore, this technique becomes promising for coating catalytically active layers, as demonstrated in different works with applications in methanation,

hydrogenation and photocatalytic degradation reactions [97, 98, 99]. In a previous work, a double layer catalytic system was prepared via inkjet printing and tested for direct synthesis of DME [97, 100].
The *screen printing* process belongs to the slurry-deposition method and will be explained in detail in section 2.5.

2.4.3 Other coating techniques

By *electrochemical deposition* it is possible to obtain metallic layers using electric current. The substrate to be coated is negatively charged (cathode) and immersed in a solution containing the metallic precursor [84]. The deposition takes place only when an electric potential is applied across the electrodes, and happens only on the conducting working electrode. For this reason, this technique allows for an easy control of the film thickness, which can be adjusted acting on the deposition current density [85]. It is reported in literature for applications in (photo)-catalysis [84, 85, 101]. *Electrophoretic deposition* consists of applying an electric field between the substrate to be coated (cathode) and either an aluminum or a stainless steel foil. The charged suspension is set in between and migrates to the cathode. In this case, the thickness of the film can be adjusted by controlling the distance between the electrodes [84, 102]. The *chemical vapour deposition*, which is also used for the production of bulk materials and powders with high purity, takes place while flowing the precursor gases in a chamber containing the heated substrate to be coated (in the range $200\,^{\circ}\mathrm{C} \leq T \leq 1600\,^{\circ}\mathrm{C}$). The chemical byproducts are exhausted out of the chamber. In order to enhance the deposition rate, many variants of the original process have been developed (e.g. plasma assisted, metal-organic chemical vapour deposition) [103]. *Physical vapour deposition* methods include sputtering, electron-beam evaporation and pulsed laser deposition. In the *sputtering*, the substrate acts as anode and the coating material as cathode. The latter is charged by the plasma, generated between the electrodes, and is accelerated electrically towards the substrate. In simple terms, it is the process of erosion of the surface containing the coating material and its accumulation on the substrate. The technique is used in several applications, in both directions: it is applied for cleaning surfaces as well as for deposition on semiconductor wafers or magnetic media as well as in catalysis [84, 104]. During the *electron-beam evaporation*, the material to be coated is evaporated by an electron beam with high kinetic energy and directed to the substrate. The operational parameters for this application are the energy supplied to the target material, the consequent evaporation rate, and the temperature of the substrate [84, 105]. For the *pulsed laser deposition*, the target material is ablated from laser pulses in a chamber under vacuum and, similarly to the sputtering process, the substrate is coated. The laser puls frequency controls the thickness of the layer [84]. Also these methods are reported for application in catalysis, despite the layers obtained by physical vapour deposition present a low catalyst surface area due to the formation of uniform metal surfaces with thickness in the nanometer-scale [83].

In order to obtain zeolite layers, beside the conventional deposition via dip-coating, which results in randomly oriented crystals in the layer, different methods are possible, where the material is directly synthesized on the substrate. The advantage of a direct growth of the zeolite layer compared to dip-coating a support is that complete coverage of an oriented zeolite crystal layer can be achieved. The film can be deposited on the substrate where the coating is desired [84]. A H-ZSM-5 layer prepared via hydrothermal synthesis in micro-channels is reported by Lee [100].

2.5 Screen Printing

Screen printing enables the coating of a material in the form of a paste onto a substrate with a defined geometry [106]. During the process, the paste is moved and pressed with a squeegee over a screen containing a structured mesh, which allows the passage of the paste only where the coating is desired. The screen is fixed in a metal frame and the squeegee runs on it with a set speed. Both the screen and the squeegee consist of polymers. The rheological behaviour of the paste, such as fluidity, thixotropy, and viscoelasticity, is of crucial importance because it influences strongly the properties of the printed layer [106, 107, 108]. These aspects will be outlined in section 2.5.1. Beside this, the quality of the layer depends on the substrate, on the screen as well as on the process parameters [106]. In general, the technique permits the coating of different structures, depending on the geometry of the mesh; the resulting layer thickness is in the range from few µm up to 100 µm and depends on the distance between the screen and the substrate (the so-called *snap-off* distance), the screen mesh type, the speed, the pressure and the hardness of the squeegee and, as already mentioned, on the rheological properties of the paste [106, 107, 108].
One of the first application fields of the screen printing process was in microelectronics, for production of electrical resistors and conducting paths as well as for application of dielectric layers [106]. Its exploitation has been increasing in the last decades and the technique has been used in the automotive industry, in photovoltaics, and in catalysis [83, 107, 109, 110, 111]. For the latter case, screen printed layers for catalytic combustion and Fischer-Tropsch synthesis combined with hydrocracking were successfully prepared and tested [83, 111].

2.5.1 Rheology

Rheology is the science of the flow and deformation of matter which describes the correlation between force, deformation and time [112]. In this section, the principles of this discipline fundamental for the full understanding of the screen printing process are briefly outlined.
In general, deformation occurs as a consequence of the application of a force; during the screen printing, the squeegee applies a force to the paste in the direction of the screen, therefore only the parallel component (x-direction) is considered. The force applied acting over a unit area is defined as the *shear stress* ($\boldsymbol{\sigma}$, see Equation 2.1) and generates a shear flow, which can be described as parallel layers of the material sliding over one another, each with a proper velocity. The *shear strain* (γ, see Equation 2.2) and the *shear rate* ($\dot{\gamma}$, see Equation 2.3) are defined as the deformation along the stress direction compared to that orthogonal to it, and its change over the time, respectively. The shear stress $\boldsymbol{\sigma}$ is measured in [Pa], the shear strain γ is dimensionless, and the shear rate $\dot{\gamma}$ is measured in [s^{-1}].

$$\boldsymbol{\sigma} = \frac{\mathbf{F}}{A} \tag{2.1}$$

$$\gamma = \frac{\mathbf{x}}{\mathbf{y}} \tag{2.2}$$

$$\dot{\gamma} = \frac{d\gamma}{dt} \tag{2.3}$$

For the so-called *newtonian fluids*, the shear stress is directly proportional to the shear rate through a coefficient, the *dynamic viscosity* (η), measured in $[\mathrm{Pa} \cdot \mathrm{s}]$. For the *non-Newtonian* fluids, the viscosity varies

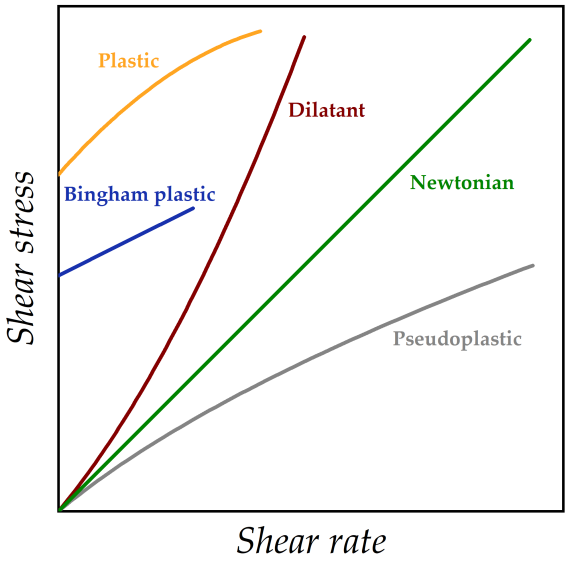


Figure 2.1: Shear stress (σ) vs. shear rate ($\dot{\gamma}$) plot for diverse kinds of fluids.

as a function of the shear rate and shear stress: *pseudoplastic* (or shear thinning) materials are characterized by a viscosity decrease with increasing shear rate; on the contrary, *dilatant* fluids are characterized by a viscosity increase as the shear rate increases. *Plastic* materials present the so-called *yield stress*, below which the viscosity becomes infinite, hence the materials behave as solids (they start to flow only for shear stress values higher than the yield stress). Beyond the yield stress, the behaviour of a plastic materials behaviour can be either dilatant, pseudoplastic or Newtonian. In this latter case the material is called *Bingham plastic* [112]. Figure 2.1 shows a plot of the shear stress vs. shear rate for the mentioned types of fluids. The presence of the yield stress in case of the paste to be printed should be taken into account in order to obtain a successful coating.
The yield stress can be measured performing a shear rate measurement and determining the stress at which a viscosity peak appears. Prior to this viscosity peak, the material is undergoing elastic deformation and the sample is only stretching. The peak in viscosity represents the point at which this elastic structure breaks down (yields) and the material starts to flow [112].
Beside this, some materials present a thixotropic behaviour. This means the rheological properties are time-dependent: the change in viscosity is related to the time at which the shear stress is applied. A pseudoplastic material may be thixotropic but a thixotropic material will always be pseudoplastic [112]. This effect should be also taken into account during the preliminary study about the printability of a certain paste.

Based on this knowledge, the screen printing process can be described. As Figure 2.2 shows, it occurs within distinct phases:

1. the paste is deposited on the screen, placed at a defined distance from the substrate;
2. the paste is pressurized downward and the squeegee moves forward;
3. the paste passes through the mesh;

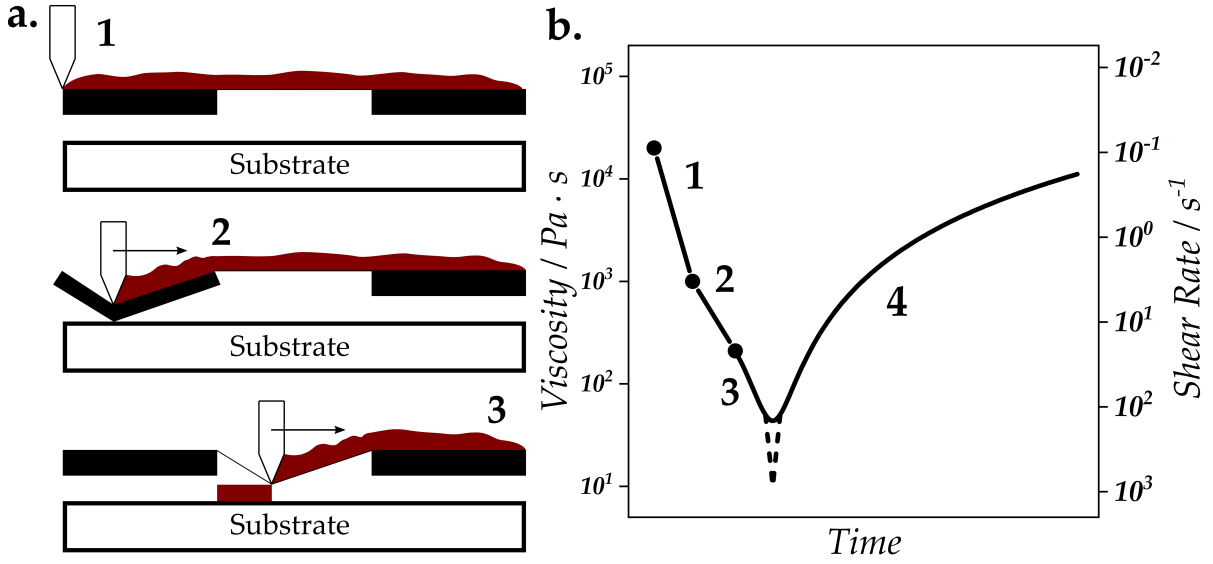


Figure 2.2: a) Schematic representation and b) viscosity and shear rate vs. time (adapted from [113]) of the different phases of the coating via screen printing.

4. the paste is deposited on the substrate, levelling of the coated layer occurs, while the squeegee continues moving forward (not shown in Figure 2.2a).

The phases 1 - 3 are schematically represented in Figure 2.2a, while Figure 2.2b depicts the plot of the viscosity and shear rate over time during the coating process. The crucial step is the screening itself (step 3 in Figure 2.2a - b): the paste is passaging through the mesh and a shear rate up to $1000\,s^{-1}$ is applied. At this moment of the process, the viscosity of the paste should be low enough, in order to allow its passage through the mask, and not too high, in order to avoid blockage with the consequent formation of an irregular layer. However, as the highest shear rate is applied for a only very short time, it is commonly accepted to investigate the rheology of the paste up to $100\,s^{-1}$ [106]. On the other side, it is important that the viscosity at low shear rate ($< 0.1\,s^{-1}$) is high enough, in order to avoid passage of the paste through the screen before the squeegeeing as well as to prevent both agglomeration and sedimentation of the particles [106]. All these considerations are summarized in Figure 2.2b, where the order of magnitude of the applied shear rate and the proper viscosity of the paste during the screening procedure are depicted. Step 4 (see Figure 2.2b) represents the formation of the layer in relation to its levelling. At this point, the thixotropy of the paste plays an important role for the succesful formation of an even layer without gaps. After the printing process, the paste should reach the original viscosity (before the coating) within a certain time. This time should be long enough for the succesful levelling of the film; in this way, lack of paste along the channel, due to the presence of the screen wires in the mask, can be closed; it should not be too long, in order to avoid the flow of the paste on the substrate. This behaviour corresponds to the step 4 of Figure 2.2b and is represented in Figure 2.3: the original viscosity is not reached immediately, but after a time lapse in the same order of magnitude as the duration of the printing process. A further method for measuring the thixotropic behaviour is determining the area of the hysteresis loop between the up-sweep and down-sweep of the viscosity vs. the shear rate curve [108]. During the preparation of the paste for screen printing, it could be useful to establish criteria defining its printability in advance. Sun claimed that for a shear rate of $100\,s^{-1}$, the viscosity should remain in

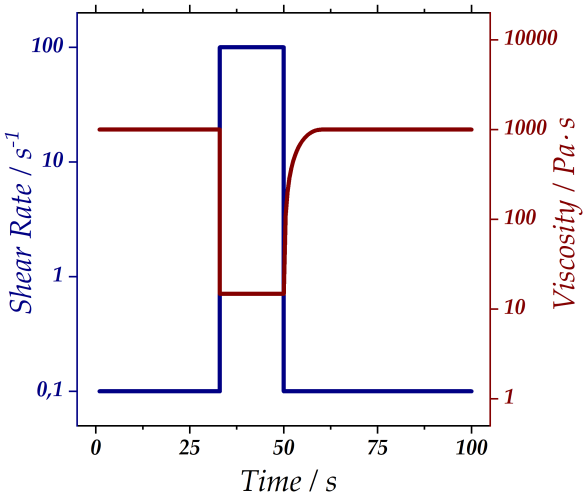


Figure 2.3: Thixotropic behaviour of a printable paste during coating via screen printing and levelling.

the range of 10 - 20 Pa · s [114]. Similar ranges were reported in the works of Ried et al. and Sanson et al., while Somalu et al. claimed a viscosity in the range 15 - 45 Pa · s at the same shear rate as suitable for the printing [115, 116, 108]. Wu et al. reported that the ideal paste for thick films should have a proper degree of pseudoplasticity and thixotropicity [117]. According to the authors, it is necessary to investigate the behaviour of the paste for all shear rates applied during the screen printing process, and not only at the maximal one of 100 s^{-1} [108]. A further important feature is the presence of a yield stress in the shear stress vs. shear rate curve (see Figure 2.1) of the paste. This could be an advantage as it prevents the flow of the paste before the squeegeeing and increases the storage stability [106]. On the other hand, the yield stress may damage the mesh and cause an irregular coating [108]. During the preparation of the paste, it should be ensured that the yield stress is in a sufficiently low range so that it is reached early enough during the printing process.

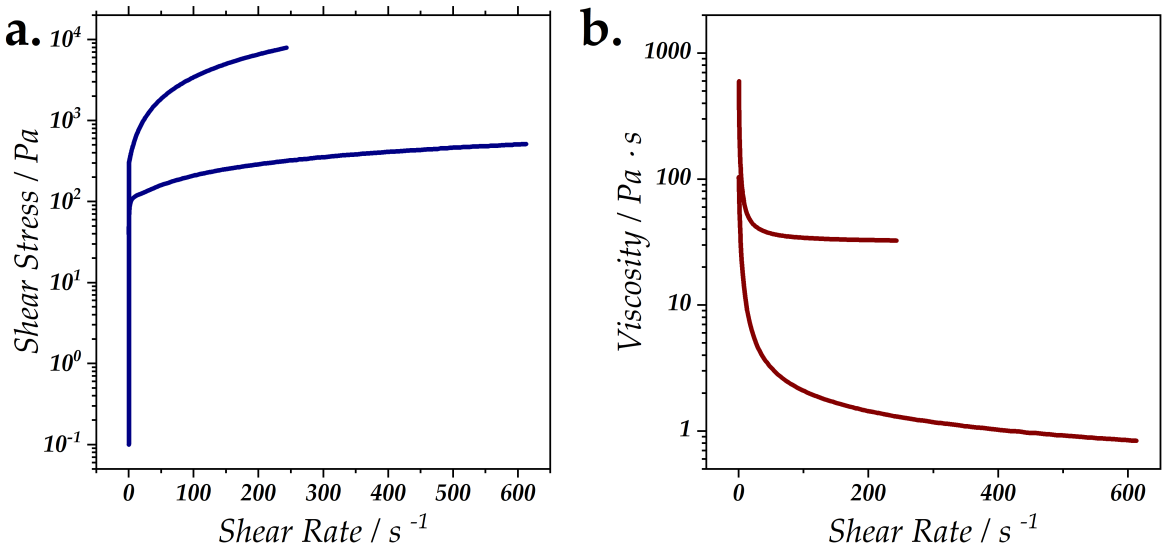


Figure 2.4: Printability range of a paste respectively the criteria of the a) yield stress and b) viscosity.

In summary, it is important to define criteria in order to know the printability of a paste in advance. In the frame of this work, printable ranges with respect to the presence of the yield stress as well as the viscosity of the paste were defined, combining the study of Stolz (see Ref. [106]) with experiments obtained here. The results are shown in Figure 2.4: the pastes with a rheological behaviour between the depicted limits were considered as printable.

2.5.2 Paste formulation

At this point it is important to explain what the paste to be coated is composed of and how it is possible to adjust its rheological properties in order to make it printable. In general, the paste is composed of the particles (electrodes or catalyst powder, depending on the application) to be coated, a solvent, a binder and a dispersant [108].
The particles in the form of powder should be in the size range between 10^{-2} µm up to few µm. The solid loading and, consequently, the amount of the solvent in the paste depend on the particle size distribution and the specific surface area of the powder used. According to Somalu et al., using nanoparticles with high surface area ($> 100\,m^2\,g^{-1}$) could lead to a low solid content, as the strong interactions among the particles increase the viscosity of the final paste [108]. In the open literature, solid loadings up to 50 wt.% are reported [106, 107, 108, 117].
The solvent is an organic component and should not undergo a phase change during the printing process, in order not to affect the viscosity [106]. It influences the rheological behaviour of the final paste as well as the maximum feasible solid content. Common solvents are terpineol, acetates, texanol and ethanol [108].
The binder can enhance the interaction among the particles and influence the printability of the paste. Common binders are ethylene cellulose (with different grades of viscosity), polymethyl methacrylate and polyvinyl acetal [108]. In literature, binder loadings up to 6 wt.-% are reported [107, 108].
The dispersant should form an electrostatic barrier around the particles, in order to avoid its agglomeration and reduce the viscosity, allowing for an increase of the solid loading. Furthermore, it could decrease the roughness of the layer, as it enables the formation of a more homogeneous and well dispersed paste. The loading of the dispersant is reported to be in relation to the specific surface area of the particles and should be up to 4 wt.-% [108].
In general, a high solid content is more suitable for sparing material, but this could be lowered when a porous layer is required [108]. Before examining the rheological and thixotropic properties of the paste, as well as before the screen printing process, the paste should be homogenized for destroying all solid agglomerates and reaching a narrower particle size distribution of the powder. This operation is commonly carried out in the triple roll mill [108].

3 Modelling

Modelling tools are used to evaluate the bare effect of the catalyst configuration independently of the potential catalyst alterations and deactivation caused by the material interactions and without the influence of possible side reactions. The aim of this work is to investigate the performance of the catalysts in the STD process in terms of X_{CO} and S_{DME} in a packed-bed-reactor (PBR) and a micro-channel-reactor (μ-CR). Starting from the material properties obtained from the characterization of the synthesized catalysts (see chapters 4 and 5 for details) and the description of the transport processes and the kinetics thereof, the catalyst configurations were compared in terms of the influence of the CZA/zeolite mass ratio (expressed as zeolite mass fraction ω_{Zeo}) and the process parameters (temperature, *F/W*, feed composition) on the catalytic performance, i.e., X_{CO} and product selectivity. All the catalyst structures considered as well as the range of the CZA/zeolite mass ratio investigated and the implementation of the model thereof are schematically represented in Figure 3.1. In general, the challenges of the modelling can be summarized as follows:

- the description, where necessary three dimensional, of the catalysts in terms of spatial arrangement, diffusion and reaction;
- the description of the reactor used and the implementation of the catalyst model into the reactor scale.

In the following the modelling approach and the results obtained are shown. The description of the catalysts, the reactors considered, the diffusion and reaction of the gas species in the catalyst medium as well as the implementation thereof in the model are described in section 3.1. The results of this study are presented in section 3.2, focusing on the influence of the catalyst composition and structure as well as of the operational parameters (temperature, *F/W*, feed composition). Finally, the main conclusions of this study are summarized in section 3.3.

3.1 Model development

In the following all relevant information on the development of the model, including the catalytic structures, the reactors considered as well as the background on diffusion and reaction kinetics are outlined.

3.1.1 The catalysts

In this work CZA and zeolite H-ZSM-5 (Si/Al-ratio = 50) catalysts, prepared via flame spray pyrolysis and hydrothermal synthesis, respectively, were considered. Synthesis procedures of CZA+Z, CZA@Z, CZA&Z, CZA#Z and CZA//Z are reported in chapter 4, while the CZA&/Z is considered only theoretically.
In order to describe both, the anisotropy of the zeolite ZSM-5 (MFI-type zeolite) pore structure as well as the polycrystallinity of the MTD catalyst system, the 3D-crystallite pore network model (3D-CPNM)

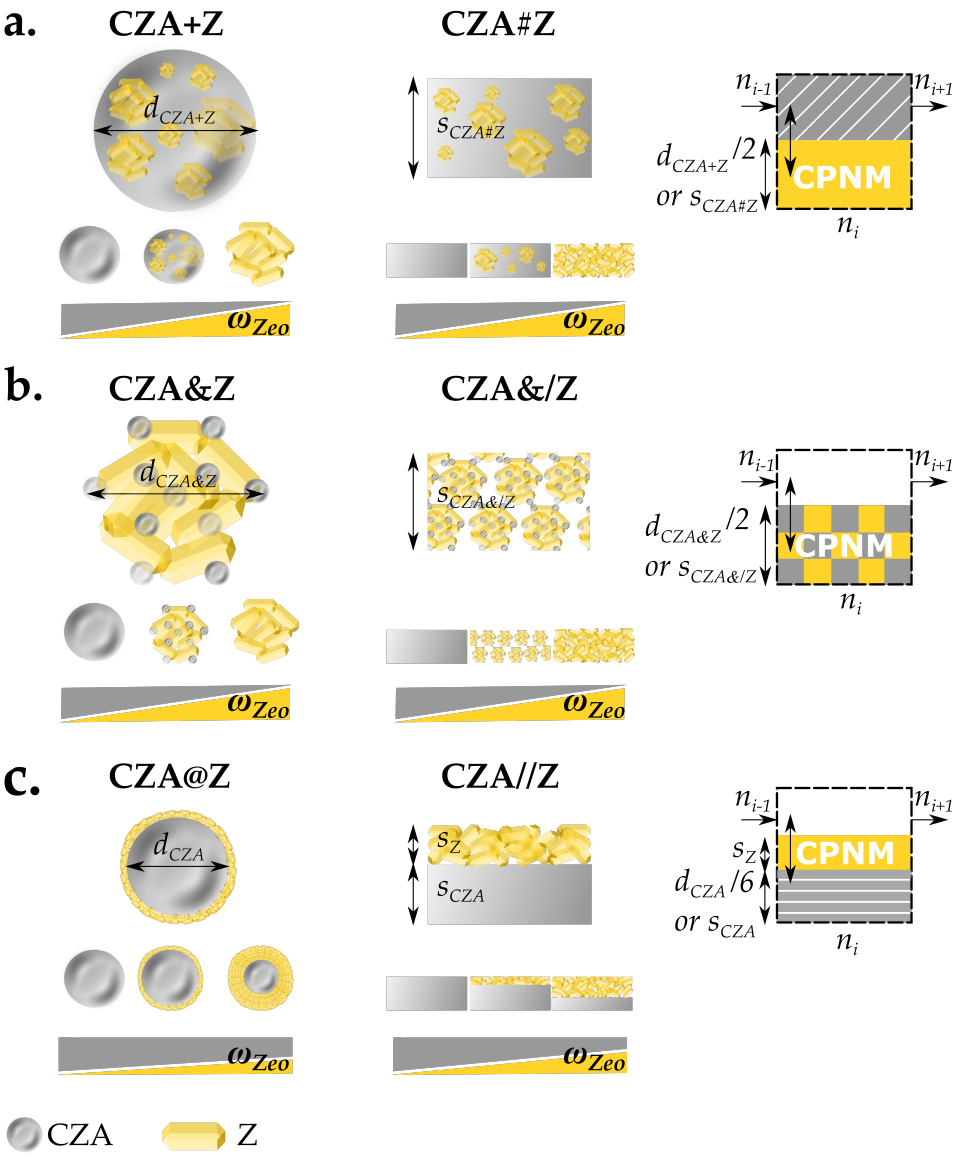


Figure 3.1: Illustration of the catalyst configurations investigated. a) Hybrid configurations on the pellet/layer level with close proximity of the two catalysts in micrometer scale, b) hybrid configurations with medium proximity of the two catalysts in sub-micrometer scale and c) structured catalysts core@shell and double layer configurations. Simplified, the range of ω_{Zeo} investigated and the model of a cell used for the simulation thereof in the accordant reactor are shown.

was applied (see [118] for details). In brief, following this model, the MTD catalyst (i.e. zeolite) is built up by the three-dimensional arrangement of three kinds of nodes (zeolite crystal, interface nodes and intercrystalline nodes) and two kinds of connections (zeolitic micropores and intra- or intercrystalline pores, e.g. originating from defects within the zeolite crystal or the layer, respectively). Each zeolitic crystal node is connected through a zeolitic micropore to an interface node, which is also connected to an intercrystalline node via a defect pore (either intra- or intercrystalline). The connectivity was introduced to define the connection between the intercrystalline and the interface nodes, giving the average number of the intercrystalline nodes connected with a second node (either intercrystalline or interface). In order to implement the orientation of the crystals in the 3-dimentional space, the angles ψ and χ are defined to describe the rotation of the crystal with respect to the *xy*- and *xz*-planes in the *xyz*-coordinate system, respectively [118, 119].

Table 3.1: Parameters used for the modelling of each catalyst configuration.

Parameter	*Unit*	*Value*	*Source*
CZA skeletal density	$kg^3\ m^{-1}$	3890	Hg-porosimetry
H-ZSM-5 skeletal density	$kg^3\ m^{-1}$	1835	[118]
H-ZSM-5 micropore diameter	nm	0.56	[120]
H-ZSM-5 mesopore diameter	nm	16	N_2-physisorption
H-ZSM-5 microporosity	vol.-%	10	[118]

In general, the 3D-CPNM enables a description of the polycrystallinity and anisotropy of the zeolite and allows for an evaluation of the influence of the zeolite properties (porosity, layer thickness, etc. resulting from, e.g., synthesis parameters) on the STD reaction when being part of a bifunctional catalyst system. Therefore, the diffusion of the reactants within the catalyst system and the reaction rates for STM and MTD are to be implemented in addition. For each configuration considered in this work, the same specific material parameters obtained from the characterization of the individual catalysts used and from literature have been applied - the material parameters common to each configuration either extracted from literature or obtained from characterization are listed in Table 3.1.

Hybrid catalyst systems

Hybrid catalysts of medium proximity on the pellet/layer level (CZA+Z and CZA#Z, respectively) as well of close proximity as particulate/coated systems (CZA&Z and CZA&/Z, respectively) were considered (see Figure 3.1). Details about the preparation procedure are given in chapter 4. The more intimate proximity between CZA and zeolite in the hybrid systems CZA&Z and, thus, CZA&/Z compared to the CZA+Z and CZA#Z systems which are to be expected according to the preparation procedure could also be observed by microscopy (TEM and EPMA) as will be shown in chapter 5.
For the modelling, all hybrid particulate (CZA+Z, CZA&Z) and layered (CZA#Z, CZA&/Z) catalyst configurations were approximated as a layer (see Figure 3.1, right), with a height equal to the radius of the particulate systems (rotational symmetry) and the actual thickness of the coating, respectively. Details on the structural parameters of all the different hybrid configurations considered are given below. According to the potential application of the catalysts, the particulate CZA+Z, CZA&Z configurations were investigated for a PBR, the planar CZA#Z and CZA&/Z were considered for μ-CR.

Hybrid catalyst configurations of medium proximity (CZA+Z and CZA#Z)

Table 3.2 summarizes the parameters obtained from the characterization and implemented for the CZA+Z and the CZA#Z systems. As reported in the work of Ding [119], the resistance for mass transport within the CZA catalyst can be neglected compared to the transport resistance in the zeolite micropores. Building on this, both the CZA+Z and the CZA#Z hybrid systems were implemented into the model by assuming a pseudo homogeneous distribution of the CZA catalyst in the gas phase and describing only the H-ZSM-5 by the 3D-CPNM. In this way, for the CZA the STM reaction rate was applied for the bulk gas phase conditions, while for the zeolite besides the MTD reaction rate also the diffusion was

Table 3.2: Parameters used for the modelling of the hybrid catalyst configurations of medium proximity (CZA+Z and CZA#Z).

		Value	
Parameter	***Unit***	**CZA+Z**	**CZA#Z**
H-ZSM-5 crystal size	nm	51	51
H-ZSM-5 intercrystalline porosity	vol.-%	64	54
CZA meso- and macro-porosity	vol.-%	50	50
CZA size	nm	10	10
CZA+Z pellet size	µm	75	-
CZA#Z layer thickness	µm	-	60

considered.

Hybrid catalyst configurations of close proximity (CZA&Z and CZA&/Z)

For the modelling of the hybrid configurations of close proximity, both as particulate and coated system, the CZA&Z CZA&/Z catalysts were considered as a matrix of H-ZSM-5 nanocrystals with the nanosized CZA catalyst being situated within the non-zeolitic pores at the intercrystalline nodes in the 3D-CPNM of the zeolite matrix, which is in accordance with the TEM-images of the synthetized particles (see also Figure 5.11). The total mass of CZA situated in the zeolite matrix was predetermined by the chosen $\omega_{STM}/\omega_{MTD}$ ratio. The structural parameters obtained from the characterization of the particulate system, and which are used in the model, are summarized in Table 3.3. The STM reaction rate was referred to the mass of CZA present at the considered node, the dehydration reaction rate was referred to the mass of the zeolite and connected to the nodes representing the zeolitic crystals. The same assumptions were used for the modelling of the correspondent hybrid layered system CZA&/Z.

Table 3.3: Parameters used for the modelling of the hybrid catalyst configurations of close proximity (CZA&Z and CZA&/Z).

Parameter	***Unit***	***Value***
H-ZSM-5 crystal size	nm	51
CZA size	nm	10
H-ZSM-5 intercrystalline porosity	vol.-%	32
CZA&Z particle size	nm	400
CZA&/Z layer thickness	µm	60

Structured core@shell (CZA@Z) and double layer (CZA//Z) configuration

Structured catalysts with a dedicated ordering of the two individual catalysts were investigated in spherical (CZA@Z) and planar (CZA//Z) configuration. In this context it is important to mention that, while the purpose of the CZA@Z system is to enwrap the CZA core with a dense zeolitic membrane in order to maximize S_{DME}, in case of the coated CZA//Z the upper layer should consist of a non-dense zeolitic film, aiming to enhance the diffusion of the reactants. Therefore, even if the arrangement of the two structures follows a similar approach in either a spherical (CZA@Z) or planar (CZA//Z) geometry, the

Table 3.4: Parameters used for the modelling of the structured core@shell (CZA@Z) and double layer (CZA//Z) configurations.

		Value	
Parameter	***Unit***	**CZA@Z**	**CZA//Z**
H-ZSM-5 crystal size	µm	2	2
H-ZSM-5 intercrystalline porosity	vol.-%	0.1	32
CZA mesoporosity	vol.-%	50	50
CZA core diameter	µm	72	-
H-ZSM-5 shell thickness	µm	2 - 50	-
CZA layer thickness	µm	-	20
H-ZSM-5 layer thickness	µm	-	2 - 50

specific concepts differ in the purpose of the zeolite layers properties and in the preparation principles applied (see also chapter 4). According to previous work, as the zeolitic shell in the CZA@Z configuration is much thinner than the diameter of the CZA core, the CZA@Z system can be approximated as a planar double layer and modelled comparable to the CZA//Z configuration [119]. For this geometric transformation, the shell thickness was varied in the simulation, while the thickness of the CZA layer was predefined by converting the core diameter of the actual catalyst by $d_{CZA-core}/6$, in order to obtain the same CZA/H-ZSM-5 volumetric ratio in the model as present in the actual spherical CZA@Z catalyst. The structural parameters of CZA@Z and CZA//Z catalysts are listed in Table 3.4.
After the aforementioned transformation of the CZA@Z from spherical to planar geometry, the same assumptions for both structured configurations were applied: due to the given pore structure, the diffusion of each gas species is much faster in the CZA catalyst than in the H-ZSM-5. Therefore, following the method of Ding et al., for the modelling of the double layer systems the CZA catalyst was discretized into 4 layers only, while the H-ZSM-5 layer was described by the 3D-CPNM [119]. In the CZA@Z system, H-ZSM-5 shell thicknesses of up to 50 µm covering CZA-core diameters of up to 72 µm were modelled corresponding to $\omega_{Zeo} = 6$ - 56 wt.-%. In the CZA//Z system, CZA- and H-ZSM-5-layers of 20 µm and 2 - 50 µm, respectively, were considered, corresponding to $\omega_{Zeo} = 2$ - 40 wt.-%.
The CZA@Z system was investigated as in a PBR, while the CZA//Z system was implemented as a wall coating in a µ-CR.

3.1.2 Diffusion

The diffusion of all the components involved in the STD reaction for the CZA@Z system was described by Ding in Ref. [118]. This approach was used here for simulation of all bifunctional catalyst configurations. In brief, the mass transport in the intercrystalline zeolitic pores as well as in the CZA catalyst is described by the Knudsen diffusion model, which is to be used when the mean free path length of a gas molecules is in the same range as the pore diameter and hence molecule-wall collisions dominate over molecule-molecule collisions [121]. As opposed to this, in the micropores of the H-ZSM-5 crystals, transport takes place predominantly in adsorbed state and is treated by the generalized Maxwell-Stefan surface diffusion model which takes into account the interaction between the diffusing molecules and the adsorption sites as well as among the adsorbed molecules [121]. In doing so, the diffusion of each

component in the x-, y- and z-directions can be described [118, 119]. For the CZA&Z as well as for the layered configurations CZA&/Z and CZA//Z, the diffusion in the CZA catalyst was also considered. Due to the simplifying modelling assumption for the CZA+Z and CZA#Z systems described in section 3.1.1, for these latter two configurations the diffusional resistance in the CZA was neglected. This hypothesis is in line with what was reported by Ding et al., who showed that a discretization of the CZA into only 4 layers for the CZA@Z system lead to an absolute difference of species concentrations throughout the core of less than 1 % [119].

3.1.3 Reaction kinetics

In order to investigate the influence of the catalyst configuration and the STD process parameters on X_{CO} and S_{DME}, both diffusion and reaction have to be considered and solved simultaneously. For all modelling results discussed in this work, the STM kinetics from the recent study of Seidel et al. was implemented [30]. For the MeOH dehydration reaction over H-ZSM-5, the kinetics determined in previous works of Tauro and Ding was used [119, 122].
In general, diffusion and reaction within the catalyst was treated with the 3D-CPNM. Only for CZA+Z and CZA#Z, due to the assumptions taken for these hybrid catalysts (see section 3.1.1), the component balance in the gas phase included the STM reaction (see also section 3.1.4).

3.1.4 Reactor modelling

As mentioned, in this study several catalyst configurations were implemented in two different reactors: the packed-bed-reactor (PBR) for particulate systems and the micro-channel-reactor (µ-CR) for wall-coated catalyst layers. The following assumptions concerning the ideal behaviour of both reactors were applied:

- absence of axial dispersion ($Bo > 100$);
- negligible radial temperature gradients in the catalyst bed resp. layer;
- absence of external heat and mass transport limitations;
- absence of intraparticle temperature gradients.

All the hypotheses were proven experimentally and by calculation according to the criteria discussed in the work of Tauro, who investigated the STD reaction in mixed catalyst beds in both types of reactors [122]. The dimensions of the two reactors are given in Table 3.5. For the description of the mass transport in the PBR and the µ-CR, the Sh (Sherwood) number can be determined according to Equations 3.1 - 3.5 taken from [123], with f_a being the form factor (function of porosity), Re the Reynolds number, Sc the Schmidt number and ϵ the porosity of the catalyst bed.

$$Sh_{PBR} = f_a \left(2 + \sqrt{Sh_{lam}^2 + Sh_{turb}^2}\right) \tag{3.1}$$

$$Sh_{lam} = 0.664 \sqrt{Re} \sqrt[3]{Sc} \tag{3.2}$$

$$Sh_{turb} = \frac{0.037\, Re^{0.8}\, Sc}{1 + 2.443 \cdot Re^{-0.1} \cdot \left(Sc^{2/3} - 1\right)} \tag{3.3}$$

Table 3.5: Dimensions of the PBR and μ-CR.

PBR			μ-CR		
Parameter	***Unit***	***Value***	***Parameter***	***Unit***	***Value***
Catalyst bed length	cm	9.5	micro-channel length	cm	15
Reactor diameter	mm	8	micro-channel W x D	μm x μm	250 x 130

$$f_a = 1 + 1.5\,(1 - \epsilon) \tag{3.4}$$

$$Sh_{\mu-CR} = 4.36 \tag{3.5}$$

For the simulation, both reactors had to be discretized. The PBR and the μ-CR were discretized with respect to its total length and to the length of one channel, respectively: the length of the reactor (i.e. length of the tube or channel) was divided into a number of cells (N_{Rea}) of the same length (Δx). In each cell n_i, the gas phase was considered as ideally mixed, and the catalyst was described according to the considerations discussed in section 3.1.1. Composition and flow rates of the gas phase at the outlet from the cell n_i were used as the inlet of the following cell n_{i+1}. It was proven that $N_{Rea} = 100$ enabled a precise description of the reactor within reasonable computational time (the results deviate by 10^{-5} for $N_{Rea} > 100$). For calculation of the mole flow between the bulk gas phase and the catalyst phase in each cell, the model calculates the molar fluxes at the external surface of the catalyst ($\dot{j}_{i,tr}$) by solving the reaction-diffusion equations for the catalyst phase and multiplying this with the total external surface area of the catalyst present within the cell (A_{cat}^{cell}). In general, the balance is explained in Equation 3.6. Due to the assumptions taken for CZA+Z and CZA#Z, for these catalysts the STM-reaction rate is to be referred to the bulk gas phase where the CZA is distributed: therefore the term $m_{CZA}^{CZA+Z/CZA\#Z} \cdot (\nu \cdot r)_{i,CZA}$ should be considered for these catalysts (see Equation 3.7).

$$\dot{N}_{i,in} - \dot{N}_{i,out} + A_{cat}^{cell} \cdot \dot{j}_{i,tr} = 0 \tag{3.6}$$

$$\dot{N}_{i,in} - \dot{N}_{i,out} + m_{CZA}^{CZA+Z/CZA\#Z} \cdot (\nu \cdot r)_{i,CZA} + A_{cat}^{cell} \cdot \dot{j}_{i,tr} = 0 \tag{3.7}$$

3.1.5 Implementation of the model in MatLab®

The simulation of diffusion and reaction for the different catalyst configurations in the accordant reactor system (PBR or μ-CR) was performed via MatLab® for different process conditions (T, *F/W*, feed composition) and catalyst parameters ($\omega_{STM}/\omega_{MTD}$). The flowchart of the model solving procedure is shown in Figure 3.2. For the simulation of the catalyst performance via MatLab®, first, all parameters regarding the catalyst structure, diffusion, reaction kinetics and the reactor were read to build up the 3D-CPNM. Starting from initial guess values, the non-linear equation system **F(c)** was iteratively solved at each node with the function *fsolve* from the Optimization Toolbox®, with its default algorithm *trust region dogleg* (see Refs. [119] and [124] for details regarding equations). The iteration process was stopped until the component material balance at all nodes was fulfilled, namely the value of $\frac{1}{2}\,||\boldsymbol{F}(\boldsymbol{c})||^2$ was smaller than the termination tolerance *TolFun*, equal to 10^{-30}. This procedure was repeated for each cell

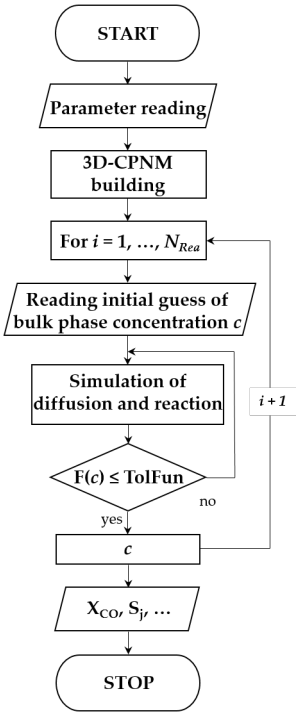


Figure 3.2: Flowchart of the model implemented in MatLab®. *TolFun* = 10^{-30} (termination tolerance).

of the reactor, using the outlet composition of the cell n_i as input for the cell n_{i+1}. At the outlet of the reactor, the atom balance for C, H, O and N as well as conversion, selectivity, yield and productivity were calculated, according to Equations 3.8 - 3.12.

The conversion of CO (X_{CO}) resp. CO and CO_2 together (X_{CO_x}), the selectivity towards MeOH and DME (indicated as S_i with respect to carbon conversion) were calculated according Equations 3.8 - 3.10. The yield (Y_i) and the DME-productivity (P_{DME}) were calculated according to Equations 3.11 - 3.12.

$$X_{CO} = \left(1 - \frac{\dot{N}_{CO,out}}{\dot{N}_{CO,in}}\right) \cdot 100\ \% \tag{3.8}$$

$$X_{CO_x} = \left(1 - \frac{\dot{N}_{(CO+CO_2)_{out}}}{\dot{N}_{(CO+CO_2)_{in}}}\right) \cdot 100\ \% \tag{3.9}$$

$$S_i = \frac{\nu_i \ \left(\dot{N}_{i,out} - \dot{N}_{i,in}\right)}{\dot{N}_{(CO+CO_2)_{in}} - \dot{N}_{(CO+CO_2)_{out}}} \cdot 100\ \% \tag{3.10}$$

$$Y_i = \frac{\nu_i \ \left(\dot{N}_{i,out} - \dot{N}_{i,in}\right)}{\dot{N}_{(CO+CO_2)_{in}}} \cdot 100\ \% \tag{3.11}$$

$$P_{DME} = \frac{\dot{N}_{DME,out}}{m_{CAT}} \tag{3.12}$$

Based on detailed studies on the individual effects of reaction temperature, feed gas composition, and *F/W* (see section 3.2.3 - 3.2.5), the following parameters have been fixed for all simulations aiming to compare the sole effect of catalyst configuration: feed gas composition: $H_2/CO/CO_2$ = 16/8/1, 10 vol.-% N_2, reaction temperature: 250 °C, *F/W* = 2000 mL h^{-1} g_{CAT}^{-1}. The *F/W* was referred to the total catalyst

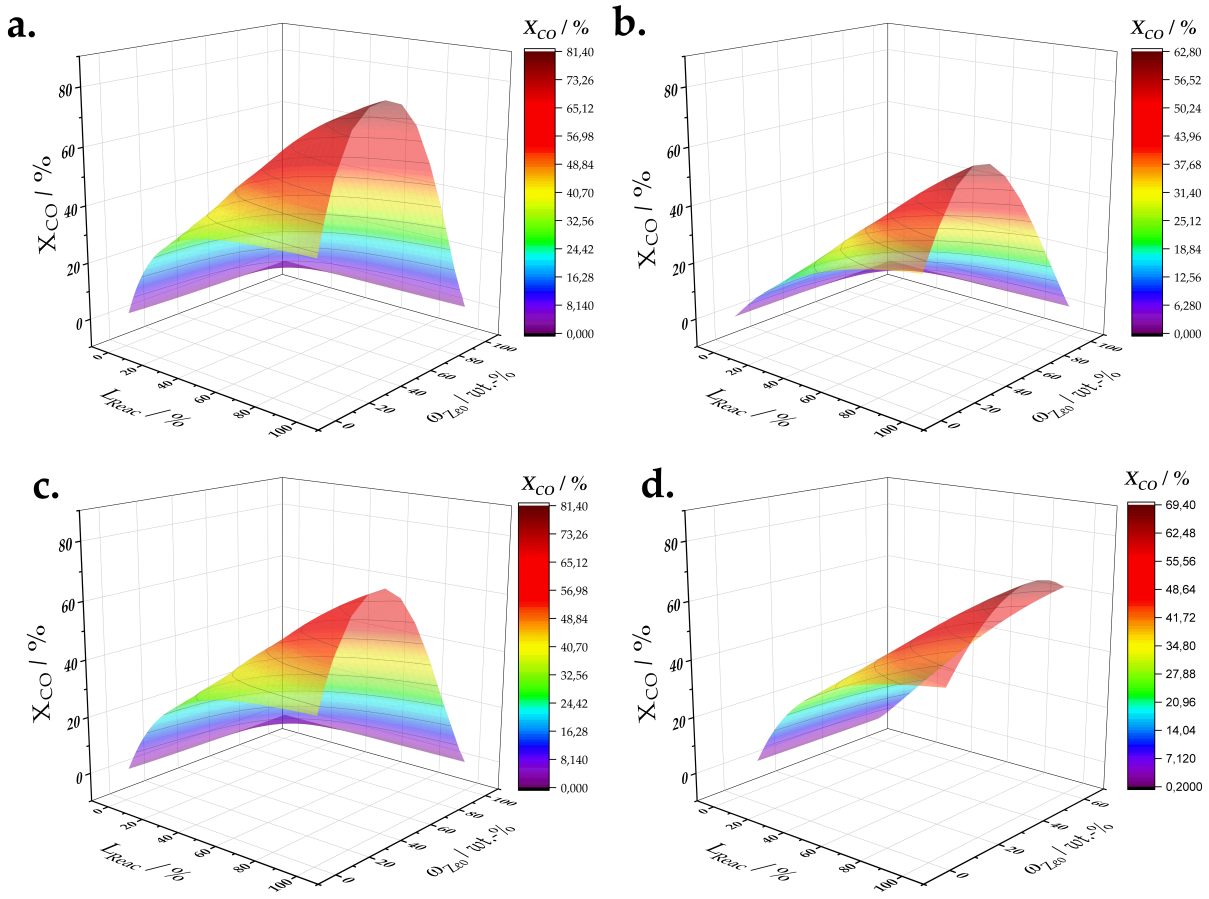
mass in the reactor, namely both CZA and H-ZSM-5. As being commonly used, absolute pressure was set to 40 bar.

3.2 Results & discussion

In the following, the simulation results concerning the performance of the different catalyst systems (described in sections 3.1.1) in the STD process are discussed. Superimposing limitations at the process conditions chosen can be ruled out for both the PBR and the μ-CR: the performance of the reaction system is affected by the configuration of catalyst only (see section 3.2.1). Based on this, in section 3.2.2, the STD performance in terms of X_{CO} and product selectivity is compared among the different catalyst systems. In sections 3.2.3 - 3.2.5, the influence of the operational parameters is discussed.

3.2.1 Influence of the relative amounts of the two catalysts

The performance of the STD reaction in the PBR and μ-CR along their accordant length coordinate in terms of X_{CO} was evaluated for determining possible superimposing limitations due to the process conditions considered.



CONDITIONS: p = 40 bar; T = 250 °C; F/W = 2000 mL h^{-1} g^{-1}_{CAT}

Figure 3.3: X_{CO} as a function of the relative reactor length (L_{Reac}) and ω_{Zeo} for the particulate systems a) of close proximity CZA&Z and b) of medium proximity CZA+Z in a PBR, for the layered systems c) of close proximity CZA&/Z and d) structured CZA//Z in a μ-CR.

Figure 3.3 represents the CO-conversion (X_{CO}) as a function of the relative reactor length L_{Reac} and CZA/zeolite weight ratio (represented by the mass fraction of the zeolite ω_{Zeo} in the catalyst configuration considered). The results are shown for the hybrid particulate catalysts of close and medium proximity, namely CZA&Z and CZA+Z, in the PBR (Figure 3.3a - b) as well as for the planar hybrid system of close proximity and the structured double layer, namely CZA&/Z and CZA//Z, in the μ-CR (Figure 3.3c - d).
For each case considered, the X_{CO} increases in the first 20 % of the reactor length almost linearly up to about X_{CO} = 20 - 30 % before the conversion further increases with a strong dependency on the zeolite content showing already the beneficial effect of the direct dehydration of the MeOH being formed. In general, when the catalysts contain a low amount of zeolite ($\omega_{Zeo} < 10$ wt.-%), the X_{CO} increases only slightly in the second half of the reactor ($X_{CO} = f(L_{Reac} > 50\,\%) \simeq$ const.). This can be attributed to the reaction system and its thermodynamics: for small values of ω_{Zeo} the amount of acidic catalyst is not sufficient to dehydrate (MTD) all the MeOH being formed (STM) and, thus, the system is still controlled by the STM reaction equilibrium. This general behaviour is observed for all configurations (incl. CZA@Z and CZA#Z, not shown) and does not depend on the catalytic structure but on the kinetics of the whole system. Similar conclusions can be drawn for high values of ω_{Zeo} (> 90 wt.-%): here, the amount of CZA in the reactor is not sufficient for reaching a high conversion of the synthesis gas. In conclusion, superimposing limitations at the process conditions chosen can be ruled out for both the PBR and the μ-CR: the performance of the reaction system is affected by the configuration of the catalyst only.

3.2.2 Influence of catalyst configuration and its composition

In the following, the STD performance in terms of conversion and selectivity of the different bifunctional catalyst configurations in the accordant reactors (particulate catalysts in PBR and layered systems in μ-CR) is presented and discussed. In particular, the influence of the ω_{Zeo} for each configuration was investigated, in order to determine the optimal composition for each system in terms of maximum X_{CO} and/or S_{DME}. It should be emphasized that only the results showing a maximum in the X_{CO} significantly away from the STD equilibrium ($X_{CO}^{STD,eq.}$ = 93.8 % at the predefined process conditions) were considered, in order to rule out erroneous conclusions affected by thermodynamics. Moreover, while for the hybrid and double layer configurations, the amount of zeolite can be defined freely due to the preparation principle (see also section 2.3), in the CZA@Z catalyst system ω_{Zeo} is predetermined by the shell thickness which can be achieved by the synthesis procedure applied: due to the concept and the synthesis of such catalysts, a shell thickness of more than 10 μm, corresponding to ω_{Zeo} = 4 %, is meaningful for the modelling in order to get a deeper insight in such catalyst systems but do not necessarily reflect a feasible catalyst, as further discussed in chapter 4. Thus, here even a practically unfeasible shell thickness of up to 50 μm covering a core catalyst of 72 μm in diameter was considered.

Figure 3.4 shows X_{CO} and S_{DME} and S_{MeOH} versus ω_{Zeo} for the particulate configurations CZA&Z, CZA+Z and CZA@Z in the PBR.
In general, the trend of X_{CO} for each of the three configurations shows a maximum, which is sufficiently below the CO-equilibrium conversion of the STD reaction and does not show a plateau, for which reason, at the operational conditions considered, thermodynamic limitations can be excluded. At low ω_{Zeo}, the X_{CO} is close to the STM equilibrium ($X_{CO}^{STM,eq.}$ = 39.1 %), before increasing with higher amount

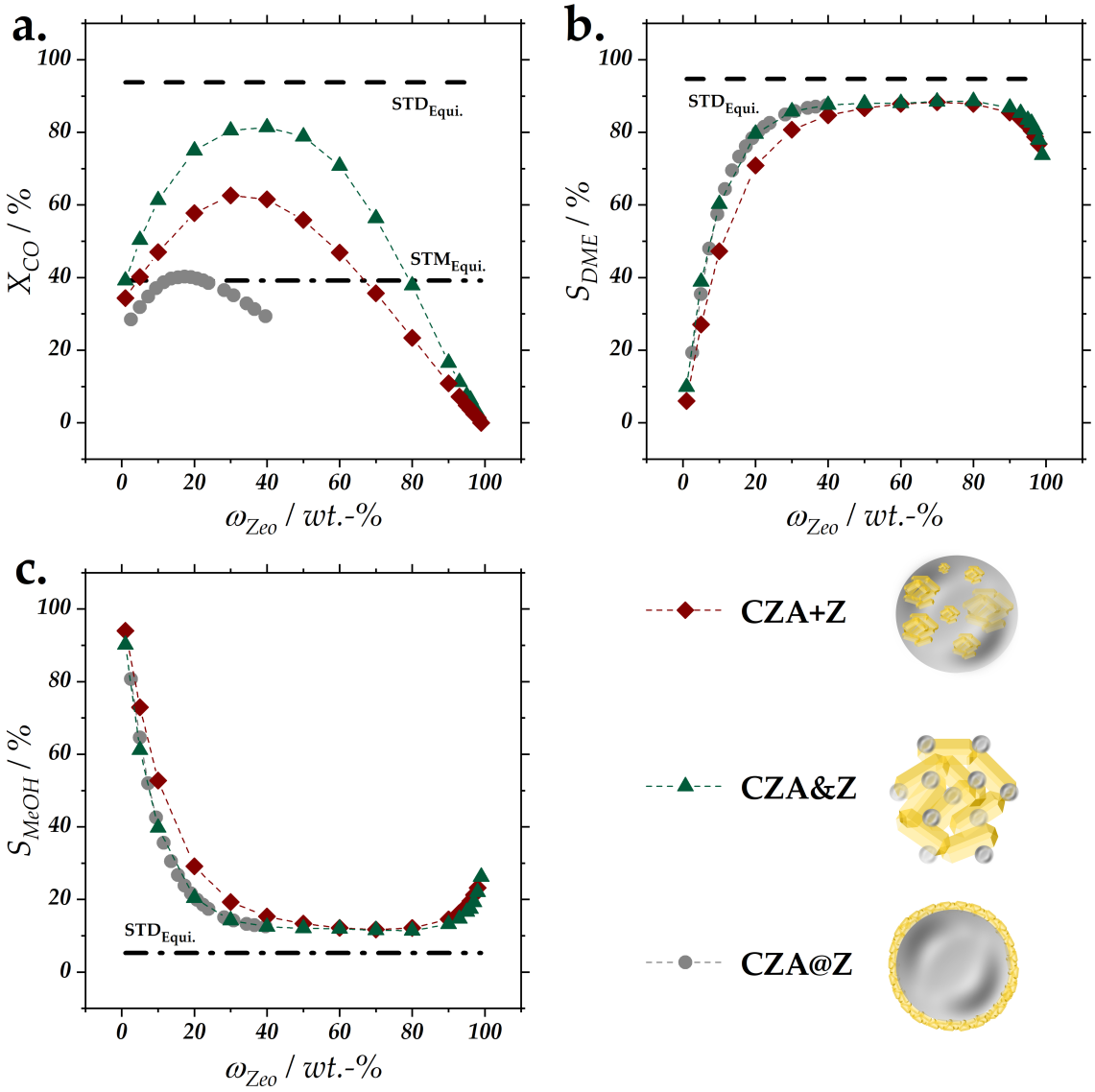


Figure 3.4: a) X_{CO}, b) S_{DME}, c) S_{MeOH} for the particulate catalyst systems CZA&Z, CZA+Z and CZA@Z in a PBR.

of zeolite until reaching a maximum. With further increase of ω_{Zeo}, X_{CO} drops and falls even below the STM equilibrium conversion at a certain composition. The maxima differ largely in value and to a somewhat lesser extent also in position for the different catalyst configurations. The higher the maximum the higher the value of ω_{Zeo} where it occurs. These general trends can be explained as follows: an excess of CZA catalyst (low ω_{Zeo}) results in a limitation of X_{CO} by the STM equilibrium as the high CZA/zeolite ratio in the catalyst does not allow for a sufficiently fast dehydration of the MeOH formed by the CZA to overcome this limitation. Upon increasing ω_{Zeo}, the dehydration gets accelerated and MeOH formation decelerated, and in turn CO-conversions beyond the STM equilibrium become possible. This effect increases with increasing value of ω_{Zeo} until a maximum value predetermined by the ratio of the MeOH formation rate versus the MeOH dehydration rate is reached. This ratio apparently depends on the catalyst configuration. The highest maximum is predicted for the hybrid catalyst with close proximity of the two components. The lowest maximum is observed for the core@shell system. The hybrid catalyst with

medium proximity takes an intermediate position. An increase in X_{CO} can be attributed to two effects: first, an enhanced diffusion of the reactants through the regions of microporous zeolite and second an intimate contact between the two catalyst species. The hybrid particle systems get advantage in performing higher CO-conversions due to the higher intercrystalline porosity of the zeolite compared to the core@shell configuration (see Tables 3.2 - 3.3 in section 3.1.1), thus, allowing for an enhanced diffusion of the species. Beside this, the proximity in the sub-micrometer-scale of the CZA&Z catalyst increases the probability for the MeOH to be dehydrated by the zeolite, namely the thermodynamic benefit is more pronounced as compared to the situation in the CZA+Z particles of medium proximity, where the two catalyst species are more segregated. The diffusion limitation caused by the zeolite shell (dense zeolitic membrane in the present study), counteracts the X_{CO} in case of the CZA@Z system. These aspects will be object of further discussion. Beyond the maximum found for all three systems, X_{CO} drops with increasing ω_{Zeo} as it gets limited kinetically by the scarce amount of CZA rather than thermodynamically by the STM equilibrium.

This qualitative interpretation of the result shown in Figure 3.4a regarding X_{CO} can be mirrored for the discussion of the product selectivity. Three different regimes of ω_{Zeo} are visible: for $\omega_{Zeo} < 40$ wt.-%, S_{DME} increases with increasing ω_{Zeo} and, consequently, S_{MeOH} decreases. Here, the beneficial effect of coupling the STM with the dehydration reaction is most pronounced, as $\delta X_{CO}/\delta\omega_{Zeo}$ is the largest. Again, the system with close proximity is expected to perform better than the one with medium proximity, as indicated by higher S_{DME} and lower S_{MeOH}. Interestingly, the core@shell system behaves exactly like the one with close proximity regarding selectivity (see discussion below). The curves show a maximum of the S_{DME} and a minimum for the S_{MeOH} in the second regime (40 wt.-% $< \omega_{Zeo} <$ 80 wt. %). However, the maximum is not as distinct as in the case of the X_{CO} but represents a plateau, and the plateau values do not differ much depending on the catalyst configuration. A further increase of the share of zeolite ($\omega_{Zeo} > 80$ wt.-%, third regime) results in a decrease of S_{DME} and increase of S_{MeOH}. In this regime, CO_2 is not produced by the reaction network and it is even consumed. CO_2 is produced via the WGS reaction (Equation 1.3) over CZA from CO and water, the latter being a side product of MeOH dehydration (Equation 1.4) over the acidic catalyst. As described, a small amount of CZA results in less MeOH being formed and, thus, less water being produced by its dehydration. In turn CO_2 formation from CO via the WGS reaction is suppressed while MeOH synthesis from CO_2 (Equation 1.2) consumes CO_2 resulting altogether in a consumption of CO_2 in the overall system. The CZA&Z and the CZA@Z systems allow for higher S_{DME} than the CZA+Z configuration, which is due to the enhanced hierarchical structure of the first two systems: in the CZA@Z system, the MeOH produced in the core can only leave through the zeolite micropores (or defects) in the shell where it reacts to DME. In the CZA&Z, the CZA is decorated around the zeolite crystallites, resulting in an increased synergy between the two kinds of active sites compared to CZA+Z where aggregates of zeolite crystallites are embedded in a porous CZA matrix. The probability of MeOH dehydration for CZA@Z and CZA&Z systems therefore is higher than in the CZA+Z, where the two catalysts are more segregated due to the preparation concept (close vs. medium proximity of the two catalyst within the particle, see chapter 5). The low X_{CO} shown by CZA@Z should be addressed to the mass transport resistance of the shell: it was observed (see chapter 5) that the zeolite covering the core is a densely intergrown layer, with low concentration of non-zeolitic defect pores. Based on that, the void fraction within the shell (zeolite intercrystalline porosity in the CZA@Z system) was estimated to be only 0.1 vol.-% (see Table 3.4). This results in an enhancement of S_{DME} (low

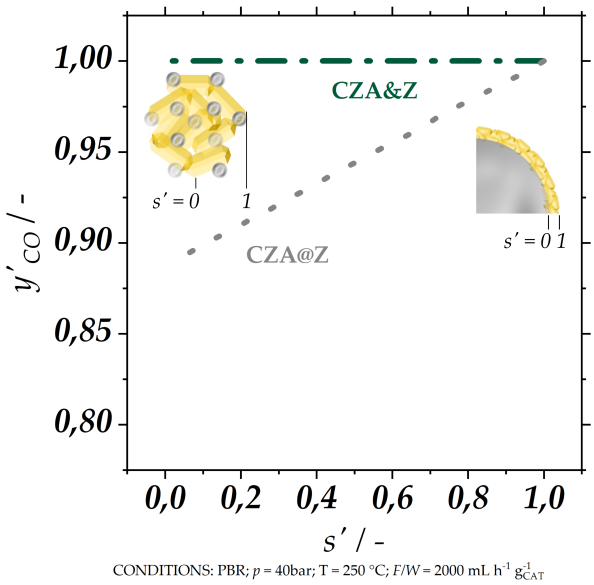
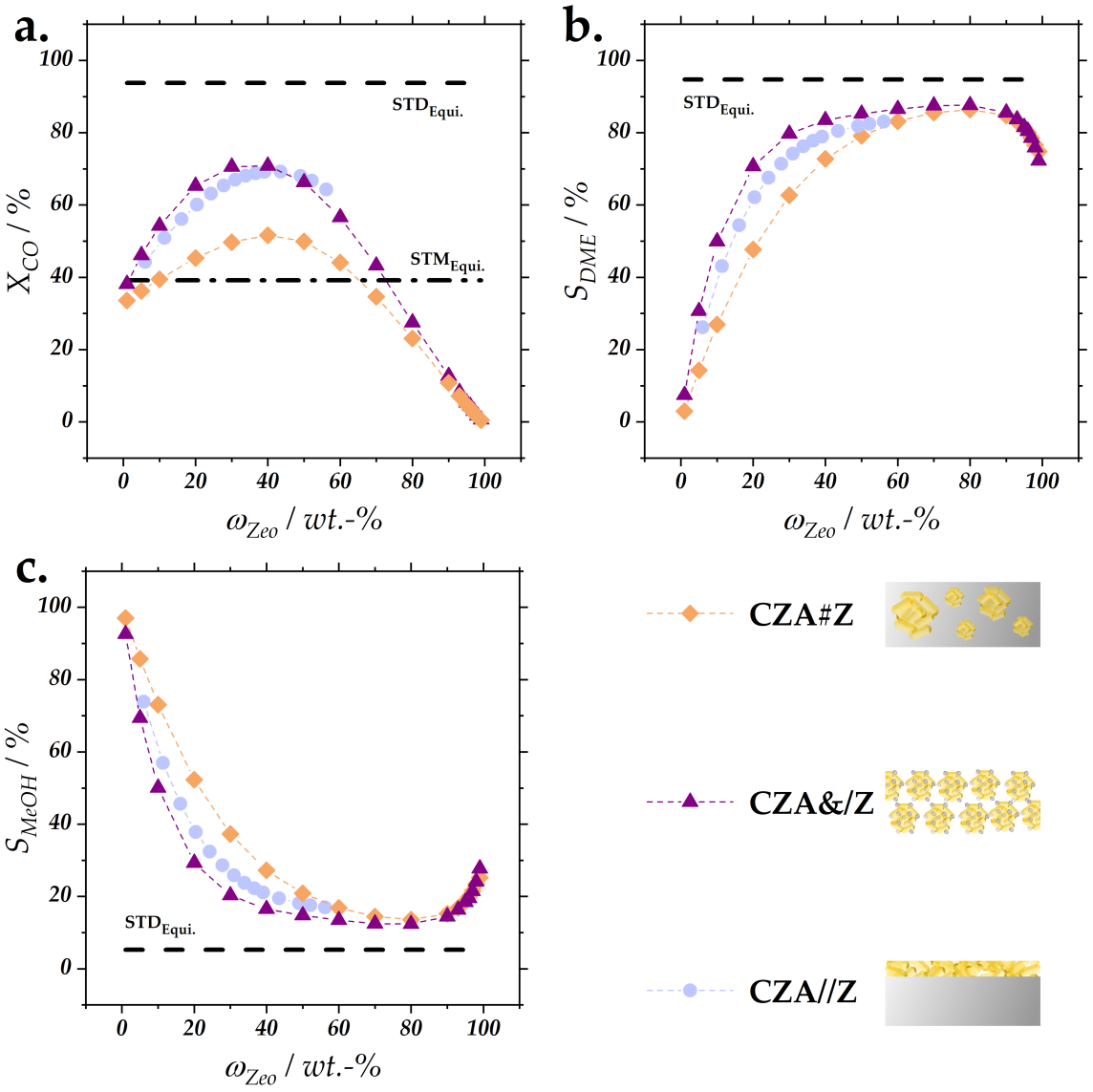


Figure 3.5: Dimensionless CO concentration (y'_{CO}) versus the dimensionless coordinate (s') of the CZA&Z and the zeolite shell of the CZA@Z system in a PBR.

probability of MeOH leaving the system without getting dehydrated) but, at the same time, hinders the diffusion of the reactants from the gas phase through the shell to the core (see below and [118]). In contrast, the zeolite intercrystalline pores in the zeolite matrix of the CZA&Z and the resulting possibility of a more direct access of the reactants from the gas phase to the CZA in the CZA+Z catalysts configuration allow for a higher X_{CO}. As already discussed above, the benefit obtained by enhancing the proximity of the two catalysts and, consequently, the synergy between STM and MTD reactions in the CZA&Z configuration is higher in comparison to the CZA+Z, as in the latter configuration the CZA and the zeolite have a less intimate contact. This results in the highest values of X_{CO} and S_{DME} for the CZA&Z among the particulate systems investigated.

The diffusion limitation caused by the dense zeolite shell in the CZA@Z system was further investigated: in Figure 3.5, the concentration of CO, normalized to the concentration in the gas phase (y'_{CO}) is shown versus the dimensionless length coordinate in the CZA&Z system and the zeolite shell of the CZA@Z (thickness of 18 µm was considered, corresponds to ω_{Zeo} = 19 wt.-%). A negligible gradient in X_{CO} was found for the CZA&Z system ($y'_{CO}(s' = 0) = 0.99$), which is to be expected in case of absent transport limitations. A slight but not negligible gradient over the shell of the CZA@Z system ($y'_{CO}(s' = 0) = 0.89$) was observed, which has to be linked to the slower diffusion in the mainly microporous structure. These results are qualitatively in line with what was reported in the previous study of Ding, also discussing an increase of X_{CO} and a consequent decrease of S_{DME} with increasing intercrystalline porosity of the zeolitic shell [118]. However, due to the high S_{DME} achievable by using CZA@Z particles, from modelling results these remain a promising configuration for the STD process.

The different transport phenomena controlling the overall transport rate in the three particulate structures can also explain why the X_{CO} exceeds the STM equilibrium conversion ($X_{CO}^{STM,eq.}$ = 39.1 % for the given process parameters) and reaches the maximum at different values of ω_{Zeo}: the STM equilibrium is overcome at 1, 5 and 13 wt.-% and the X_{CO} reaches its maximum at 40, 30 and 17 wt.-% for the CZA&Z, CZA+Z and CZA@Z systems, respectively. When the transport within the catalyst is not hindered, a



CONDITIONS: μ-CR; p = 40 bar; T = 250 °C; F/W = 2000 mL h^{-1} g$_{CAT}^{-1}$

Figure 3.6: a) X_{CO}, b) S_{DME}, c) S_{MeOH} for the layered catalyst systems CZA&/Z, CZA#Z and CZA//Z in a μ-CR.

lower amount of CZA is sufficient to reach the maximum in X_{CO}. In other words, to achieve both, high X_{CO} and high S_{DME}, on the one hand it is necessary to enhance the accessibility of the CZA by the reactants and on the other hand an intimate contact between the two catalysts has to be given.

Simulation results at the same process conditions and F/W were obtained for the layered systems in the μ-CR, adapting the geometry as described in section 3.1.4. The results are shown in Figure 3.6. In line with the CZA@Z system, for the CZA//Z, ω_{Zeo} of up to 60 wt.-% was considered.
In general, the trends of X_{CO} and product selectivity obtained for the particulate systems in the PBR can also be found for their coated counterparts in the μ-CR. This is to be expected, as the influence of ω_{Zeo} on the STD reaction should not be affected by the kind of reactor considered. At low ω_{Zeo} (< 10 wt.-%), X_{CO} is close to the STM equilibrium conversion. X_{CO} increases with ω_{Zeo} until a maximum is reached. Thereafter, X_{CO} decreases with further increase of ω_{Zeo} even below the STM equilibrium CO-conversion. In

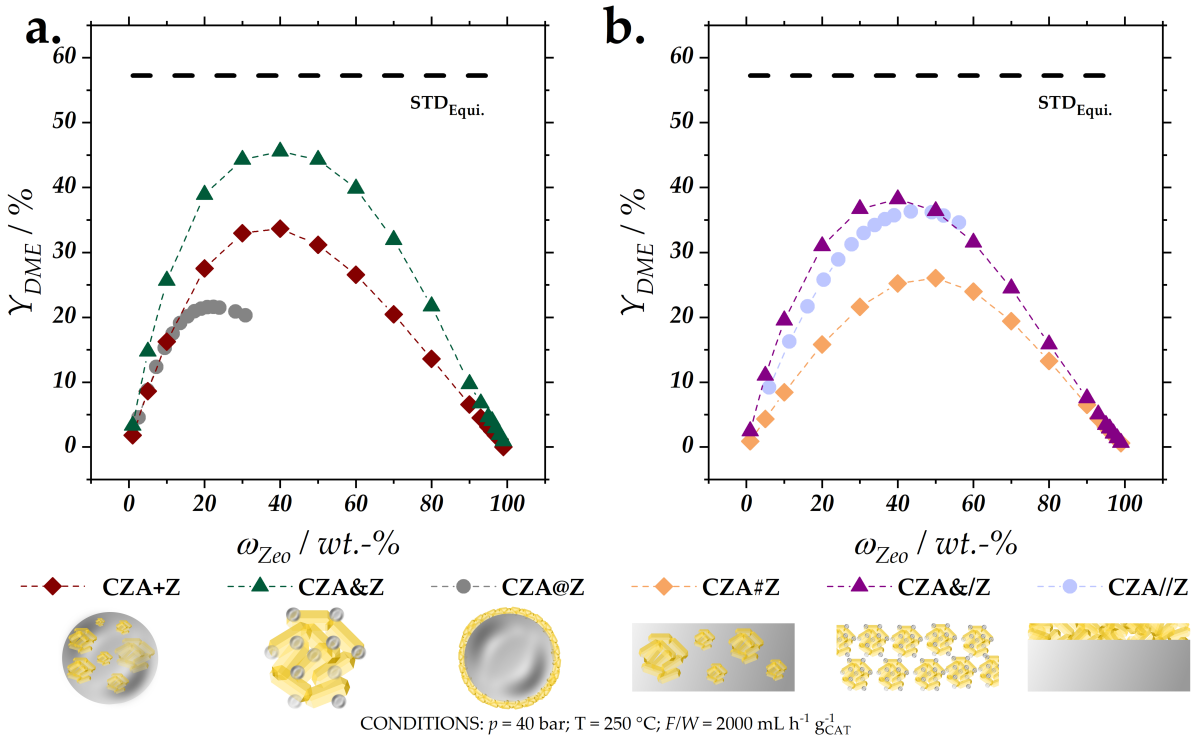


Figure 3.7: Y_{DME} as a function of catalyst composition in a) particulate configurations in a PBR and b) coated configurations in a µ-CR.

contrast to the results obtained for the particulate systems, the effect of ω_{Zeo} on the product selectivity is more pronounced for the coated systems in the µ-CR: the increase of S_{DME} (resp. decrease of S_{MeOH}) with ω_{Zeo} is smaller and the maxima are more distinct in comparison to the broad plateau found for the particulate systems (see Figure 3.4). S_{DME} versus X_{CO} for the hybrid system in both, particulate and planar configuration (CZA&Z and CZA&/Z resp. CZA+Z and CZA#Z see Figure A.1), show that the S_{DME} is barely affected by the implementation of the catalyst (particulate vs. planar). The CZA@Z as packed bed in the PBR and its coated counterpart CZA//Z in the µ-CR perform differently in terms of X_{CO}: the CZA//Z configuration shows rather similar X_{CO} as the coated CZA&/Z configuration. Thus, in contrast to the CZA@Z system, in the double layer configuration CZA//Z reactant diffusion is not hindered, which is due to the different morphology of the zeolite layers. CZA//Z is a printed double layer of CZA powder and zeolite crystallites whereas CZA@Z is a polycrystalline zeolite membrane enwrapping preformed CZA particles. This results in totally different porosity (see Table 3.4). As a consequence, X_{CO} in the CZA//Z system is enhanced while S_{DME} is not as high as for the coated CZA&/Z of close proximity (see Figure 3.6b) or the hierarchical structure in the CZA@Z with its dense zeolite shell. Once again, this is proving the opposing effect of the zeolite layer porosity on X_{CO} (promoted by intercrystalline porosity) and S_{DME} (promoted by the zeolite micropores), respectively.

In the µ-CR, the maximum in X_{CO} for all three catalyst configurations can be found at approx. ω_{Zeo} = 40 wt.-%, being similar or even slightly higher than for the particulate systems in the PBR. The maximum in S_{DME} is reached at ω_{Zeo} = 80 wt.-% for both, CZA&/Z and CZA#Z and at ω_{Zeo} = 56 wt.-% for the CZA//Z (at largest ω_{Zeo}-value investigated). Even though the maximum values are similar, for the coated systems investigated, the plateaus in S_{DME} are not as pronounced as for the particulate systems

in the PBR.

In Figure 3.7, both particulate and planar catalytic structures are compared in terms of the Y_{DME}. The hybrid structures with close proximity show the highest Y_{DME} both as particulate (CZA&Z) and coated (CZA&/Z) system, while the yield of the latter one is comparable to the one obtained with the CZA//Z system. For the particulate systems, the maximum DME-yield is reached at ω_{Zeo} = 40 wt.-% for CZA&Z and CZA+Z and at ω_{Zeo} = 22 wt.-% for the CZA@Z. For the coated systems, maximum yield is achieved likewise at approx. ω_{Zeo} = 40 wt.-% for CZA&/Z and CZA//Z, and at 50 wt.-% for CZA#Z.
In general, the optimization of the catalyst configuration and composition depends on the target. This might either be Y_{DME} (maximum product output) or maximum per-pass X_{CO} (decrease recycling). According to this simulation study, the particulate CZA&Z as well as the coated CZA&/Z and CZA//Z are promising systems.

3.2.3 Influence of reaction temperature

The temperature of a chemical process can be chosen according to different criteria, such as finding a proper compromise between the highest yield to the desired product, potential thermodynamic limitations and the requirements predetermined by the catalyst (e.g. deactivation by sintering). As side reactions as well as catalyst deactivation were not in the scope of this study, temperatures above 270 °C were not considered as sintering of the CZA catalyst (deactivation) and further reaction of the DME to hydrocarbons takes place starting from approx. 300 °C, as reported in literature [68, 78, 125, 126] (see also section 2.3). In the following, the influence of the reaction temperature on the STD reaction for the

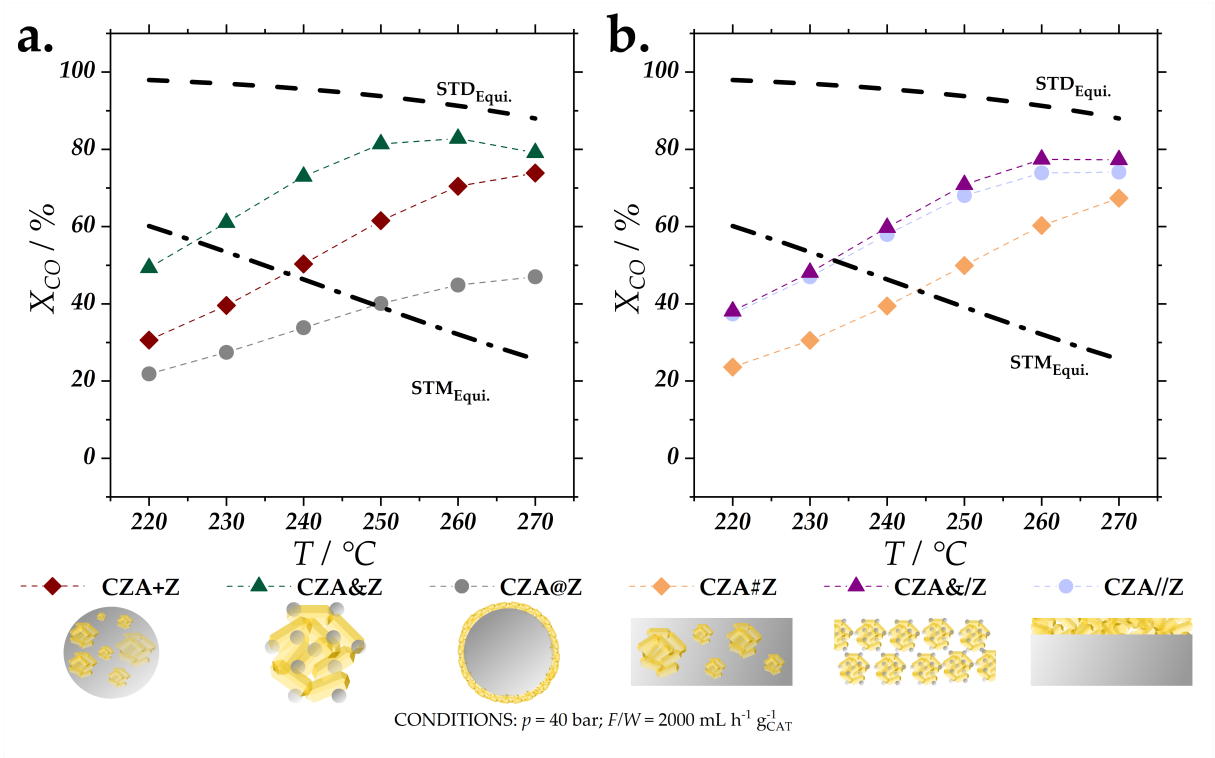


Figure 3.8: X_{CO} as a function of temperature for all catalyst structures considered: a) particulate configurations in a PBR (ω_{Zeo}(CZA+Z) = 30 wt.%, ω_{Zeo}(CZA&Z) = 40 wt.%, ω_{Zeo}(CZA@Z) = 17 wt.%) and b) coated configurations in a µ-CR (ω_{Zeo}(CZA+Z) = 40 wt.-%, ω_{Zeo}(CZA&/Z) = 40 wt.%, ω_{Zeo}(CZA//Z) = 43 wt.%).

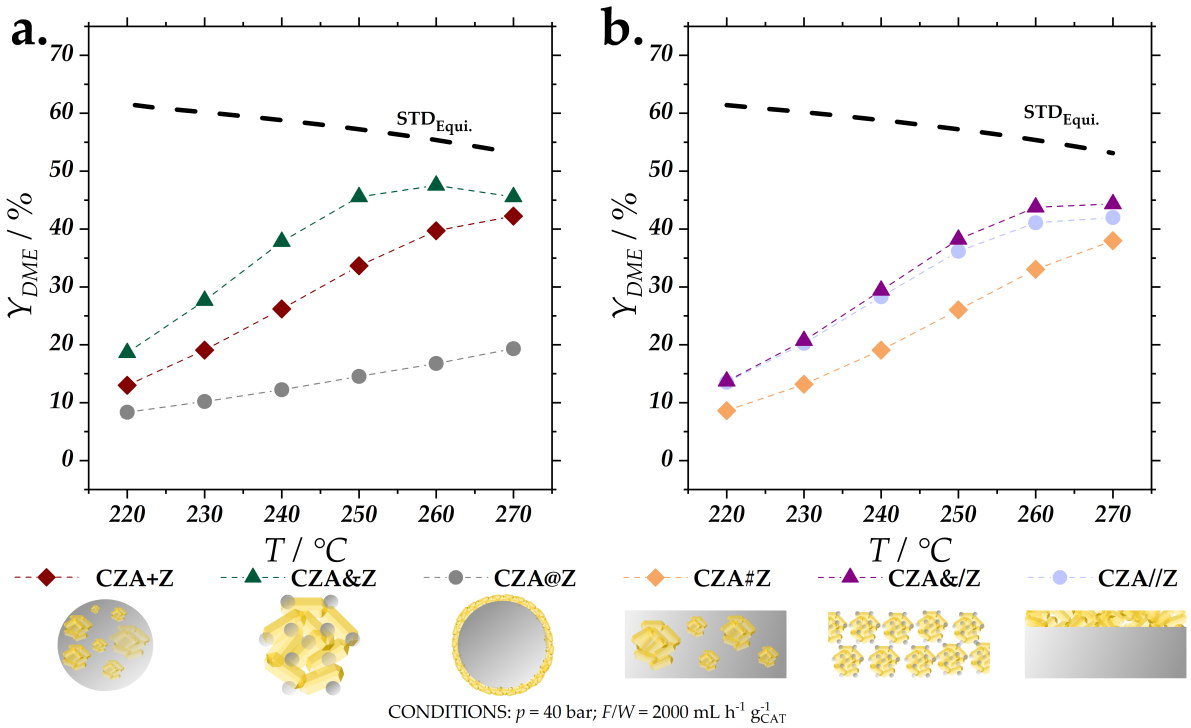


Figure 3.9: Y_{DME} as a function of temperature for all catalyst structures considered: a) particulate configurations in a PBR (ω_{Zeo}(CZA+Z) = 30 wt.%, ω_{Zeo}(CZA&Z) = 40 wt.%, ω_{Zeo}(CZA@Z) = 17 wt.%) and b) coated configurations in a μ-CR (ω_{Zeo}(CZA+Z) = 40 wt.-%, ω_{Zeo}(CZA&/Z) = 40 wt.%, ω_{Zeo}(CZA//Z) = 43 wt.%).

different bifunctional catalyst configurations is discussed in order to determine the optimum operational temperature for the materials considered.

Figure 3.8 shows X_{CO} as a function of the reaction temperature for the different particulate catalysts (Figure 3.8a) as well as for the coated systems (Figure 3.8b). For each catalyst, the composition in terms of ω_{Zeo} was defined based on the composition yielding maximum X_{CO} as determined from the results of the simulations discussed in section 3.2.2; these are reported in caption of Figure 3.8. In general, X_{CO} for the different catalyst configurations quantitatively orders in accordance to what was reported in section 3.2.2: the hybrid configurations with close proximity (CZA&Z and CZA&/Z) show the highest X_{CO} throughout the whole temperature range investigated independent on the configuration (particulate or coated system). In general, at low reaction temperature, the X_{CO} for all particulate systems investigated is below the STM equilibrium conversion, which is exceeded at about 230, 240 and 250 °C for the particulate systems CZA&Z, CZA+Z and CZA@Z, respectively. A comparable behaviour can be observed for the coated systems, which allow to reach the thermodynamic equilibrium at about 235 °C for CZA&/Z and the CZA//Z and at about 245 °C for CZA#Z. After exceeding the STM equilibrium conversion, for all catalysts X_{CO} steadily increases with temperature until a maximum is reached with subsequent decrease of the conversion in line with the thermodynamic limitation of the STD-reaction (see $X_{CO}^{STD,eq.}$ in Figure 3.8). From these findings, it can be confirmed that the results shown in section 3.2.2 (reaction temperature set to 250 °C) are not limited by the reaction equilibrium. In addition, for each catalyst configuration, an optimum reaction temperature resulting in a maximum of X_{CO}, can be determined: at 260 °C for the particulate CZA&Z (X_{CO} = 83 %) and for the coated system CZA&/Z (X_{CO} = 77 %) the highest X_{CO} for all catalyst configurations and compositions studied was found. In the

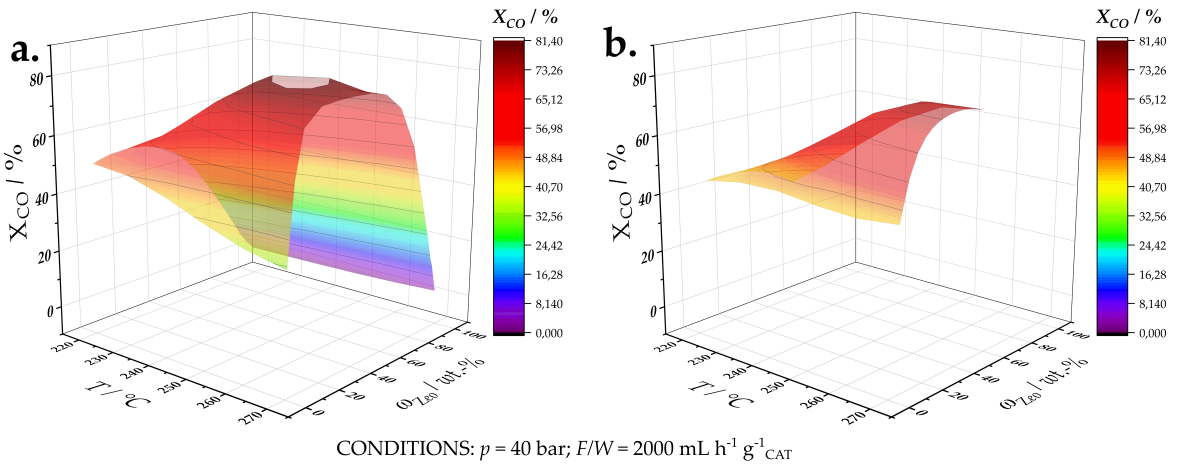


Figure 3.10: X_{CO} as a function of temperature and ω_{Zeo} for a) the particulate configuration CZA&Z in a PBR and b) the coated configuration CZA//Z in a μ-CR.

range investigated, the optimum temperature for the particulate systems CZA+Z and CZA@Z as well as for the planar systems CZA#Z and CZA//Z is the maximum temperature of 270 °C. Yet, for those systems somewhat lower CO-conversions as compared to CZA&Z and CZA/&Z are predicted (CZA+Z: X_{CO} = 74 %, CZA@Z: X_{CO} = 47 % resp. CZA#Z: X_{CO} = 67 %, CZA//Z: X_{CO} = 74 %). For the CZA//Z and the CZA&/Z, within the temperature range investigate, X_{CO} does not show a distinct maximum. However, as X_{CO} gets close to the STD equilibrium conversion at the highest temperature investigated, and as all three coated structures converged to similar values, the influence of thermodynamic limitation is undeniable and, thus, further simulations at even higher temperatures were not considered here.

Concerning Y_{DME}, shown in Figure 3.9, for the particulate systems maximum values were found at a reaction temperature of 260, 270 and 270 °C for CZA&Z (X_{CO} = 48 %), CZA+Z (X_{CO} = 42 %) and the CZA@Z (X_{CO} = 27 %), respectively. For all coated catalyst configurations, the maximum of Y_{DME} is reached at 270 °C, with X_{CO} = 44 %, 42 % and 38 % for CZA&/Z, CZA//Z and CZA#Z, respectively. In general, no deviation was observed between the temperatures resulting in maximum values of both, X_{CO} and Y_{DME}, except for the coated CZA&/Z ($T_{X_{CO,max}}$ = 260 °C, $T_{Y_{DME,max}}$ = 270 °C) system. In summary, for each structure, the reaction temperature can be chosen as to reach the highest X_{CO} without compromising Y_{DME} and vice versa.
This range of reaction temperatures is in agreement with the studies of Peláez e al. and Lu et al., who compared experimental data with results from modelling. Both studies highlight the importance of not exceeding a reaction temperature of 280 °C and concluded feasible reaction temperatures for the STD process are in the range of 250 - 270 °C, even though Lu et al., based on their simulation study, found a maximum in X_{CO} and P_{DME} at $T > 280$ °C [68, 78].

In order to determine whether the CZA/zeolite ratio has an influence on the performance at variable reaction temperature, the X_{CO} as a function of both, the temperature and ω_{Zeo} was analyzed in the present study. The results for the most promising candidates, namely the particulate CZA&Z and the coated CZA//Z systems, are shown in Figure 3.10. At temperatures above 260 °C, there is no distinct maximum in X_{CO} with respect to ω_{Zeo}: for these temperatures, X_{CO} is not depending on the catalyst composition

anymore. At lower temperatures, the maximum in X_{CO} is at ω_{Zeo} = 40 wt.-% for the particulate CZA&Z. For the CZA//Z system, the maximum shifts from ω_{Zeo} = 16 wt.-% (T = 220 °C, X_{CO} = 43 %) to 43 wt.-% (T = 250 °C, X_{CO} = 69 %): if the temperature is increased, X_{CO} increases, too.

In summary, X_{CO} in the STD reaction does not only depend on temperature, but also on the catalyst configuration and on its composition. For this reason, reaction temperature, configuration and composition of the catalyst all have to be taken into account. Similar X_{CO} can be achieved by different catalyst configurations and/or compositions and/or at different reaction temperatures. This fact could explain why Ramos et al. found that the performance of the STD was independent of the composition of the hybrid catalysts: the experimental tests could have been limited by other process parameters, such as the temperature [47]. A criterion for the choice of an appropriate temperature and ω_{Zeo} could be based on the synthesis effort of the catalyst versus the operational costs of the process at different temperatures. However, other aspects such as e.g. deactivation would have to be considered and such optimizations were not among the objectives of this work.

3.2.4 Influence of *F/W*

The *F/W*, defined as the ratio between the total inlet volumetric flow and the mass of the catalyst, is an important parameter in a chemical process and for its scale up. Simulation results of X_{CO} versus *F/W*, at 250 °C and the optimum ω_{Zeo} in terms of X_{CO} for each catalyst configuration (see caption of Figure 3.11), are shown in Figure 3.11.

As expected, X_{CO} decreases with increasing *F/W*. In addition, the ordering in the activity among the con-

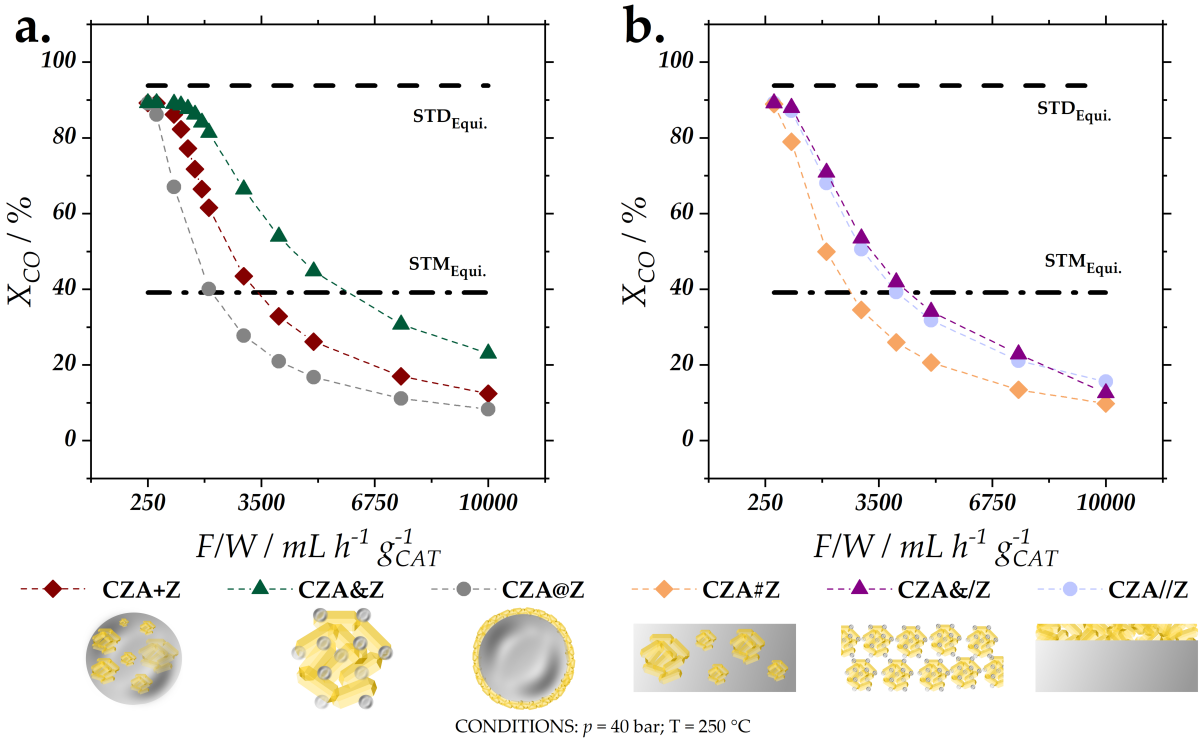


Figure 3.11: X_{CO} as a function of *F/W* for all catalyst structures considered: a) particulate configurations in a PBR (ω_{Zeo}(CZA+Z) = 30 wt.%, ω_{Zeo}(CZA&Z) = 40 wt.%, ω_{Zeo}(CZA@Z) = 17 wt.%) and b) coated configurations in a μ-CR (ω_{Zeo}(CZA+Z) = 40 wt.-%, ω_{Zeo}(CZA&/Z) = 40 wt.%, ω_{Zeo}(CZA//Z) = 43 wt.%).

figurations in terms of X_{CO} is consistent with other results obtained from simulation discussed above (e.g. $X_{CO} = f(\omega_{Zeo})$). For *F/W* values up to approx. 1000 mL h^{-1} g_{CAT}^{-1}, for both, particulate and coated configurations, the reaction system is limited by the STD thermodynamic equilibrium and all systems reach X_{CO} = 89 %. Starting from 1000 mL h^{-1} g_{CAT}^{-1}, X_{CO} decreases with increasing *F/W* for all systems as expected, but marked differences between the different configurations are observed.
In choosing the most convenient *F/W*, both too low and high values should be avoided, so that X_{CO} is not limited by the STD equilibrium and does not lay below STM equilibrium. In this way it is possible not to waste catalyst material and to get benefit from the STD process itself. Starting from these results and considerations, it is reasonable to operate the particulate catalysts CZA&Z in the range of 1500 - 3000 mL h^{-1} g_{CAT}^{-1}, CZA+Z in the range of 1000 - 2000 mL h^{-1} g_{CAT}^{-1} and CZA@Z at about 1000 mL h^{-1} g_{CAT}^{-1}, while the coated catalysts CZA&/Z and CZA#Z in the range of 1000 - 3000 mL h^{-1} g_{CAT}^{-1} and CZA//Z in the range of 1000 - 2000 mL h^{-1} g_{CAT}^{-1}. In the present study, the comparison of all catalyst structures was carried out at the *F/W* of 2000 mL h^{-1} g_{CAT}^{-1}.

3.2.5 Influence of feed composition

Feed composition is strongly influencing X_{CO} and, thus, is a crucial factor for the STM resp. STD process. Moreover, in the context of the Power-to-X concept with its fluctuating renewable energy input, changes in feed-composition could be relevant thus demanding knowledge about the behaviour of the reaction under different feed compositions. This study aims at investigating the theoretical behaviour of the catalysts without taking into account deactivation and response under dynamic operation, which has to be the objective of further studies.
In the frame of this work, the influence of the concentration ratio of CO_2/CO in the feed on X_{CO} and Y_{DME} as well as of the ratio of the concentration of H_2 versus CO and CO_2, $y_{H_2} / \left(y_{CO} + y_{CO_2}\right)$, on the CO_x-conversion (X_{CO_x}, Equation 3.9) and the DME-productivity (P_{DME}, Equation 3.12) were studied for one of the most promising candidates according to the findings discussed above, namely the particulate system with close proximity (CZA&Z). X_{CO_x} and Y_{DME}/P_{DME} compared to the maximum values given by thermodynamics ($X_{CO_x}^{eq.}$ and $Y_{DME}^{eq.}$) versus the feed composition are shown in Figure 3.12.
Figure 3.12a reports the influence of the y_{CO_2}/y_{CO} ratio on X_{CO_x} and Y_{DME}, (feed concentration H_2: 57.6 vol.-% = const., N_2: 10 vol.-% = const.). Starting from a pure CO feed, with increasing CO_2 co-feeding until 14.4 vol.-% CO_2, at y_{CO_2}/y_{CO} = 0.06 ($y_{CO_2,feed}$ = 1.8 vol.-% and $y_{CO,feed}$ = 30.6 vol.-%) both X_{CO_x} and Y_{DME} present a weak maximum. Further increasing CO_2 content results in a decrease of both values. When feeding CO as the only carbon source, MeOH can only be formed via Equation 1.1. The water being produced by the subsequent dehydration step yielding DME (Equation 1.4) and the absence of CO_2 shift the equilibrium of the WGS-reaction (Equation 1.3) to the right resulting in less CO_2 being produced by the STM catalyst. Overall, the formation of MeOH is kinetically limited by the absence of CO_2 in the feed resulting in low values of X_{CO_x} and Y_{DME}. When co-feeding CO_2, MeOH can be formed from both, CO and CO_2, which results in higher X_{CO_x} and Y_{DME} until reaching a maximum. When the y_{CO_2}/y_{CO} ratio exceeds 0.06, the X_{CO_x} is negatively affected by the catalyst system, because the high concentration of CO_2 promotes the formation of water via the reverse WGS reaction, which eventually hinders DME dehydration. This is in line with the studies of Peláez et al. and of Ng et al., who observed experimentally and by modelling the benefit of adding up to 4 - 6 vol.-% of CO_2 in the feed gas, while

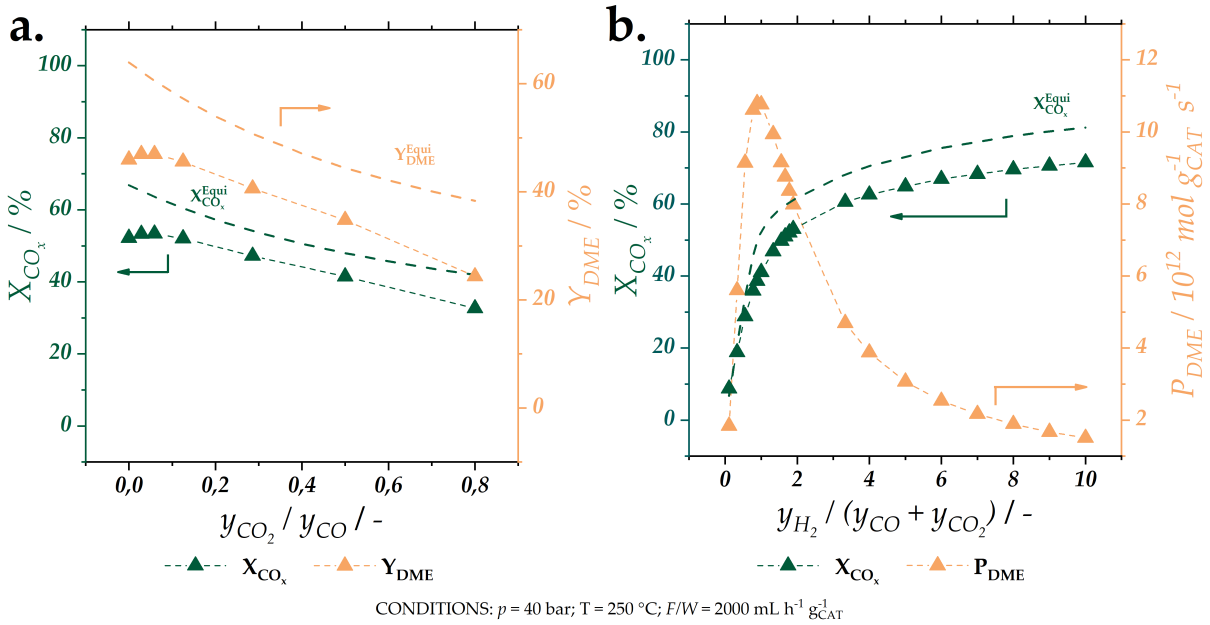


Figure 3.12: Influence of the feed composition for the particulate CZA&Z system on X_{CO_x} and a) Y_{DME} as a function of y_{CO_2}/y_{CO} (H_2 = 57.6 vol.-% = const.) b) P_{DME} as a function of $y_{H_2}/\left(y_{CO}+y_{CO_2}\right)$ (y_{CO_2}/y_{CO}= 1/8 = const.) in a PBR. (ω_{Zeo} = 40 wt.-%).

for larger shares a decrease in conversion associated with an increase in S_{MeOH} was detected [68, 127].

Figure 3.12b shows the influence of the H_2/CO_x ratio $y_{H_2}/\left(y_{CO}+y_{CO_2}\right)$, ($y_{CO_2}/y_{CO}$ = 1/8 = const., 10 vol.-% of N_2 in the feed) on X_{CO_x} and P_{DME}. An increase of the share of H_2 in the feed results in a monotonic increase of X_{CO_x}. In contrast, P_{DME} presents a maximum at $y_{H_2}/\left(y_{CO}+y_{CO_2}\right)$ = 0.9. According to literature, the $y_{H_2}/\left(y_{CO}+y_{CO_2}\right)$-ratio should be at least equal to 1 in order to prevent deactivation of the catalyst caused by formation and deposition of coke [128]. The influence of the feed composition either on X_{CO_x}, Y_{DME} or P_{DME} is reported in several studies [68, 78, 127] while mostly the y_{H_2}/y_{CO}-ratio in the feed gas was studied. According to these studies, while the STM reaction is favoured at y_{H_2}/y_{CO} = 2, MeOH dehydration profits most at y_{H_2}/y_{CO} = 1 [68, 78]. Ng et al. studied the $y_{H_2}/\left(y_{CO}+y_{CO_2}\right)$ ratio and observed a maximum of Y_{DME} at about 1.6. A lower $y_{H_2}/\left(y_{CO}+y_{CO_2}\right)$ ratio favours the removal of water via the WGS reaction and thereby the formation of DME while a larger ratio has the opposite effect [127]. Hence, in this study, the reference value set was set to $y_{H_2}/\left(y_{CO}+y_{CO_2}\right)$ = 1.8, with CO_2: 3.6 vol.-%, H_2: 57.6 vol.-% and N_2: 10 vol.-%, which is a compromise between high productivity and the avoidance of an eventual coking process. Moreover, it allows for comparison to values reported in literature.

3.3 Summary

The modelling focused on the analysis of the performance of the different catalyst structures considered in the frame of this work in terms of CO-conversion (X_{CO}) and DME-selectivity (S_{DME}) at different catalyst compositions (i.e. zeolite mass fraction, ω_{Zeo}), temperature, F/W and feed composition in a packed-bed-reactor (PBR) and a micro-channel reactor (µ-CR). The modelling of these catalyst structures was based on the 3D-crystallite pore network model (3D-CPNM), developed in a previous work [119, 124],

introducing assumptions based on the synthesis and characterization of the catalysts. The diffusion of the chemical species through the catalyst and the MeOH dehydration kinetics were implemented according to the previous work of Ding [119], the kinetics of the MeOH synthesis according to the recent study of Seidel et al. [30]. The results reveal that:

- At fixed operating conditions (p = 40 bar, T = 250 °C, F/W = 2000 mL h^{-1} g_{CAT}^{-1}, feed composition: $H_2/CO/CO_2$ = 16/8/1, 10 vol.-% N_2), X_{CO} shows a maximum for each configuration at different ω_{Zeo}. Furthermore, the sequence in maximum activity in terms of X_{CO} is CZA@Z < CZA+Z < CZA&Z and CZA#Z < CZA//Z ≤ CZA&/Z for the particulate and layered systems, respectively. The close proximity of the two catalysts present in the hybrid CZA&Z and the structure of the CZA//Z configuration improve both X_{CO} and S_{DME} in comparison to the CZA+Z and the CZA#Z systems of medium proximity.

- Due to the different concept of the CZA@Z and the CZA//Z, these catalyst configurations present different activity. The reason lies in the different intercrystalline porosity (mesopores between the zeolite crystals forming the layers) assumed (based on characterization): the slower diffusion through the micropores in the H-ZSM-5 shell of the CZA@Z hinders the transport of the reactants through the shell, which is not the case for the CZA//Z where the zeolite crystals do not form an intergrown polycrystalline layer with preferred uniform orientation of the crystals but a loose arrangement of randomly oriented crystal. The coated CZA//Z system does not face transport-limitation and therefore allows for higher X_{CO}. At the same time, the CZA@Z enables a higher S_{DME}, as the probability for MeOH to diffuse through intercrystalline mesopores without getting dehydrated at the active sites within the micropores is lower.

- With a view to finding suitable operational conditions, from this study the convenience of running the STD process at a temperature and a F/W in the range of 250 - 260 °C and 1000 - 2000 mL h^{-1} g_{CAT}^{-1}, respectively, comes up. In doing so, it is possible to avoid thermodynamic limitations. The choice of the operational conditions should also take into account the catalyst configuration and its composition (ω_{Zeo}).

- The influence of the feed composition was investigated for the CZA&Z configuration in the PBR. A maximum in Y_{DME} and P_{DME} was found at $y_{CO_2}/y_{CO} = 0.06$ and $y_{H_2}/\left(y_{CO} + y_{CO_2}\right) = 1.6$, respectively.

- The hybrid particulate and layered systems of close proximity (CZA&Z and CZA&/Z) as well as the double layer system (CZA//Z) were found to be the most promising structures, especially for ω_{Zeo} = 40 wt.-% when applied at p = 40 bar, T = 260 °C (CZA&Z and CZA&/Z) or T = 270 °C (CZA//Z), F/W = 2000 mL h^{-1} g_{CAT}^{-1}, and feed composition: $H_2/CO/CO_2$ = 16/8/1, 10 vol.-% N_2.

4 Synthesis

In the following the synthesis of the single CZA as well as of the catalyst configurations for the STD reaction is described. Materials and equipment used are listed in section 4.1. The STM-catalyst preparation is delineated in section 4.2. Regarding the STD-catalyst systems, sections 4.3 and 4.4 describes the preparation procedure of the particulate and planar (coated) configurations, respectively.

4.1 Materials and equipment

For the synthesis of the STM catalyst via flame spray pyrolysis (FSP, see Figure 4.1), the following materials and equipments were used: copper(II) nitrate tri-hydrate $Cu(NO_3)_2 \cdot 3\ H_2O$ (Carl Roth GmbH, $\geq$ 99 %), zinc nitrate hexa-hydrate $Zn(NO_3)_2 \cdot 6\ H_2O$ (Carl Roth GmbH, $\geq$ 99 %), aluminum nitrate nona-hydrate $Al(NO_3)_3 \cdot 9\ H_2O$ (VWR Chemicals, $\geq$ 98 %), ethanol (EtOH) (Merck kGaA, $\geq$ 99.5 %), mixture of Xylene isomers (X) (Merck KGaA, $\geq$ 98.5 %), diethylene glycol monobutyl ether (DEGBE) (Merck KGaA, $\geq$ 98 %) and 2-ethyl hexanoic acid (EHA) (Merck kGaA, $\geq$ 99 %). The metal precursor solution was fed to the flame generator (NanoPowderNozzle®, Tethis Spa, Milan) by a syringe pump (PHD Ultra™, Harvard). The powder produced was collected either in batch on a glass fibre filter (Whatman®, grade GF/F, $\phi = 257$ mm) set at the top of the FSP-cylinder or semi-continuously in a bag-house filter (Wegner Consulting, Zürich). The volumetric flows of the gases were driven by mass flows controllers (MFS, Brooks). The agglomeration of the STM catalyst via spray drying (see Figure 4.5) was carried out in a mini Spray Drayer B-290 (BÜCHI Labortechnik AG, Flawil).
For the nanosized zeolite particles as well as for the shell synthesis, the following materials were used: tetraethyl orthosilicate (TEOS) (Alfa Aesar GmbH, $\geq$ 98 %), tetrapropylammonium hydroxide solution 1 M (TPAOH) (Sigma Aldrich), $Al_2(SO_4)_3 \cdot 18\ H_2O$ (Merck, 51 - 59 wt.-%) and $Al(NO_3)_3 \cdot 9\ H_2O$ (Fluka, $\geq$ 98 wt.-%) as silicon source, template and aluminium source, respectively.
For the synthesis of the planar catalyst configurations, stainless steel foils (Ätztechnik Herz GmbH & Co. KG) containing 50 semicircular micro-channels (see Figure A.2) were coated using FSP-CZA and zeolite H-ZSM-5 as catalysts powder, terpineol (T) (mixed isomers, 98 %, Alfa Aesar GmbH) and deionized water as solvents, ethyl cellulose (EC) (viscosity 0.1 Pa $\cdot$ s, Sigma Aldrich) and methyl cellulose (ME) (viscosity 0.4 Pa $\cdot$ s, Alfa Aesar GmbH) as binder and Hypermer KD1-SO-(AP) (Croda Inc.) as dispersant. A three roll mill (EXAKT 50; EXAKT Technologies, Inc., USA) was used for the homogenization of the pastes to be coated by a semi-automatic screen printer (M2, EKRA Automatisierungssysteme GmbH, ASYS GROUP) at the Institute for Applied Materials - Energy Storage Systems (IAM-ESS) using a screen (Koenen GmgH) with a 80 mesh sieve and a mask opening of 100 µm (see Figure A.3).

4.2 FSP-CZA

In a previous work, Lee et al. studied the influence of the metal molar ratio as well as of the precursor solution on the performance of the catalyst in the STD reaction in terms of X_{CO} and DME-

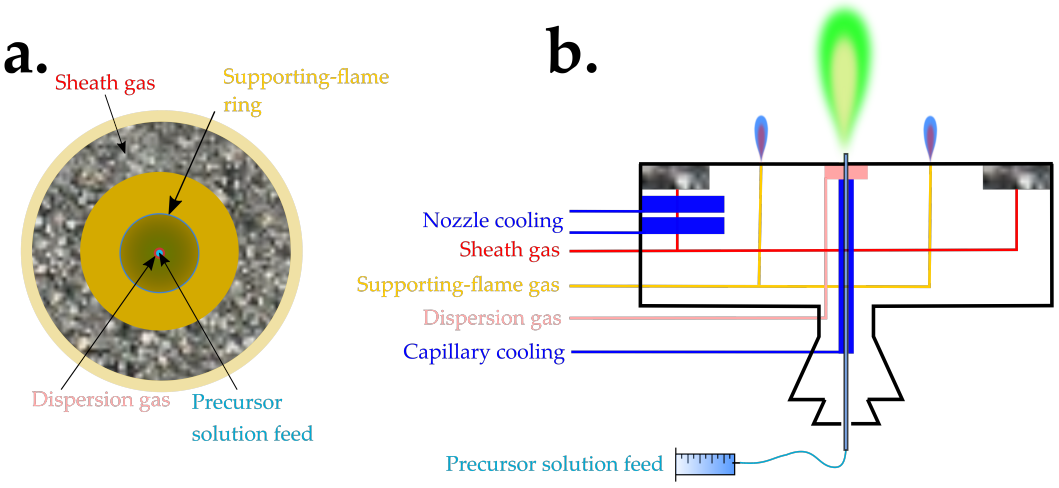


Figure 4.1: Illustration of the FSP-nozzle: a) top- and b) lateral-view.

productivity [129]. It was concluded that the most proper metal molar ratio is Cu : Zn : Al equal to 6 : 3 : 1, which is also in accordance with many studies reported in literature [38, 50, 130].

The precursor solution for the FSP synthesis was prepared by dissolving the metal nitrates in the metal molar ratio proposed by Lee et al. (Cu : Zn : Al equal to 6 : 3 : 1) with a molarity of 0.5 M. Two different solvents were used: *solution 1*, which consisted of pure EtOH, and *solution 2*, which consisted of the mixture X : EHA : DEGBE : EtOH equal to 1 : 1 : 1 : 1 (vol. ratio). The obtained solution was magnetically stirred until the salts were completely dissolved. A scheme of the flame spray pyrolysis (FSP) nozzle is illustrated in Figure 4.1. First, the supporting-flame gas ($CH_4/O_2 = 1/4$) was ignited, forming the supporting flame ring. Together with the nozzle, the dispersion gas (O_2; 3.5 - 5.5 L min^{-1}; $p = 2$ bar) enables the formation of droplets of the precursor solution, which was fed with a flow rate in the range of 5 - 10 mL min^{-1} (see section 4.2.1 for details). An additional O_2-flow was fed as sheath gas (5 L min^{-1}) for confinement of the flame and consequent limitation of powder loss during the synthesis. The nozzle and the capillary were cooled with deionized water.

The powder was collected either with a common batch system (see Figure 4.2a) or with a bag-house filter (see Figure 4.2b). The batch synthesis had to be stopped when the filter capacity was reached (c.a. 2 g of powder); the powder was then scratched from the glass fibre filter with a spatula and the eventual presence of filter impurities in the final nanopowder was avoided by sieving it below 200 µm. Otherwise the synthesis was conducted semi-continuously: the FSP-cylinder was connected to the bag-house filter, consisting of a stainless steel housing containing 4 polytetrafluoroethylene (PTFE) filters supported by metallic cages. The powder-rich air was vacuum-cleaned to the bag-house filter; the particles were trapped at the filter surface, the cleaned air was directed to the hood. When the temperature at the entrance of the housing reached 180 °C, the synthesis was stopped, continuing the air vacuum-cleaning. In this way, it was avoided to exceed the maximum-operating temperature of the housing of 200 °C. This temperature was generally reached after 30 min, which, in this thesis, is denoted as *time of synthesis run*. For the collection of the powder, the vacuum pump was stopped and pressurized air ($p = 5$ bar) was pulsed for 0.05 s every 5 s into the 4 PTFE-filters from an electrically-controlled tank. The product was then collected at the bottom of the housing. With the bag-house collection system the synthesis time was not limited from the low capacity of the glass fibre filter; furthermore, no treatment (sieving) of the

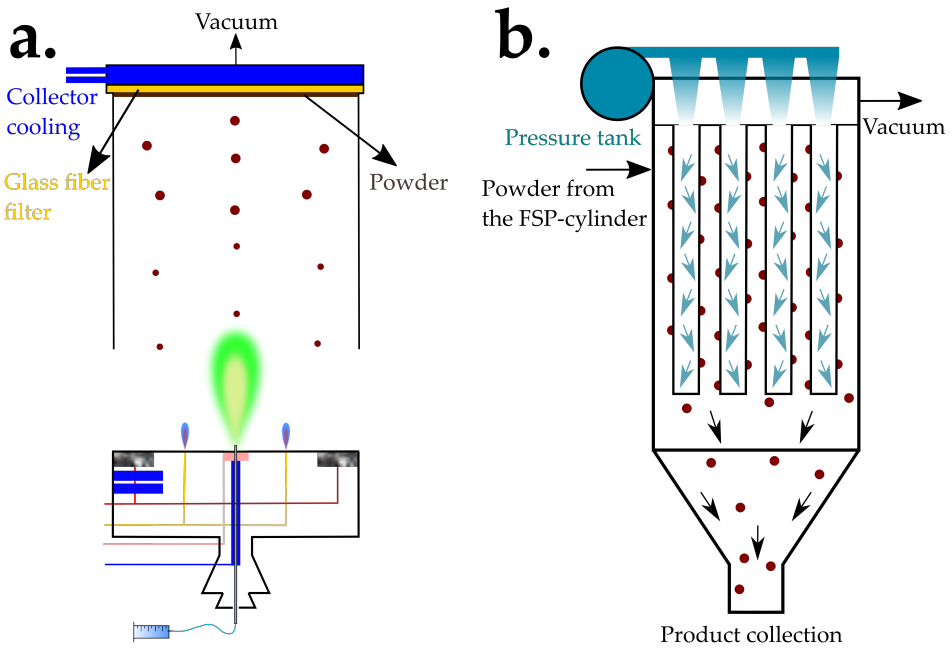


Figure 4.2: Scheme of the a) batch and b) semi-continuous powder collection systems for the FSP synthesis.

product was necessary.

FSP-CZA denotes, in general, CZA nanopowder prepared via FSP. The obtained nanopowder is denoted as CZA-*i*-*x*, where *i* indicates the precursor solution (either *1* or *2*) and *x* denotes the collecting system (either *b*, when batch, or *f*, when semi-continuous). The FSP-CZA nanopowder was at first characterized for finding out its physico-chemical features, namely the specific surface area, crystallinity, primary particle size, composition and activity for the STM reaction (see chapter 5). As the FSP-CZA could not be directly used for the activity test in the STM reaction, it was necessary to press it into tablets, crush and sieve into particles (denoted as P-CZA-1 and P-CZA-2, obtained from the CZA-1-f and CZA-2-f, respectively) with equivalent diameters in the range of 50 - 100 µm. The CZA-1-f sample was used for the synthesis of the hybrid particulate systems of medium and close proximity, namely the CZA&Z and CZA+Z, and all the planar (coated) catalyst systems. Moreover, the CZA-1-f was either agglomerated via spray drying (SD-CZA, see section 4.3.3) or pressed into tablets, crushed and sieved into particles with equivalent diameters in the range of 100 - 200 µm and used as core materials for the synthesis of either SD-CZA@Z and SD-CZA_core or P-CZA@Z catalysts, respectively (see section 4.3.3).

4.2.1 Semi-continuous collection of the nanopowder

The synthesis of the CZA-1-f was subject to a preliminary study with respect to the most proper flow rate of the precursor solution to the FSP-nozzle, which was then applied for the synthesis of the CZA-2-f nanopowder. For this investigation, the CZA-1-f was synthesized at three different precursor flow rates (5, 7.5 and 10 mL min^{-1}) while maintaining the ratio between the flows of precursor and dispersion gas constant at 1/700. The nanopowder was collected using cleaned PTFE filters. By observing Figure 4.3a, at the three different precursor flow rates, it can be seen that the nanopowder collection becomes linear after the *induction time*. When the filtering process occurs over cleaned filters, the so-called *filter-cake*

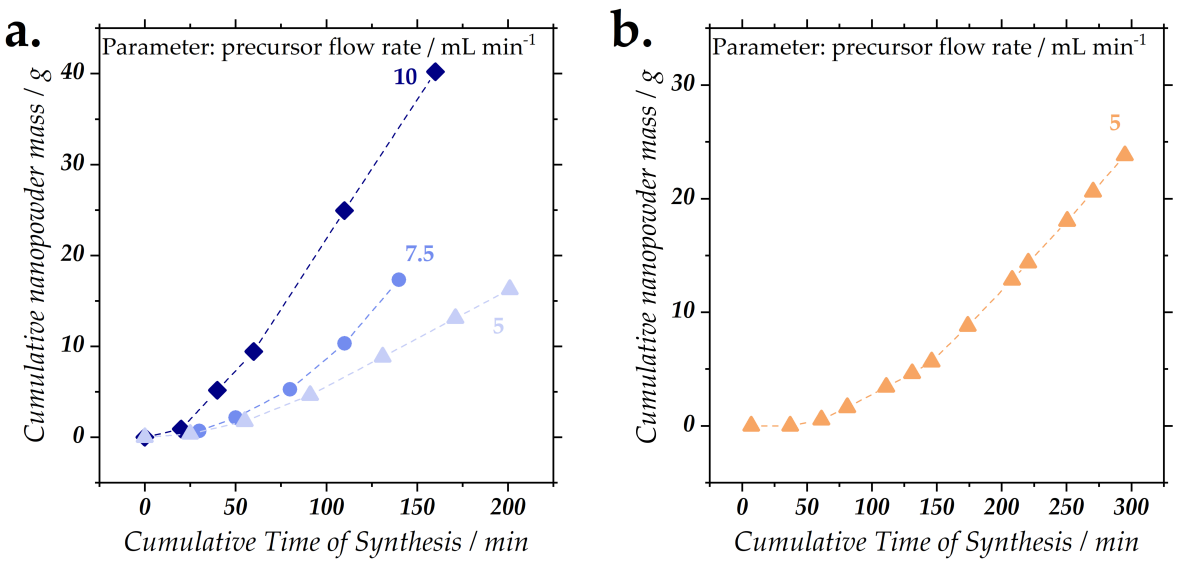


Figure 4.3: Cumulative mass of a) CZA-1-f for different precursor flow rates and b) CZA-2-f for the precursor flow rate equal to 5 mL min^{-1} synthesized via FSP and collected using the bag-house filter. *Cumulative time of synthesis*: sum of time of several single synthesis runs.

effect is notable: this consists of the dust layer built up by the particles over the PTFE surface with consequently slower increase of the pressure drop and modest separation efficiency. The pressure drop over the filter then reaches a constant value and the separation efficiency becomes linear over time (*depth filtration*). PTFE material is known for acting itself as *filter-cake*, lowering strongly the *induction time* (surface filtration mechanism) [131]. Figure 4.3a shows that the filtration process becomes linear over time after about 1 h, independent of the solution used.

Besides this aspect, as expected, the higher the precursor flow rate, the higher the amount of powder that can be produced over time. From Figure 4.3a the productivity, defined as the ratio of the collected nanopowder over the cumulative synthesis time in the linear range, could be extrapolated and was found equal to 0.1, 0.2 and 0.3 g min^{-1} for precursor flow rates of 5, 7.5 and 10 mL min^{-1}, respectively: no direct proportionality between the precursor flow rate and the productivity was found (a factor 2 in the precursor flow rate corresponds to a factor 3 in the productivity). This suggests that the efficiency of the pyrolysis is correlated to the amount of precursor solution present in the nozzle at a certain time: at higher precursor flow rate, more solvent, namely liquid with higher combustion enthalpy, is burned in the flame zone at a given time with a consequent increase of the temperature, improving the efficiency of the nanopowder production. This benefit, added to the higher amount of metal precursors present in the flame, makes a higher productivity possible. Notwithstanding the advantage regarding productivity, when the pyrolysis took place at precursor flow rates higher than 5 mL min^{-1}, needle blockage, with consequent need of its cleaning, occurred more frequently. For this reason, 5 mL min^{-1} was used as standard precursor flow rate for all samples reported in this thesis. This operation enabled a production of up to 20 g per day of catalyst. It is noteworthy to mention that, using the batch collection system, only 5 g per day could be synthesized: an indisputable advantage of the semi-continuous collection system is therefore proved.

The precursor flow rate of 5 mL/min was applied for the synthesis of the CZA-2-f nanopowder and the

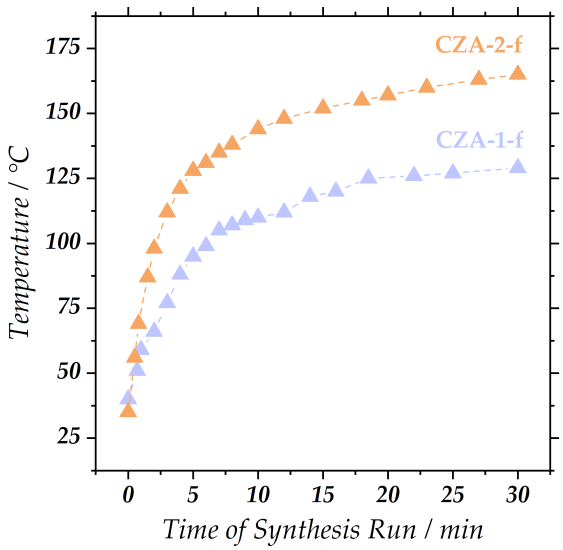


Figure 4.4: Temperature at the entrance of the bag-house filter over synthesis time for the CZA-1-f and CZA-2-f systems. *Time of synthesis run*: time of a single run.

cumulative synthesized mass over the cumulative time of synthesis is shown in Figure 4.3b. In this case a productivity of 0.13 g min^{-1} can be determined, which is more or less in agreement with what was found above for the CZA-1-f. The slight increase in the nanopowder productivity may be attributed to the higher combustion enthalpy of *solution 2* and the associated higher efficiency of the pyrolysis for the reasons discussed above.

In Figure 4.4 the temperature measured at the entrance of the bag-house filter during the time of one synthesis run of the CZA-1-f and CZA-2-f is depicted. For both cases, the temperature rises rapidly during the first half of the run time and then approaches constant values. The temperature during the synthesis as well as the final temperature reached at the end of the run is, in general, higher for the CZA-2-f compared to the CZA-1-f: after 30 min of synthesis, 125 °C and 160 °C were reached during the production of the CZA-1-f and CZA-2-f, respectively. Once again, this effect should be attributed to the higher combustion enthalpy of *solution 2* compared to *solution 1*, resulting in a higher temperature of the flame and of the gas entering the bag-house filter.

4.3 Particulate catalyst configurations

The synthesis of the particulate catalyst configurations, namely the hybrid particles of medium (CZA+Z) and close (CZA&Z) proximity and the structured core@shell (CZA@Z) catalysts, was carried out combining the CZA-1-f, prepared as described in section 4.2, with the zeolite H-ZSM-5 (Z), within a cooperation with the Chair of Chemical Reaction Engineering (CRT) at the University of Erlangen-Nürnberg and the Institute of Particle Technology (MVT) at the Technical University of Clausthal. In the following the synthesis procedure is described in detail.

4.3.1 Hybrid particulate catalyst of medium proximity (CZA+Z)

For the CZA+Z system, the CZA and the H-ZSM-5 were separately synthesized as nanopowder and afterwards combined into hybrid particles at the pellet level, namely of medium proximity as it will be shown in section 5.4.1. The synthesis of the CZA-1-f was described in section 4.2. The nanosized zeolite (n-Z) was prepared by CRT (FAU) as follows.
The synthesis mixture was prepared at room temperature in a polypropylene bottle (PP-bottle). Initially 80 wt.-% of the total amount of TPAOH solution was stirred together with 65 % of the total amount of deionized water. After five minutes, TEOS was added dropwise under stirring at 600 rpm using an overhead stirrer to form *solution A*. Meanwhile, the remaining amount of TPAOH solution (20 wt.-%) and deionized water (35 %) were used to dissolve $Al_2(SO_4)_3 \cdot 18\ H_2O$ in a separate beaker to form *solution B*. After stirring each solution for 24 h, *solution B* was added dropwise to *solution A*. The final synthesis mixture was aged for 1 h under stirring to form a clear colloidal solution with a molar ratio of $SiO_2 : TPA_2O : Al_2O_3 : H_2O : EtOH$ equal to 1 : 0.181 : 0.01 : 19 : 4 (SiO_2/Al_2O_3 = 100). This solution was then crystallized in a 2 L autoclave (Halmosi GmbH) at 100 °C for 20 h. Thereafter, the nanosized crystals were recovered via a series of centrifugation and washing steps by using deionized water and drying at 75 °C for 16 h. The recovered sample was initially calcined with flowing air at 550 °C for 4 h (heating rate: 1 K min^{-1}). The calcined sample was then ion exchanged by stirring for 16 h at 70 °C in a 1 M $NH_4(NO)_3$ solution. The solid/liquid weight ratio was 1/30. Thereafter, the ion exchanged crystals were centrifuged, washed and dried at 75 °C. This procedure was repeated three times to obtain the ammonium form of ZSM-5 zeolite. After final calcination (conditions as described above), the nanosized zeolite in the H-form was obtained (denoted as n-Z).

CZA-1-f and n-Z were mixed together in the desired ratio (weight ratio $\omega_{CZA}/\omega_{Zeo}$ = 1 and $\omega_{CZA}/\omega_{Zeo}$ = 5) in a mortar and ground with a pestle to form a homogeneous fine powder. The resulting hybrid powder was then pressed to tablets, which were subsequently crushed and sieved to form hybrid particles for measurements in a μ-Berty reactor (50 - 100 μm) (see section 5.1). Samples are denoted as CZA+Z_1 and CZA+Z_5 for $\omega_{CZA}/\omega_{Zeo}$ ratio of one and five, respectively. For comparison, a core@shell catalyst with hybrid catalyst cores (mass ratio $\omega_{CZA}/\omega_{Zeo}$ = 5) was synthesized. Therefore, a second fraction of CZA+Z_5 of 100 - 200 μm in size was prepared and enwrapped with a zeolite shell following the procedure described in section 4.3.3. This sample is denoted as CZA+Z_5@Z.

4.3.2 Hybrid particulate catalyst of close proximity (CZA&Z)

The CZA&Z catalyst system was synthesized by MVT using spray drying. For this, the CZA-1-f nanopowder was suspended in the zeolite mother liquor, prepared as described in section 4.3.1 and containing zeolite crystals, amorphous silica, template (TPAOH) and solvent (EtOH). The ratio ω_{Zeo} in the suspension was equal to 92 wt.-% (higher CZA loading resulted in an inhomogeneous suspension and could therefore not be investigated). The suspension was then spray dried in order to obtain spherical particles with a homogeneous distribution of the CZA-1-f in the matrix of the zeolitic structure. Details about the equipment used for the spray drying are reported in Ref. [132]. The product still contained amorphous silica, not active for the dehydration step; therefore it was treated by steam assisted crystallization (SAC) in order to get the crystallization of the amorphous silica to MFI-type zeolite (this step

was carried out at CRT) [133]. The SAC step was carried out at 150 °C for 96 h. In this way it was possible to increase the conversion of amorphous silica present in the mother liquor to MFI-type zeolite in the final particles (see also [133]). The final catalyst was then calcined under flowing air at 550 °C for 4 h (heating rate: 1 K min^{-1}). The close proximity of the two catalysts within the CZA&Z hybrid particles will be shown in section 5.4.2.

4.3.3 Structured core@shell particulate catalyst (CZA@Z)

Structured core@shell catalysts were prepared by enwrapping the CZA core catalyst with a zeolite H-ZSM-5 shell. For this purpose, FSP-CZA powder was either shaped to spherical and mechanically resistant particles via spray drying (see below) or processed into particles as described in section 4.2.

Agglomeration via spray drying

The spray drying is a common technique initiated by atomizing/spraying a suspension of droplets and followed by a drying process, resulting in the production of solid particles [135]. It is generally used in the pharmaceutical industry to get particles with defined physical and chemical properties as well as in the food processing technology (e.g. powdered milk and juice, animal feeds, ...) [136, 137]. Examples of application in catalysis are also reported in literature [138, 139]. A general spray dryer equipment is schematically illustrated in Figure 4.5. The diameter of the needle and the size of the spray cylinder influence the particle size range of the product. As a rule of thumb, the larger the needle diameter and the spray cylinder, the larger the droplets and the longer the residence time in the cylinder, namely bigger particles are produced [140]. Properties of the suspension, such as solid loading, viscosity and surface tension, together with process parameters, such as feed and spraying gas flow rates, inlet temperature (T_{IN}), can strongly influence the features of the product. Correlations between the spraying conditions and the final properties are reported in the open literature, starting from experimental studies [135, 141]. As an example, the addition of colloidal components allows to obtain agglomerates with different sha-

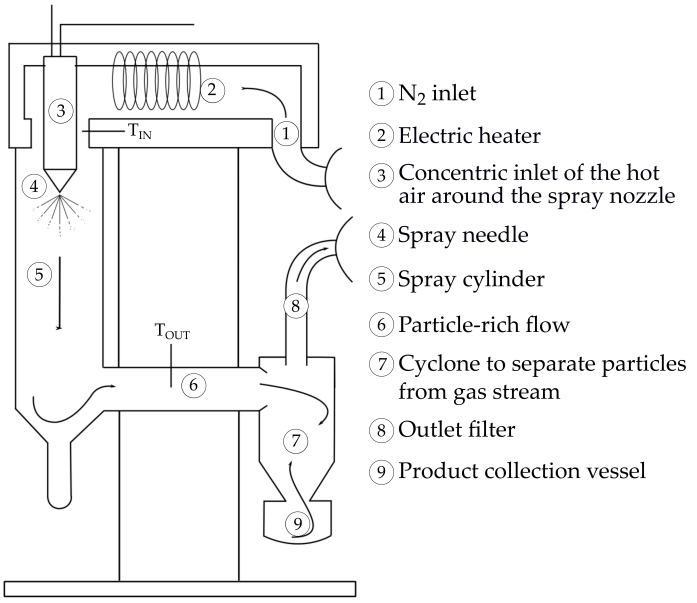


Figure 4.5: Illustration of a spray dryer equipment (Figure adapted from [134]).

Table 4.1: Investigation range of the process parameters for the preliminary study and optimized values used during the spray drying.

Parameter	*Unit*	*Preliminary study*	*Optimized values*
Suspension loading	wt.-%	30 - 35	30
Suspension feed	$mL\,min^{-1}$	5.4 - 9	6
T_{IN}	°C	110 - 150	150
N_2 flow	$L_S\,h^{-1}$	280 - 440	440

pe (e.g. hollow) or porosity (pores in several size scales) [135]. Some research groups proposed criteria based on theoretical calculations with the aim of choosing the solvents and the process parameters depending on the starting material and on the targeted product properties [136, 137].
In the frame of this work, the spray drying of the FSP-CZA took place as follows. Prior to the agglomeration procedure, the equipment was inertized and heated up to the desired T_{IN} by blowing pre-heated N_2 (1 - 2 in Figure 4.5). When the T_{IN} was reached, first water and then the suspension (CZA-1-f in deionized water), maintained homogeneous by magnetic stirring, were fed, starting the spraying process. The feeding through the nozzle inside the needle (3 - 4 in Figure 4.5) took place with a peristaltic pump at the set flow rate. The water in the droplets was heated from the hot spraying gas (N_2) and evaporated in the cylinder (5 in Figure 4.5). The nozzle was cleaned during the agglomeration process by nitrogen pulses and, at the end of the process, by feeding water. The product was separated from the gas medium in a cyclone (6 - 7 in Figure 4.5) and collected in a vessel (9 in Figure 4.5). The gas was filtered (8 in Figure 4.5) and directed to the hood.

Aim of this work was to get the agglomeration of the CZA-1-f nanopowder into spheres up to 50 µm, which could be used as core. As a particles preliminary study, different spraying parameters were applied to commercial nanopowder (a mixture of CuO, ZnO and Al_2O_3 in the same molar ratio as the CZA-1-f). During six different runs (denoted as Nr. 1 - 6) the process parameters were changed as reported in Table 4.1. The particle size distribution of the product was then measured. This preliminary investigation allowed to set optimal process parameters used for spray drying the CZA-1-f nanopowder (see Table 4.1).
Table 4.2 summarizes the parameters used in the six runs and the results in terms of product size ($d_{[4,3]10}$, $d_{[4,3]50}$, $d_{[4,3]90}$) and yield, which was calculated as the ratio between the amount of powder collected and that contained in the suspension. Observing the values of the $d_{[4,3]i}$, it can be noticed that the product is not affected from T_{IN} (see runs Nr. 1 and 2). Therefore, T_{IN} was maintained at 150 °C, favouring a faster evaporation compared to 110 °C; in doing so, the amount of byproduct (collected at the bottom of the spraying cylinder) decreased, as its formation is due to incomplete drying of the droplets. T_{IN} could not be further increased, otherwise the evaporation took place already along the nozzle before the formation of the droplets. The suspension flow rate has a slight influence on the final size but affects the yield strongly (see runs Nr. 3 to 5). When the suspension flow rate is increased, bigger droplets, namely larger particles, arise but the drying of the droplets is not efficient due to the low residence time. Bigger but wettish particles and, as a consequence, a higher amount of byproduct are obtained, as a wet

Table 4.2: Preliminary study of the spray drying on commercial particles: process conditions and product properties.

Run Nr.	V_{N_2} / $L_S\ h^{-1}$	*Feed* / $mL\ min^{-1}$	T_{IN} / °C	*Loading* / *wt.-%*	$d_{[4,3]10}$ / μm	$d_{[4,3]50}$ / μm	$d_{[4,3]90}$ / μm	*Yield* / %
1	440	6	**110**	30	7.3	18.1	34	34
2	440	6	**150**	**30**	6.5	17.5	35.3	35
3	440	**6**	150	**35**	7.4	17.6	32.7	41
4	440	**9**	150	35	6.7	18.6	38.8	16
5	**440**	**8.1**	150	35	6.8	18.2	38.2	21
6	**285**	7.5	150	35	13	26.8	43.7	7

For each run, the parameter in bold type was subject to investigation.

particle is heavier and cannot be transported by the gas flow to the cyclone and either hits the walls of the glass cylinder sticking there or drops into the byproduct collector. The spray gas flow (V_{N_2}) has the strongest impact on both product size and yield (see runs Nr. 5 and 6): lowering the N_2 volumetric flow, the droplets become bigger causing the formation of larger particles. At the same time, the evaporation either takes longer or is incomplete; most of the droplets fall in the byproduct collector. In order to overcome this challenge, for these two investigation runs, the suspension feed was adjusted in a way that the drying could occur properly. The drastic decrease of the yield with lower spray gas flow suggested to set it at 440 $L_S\ h^{-1}$. Runs Nr. 2 and Nr. 3 were used for an investigation on the influence of the solid loading in the suspension. In general, slight influence on the product size and an advantage in the yield when increasing the solid loading were observed. As more stable suspensions could be prepared with a solid loading of 30 wt.-%, this amount was chosen for the preparation of the SD-CZA. The stability of the suspension hinders eventual pulsations of the peristaltic pump and, as a consequence, variations of the composition of the droplets (solid/liquid ratio) over the spraying time.
After this preliminary investigation, it was possible to set the conditions for spray drying the CZA-1-f; these are summarized in Table 4.1 and are indicated as *Optimized values*. The core catalyst obtained is denoted as SD-CZA.

Synthesis of the shell

Both the P-CZA and SD-CZA were enwrapped with the zeolite shell at CRT with a two-step synthesis and the P-CZA@Z and SD-CZA@Z, respectively, were obtained. As starting material, either the calcined P-CZA (P-CZA_c) or the SD-CZA (SD-CZA_c) (see section 4.3 for conditions) were used. In general, the zeolite shell was formed via a two-step hydrothermal synthesis procedure by using *in-situ* seeding followed by secondary growth. *In-situ* seeding was performed by tumbling autoclaves containing the core particles suspended in the synthesis mixture at 175 °C for 20 h. The synthesis mixture was prepared as follows: initially, the desired amount of TPAOH was diluted with deionized water and the solution was agitated at 600 rpm using an overhead stirrer in a PP-bottle at room temperature. Then, TEOS was added dropwise into the above solution under intensive agitation for 20 h at room temperature. Finally, a clear solution with molar ratio of SiO_2 : TPA_2O : H_2O : EtOH equal to 1 : 0.181 : 19 : 4 (SiO_2/Al_2O_3 = ∞) was obtained. The mixture was transferred into 45 mL PTFE-lined stainless steel autoclaves (28 g synthesis mixture per autoclave) each one already containing 0.8 g of P-CZA_c (or SD-CZA_c) core par-

ticles. After sealing the autoclaves, hydrothermal synthesis was carried out at 150 °C in a tumbling oven at a rotational frequency of 3 rpm to prevent sedimentation of the core particles. After 20 h, the synthesis was stopped by rapid cooling of the autoclaves using water. The seeded cores were recovered from the synthesis mixture via a series of washing, decantation, centrifugation and sedimentation steps. The washed seeded cores were finally dried at 75 °C for 16 h. The *in-situ* seeded core material is denoted as isS_P-CZA (isS_SD-CZA).

The dried seeded core material was used as starting material for the secondary growth step, eventually yielding the dense zeolite shell. Initially, a synthesis gel was prepared by stirring TPAOH together with 75 % of the total amount of deionized water in a PP-bottle. Then, TEOS was added dropwise to this solution under stirring at 600 rpm using an overhead stirrer at room temperature. 23 % of the total amount of deionized water was used to dissolve $Al(NO_3)_3 \cdot 9\ H_2O$ in a separate beaker under stirring at 600 rpm by using a magnetic stirrer at room temperature. After 2 h of hydrolysis, the aluminum solution was added dropwise to the TEOS-containing solution under intensive agitation. The final synthesis mixture was stirred for 2 h to form a gel with a molar ratio of $SiO_2 : TPA_2O : Al_2O_3 : H_2O$: EtOH equal to 1 : 0.3 : 0.01 : 40 : 4 (SiO_2/Al_2O_3 = 100). The actual secondary growth was performed by first impregnating 0.8 g of the *in-situ* seeded core particles first with the remaining 2 % of deionized water in a 45 mL PTFE-liner. Thereafter, 28 g of the synthesis mixture was added into the liner. The synthesis was carried out in a tumbling oven at a speed of 3 rpm at 175 °C for 20 h. After the hydrothermal synthesis, the autoclave was rapidly cooled using water. The recovery of the P-CZA@Z (or SD-CZA@Z) particles was done similar of the seeded cores described in section 4.3.1. The recovered samples were at first calcined as described in section 4.3 and then ion exchanged twice in a 0.5 M NH_4NO_3 solution with a solid/liquid weight ratio of 1/40 at 65 °C for 3 h. A third ion exchange step was performed under similar conditions, but overnight. After drying at 75 °C for 16 h, the ion exchanged material was calcined as described in section 4.3 to get the final core@shell catalysts with H-ZSM-5 shell. These are denoted as P-CZA@Z and SD-CZA@Z.

The same synthesis was carried out on the calcined CZA+Z_5 (see section 4.3 for calcination conditions), obtaining the sample denoted as CZA+Z_5@Z.

For the comparison of the catalytic activity of the bare core before and after the shell synthesis procedure, starting from the SD-CZA, a sample was prepared using similar synthesis conditions without a zeolite shell being grown on the core particles. This latter sample is denoted as SD-CZA_core. For the preparation of the SD-CZA_core, SD-CZA material as prepared was calcined and *in-situ* seeded as described above. The recovered seeded core material (isS_SD-CZA) was used for a modified secondary growth with variation in the preparation of the synthesis mixture. Initially, a synthesis gel was prepared by stirring 80 % of the total TPAOH together with 65 % of the total amount of deionized water in a PP-bottle. Then, TEOS was added dropwise to this solution under stirring at 600 rpm using an overhead stirrer at room temperature, obtaining the *solution A**. The rest of the total amount of deionized water was used to dissolve $Al(NO_3)_3 \cdot 9\ H_2O$ and the remaining TPAOH in a separate beaker under stirring at 600 rpm by using a magnetic stirrer at room temperature, obtaining the *solution B**. The two solutions *A** and *B** were further stirred (600 rpm) separately for 24 h at room temperature, afterwards *solution B** was added dropwise into *solution A** under stirring (600 rpm), resulting in a synthesis mixture with a molar ratio of $SiO_2 : TPA_2O : Al_2O_3 : H_2O$: EtOH equal to 1 : 0.181 : 0.01 : 19 : 4 (SiO_2/Al_2O_3 = 100).

Thereafter, the same procedures of secondary growth, particle recovery, ion exchange and calcination were performed as described above.

4.4 Planar catalyst configurations

For the application in the μ-CR, both the CZA and the H-ZSM-5 catalysts should be combined in a planar geometry, which was achieved by coating the micro-channels via screen printing. As reported in section 2.5, a suspension of the catalyst powder, denoted as paste, is used as precursor for the coating process. Table 4.3 summarizes the denomination of the pastes prepared in the frame of this work and their composition. In general, *CZA*, *Zeolite* and *Hybrid* denote the presence of the sole STM-catalysts, of the sole MTD-catalyst and of both catalysts, respectively. CZA-1-f (see section 4.2) was used as STM-catalyst; zeolite H-ZSM-5 synthesized at CRT (see section 4.3.1) was used for the preparation of the *Hybrid-Ti* pastes, while a commercial zeolite (Clariant) was used for all the other pastes containing zeolite, namely the *Hybrid-W* and the *Zeolite-i*. In this way it was possible to synthesize the hybrid planar system of medium proximity (CZA#Z) and the structured double layer (CZA//Z) configurations. Due to experimental challenges (see section 5.4), the planar hybrid system of close proximity was not synthesized. For the CZA#Z the mass ratio $\omega_{CZA}/\omega_{Zeo}$ = 1 was used. Either terpineol and ethyl cellulose or deionized water and methyl cellulose were used as solvent and binder, respectively, as explained in Table 4.3.

Where not specified, the preparation of all pastes was carried out as follows. At first, the particles were suspended in 10 wt.-% of the total amount of the solvent. Separately, the rest of the solvent and the binder were admixed at 70 °C. Afterwards, the suspension and the solution, eventually together with the dispersant, were combined and mixed for 12 h in a closed vessel using a overhead stirrer, maintaining the temperature at 70 °C. The chosen conditions allow a complete dissolution of the binder in the

Table 4.3: Composition of the pastes prepared in this work.

	Solvent		*Binder*		*Dispersant*	*Particles*
Name of the Paste	*Loading / wt.-%*	*Type*	*Loading / wt.-%*	*Type*	*Loading / wt.-%*	*Loading / wt.-%*
Hybrid-T1	65	T	1	EC	0	34
Hybrid-T2	64.2	T	0.9	EC	0.7	34.2
Hybrid-T3	67	T	0.7	EC	3.2	29.1
Hybrid-T4	65.2	T	0.7	EC	5.8	28.3
Hybrid-W	77.5	H_2O	2	MC	0	20.5
CZA-1	77.9	T	1.6	EC	2.6	17.9
CZA-2	76.2	T	1.6	EC	0	22.2
CZA-3	74.3	T	1.5	EC	2.5	21.7
Zeolite-1	85.5	H_2O	2	MC	0	12.5
Zeolite-2	85.5	H_2O	3	MC	0	11.5
Zeolite-3	84.5	H_2O	4	MC	0	11.5

T = terpineol; EC = ethyl cellulose; MC = methyl cellulose; Dispersant = Hypermer KD1-SO-(AP)

solvent and avoid of the solvent to evaporate. The resulting suspension (paste) was then homogenized in a three roll mill. At the end of this procedure, a homogeneous, agglomerates-free paste was obtained, and the rheological properties could be studied.
Before the coating, the foils were calcined under flowing air at 650 °C for 6 h, in order to enhance the adhesion of the layer to the substrate [83].
For the screen printing, carried out at the IAM-ESS, the distance between substrate and screen was set to 0.6 mm, a squeegee with a hardness of 60 Shore was used at a speed of 30 mm s^{-1} and a pressure of 2 bar. The coated foils were dried at room temperature and then calcined under flowing air at 400 °C (heating rate: 1 K min^{-1}).

In the following, a preliminary investigation with respect to the printability, carried out using the paste *Hybrid-T1* and considering the work of Sun [114] as a starting point, is described.

4.4.1 Preliminary investigations

The paste *Hybrid-T1* was used in the preliminary investigation about the printability and was obtained according to the criteria proposed by Sun [114] (see chapter 2). The composition of the paste is reported in Table 4.3. A viscosity of 17.5 Pa s was measured at a shear rate of 100 s^{-1}, namely a printable paste according to Sun [114]. A microscope picture of the coated foil, obtained at IAM-ESS, is shown in Figure 4.6: only an incomplete coating of the micro-channels could be obtained, even if the paste should be suitable for the process, possibly because of the different materials used (here CZA with H-ZSM-5, in the work of Sun Co-Re/Al_2O_3 with Pt-HZSM5 [114]).
Further investigations about the possible presence of a yield stress were carried out and the results are shown in Figure 4.7: from the shear stress/shear rate plot, the yield stress at 800 Pa s is clearly visible. For this reason, the paste *Hybrid-T1* was defined as not printable (see Figure 2.4). However, this test could prove the feasibility of the coating via screen printing for the micro-channels and the screen used: the coating was detected only within the micro-channels. This is important, as during the reaction the gas is supposed to flow and react only within the micro-channels.

After the first printing attempt, it can be concluded that:

- the possible presence of a yield stress should be taken into account for the succesful synthesis of a printable paste;

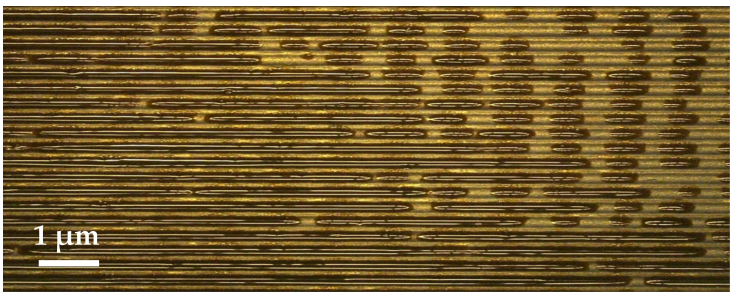


Figure 4.6: Microscope picture of the coated foil obtained by screen printing the paste *Hybrid-T1*.

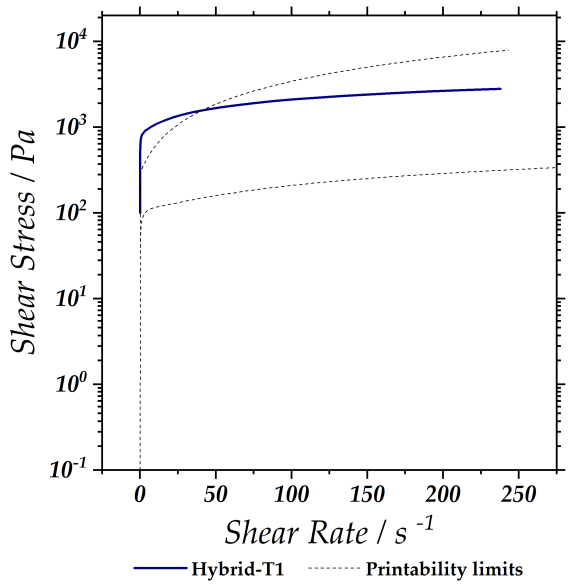


Figure 4.7: Rheology of the paste *Hybrid-T1*: shear stress/shear rate plot.

- the screen as well as the operational parameters chosen for the screen printing procedure were proper, as the paste was detected within the micro-channels and not between them.

Unfortunately, after this preliminary test, the screen printing machine at IAM-ESS was not available any more due to an irreversible damage. For this reason, the successive coating had to be carried out manually: the foil was placed on a holder and the squeegee was moved forward along the foil by hand. However, all the pastes were homogenized in the triple roll mill, and their rheology was investigated according to the criteria explained above and in chapter 2. In this way, a pure CZA-layer, the hybrid planar structure of medium proximity (CZA#Z) as well as the double layer structure (CZA//Z) could be prepared successfully. The characterization of these layers is described in chapter 5.

4.5 Summary

In the frame of this work, target of the synthesis was to be able to prepare the catalysts considered by modelling, with focus on $CuO/ZnO/Al_2O_3$ (CZA), obtained via flame spray pyrolysis (FSP) and its combination with the zeolite H-ZSM-5 (Z) in the various catalyst configurations considered. This was carried out in cooperation with the Institute of Particle Technology (MVT) (TU Clausthal) and the Chair of Chemical Reaction Engineering (CRT) (Friedrich-Alexander-University of Erlangen-Nürnberg, FAU). In summary, regarding the FSP-CZA:

- The FSP-CZA nanopowder was prepared collecting the product either in batch on a glass fiber filter or semi-continuously in a bag-house filter; the latter system allowed to increase the productivity of the nanoparticles up to 20 g per day. Correspondence between precursor flow rate and the productivity within the synthesis time was found.

- The FSP-CZA was then spray dried for the synthesis of a core CZA catalyst: a preliminary investigation aimed to find out the optimized operational conditions to be set in order to obtain a proper size of the product as well as a good yield of the procedure.

Moreover, regarding the catalyst structures for the direct synthesis of DME:

- The FSP-CZA together with the nanosized zeolite was pelletized, crushed and sieved for the obtaining hybrid particles of medium proximity (CZA+Z).
- The CZA nanopowder suspended in the zeolite mother liquor was first spray dried at MVT and then crystallized at CRT by steam assisted crystallization in order to obtain hybrid particles of close proximity (CZA&Z).
- A two-step hydrothermal synthesis (*in-situ* seeding followed by secondary growth) was carried out on the CZA, either as pelletized particles or as spray dried cores, for synthesis of the core@shell (CZA@Z) system at CRT.
- The planar catalyst systems, both the hybrid layer system of medium proximity (CZA#Z) and the double layer configuration (CZA//Z) were coated in micro-channels: a preliminary investigation allowed to set the printability range of a paste starting from its rheological investigations.

5 Characterization

In the following the physico-chemical characterization results as well as the activity for the STM/STD reaction of the synthesized catalysts are presented. The equipment used and the procedure of the analyses are described in section 5.1. First, the results regarding the FSP-CZA catalyst are presented (sections 5.2 - 5.3); second, the characterization and activity for the STD reaction of the particulate and planar catalyst configurations are delineated from section 5.4 to 5.8; finally, in section 5.9, the kinetic study of the STM reaction over the self-made FSP-CZA catalyst and further modelling results in addition to those reported in chapter 3 are presented.

5.1 Methods

Textural properties were obtained from N_2-sorption measurements at 77 K using a Quadrasorb SI (Quantrachrome) after outgassing the sample at 250 °C for 12 h. The specific surface area was evaluated according to the method of Brunauer, Emmett and Teller [142], using the adsorption data within p/p^0 = 0.06 - 0.25.

Reducibility of the CuO phase was studied via temperature programmed reduction (TPR) measurements with a ChemBet TPR/TPD *Chemisorption Analyzer* (Quantachrome Instruments): after outgassing the sample under He at 250 °C for 2 h, the reduction was performed by ramping the sample with 1 K min^{-1} to 500 °C under a flow of 5 % H_2 in Ar. The H_2-consumption was followed using a thermal conductivity detector (TCD).

The elemental composition of the samples was obtained by using inductively coupled plasma optical emission spectrometry (ICP-OES). All solid samples were initially digested in a microwave oven for 45 min with a mixture of 2 mL HNO_3, 2 mL HCl, 8 mL HF. Afterwards, the obtained aqueous sample was diluted with double deionized water and analysed using a *SPECTRO CIROS^{CCD}* spectrometer.

X-ray diffraction (XRD) was performed on a *PANalytical Empyrean Series 2* diffractometer equipped with a line-detector (scanning parameters: 0.013° 2Θ $step^{-1}$ and 8.67 s $step^{-1}$). Reference data were taken from the *International Center for Diffraction Data (ICDD)* (pdf No. 00-002-1040, 00-001-1136 and 01-079-1638 for CuO, ZnO and zeolite MFI, respectively). The copper-anode was operated at 40 kV/40 mA.

Thermal gravimetric analysis (TGA) were carried out with a *NETZSCH STA 409 C/CD* (NETZSCH-Gerätebau GmbH) after outgassing the sample at 100 °C for 30 min, under air and a heating rate of 1 K min^{-1} up to the desired temperature (in general 600 °C), which was maintained for 4 h.

The final catalysts were further characterized via electron probe micro analysis (EPMA) (*JXA-8530F, JEOL*) with both back-scattered electron (EPMA/BSE) and elemental mapping via wave-length-dispersive X-ray spectroscopy (EPMA/WDX). Transmission electron micrographs (TEM) were taken by a *JEOL JEM2100* operated at 160 kV. Scanning electron (SE) microscopy (*ULTRA 55*; Carl Zeiss AG) was used for observing the coverage grade of the shell on the core catalyst.

The particle size distribution of the catalyst samples was measured via static light scattering (*LS230* -

Beckman Coulter).
The rheological as well as the thixotropic properties of the pastes were evaluated by measurements in a rotating rheometer (*Rheostress 1*, Thermo Scientific, Haake). The paste was placed between the holder and the cone with a side angle of 1°. The flow plot was obtained running a shear stress linear ramp from 0.1 Pa up to 1200 Pa and the resulting shear rate was recorded. Beside this, the viscosity of the paste was measured under a constant shear rate of 0.1 s^{-1} first, then switching to 100 s^{-1}, and finally back to 0.1 s^{-1}.

Reaction tests were carried out either in a μ-Berty reactor (Autoclave Parker Engineering, Erie, Pennsylvania, USA), where the catalyst was tested in the form of powder, or in a μ-CR, manufactured in nickel-chromium-iron alloy (Material No. 1.4876) at IMVT, where the catalyst was tested in the form of coated layer. The scheme of the foils used for catalyst coating as well as of the μ-CR are represented in Figure A.2 and A.4, respectively. The desired amount of foils was inserted in the μ-CR and a metal plate was added in order to fill all the reactor volume.
Prior to each catalytic test, the reactor was purged with a N_2-flow at 100 °C for 1 h. Then the reduction took place in 4 vol.-% H_2 in N_2 while raising the temperature to 230 °C within 10 h. After 5 h at 230 °C, the flow was switched to pure H_2 and the temperature was further increased up to 250 °C (0.33 K min^{-1}) and held for 4 h.
Except where indicated otherwise, the reaction tests took place at p = 45 bar; 200 °C $< T <$ 290 °C; feed composition of $H_2 : CO : CO_2$ equal to 16 : 8 : 1 with 10 vol.-% N_2 used as an internal standard for determination of the contraction factor Z (Equation 5.1), which is needed to consider the gas volume changes taking place during the STM and STD reactions for the calculation of conversion and selectivity (see Equations 5.2 - 5.1). In the μ-Berty reactor, a speed of 2000 rpm of the motor was kept and, in general, the $(F/W)^*$ (reagent molar flow per mass of catalyst) was equal to 6750 $mL_{Reagents}$ h^{-1} g_{CAT}^{-1}.
The effluent gas was analysed using gas chromatography (*GC 7890A*, Agilent Technologies) equipped with a methanation unit, two columns (HP-Plot Q (30 m x 0.530 mm x 40.00 μm) and HP-Molesieve (5 m x 0.530 mm x 25.00 μm) and two detectors (thermal conductivity detector (TCD) and a flame ionization detector (FID)).

$$Z = \frac{y_{N2}^0}{y_{N2}} = \frac{\dot{N}}{\dot{N}_0} = \frac{\dot{V}}{\dot{V}_0} \tag{5.1}$$

$$X_{CO} = \left(1 - Z \cdot \frac{y_{CO}}{y_{CO}^0}\right) \cdot 100\ \% \tag{5.2}$$

$$S_i = \frac{\nu_i \ \left(Z \cdot y_i - y_i^0\right)}{y_{CO+CO_2}^0 - Z \cdot y_{CO+CO_2}} \cdot 100\ \% \tag{5.3}$$

In general, for the evaluation of X_{CO} and product selectivity mean values were calculated based on the online GC-data when the reaction was stable in an approximatively 4 h time on stream regime for each set of reaction temperature. For all data used for determining the accordant mean value, Z was within +/- 1 % and the carbon balance was fulfilled within a range of +/- 5 %. In addition, for each catalyst system, the temperature was varied starting from the lowest one. In order to check for potential deactivation during the reaction test, after reaching the highest temperature investigated, lower temperatures

were tested again. In doing so, for each catalyst system investigated, within the total time on stream of max. 40 h, at the same conditions the same X_{CO} and product distributions were detected independent on the time on stream. Superimposing deactivation effects within these 40 h could be excluded for all catalysts investigated in the present study (see also Table A.1).

5.2 FSP-CZA: physico-chemical characterization

Different FSP-CZA nanopowder samples were synthesized, as described in chapter 4, either collecting the powder in batch or semi-continuously and changing the solvent in the precursor solution. A deep physico-chemical characterization about the FSP-CZA catalyst, the potential influence of the collection system and of the solvent was achieved and the results are presented and discussed in sections 5.2.1 to 5.2.3. Furthermore, as both CZA&Z and CZA@Z bifunctional systems should be calcined during their syntheses, the influence of the thermal treatment on the pure CZA catalyst was studied (section 5.2.4). Finally, the fulfilment of the alternative CZA core via spray drying is demonstrated in section 5.2.5.
Generally, N_2-physisorption, X-ray diffraction (XRD), temperature programmed reduction (TPR), thermal gravimetric analysis (TGA) and transmission electron micrograph (TEM) were carried out, as described in section 5.1, for the physico-chemical characterization of the FSP-CZA systems.

5.2.1 Influence of the collection system

The higher productivity of nanopowder produced semi-continuously should not influence the properties of the final product. Müller et al. proved the absence of any effect of the collection system on the final nanopowder (silica); however, in that work, the batch collection was not carried out directly above the cylinder, but just before the entrance of the gas medium into the bag-house filter and the glass fiber filter was not quenched [143]. Therefore, it was decided to carry out a comparison of the products obtained from batch-type and semi-continuous FSP in the frame of this work. The investigation was applied to

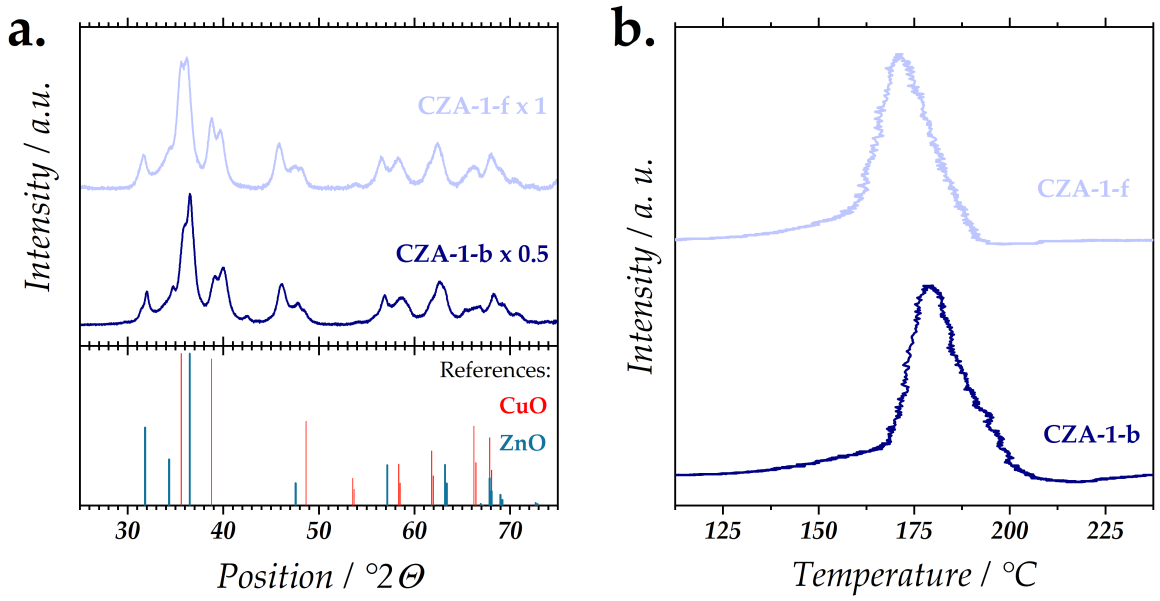


Figure 5.1: a) XRD patterns of the CZA-1-b, CZA-1-f (with adjusted intensity) and the references for CuO and ZnO structures (International Center for Diffraction Data (ICDD)); b) TPR profiles of the CZA-1-b and CZA-1-f nanopowder.

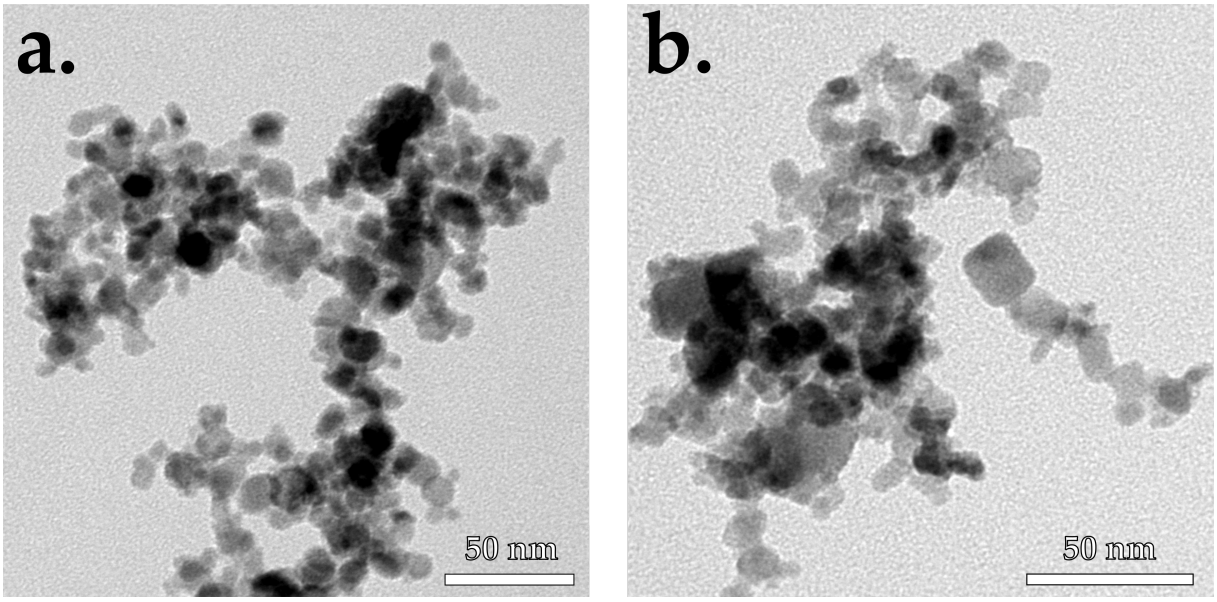


Figure 5.2: Transmission electron micrograph of the a) CZA-1-b and b) CZA-1-f.

the samples CZA-1-b and CZA-1-f.

The specific surface area of the CZA-1-b and CZA-1-f was 75 $m^2\ g^{-1}$ and 84 $m^2\ g^{-1}$, respectively. Thus only a slight deviation was found. Figure 5.1a shows the XRD patterns of the two nanopowder samples. The corresponding reference patterns for CuO and ZnO confirm the presence of the two phases. In general, the correspondence of the reflections in both samples can be observed, with the only exception at 2Θ = 42.7°, detected only for the CZA-1-b powder and related to the presence of Cu_2O, based on the reference data taken from the *ICDD* (pdf No. 00-002-1067, not shown). Beside this, some differences between the two patterns can be found in the relative intensities at 2Θ equal to 34.4°, to be correlated to the ZnO phase, 35.6°, to be correlated to the CuO phase, and 39.7°, to be correlated to the Al-oxides, according to Ref. [129]. Based on the CuO[111] reflection at 2Θ = 38.8°, the CuO crystallite size in the two samples was determined by using the Scherrer equation to be 9.5 nm and 8.8 nm for CZA-1-b an CZA-1-f, respectively (see also Table 5.1). In Figure 5.1b the TPR profiles of the two samples are depicted, in order to compare the reducibility. The reduction peaks were found to be 180 °C and 170 °C for CZA-1-b and CZA-1-f, respectively. In general, a shift to higher reduction temperature should be ascribed to an increase of the presence of CuO-clusters [144]. However, the discrepancy between the two nanopowders is modest and both of them are completely reduced at 210 °C. The primary particle size was observed by TEM images, shown in Figure 5.2, which confirm a similar size of both nanopowders in the range of 10 - 15 nm (in agreement with the results obtained from the Scherrer equation).

In summary, from the physico-chemical point of view, the nanopowder produced via FSP is only slightly affected by the collection system. The small discrepancies in the specific surface area, reducibility and primary particle size should be ascribed to the water quenching above the fiber filter used during the batch collection (absent in the semi-continuous procedure). Due to the rapid cooling of the powder, physical aggregation of the primary particles can take place, which affects the specific surface area and reducibility, but not the crystal structure. Starting from the results obtained, a strong influence of the

collection system should be excluded. In any case, the tendency observed and presented above, namely smaller Cu-crystallite size, higher specific surface area, and enhanced reducibility for the powder made with semi-continuous process, indicate a better performing CZA catalyst at STM operation conditions (see section 2.1.1). These results, together with the benefit during the synthesis using the bag-house filter regarding higher productivity (see section 4.2.1), made the semi-continuous collection system the standard method. Therefore, CZA-1-f is considered the basis for comparison in the next sections.

5.2.2 Influence of the solvent

In section 2.2, the eventual advantage of dissolving nitrates in solvents with high combustion enthalpy is given. In the frame of this work, the FSP-CZA nanopowder was prepared starting either from pure ethanol or from an organic mixture (see section 4.2), obtaining the CZA-1-f and the CZA-2-f, respectively.

The specific surface area of the CZA-2-f was 114 $m^2\ g^{-1}$, higher than the CZA-1-f (84 $m^2\ g^{-1}$) (see also Table 5.1). Figure 5.3a shows the XRD patterns of both samples with the references for the CuO and ZnO phases, respectively. In general, there is correspondence in the position and in the intensities of the reflections; however, some discrepancies can be observed at 2Θ equal to 34.4°, related to the ZnO phase, not detected for the CZA-2-f, 35.6° and 36.6°, related to the CuO and the ZnO phase, respectively, not well distinct for the CZA-2-f compared to the CZA-1-f, and 39.7°, related to the Al-oxides, absent in the CZA-2-f pattern. Based on the CuO[111] reflection at 2Θ = 38.8°, the CuO crystallite size in the CZA-2-f was determined by using the Scherrer equation to be 9.8 nm, which agrees with the size calculated for the CZA-1-f (8.8 nm, see Table 5.1). The reducibility of the FSP-CZA was found to be influenced from the solvent used in the precursor solution, as Figure 5.3b shows. For the CZA-2-f, the reduction peak is detected at a temperature of 230 °C (at the same temperature the CZA-1-f was already completely reduced). In many works, the shift of the reducibility toward higher temperatures is ascribed to the increase in size of the CuO-clusters; this aspect will be discussed in section 5.2.4. By observing the TEM

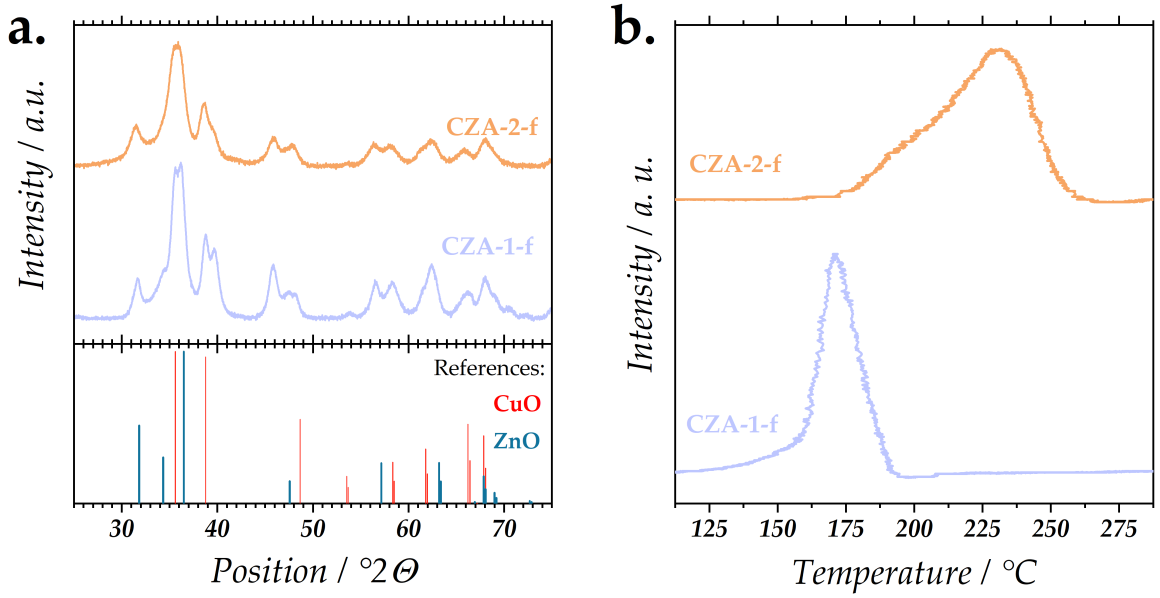


Figure 5.3: a) XRD patterns of the CZA-1-f, CZA-2-f and the references for CuO and ZnO structures (International Center for Diffraction Data (ICDD)); b) TPR profiles of the CZA-1-f and CZA-2-f nanopowder.

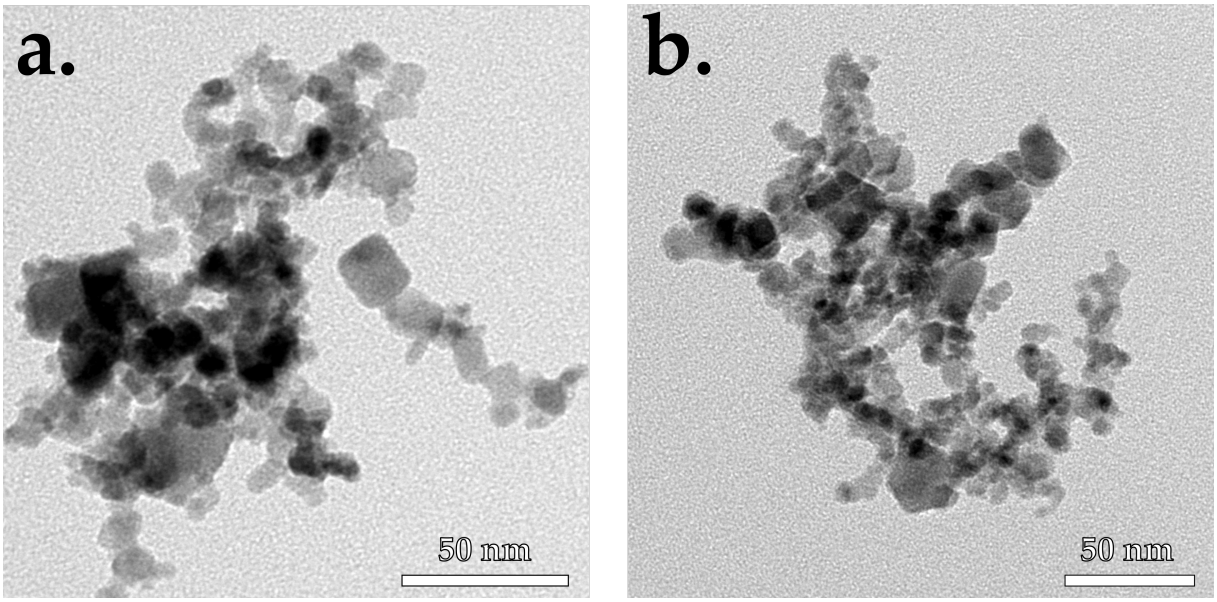


Figure 5.4: Transmission electron micrograph of the a) CZA-1-f and b) CZA-2-f.

images, displayed in Figure 5.4, similar size of primary particles in the two samples can be confirmed. The images suggest rather a more homogeneous size distribution of the CZA-2-f compared to the CZA-1-f.

The results of the characterization of the two nanopowders showed a higher specific surface area of the CZA-2-f sample, more or less equivalence in the crystal structure, a similar size of CuO crystallites, a hindered reducibility, and a more homogeneous distribution of the primary particle size for the CZA-2-f. It should be reminded that the advantage of using mixed organic solvents with higher combustion enthalpy compared to pure ethanol is reported to be stronger especially during synthesis of Al_2O_3 and, with a lower impact, of ZnO nanopowder [41]. The same benefit was not reported for CuO [41]. This may explain why no real discrepancy in the CuO crystal size was found between the two samples. Therefore, the ZnO crystallite size in both CZA-1-f and CZA-2-f was determined by using the Scherrer equation. Based on the reflection at $2\Theta = 31.8°$, the ZnO crystallite size was calculated to be 14.8 nm and 10.8 nm for the CZA-1-f and the CZA-2-f, respectively. This indicates that the higher specific surface area obtained from solvent 2 should be ascribed to the effect of the mechanism of formation of ZnO and, probably, of Al_2O_3, resulting in smaller particles of these two oxides. This could not be proved for Al_2O_3, as the presence of its characteristic reflections was not detected due to overlapping in the patterns. However, these considerations still cannot explain the higher reduction temperature of the CZA-2-f sample, as only CuO is supposed to be involved in the reduction. Further investigation are necessary in order to understand this open point.
Figure 5.5 shows the result of the TG-analysis carried out up to 600 °C for the CZA-1-f, CZA-2-f and the CZA-1-f_c (for comparison). The calcined sample (the calcination took place up to 550 °C, see section 4.3 for conditions) does not show any loss in mass, which is not the case for the pristine powder. This suggests that the fresh sample is containing components that either burn or evaporate during the calcination, which occurs under flowing air. Therefore, either some solvents are still remaining in the sample after the pyrolysis, which is unlikely, due to the high temperature reached during the flame syn-

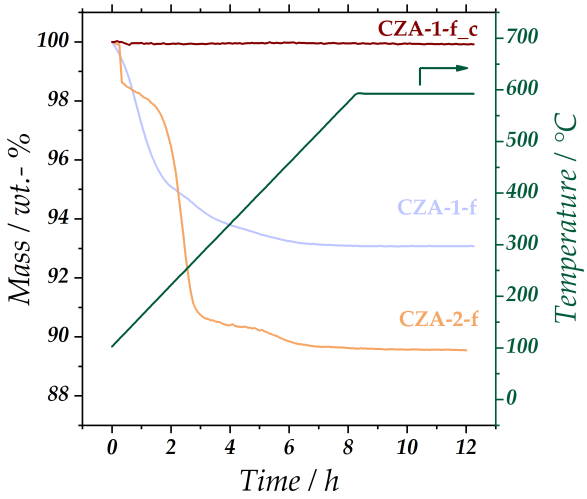


Figure 5.5: Mass loss over temperature during the TG-analysis of the CZA-1-f, CZA-2-f and, for comparison, of the CZA-1-f_c.

thesis, or carbon-containing products are formed during the flame synthesis. The mass fraction at the end of the analysis was 93.1 wt.-% and 89.5 wt.-% for the CZA-1-f and the CZA-2-, respectively. In the open literature, the formation of carbonates during FSP synthesis, as main- or as side-products during the preparation of metal oxides, is reported in many works [145, 146, 147, 148, 149]. Huber et al. report the synthesis of calcium carbonates via FSP using calcium 2-ethylhexanoate as precursor [145]. The authors proved the production of calcium carbonate with XRD and TG-analysis [145]. Jung et al. prepared Ba/Sr/Ti-based nanoparticles using barium carbonate as precursor, which is remaining in the pristine product and can be removed with the thermal treatment under air up to 1000 °C [146]. Haider et al. mentioned and proved that, during the FSP synthesis of a ternary Cu/Mg/Al-based system, the high partial pressure of CO_2 in the quenching zone of the flame favours the formation of carbonates; Cu-nitrates and a mixture of acetic acid and MeOH were used for CuO production [147]. A similar statement is reported in the work of Chen et al., who claim as unavoidable the formation of carbonates at the surface during the synthesis and collection of the nanoparticles (Cu-nitrate solved in ethanol was used as precursor solution) [148]. The possible formation of carbonates at the FSP synthesis condition is also taken into account in the work of Teoh et al. [150]. Moreover, copper carbonates such as $CuCO_3 \cdot Cu(OH)_2$ malachite and $Cu_3(CO_3)_2(OH)_2$ azurite decompose to Cu-oxides at about 400 °C and in the range of 300 - 400 °C, respectively [151], which corresponds to the results obtained by TG-analysis.

What is reported in literature in line with the results of the TG-analysis obtained in this work confirms the likely co-production of carbonates with the metal oxides during the pyrolysis. This is difficult to prove by XRD, due to their low amount compared to the oxides, but could be demonstrated by IR-spectroscopy. The presence of carbonates on the surface, as reported in [148], could also be the reason of the shift in reducibility towards higher temperature in case of the CZA-2-f, which should also contain a higher amount of carbonates, due to the higher mass loss during the TG-analysis; the hydrogen could be adsorbed on the carbonate species on the surface without reducing them; the reduction is then delayed. However, this is still a hypothesis and should be confirmed by further investigations, which were not in focus of this work.

Table 5.1: Summary about the physico-chemical characterization of FSP-CZA samples.

Sample	a_{BET} / $m^2\,g^{-1}$	[a] d_{CuO} / *nm*	$T_{red.}$ / °C	[b] *Cu content / wt.-%*	[b] *Zn content / wt.-%*	[b] *Al content / wt.-%*
CZA-1-f	84	8.8	170	N/A	N/A	N/A
CZA-2-f	114	9.8	230	N/A	N/A	N/A
P-CZA-1	69	10.1	N/A	56.5	28.4	2.5
P-CZA-2	99	13	N/A	54.1	28.1	2.6
CZA-1-f _c	29	21.2	190	N/A	N/A	N/A
CZA-2-f_c	86	14.9	205	N/A	N/A	N/A
P-CZA-1_c	11	21.9	N/A	54.9	25.8	2.9

[a] based on [111] reflection (Scherrer equation), [b] metal amount from ICP/OES measurement

5.2.3 Further characterization of the FSP-CZA

In sections 5.2.1 and 5.2.2, the comparison of the FSP-CZA material produced by changing the collection system and the solvent in the precursor solution was delineated. It was concluded that using either the batch or the semi-continuous set-up does not influence the physico-chemical structure of the product. The solvent affects the nanopowder, at most, in terms of specific surface area and reducibility; furthermore, the presence of carbonates in the nanopowder was hypothesized, starting from the TG-analysis and from what stated in the open literature. This section gives a complete description of the physico-chemical structure of the STM catalysts prepared in this work, adding more information to the comparison in sections 5.2.1 and 5.2.2. CZA-1-f, CZA-2-f as well as the related pelletized particles, namely P-CZA-1 and the P-CZA-2 (see section 4.2 for details of the preparation), are considered.

Table 5.1 summarizes the results, partially already presented in the previous sections, obtained for the FSP-CZA samples before and after calcination (the latter will be discussed in section 5.2.4). The specific surface area is in line with literature data of similar catalysts [38, 69, 152].
The XRD patterns of the CZA-1-f and CZA-2-f shown in Figure 5.3 confirm the presence of the CuO and ZnO phases. The diffraction peak at 2Θ = 39.7°, according to [129], can be related to the Al-oxide, while no further specific reflections of alumina were observed. Ahmad et al. prepared and characterized a similar CZA catalytic system and related the reflections at 2Θ = 53.0° and 59.8° to the presence of Al_2O_3 [38]. These two reflections should be overlapped by the characteristic ones of CuO at diffraction angles of 53.58° and 58.50°. For this reason, the presence of an Al_2O_3 crystal phase cannot be clearly proven in this work. Due to the overlapping of the characteristic reflections of the different oxides, no conclusion about the eventual presence of spinels in the FSP-CZA can be deduced from XRD [38]. The diffraction peak at 2Θ = 45.8° could potentially be related to the presence of a ZnO_2 phase, as also reported by Ding et al. [119] (based on the reference data taken from the *ICDD*, pdf No. 00-002-1040, not shown). The CuO crystallite particle size was determined by using the Scherrer equation (XRD patterns of the P-CZA-1 and P-CZA-2 are shown in Figure A.5): an increase after pelletizing the pristine CZA-1-f and CZA-2-f was observed (see Table 5.1), which is in agreement with the decrease of the specific surface area.

The ICP/OES results (see Table 5.1) prove the compliance in composition of the final materials; the presence of impurities (potassium and sodium, important for the further characterization of the core@shell system, see section 5.4.3) in the P-CZA-1 and P-CZA-2 samples was excluded (not shown in Table 5.1).

5.2.4 Influence of the calcination

The calcination is necessary for the successful formation of the zeolite layer and for the removal of the organic template after hydrothermal synthesis of the zeolite shell (core@shell system) as well as during the preparation of the CZA&Z particles (see sections 4.3.2 and 4.3.3). In order to evaluate the effect of the thermal treatment (see section 4.3 for conditions) on the CZA system, this was investigated: the results are summarized in Table 5.1 as well as in Figures 5.6 and 5.7.

The XRD patterns after calcination of the pristine FSP-CZA material and of the P-CZA are shown in Figure 5.6a. In general, the calcined samples show more distinct x-ray reflections as compared to the original nanopowder. Furthermore, diffraction peaks at 2Θ = 39.7° and 45.8° disappeared after the calcination, while at 2Θ = 32.5° a new peak arose, which can be assigned to CuO. Nevertheless, all characteristic reflections for CuO and ZnO are still present after the calcination and, thus, changes in phases by e.g. alloying - known to be relevant in reducing conditions [28, 153] - can be excluded for the calcination. Based on XRD (Scherrer equation, CuO[111]), by calcination the CuO crystallite size increases from 8.8 nm to 21.2 nm and from 9.8 nm to 14.9 nm for CZA-1-f_c and CZA-2-f_c, respectively (see Table 5.1). This is also confirmed by TEM images, shown in Figure 5.7. Comparing the CZA-1-f_c with the CZA-2-f_c XRD-patterns (Figure 5.6a), some differences in the peaks relative to the ZnO phase can be observed: at 2Θ equal to 34.4° and 69.1°, the reflections disappear for the sample CZA-2-f_c; at 2Θ equal to 36.5°, 47.6° and 63.2°, the reflections of the CZA-2-f_c are not as distinct as in the CZA-1_c samples. A similar behaviour was already observed comparing the pristine CZA-2-f to the CZA-1-f (see section 5.2.2), sug-

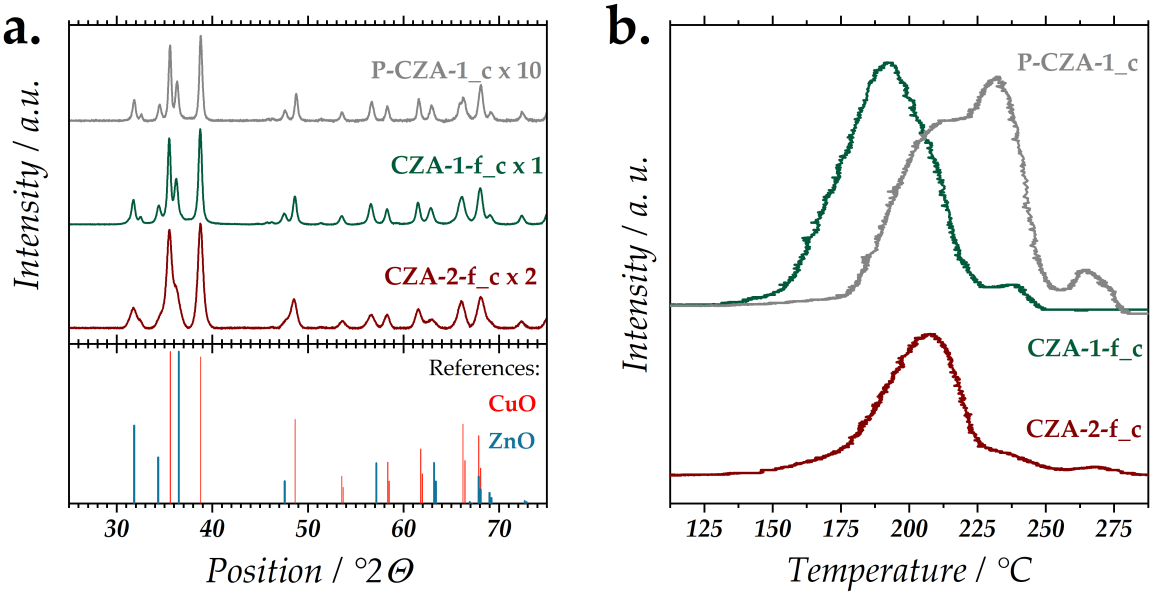


Figure 5.6: a) XRD patterns of the CZA-2-f_c, CZA-1-f_c, P-CZA_c (with adjusted intensities) and the references for CuO and ZnO structures (International Center for Diffraction Data (ICDD)); b) TPR profiles of the CZA-2-f_c, CZA-1-f_c and P-CZA_c samples.

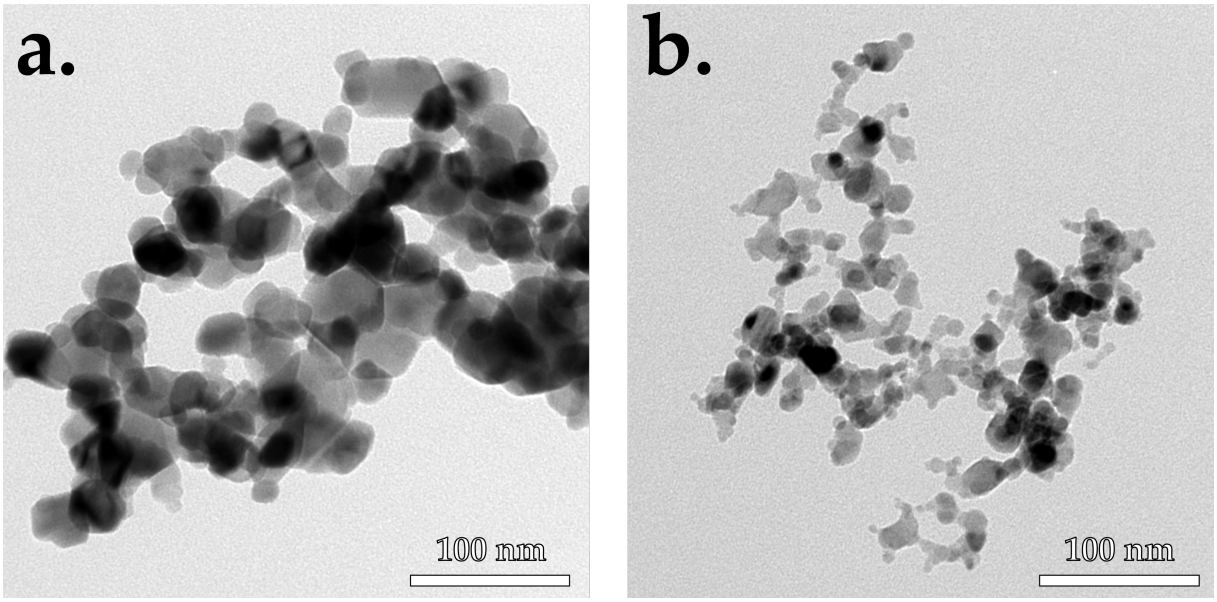


Figure 5.7: Transmission electron micrograph of the a) CZA-1-f_c and b) CZA-2-f_c.

gesting that the influence on the crystal structure due to the calcination is milder for CZA-2-f compared to the CZA-1. This can be confirmed by the size of the ZnO crystals, calculated by using the Scherrer equation based on the reflection at $2\Theta = 31.8°$. 22.7 nm and 14.8 nm are detected for the CZA-1-f_c and the CZA-2-f_c, respectively.
Figure 5.6b shows the TPR profile of the same samples after thermal treatment. Peak reduction temperature of the CZA-1-f is 170 °C (total reduction at 200 °C). Reduction temperatures in the range of 150 °C to 330 °C, depending on the preparation procedure, are reported in literature for both Cu-based STM catalyst and STD bifunctional systems. Ahmad et al. reported a TPR peak at 210 °C with a shoulder at 176 °C for the pure CZA [38]. García-Trenco et al. reported a slight influence of the type of acid catalyst in a hybrid CZA/MTD-catalyst system within a window between 200 - 210 °C similar to what was determined for pure CZA [66]. For thermally treated Cu-based hybrid systems, Li et al. reported a decrease in reducibility with increasing calcination temperature [125]. A shift to higher reduction temperature was also reported by Jiang for calcined Cu-Al-systems (200 - 330 °C) [51] and by Zhu et al. for samples with larger CuO-clusters [144]. Similar observations were made in the present study. Particularly after calcination, the peak reduction temperature of the CZA-1-f_c increased to 190 °C (see Figure 5.6b). The same tendency could, however, not be observed for the CZA-2-f_c powder. Here, the reduction temperature was 205 °C which is lower compared to the pristine CZA-2-f (230 °C, see also Table 5.1). This behaviour, in general, is in contrast with what was found for the CZA-1 system in literature. In section 5.2.2, the formation of carbonates at the surface, to a larger extent in case of CZA-2-f compared to CZA-1-f, was hypothesized as a possible reason of hindered reduction of the former powder. During the calcination, the carbonates are removed and, as a consequence, the reduction takes place at lower temperature, despite the larger CuO particles. This could further support the hypothesis of the co-production of carbonates, especially when starting from the solvent 2.

Macroscopically, some Cu- or Zn-segregation due to calcination was observed as shown in the cross sectional EPMA/WDX elemental maps in Figure A.6. However, both elements remain homogeneously

distributed throughout the whole CZA particle. Besides the increase in reduction temperature and CuO crystallite size due to calcination, a decrease in the BET surface area from 69 $m^2\ g^{-1}$ to 11 $m^2\ g^{-1}$ was also observed. The synergy between Cu and ZnO phases is fundamental in the STM reaction, as reported in different works [28, 35, 36]. Starting from thermodynamic calculations, Kuld et al. proposed an influence of the coverage of Cu active sites by Zn-based phases on the activity of CZA catalysts under STM reaction conditions. The authors found that a higher Zn coverage on Cu nanoparticles enhances the activity of the CZA system [35]. It is also reported that the presence of synthesis gas favours the reduction of ZnO_x to Zn and the consequent formation of the Cu-Zn alloy, which, together with the metallic Cu sites, represents the surface active site for the STM reaction [28, 35, 153, 154, 155]. Based on these considerations, it should be taken into account that changes in the Cu- and Zn-phases of the CZA material occurring during the calcination can affect the performance in the STM reaction. In this study, the observations described above indicate a partial modification of the CZA catalyst during thermal treatments.

5.2.5 Agglomerated SD-CZA

Spray drying was used as an alternative technique to obtain the STM core catalyst with mechanical resistance and particle size in the range of 20 - 50 µm (see section 4.3.3). As spray drying is not supposed to change the chemical structure of the powder but only its shape and size (due to the conditions), the same properties in crystal structure and reducibility compared to the original CZA-1-f powder were assumed.

The spherical shape of the product was proved by SEM image, depicted in Figure 5.8a. The mechanical resistance was proved by measuring the change in particle size distribution before and after 10 min of sonication. As deducible by analysing Figure 5.8b, the sonication can destroy only the biggest particles (over 75 µm) but not those in the size range 20 - 50 µm. After the procedure, the $d_{[4,3]50}$ value decreased

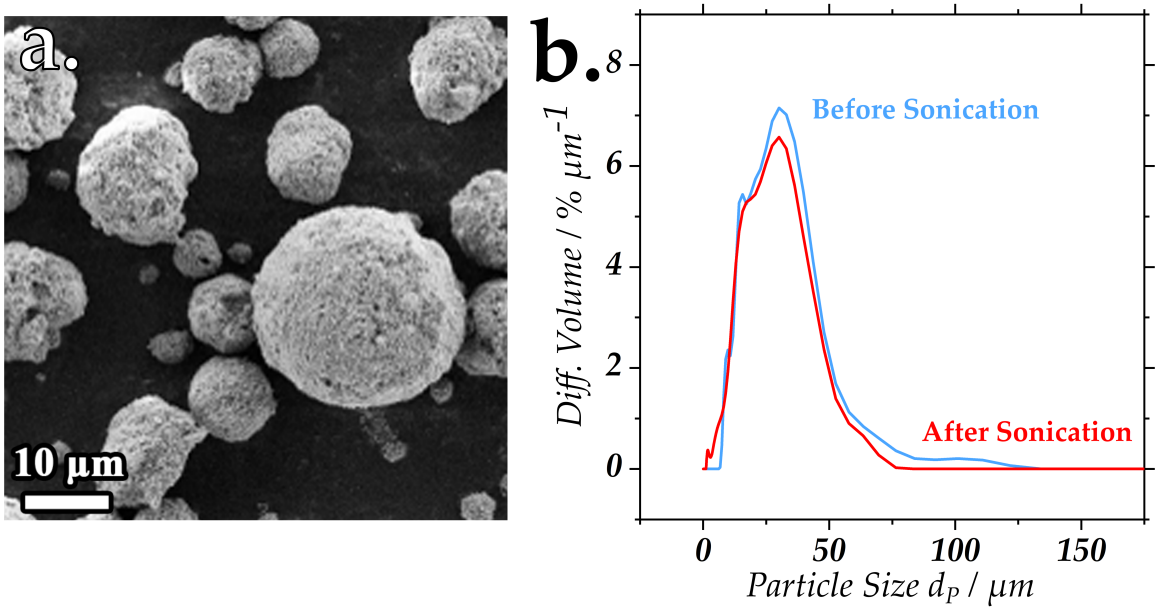


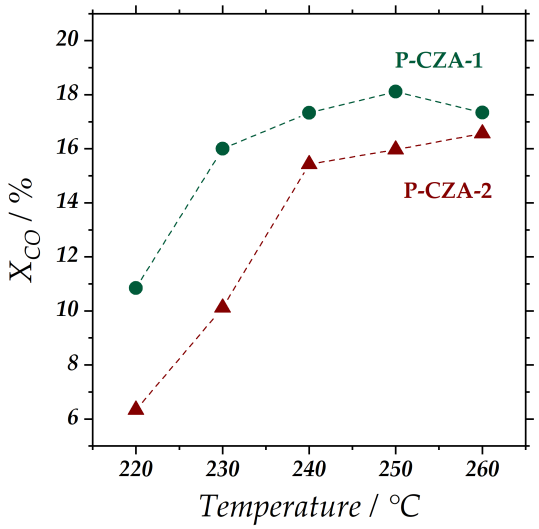
Figure 5.8: SD-CZA characterization: a) SEM image and b) influence of the sonication on the particle size distribution for the evaluation of the mechanical stability.

from 26 µm to 23 µm. The particles bigger than 75 µm are generated mostly by the result of further collisions after the drying process, but do not originate from just one droplet during the spraying process. Their mechanical resistance is therefore lower. On the other hand, the mechanical strength of the spray dried core catalyst SD-CZA could be proved.
From cross-sectional EPMA/WDX analysis (Figure A.6), it can be confirmed that Cu and Zn are homogeneously distributed within the SD-CZA material before and after calcination while some clustering of Zn after calcination can be observed (see section 5.2.4).

5.3 FSP-CZA: reaction tests

The FSP-CZA synthesized catalysts were tested in the form of pelletized particles (P-CZA-1 and P-CZA-2) as well as spray dried agglomerates (SD-CZA) in a µ-Berty reactor, as described in section 5.1.

Figure 5.9 shows a comparison of the activity of the P-CZA-1 and P-CZA-2 catalysts at p = 45 bar; $(F/W)^*$ = 16 250 $mL_{Reagents}\ h^{-1}\ g_{CAT}^{-1}$ and feed gas composition: $H_2/CO/CO_2$ = 16/7/7, N_2: 10 vol.-% . A similar X_{CO} is reached on both catalysts at T = 260 °C ($X_{CO;260\,°C}$ = 17.3 %; $X_{CO;260\,°C}$ = 16.6 % for P-CZA-1 and P-CZA-2, respectively), and the mild dependence of the X_{CO} on the reaction temperature at $T \leq 240$ °C suggest that in this range the systems are thermodynamically limited. However, at lower temperatures, the kinetics is limiting the overall process and a comparison of the STM reaction performance of the two catalysts is possible: a higher X_{CO} is reached on the P-CZA-1 catalyst ($X_{CO;230\,°C}$ = 16 %; $X_{CO;230\,°C}$ = 10.1 % for P-CZA-1 and P-CZA-2, respectively). In literature enhanced activity in the STM reaction is reported for catalysts with smaller primary Cu particles and lower reduction temperatures [125]. As listed in Table 5.1, CuO particles in the same size were found for the two samples, but the reducibility of the two catalysts is strongly different ($T_{red.}$ = 170 °C; $T_{red.}$ = 230 °C for CZA-1-f and CZA-2-f, respectively). For this reason, the CZA-1 system was further investigated for the STM synthesis and



CONDITIONS: µ-Berty; p = 45 bar; $(F/W)^*$ = 16250 $mL_{Reag.}\ h^{-1}\ g_{CAT}^{-1}$
Feed Composition: H_2 : CO : CO_2 = 16 : 7 : 2; 10 vol.-% N_2

Figure 5.9: Activity for the STM reaction in the µ-Berty reactor of P-CZA-1 and P-CZA-2 in terms of X_{CO} as function of the temperature.

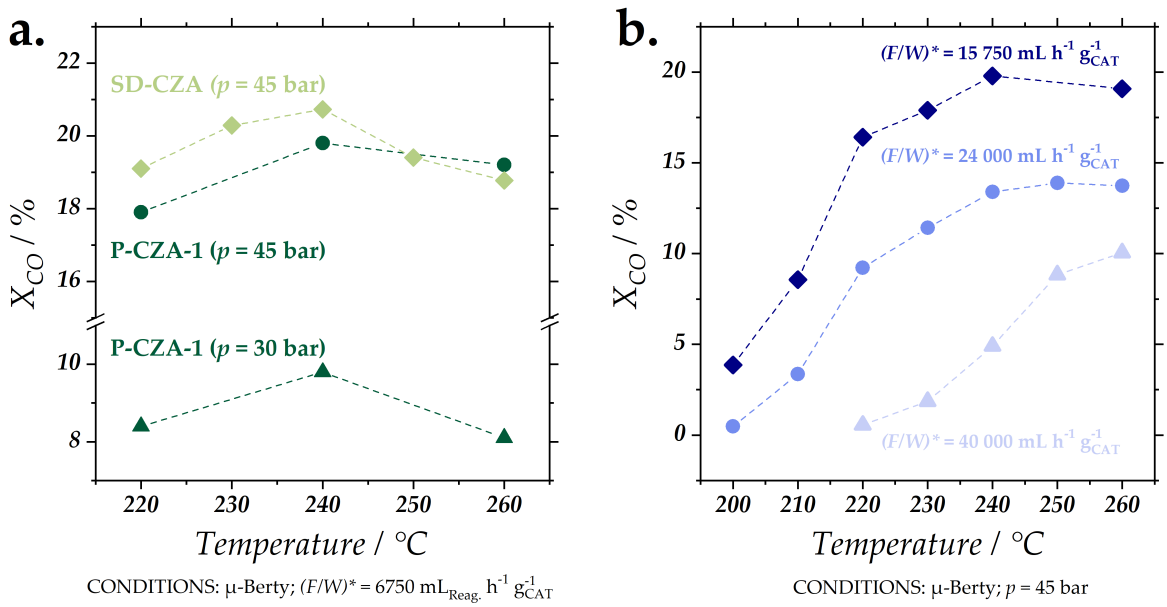


Figure 5.10: Activity for the STM reaction in the μ-Berty reactor of the a) SD-CZA and P-CZA-1 as function of the temperature at different pressure (at p = 45 bar: $X^{eq.,out}_{CO;220\,°C}$ = 53.4 %; $X^{eq.,out}_{CO;260\,°C}$ = 23.7 %); b) P-CZA-1 as function of the temperature over different $(F/W)^*$.

was chosen as starting material for the bifunctional catalysts prepared in this work.

Figure 5.10a shows the activity of the CZA-1-f powder in the form of pelletized particles (P-CZA-1) and spray dried agglomerates (SD-CZA). The samples were tested at the same conditions: p = 45 bar; 220 °C $\leq T \leq$ 260 °C, $(F/W)^*$ = 6750 $mL_{Reagents}\ h^{-1}\ g^{-1}_{CAT}$ and feed gas composition: $H_2/CO/CO_2$ = 16/8/1 (N_2: 10 vol.-%); furthermore, the P-CZA-1 was tested at p = 30 bar. As expected, a strong influence of pressure on catalyst activity is found comparing the performance of P-CZA-1 at 45 bar and 30 bar: by decreasing pressure, a marked drop of conversion was detected (at T = 220 °C: $X_{CO;45\,bar}$ = 17.9 %; $X_{CO;30\,bar}$ = 8.4 %). Moreover, the CZA-1 material shows a comparable activity, independent of procedure applied to CZA-1-f nanopowder to form larger particles, either via pelletization, crushing and sieving or spray drying for P-CZA-1 and SD-CZA, respectively. The possible different morphology i.e. in shape and porosity of the two CZA-1 materials do not influence the activity of the catalyst in absence of mass transfer limitation within the particle. From 240 °C onwards X_{CO} decreases with temperature, namely the reaction is not kinetically limited. Both SD-CZA and P-CZA-1 converge to a similar value at T = 260 °C and p = 45 bar ($X_{CO;SD-CZA}$ = 18.8 % and $X_{CO;P-CZA-1}$ = 19.2 %). Calculating X_{CO} at the equilibrium of the gas composition at the reactor outlet ($X^{eq.,out}_{CO}$), that corresponds to the gas composition in the reactor as the μ-Berty reactor is assumed to behave as a CSTR, it was observed that this is close to the measured X_{CO} at T = 260 °C, while the same value is far from the measured X_{CO} at T = 220 °C (see values in caption of Figure 5.10). Therefore, the decrease of X_{CO} over temperature is due to thermodynamic limitations.

Figure 5.10b shows the activity of the P-CZA-1 catalyst at p = 45 bar and various values of $(F/W)^*$ and temperature. An increase of $(F/W)^*$ corresponds to a shorter contact time of the gas mixture, namely conversion is expected to decrease. At $(F/W)^*$ = 15 750 $mL_{Reagents}\ h^{-1}\ g^{-1}_{CAT}$, the system is not kinetically limited at 240 °C ($X_{CO;240\,°C}$ = 19.8 % at both 6750 and 15 750 $mL_{Reagents}\ h^{-1}\ g^{-1}_{CAT}$; $X_{CO;260\,°C}$ = 19.2 %

and $X_{CO;260\,°C}$ = 19.1 % at 6750 and 15 750 $mL_{Reagents}\ h^{-1}\ g_{CAT}^{-1}$, respectively). Carrying out the STM reaction at $(F/W)^*$ up to 40 000 $mL_{Reagents}\ h^{-1}\ g_{CAT}^{-1}$, a dependence of X_{CO} on temperature is visible and a kinetic limitation is occurring. Figure 5.10b underlines the challenging choice of proper conditions for a kinetic study in the frame of this work, due to the relevant range between the minimum detectable X_{CO} with standard equipment and the equilibrium conversion, which is rather low ($X_{CO}^{eq.}$ = 33.6 % at p = 45 bar and T = 260 °C) and even lower if the equilibrium conversion of the gas composition in the reactor is taken into account (see above).
The activity tests at $(F/W)^*$ = 24 000 $mL_{Reagents}\ h^{-1}\ g_{CAT}^{-1}$ were used for comparison to a commercial reference catalyst, the result is shown in Figure A.7. In general, the commercial material was more active than the catalyst prepared in this work.
In section 5.2, the influence of the calcination on the FSP-CZA material was explained within the physico-chemical properties of the powder. Furthermore, the influence of the thermal treatment on the catalytic performance for the STM reaction was investigated. As this procedure was carried out during the CZA@Z synthesis, the results are shown further below together with the performance of the bifunctional catalysts in the STD reaction (see section 5.5).

5.4 Particulate catalyst configurations: physico-chemical characterization

As described in chapter 4, the CZA-1-f was used as starting material for the preparation of the different particulate catalyst configurations. The pristine CZA-1-f was used as starting material for the preparation of the hybrid particulate systems of medium (CZA+Z) and close (CZA&Z) proximity, while the P-CZA-1_c was used as core material for the synthesis of the structured particulate CZA@Z catalyst. In the following the physico-chemical characterization of the CZA+Z, CZA&Z and CZA@Z particulate catalysts is reported.

5.4.1 Hybrid particulate catalyst of medium proximity (CZA+Z)

As the CZA+Z catalyst was synthesized by pelletizing a physical mixture of the n-Z and CZA-1-f nanopowders (see section 4.3), the physico-chemical structure of the two single catalysts is supposed to be maintained in the final CZA+Z. However, the reducibility and the morphology of the sample CZA+Z_5 were investigated. Besides the expected reduction peak at 170 °C, in accordance with the original CZA-1-f, the TPR profile, shown in Figure A.8, presents a shoulder at 185 °C. The presence of this shoulder could be due to the two consecutive reduction steps ($Cu^{2+} \rightarrow Cu^{+} \rightarrow Cu^{0}$), as reported in [38] and [156], or to the reduction of the well dispersed CuO (shoulder) followed by the reduction of the CuO in the bulk (main peak) [157]. The presence of both catalysts within one single pellet is confirmed by observing the cross sectional images as well as the elemental map of the metals representative for the CZA, namely Cu and Zn, and zeolite, namely the Si (see Figure A.9).

5.4.2 Hybrid particulate catalyst of close proximity (CZA&Z)

The CZA&Z was synthesized by spray drying the FSP-CZA suspended in the zeolite mother liquor (see section 4.3). A TE-micrograph of the pristine spray dried particles is shown in Figure 5.11a: at this stage of the synthesis, the sample is still containing template and amorphous silica, which should be removed and converted to crystalline zeolite during the steam assisted crystallisation (SAC) procedure.

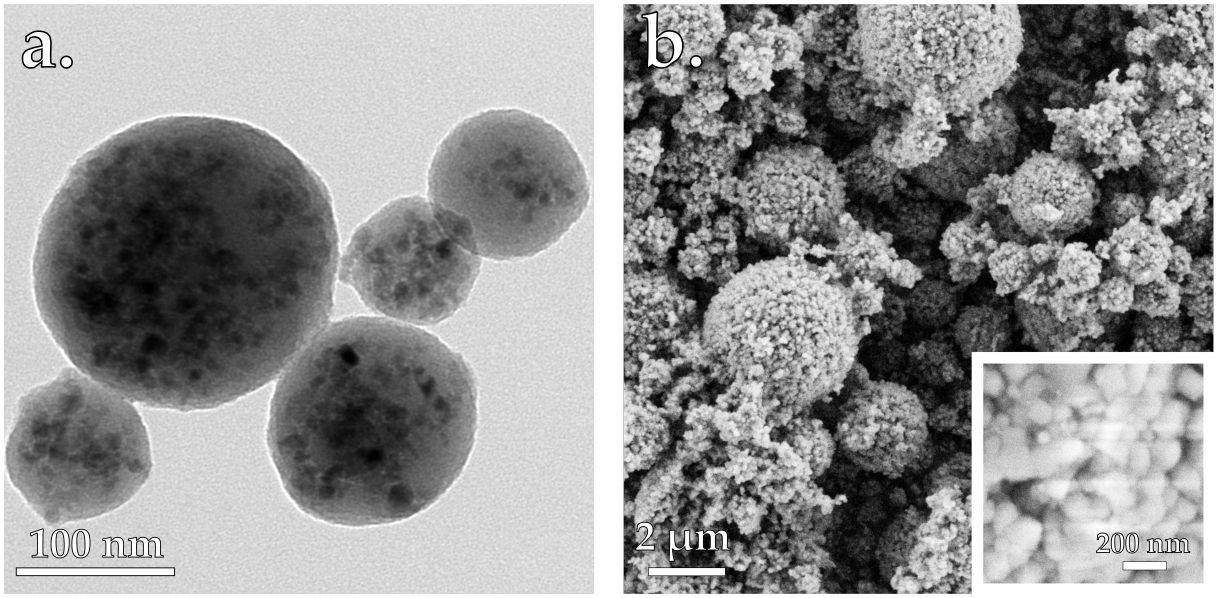


Figure 5.11: Morphological analysis of the CZA&Z: a) TE-micrograph after spray drying; b) SEM-micrograph and details of the outer surface (inset) after the steam assisted crystallization and calcination.

The TEM image in Figure 5.11a confirms the success of the spray drying in terms of spherical shape of the product and homogeneous distribution of the FSP-CZA (small and dark spots) within the zeolite particles. Moreover, from Figure 5.11, close proximity (in the sub-micrometer-scale) between the CZA and the Z catalysts is observed. This consideration is the basis of the modelling of the hybrid particles CZA&Z. However, a broad particle size distribution of the product could be observed (also from other TEM images, not shown here). Figure 5.11b presents a SEM image of the CZA&Z particles after SAC and calcination: the particle size of the powder is below 10 µm; the spherical shape of the particles is maintained after the recrystallization. In the inset of Figure 5.11b, the presence of nanosized crystals is proved and, from the XRD pattern of the particles (shown in Figure A.10), both CZA and MFI structures in the sample are confirmed. Moreover, from the reflection intensities, the higher amount of zeolite compared to CZA in the sample can be observed.

In summary, the synthesis of the CZA&Z particulate hybrid system was succesful, but some challenges should be overcome before testing it for the STD reaction. First, via spray drying it was possible to reach agglomerates in the range of 1 - 10 µm in size, which are still too small for a conventional packed-bed-reactor. Pelletization of the CZA&Z particles should be avoided, because it would break the agglomerates, losing the hierarchical structure characteristic of this configuration. However, the application in a µ-CR as layered CZA&/Z system could be considered, as the coating procedure should not affect the mechanical integrity of the particles. This option is hindered by the feasible mass ratio of STM/STD catalyst in the final product (ω_{Zeo} cannot be lower than 92 wt.-% so far). Higher CZA loading in the suspension for the spray drying affects its stability and compromises the synthesis of the particles. It is worth reminding that the equipment used for the spray drying of the CZA&Z particles is not the same as for the synthesis of the SD-CZA cores. Therefore, the feasible particle loading in the suspension as well as the size of the product are not comparable. According to the simulation carried out in this work and presented in chapter 3, it is not convenient to perform the STD reaction with such a catalyst composition, as the system is limited by the scarce amount of STM catalyst, with consequently low X_{CO}.

Furthermore, the SAC procedure, which takes place in presence of the CZA catalyst at similar conditions with comparison to the shell synthesis, affects the STM catalyst irreversibly. This was observed for the CZA@Z catalyst and is discussed below (see section 5.4.3).
Concluding, even if the bifunctional hybrid particulate catalyst system of close proximity showed a more promising performance compared to the other particulate structures by modelling, challenges linked to its preparation makes this catalyst not suitable for the STD reaction so far.

5.4.3 Structured core@shell particulate catalyst (CZA@Z)

The goal of the CZA@Z synthesis was to coat a thin but dense layer of the zeolite H-ZSM-5 on the surface of the STM catalyst core.

In Figure 5.12a, a comparison of the XRD patterns of the samples after the different steps of the synthesis (P-CZA-1, P-CZA-1_c, isS_P-CZA and P-CZA@Z) is shown.
The seeded sample isS_P-CZA shows in general lower intensities and almost no diffraction peaks of the MFI-phase in the XRD patterns. At this stage of the synthesis, beside the CZA and the zeolite seeds (nanocrystals), template and remains of the synthesis mixture are present in the sample. As the XRD patterns were obtained based on the same volume of powder, the share of the MFI-crystalline phase is in the case of isS_P CZA reasonably lower. After the secondary growth (P-CZA@Z), reflections clearly belonging to ZSM-5 appear. For the P-CZA@Z, all dominant reflections can be assigned to either MFI, CuO or ZnO_x, showing that the CZA phase is still present in the core@shell material. For all samples, the characteristic pattern of the P-CZA_c sample was retained. However, when comparing the diffraction intensities of the characteristic CuO-reflections of samples P-CZA_c, isS_P-CZA and P-CZA@Z, it can be seen that, after a first strong decrease in intensity after the seeding step, CuO-related signal intensities increase after the shell synthesis step, but do not reach the initial values of the P-CZA_c sample. This

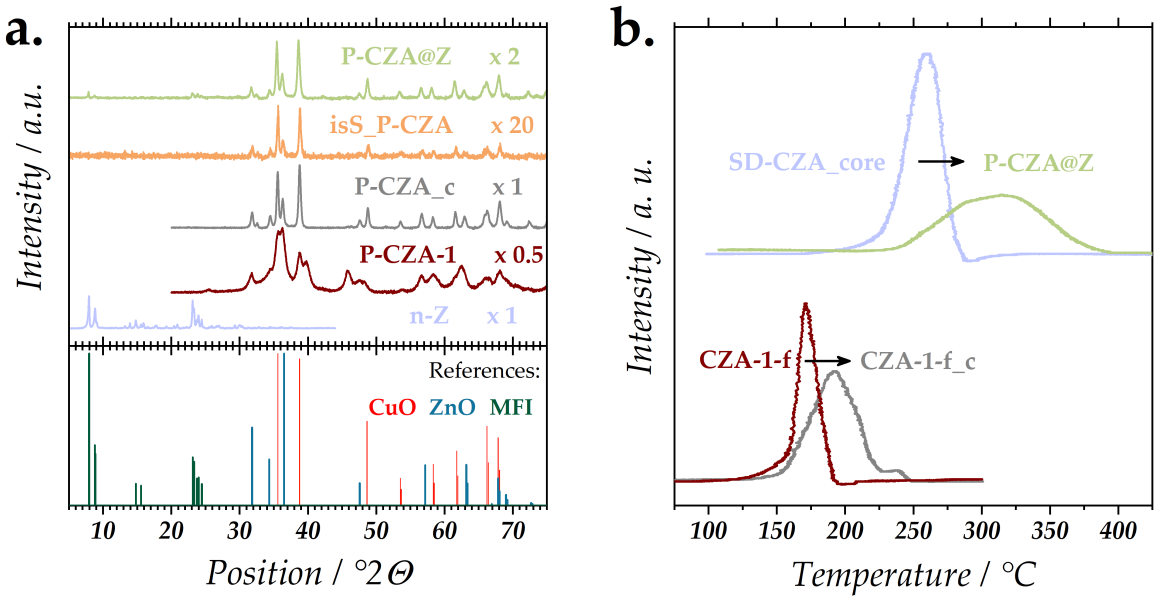


Figure 5.12: a) XRD patterns of the samples after each step of the shell synthesis (with adjusted intensities), as well as of n-Z for comparison and the references for CuO, ZnO and zeolite MFI structures (International Center for Diffraction Data (ICDD)); b) TPR profiles of the different (intermediate) materials obtained during the shell synthesis procedure.

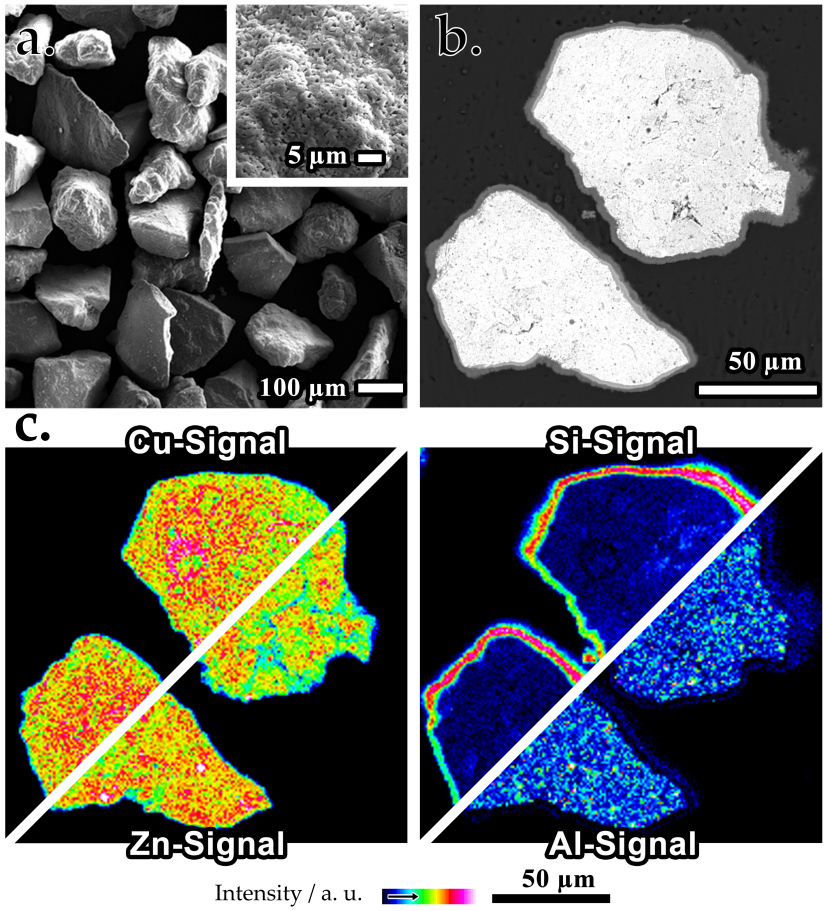


Figure 5.13: Morphological analysis of the P-CZA@Z catalyst. a) SE-micrographs of a P-CZA@Z and details of the shell outer surface (inset), b) cross-section analysis of distinct core@shell particles via EPMA/BSE and c) elemental map (EPMA/WDX) for the representative elements for the core (Cu, Zn, Al) and shell (Si, Al).

can on the one hand be attributed to the amount of CZA in the sample ($\omega_{CZA}/\omega_{Zeo} \approx 30$, see below), but also indicates that the harsh conditions during hydrothermal synthesis partially changed the core material.

From the TPR profiles (Figure 5.12b), changes in the reducibility of the core catalyst were observed after the hydrothermal synthesis of the shell. For the P-CZA@Z catalyst, the peak of CuO-reduction shifted from 190 °C of the starting material (CZA-1-f_c) to 315 °C. The shift is accompanied by a broadening of the reduction peak, eventually due to a limitation for hydrogen diffusion through the zeolite shell. In case of a complete coverage of the shell, diffusion limitation is expected to be more severe and this may shift the reduction temperature to higher values, as the same heating rate was applied for all samples. This explanation is strengthened by the TPR profile of the SD-CZA_core catalyst with almost no coverage of the CZA and, thus, without additional hindering by showing a TPR-profile similar to CZA-1-f_c with lower peak temperature than observed for P-CZA@Z. Therefore, the presence of a dense zeolitic shell over the CZA core leads to a shift of the reduction towards higher temperature, eventually due to diffusional limitation.

As shown by SEM and EPMA/BSE (Figure 5.13a-b), after the second step of hydrothermal synthesis, very large zeolite crystals densely packed together forming a continuous shell can be observed. Thus, the SEM results strongly support the findings from XRD, which confirmed the presence of ZSM-5 in the P-

Table 5.2: Impurities (K and Na) in the STD-catalysts based on ICP/OES.

Sample	*K-content / wt.-%*	*Na-content / wt.-%*
P-CZA@Z	2.4	0
CZA+Z_5@Z	1.8	0
CZA+Z_5	0	0
SD-CZA_core	0.1	0

CZA@Z material. To check for successful formation of the core@shell configuration, the cross section of the sample P-CZA@Z was further characterized by EPMA/WDX analysis (Figure 5.13c-d). The element distribution confirms that Si - being an indicator for the zeolite shell - is homogeneously distributed around the core. A low signal of Si was registered for the core area, which can be due to the partial infiltration of the synthesis mixture in the voids of the CZA core during the formation of the zeolite shell. Aluminum per se is part of the CZA core and, in small amounts (SiO_2/Al_2O_3=100), part of the H-ZSM-5 shell, which can also be confirmed by the cross sectional elemental map. Copper and zinc are present only in the core and are homogeneously distributed. From these cross-sectional images, the formation of a core@shell system with a homogeneous 3.6 µm thick shell can be concluded. From geometrical considerations assuming ideally spherical core particles of a diameter of 150 µm, 3.6 µm shell thickness and densities of the CZA core and zeolite shell of ρ_{core} = 3890 kg m^{-3} (from Hg intrusion measurement) and ρ_{shell} = 1835 kg m^{-3} [118], respectively, the weight ratio of STM/MTD catalyst is $\omega_{CZA}/\omega_{Zeo} \approx 30$.
To further understand the effects of the zeolite synthesis on the chemical composition of the core material, ICP/OES was used to determine and confirm the loss of Cu during shell preparation. P-CZA and P-CZA_c have a Cu-content 56.5 and 54.9 wt.-%, respectively (see Table 5.1). Again assuming that the core is ideally spherical in shape with a diameter corresponding to the mean of the sieve fraction used (150 µm), together with the values of the density of both zeolite and core and from the mean shell thickness obtained from the cross section images (3.6 µm), the amount of copper in the core-fraction of the P-CZA@Z catalyst was calculated and used to evaluate a potential loss of Cu during the shell synthesis. The Cu content in the final P-CZA@Z and in the core fraction was calculated to be 45.1 and 46.7 wt.-%, respectively. Therefore, a loss of almost 15 wt.-% Cu of the sole core during the shell preparation was determined. Furthermore, ICP/OES of the bifunctional catalysts was used to check for the potential presence of impurities, particularly of potassium and sodium, which could affect the activity of the H-ZSM-5. As summarized in Table 5.2, none of the samples contains Na, but all core@shell catalysts prepared contain K-impurities. As the FSP-CZA is not contaminated with K (proved with ICP/OES, not shown), the impurity has to be connected to the zeolite, and more precisely to the shell synthesis, as the CZA+Z_5 does not contain any K. Further ICP/OES analysis of the template used to form the zeolite shell showed that the TPAOH solution contains about 509 mg L^{-1} potassium and no sodium. To remove potassium in the final catalyst, the ion exchange process was done slightly differently than for the nanosized zeolite to avoid excessive dissolution of copper in the ammonium nitrate solution. Nevertheless, it was not possible to remove all potassium from the shell, even after repeated rounds of ion exchange. At this point it is worth mentioning that it was possible to exchange all potassium of the nanosized zeolite (n-Z) samples under similar conditions. Thus, it can be concluded that K is still present in the final

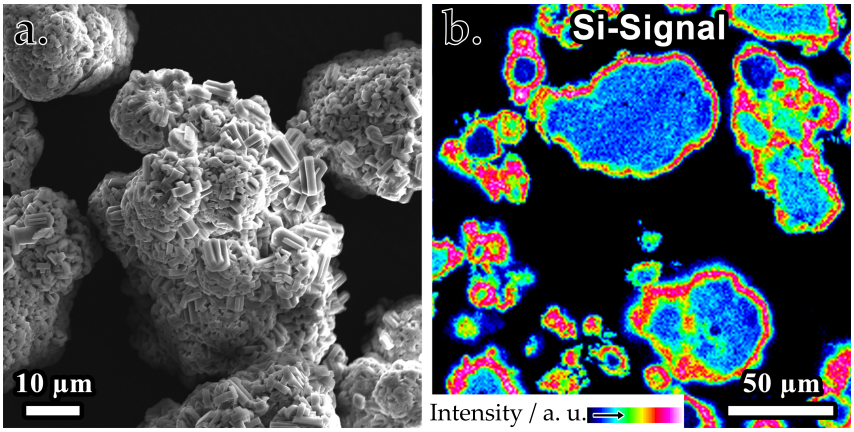


Figure 5.14: a) SEM image and b) Si-EPMA/WDX signal of the SD-CZA@Z.

core@shell material.

Core@shell particles were synthesized starting from the sample SD-CZA. A SEM image of the sample shows the complete coverage of the core by the zeolite in case of SD-CZA@Z (Figure 5.14). From the Si-elemental mapping, it is observed that a homogeneous zeolitic layer is covering the core material also in case of the smallest SD-CZA particles. Starting from this core material, the challenging synthesis step concerns the separation between CZA@Z and zeolitic excess powder, as the two materials are similar in size. For this reason, further synthesis and characterization were carried out on the P-CZA, which enabled a more handy synthesis.
Furthermore, for comparison, the sample SD-CZA_core was prepared. The synthesis of the SD-CZA_core occurred with very concentrated and alkaline conditions. These were necessary to favour nucleation over growth. Since for the formation of a dense shell, crystal growth is more important, the conditions used during this synthesis will just result in a deposition of nanoparticles and not in a dense shell. Even a further increase of the synthesis temperature or time will not yield a dense shell. Higher synthesis temperature and time under such conditions will just promote excess leaching of Cu and Zn from the core catalyst. In order to confirm that no shell grew during the synthesis of the SD-CZA_core, the sample was analyzed with electron microscopy (Figure A.11). No zeolite crystals are visible on the surface and from Si-EPMA/WDX almost no Si-signal is present in the sample.

5.5 Particulate catalyst configurations: reaction tests

As demonstrated in section 5.4, despite the advantage of the CZA&Z catalyst configuration found by modelling, due to unsolved practical challenges linked to the preparation of this system, the bifunctional hybrid particulate catalyst system of close proximity was not tested under reaction conditions. However, the performance of the hybrid particulate catalyst system of medium proximity CZA+Z and of the structured core@shell CZA@Z for the STD reaction in the µ-Berty reactor is delineated in sections 5.5.1 and 5.5.2, respectively.

5.5.1 Hybrid particulate catalyst of medium proximity (CZA+Z)

The results of the reactor tests for the hybrid particulate catalysts CZA+Z_1 and CZA+Z_5 are compared in Figure 5.15. CZA+Z_1 shows a stronger dependence of X_{CO} on temperature but constant selectivity, while for CZA+Z_5 it is rather vice versa. At similar X_{CO} ($X_{CO,CZA+Z_1}$ = 26.4% at T = 280 °C and

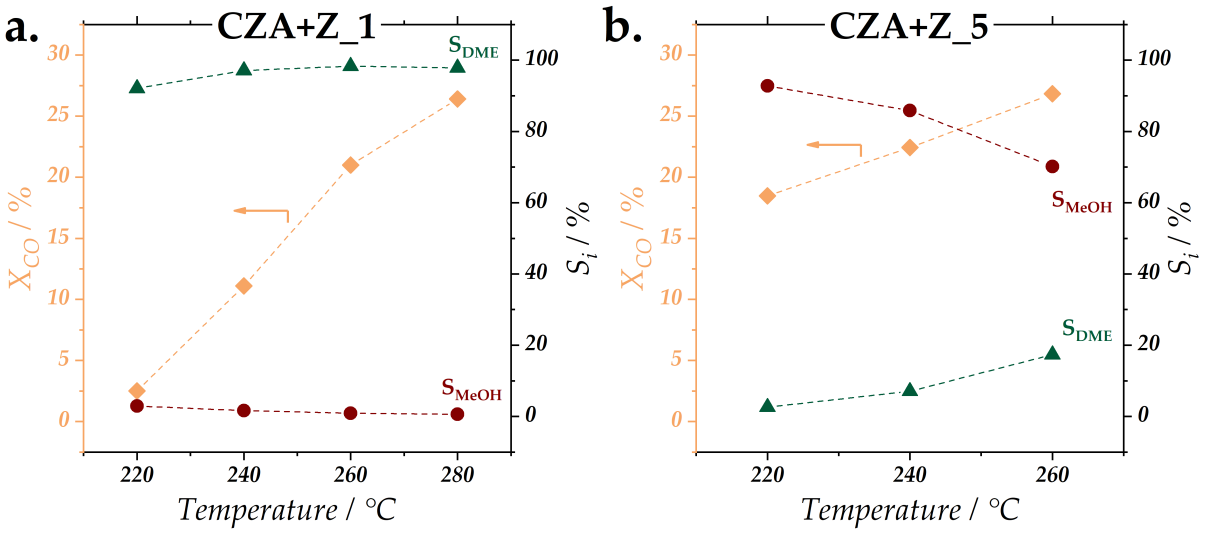


Figure 5.15: Influence of the zeolite amount in the CZA+Z catalyst on the performance in the STD-reaction. X_{CO}, S_{DME} and S_{MeOH} of a) CZA+Z_1 and b) CZA+Z_5 hybrid catalysts in the μ-Berty reactor as a function of temperature.

$X_{CO,CZA+Z_5}$ = 26.8% at T = 260 °C), the product distribution differs greatly, which is in line with the characteristic of $X_{CO,CZA+Z} = f(\omega_{Zeo})$ shown in Figure 3.4. The sample CZA+Z_1 contains enough zeolite for the dehydration of all the MeOH produced and, thus, the lower amount of the CZA is the limiting factor. Within the temperature range investigated, for CZA+Z_1, byproduct formation is negligible: S_{CH_4} decreased from 5 % at 220 °C to only 1 % at 280 °C, while C_{2+} components could only be observed at 280 °C ($S_{C_{2+}}$ = 0.6 %). Over the CZA+Z_5 catalyst, the higher CZA amount allows higher conversion even at lower temperature. Here, the MeOH dehydration rate increases with temperature, byproduct formation was not observed. Table 5.3 shows the comparison between P-CZA-1 and CZA+Z_5 at the same value of $(F/W)^*$ related to the total catalyst mass. For P-CZA-1 a virtually constant value of X_{CO} at 240 °C and 260 °C was detected (see section 5.3). In comparison, even with a lower absolute amount of CZA, at 260 °C it is possible to overcome $X_{CO}^{eq.,out}$ over the CZA+Z_5 catalyst, which perfoms higher X_{CO}. This clearly demonstrates the benefit in X_{CO} obtained when adding a dehydration catalyst.

Table 5.3: X_{CO} over P-CZA-1 and CZA+Z_5 at different reaction temperatures.

T / °C	*P-CZA-1*, X_{CO} / %	*CZA+Z_5*, X_{CO} / %
220	17.9	18.5
240	19.3	22.4
260	19.2	26.8

CONDITIONS: μ-Berty; p = 45 bar, $(F/W)^*$ = 6750 $mL_{Reagents}$ h^{-1} g_{CAT}^{-1}

(for P-CZA-1: $X_{CO;260\,°C}^{eq.,out}$ = 23.7 %)

5.5.2 Structured core@shell particulate catalyst (CZA@Z)

As described in section 5.4, the characterization of the CZA catalyst revealed changes in the structure of the core catalyst caused by the shell synthesis procedure. In order to identify the responsible synthesis step(s), the catalytic performance was studied after each crucial step of the synthesis (P-CZA-1, P-CZA_c, SD-CZA_core). It can be clearly seen (Figure 5.16) that each step of the synthesis causes a loss of activity in terms of X_{CO}. The P-CZA_c cannot perform as the fresh catalyst and a loss in X_{CO} of about 50 % was measured at T = 220 °C for the calcined sample. As already discussed in section 5.4, several deactivation effects are occurring during the calcination such as sintering of Cu in the CZA (decrease in surface area) as well as changes in the ZnO phase resulting in the segregation of the Cu and Zn-phases lowering the synergy between them.

The sample SD-CZA_core was prepared with a similar procedure like the P-CZA@Z but without a dense zeolite layer being grown around this core material in order to separate the effects of hydrothermal synthesis conditions and presence of a dense zeolite shell. During the shell synthesis (as discussed in section 5.4) a Cu-loss was found caused by the basic solution responsible for the dissolution of Cu, which represents the most important active site of the STM reaction. Based on that, a further decrease in X_{CO} found for this sample can be mainly attributed to the Cu-loss. This effect has not been discussed in literature so far.

The P-CZA@Z catalyst was tested at the same conditions as the bare core catalyst described above. At 260 °C X_{CO} of only 1.0 % was achieved, and no DME was observed (at the same temperature the SD-CZA_core showed X_{CO} = 6.2 %). Besides, the hybrid core CZA+Z_5 was enwrapped for synthesis of the sample CZA+Z_5@Z: X_{CO} = 1.4 % and S_{DME} = 34 %, S_{MeOH} = 66 % were obtained. The comparison of the CZA@Z samples to the SD-CZA_core shows that the dense zeolite shell reduces the catalytic activity of the core@shell system. A tentative explanation of the loss of activity is poor access of the reactants to the core catalyst, e-g., caused by diffusion limitation in the microporous shell. This interpretation

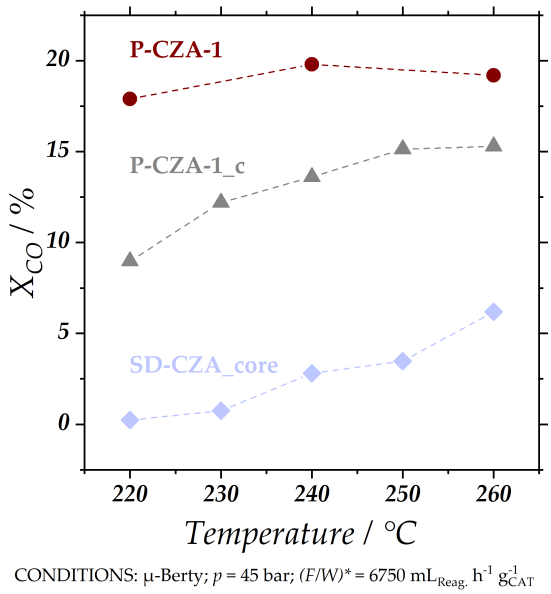


Figure 5.16: Activity for the STM reaction in the μ-Berty reactor after individual steps of the shell synthesis procedure in terms of X_{CO} as a function of the temperature.

is supported by the activity shown by the SD-CZA_core alone (Figure 5.16), where the CZA core was directly accessible for the synthesis gas during the reaction and X_{CO} could not be affected by diffusion limitation, but only from the alteration of the CZA core during the shell synthesis. However, the poor S_{DME} cannot be explained this way and is also not in line with the simulation results. Therefore, other effects should be considered. As discussed in section 5.4, potassium impurities contained in the zeolite shell, which could not be removed during the shell synthesis procedure (ion exchange), might have blocked/deactivated the active sites for DME formation. This explanation is further supported by the higher selectivity to DME observed over CZA+Z_5@Z. In contrast to the P-CZA@Z, the core@shell catalyst based on CZA+Z_5 contains a higher amount of acidic zeolite (n-Z). After the synthesis, the n-Z fraction within the core of the CZA+Z_5@Z sample most likely remains present in the active H-form.

In summary, the strong dependency of both X_{CO} and product distribution on the $\omega_{CZA}/\omega_{Zeo}$ parameter was experimentally confirmed in the case of the hybrid CZA+Z catalyst. Regarding the CZA@Z, the formation of the zeolitic shell as prepared in this thesis partially destroys the CZA core and compromises the activity of the whole catalyst configuration. Therefore, the effect in mass transfer resistance of the shell revealed by the modelling study (see chapter 3) becomes negligible if compared to this experimental challenge.

5.6 Planar catalyst configurations: rheology of the pastes

The preparation of the hybrid planar catalyst system of medium proximity (CZA#Z) and of the structured double layer configuration (CZA//Z) was achieved by coating the respective pastes in the microchannels. The preparation procedure of the pastes and their compositions are described in section 4.4 and Table 4.3, respectively. As already mentioned in chapter 4, the success of the coating via screen printing is strongly linked to both rheology and thixotropy of the paste. In the following, the characterization of these properties for all pastes prepared is outlined.

5.6.1 Hybrid planar catalyst of medium proximity (CZA#Z)

As Table 4.3 reports, beyond the *Hybrid-T1* paste, further four pastes based on mixtures of CZA and H-ZSM-5 were prepared, three using terpineol (*Hybrid-T2*, ..., *Hybrid-T4*, denoted as *Hybrid-Ti*) and one using water (*Hybrid-W*) as solvent, respectively.
The composition of the pastes containing terpineol (*Hybrid-Ti*) changes with the amount of this dispersant, which was increased from 0.7 wt.-% (*Hybrid-T2*) up to 5.8 wt.-% (*Hybrid-T4*). The preliminary study was done with the paste *Hybrid-T1*, which did not contain the dispersant and showed a yield stress at 800 Pa (see section 4.4). In literature, the correlation between the addition of the dispersant and the consequent lowering of the yield stress of the paste is reported [106, 108]. Stolz correlates the amount of dispersant to be added with the surface area of the powder to be printed, namely $1\,mg_{Dispersant}\,m^{-2}_{Powder}$ [106]. In the pastes *Hybrid-T2*, *Hybrid-T3* and *Hybrid-T4*, 10 %, 50 % and 100 % of the amount of dispersant according to the correlation of Stolz were used, respectively. Observing Figure 5.17, which shows the flow plot and the viscosity over the shear rate for the pastes *Hybrid-T2*, *Hybrid-T3* and *Hybrid-T4*, it is deducible that the addition of the dispersant strongly affects the rheology of the paste. It does not avoid the presence of the yield stress, but this is shifted to lower values: adding the dispersant loading,

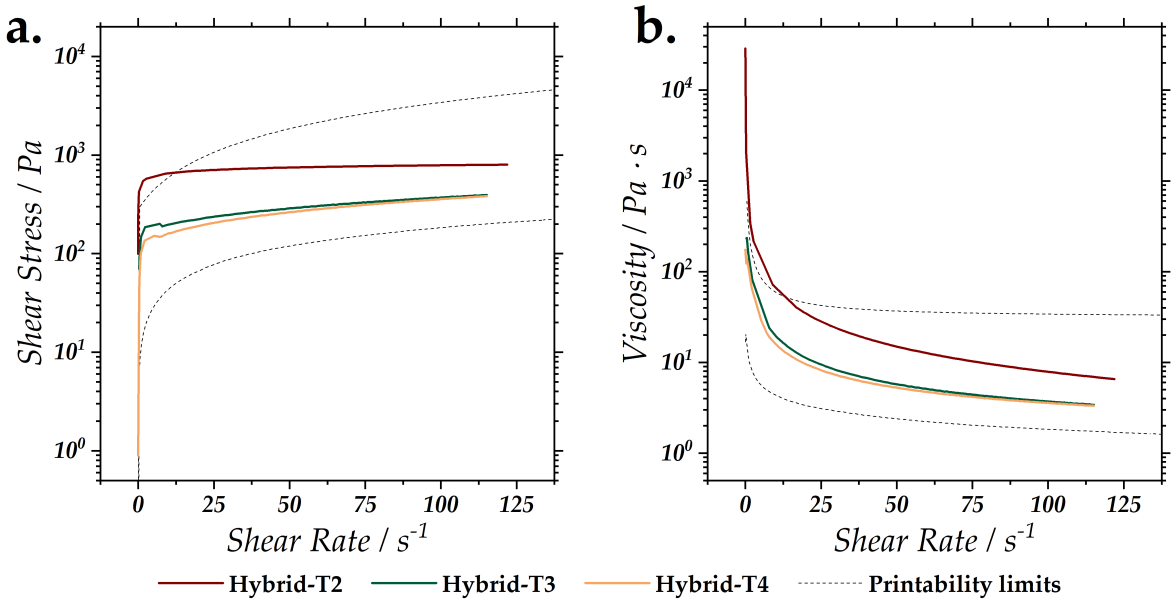


Figure 5.17: Rheological properties of the pastes *Hybrid-T2*, *Hybrid-T3*, *Hybrid-T4*: a) shear stress vs. shear rate and b) viscosity vs. shear rate.

the yield stress is registered at 600 Pa, 180 Pa and 140 Pa for the *Hybrid-T2*, *Hybrid-T3* and *Hybrid-T4*, respectively. The shift of the yield stress to lower values was necessary in order to get a printable paste, according to the criteria described in section 2.5.1, as the yield stress of the *Hybrid-T2* was still above the upper limit in printability (see Figure 5.17a). Beside the influence of the dispersant, it should also be taken into account that the *Hybrid-T2* contains higher particle and lower binder loadings, which are reason for of higher viscosity and yield stress of the final paste, as reported in Ref. [108].
A negligible difference in the rheology of the *Hybrid-T3* and *Hybrid-T4* was observed (see Figure 5.17). It should be mentioned that Stolz prepared pastes starting from ceramic powders, which present specific

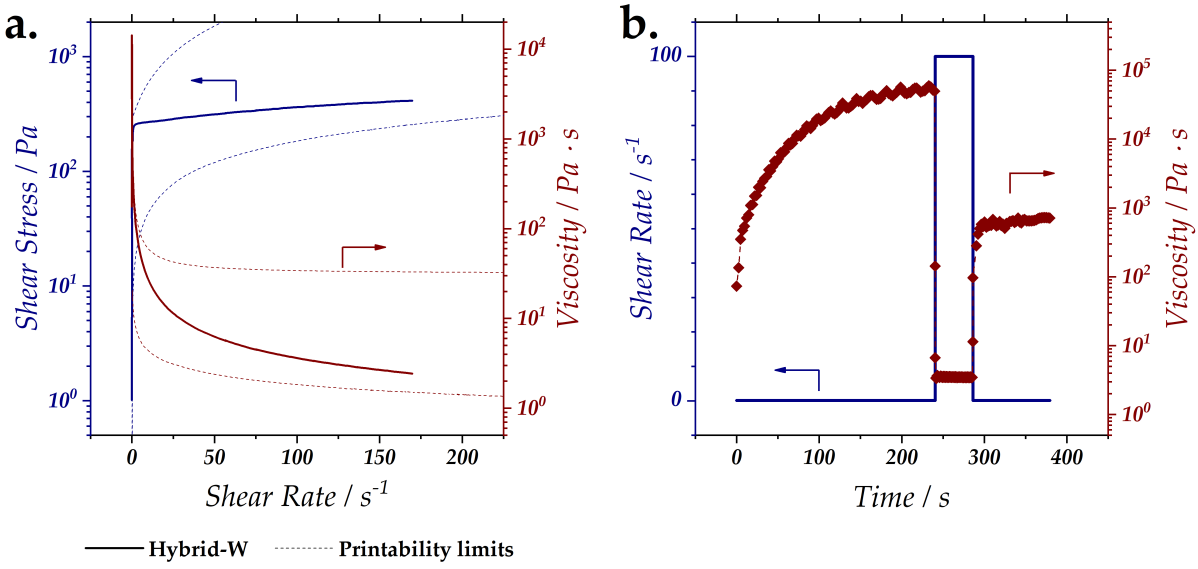


Figure 5.18: a) Rheological properties of the paste *Hybrid-W*: shear stress vs. shear rate and viscosity vs. shear rate. b) Thixotropy behaviour of the *Hybrid-W* paste.

surface area in the order of magnitude of 1 - 10 $m^2\ g^{-1}$ [106]. In the present work, the specific surface area of the starting material was higher, especially for the zeolite, the typical values are of the order of 10^2 $m^2\ g^{-1}$. This suggests that the preparation of the paste resp. the amount of its components can be generalized when the starting material has similar structural properties. This is in agreement with the study by Somalu et al., who reported that the viscosity of a paste is not depending only on the loading of both solvent and binder but also on the surface area of the powder to be printed [108]. Both the pastes *Hybrid-T3* and *Hybrid-T4* presented a viscosity below 10 Pa · s and higher than 150 Pa · s at the shear rates of 100 s^{-1} and 0.1 s^{-1}, respectively, namely they are printable pastes. For these reasons the paste *Hybrid-T3*, which is printable and contains a lower amount of dispersant and a higher particle loading, was further characterized and tested in the μ-CR for the STD reaction (see sections 5.7.2 - 5.8.1, respectively).

Because of the impossibility of using terpineol as solvent which turned out during the reaction test (see section 5.7), the synthesis of a further CZA#Z system was necessary, namely the *Hybrid-W*. The composition of this paste is reported in Table 4.3. As Figure 5.18a shows, the paste presents a yield stress at about 250 Pa, which is in the printable range, according to the criteria claimed in section 2.5.1. The viscosity of the paste was measured below 10 Pa · s at a shear rate of 100 s^{-1} and over 1000 Pa · s at a shear rate of 0.1 s^{-1}. The recovery in viscosity after the application of a shear rate of 100 s^{-1} up to about 1000 Pa · s should avoid the flow of the paste after the screen printing process within the micro-channels and a consequent proper levelling. In summary, according to the criteria proposed in this work, the paste *Hybrid-W* can be considered as printable.
The paste *Hybrid-W* was further characterized, coated in the micro-channels and tested for the STD reaction in the μ-CR.

5.6.2 Structured planar double layer catalyst system (CZA//Z)

The structured planar double layer catalyst system CZA//Z was prepared by repeating the coating and calcination steps, as described in section 4.4 first for the CZA-layer and second for the zeolitic one. The rheology of the two kinds of pastes is outlined in the following.

CZA layer

The composition of the three pastes based on the CZA catalyst is listed in Table 4.3: both the *CZA-1* and *CZA-3* contain the dispersant, while the *CZA-2* is a dispersant-free paste. Each of them lies in the printable range, according to the criteria of this work, as Figure 5.19 shows. The paste *CZA-2* was synthesized with the attempt of increasing the loading of the powder in the paste, in order to make the coating process more effective and to spare solvent material. Furthermore, in order to decrease the viscosity, the dispersant was added during the preparation of the paste *CZA-3*, aiming to lower the yield stress. Comparing the rheology of the three pastes and the relative compositions, once again, it can be concluded that addition of the dispersant lowers the yield stress of the fluid (from approximately 300 Pa to 100 Pa for the *CZA-2* and *CZA-3*, respectively) and that, at the same amount of dispersant, a higher particle loading results in a higher viscosity of the paste (see *CZA-1* and *CZA-3* in Figure 5.19b).

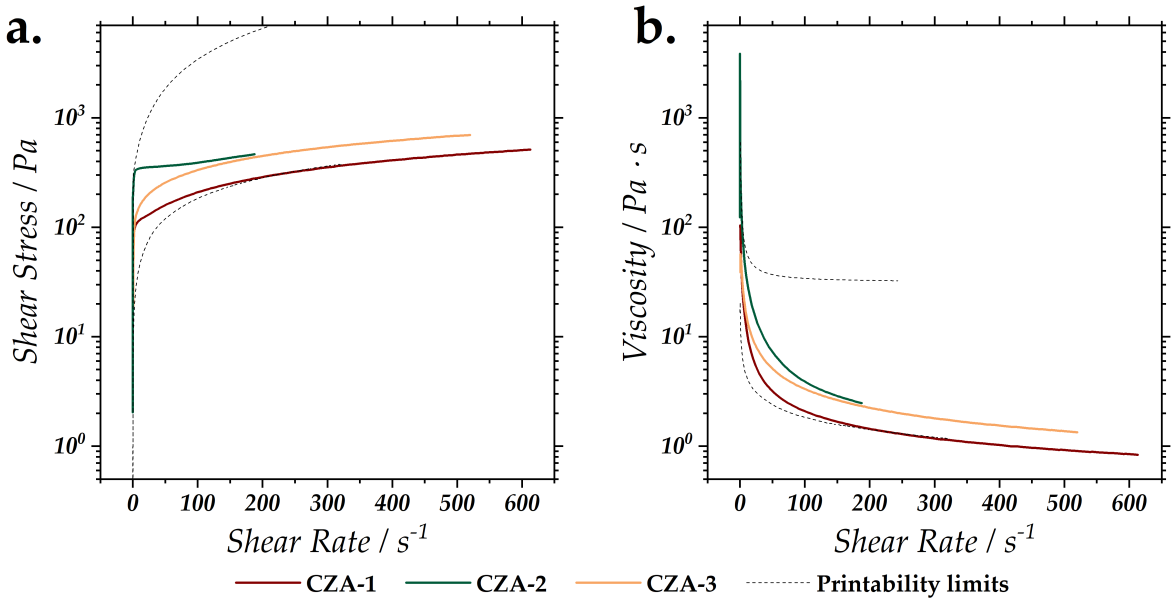


Figure 5.19: Rheological properties of the pastes *CZA-1*, *CZA-2* and *CZA-3*: a) shear stress vs. shear rate and b) viscosity vs. shear rate.

Because of the highest yield stress of the paste *CZA-2*, this was not further investigated regarding thixotropy, the results of which are shown in Figure 5.20 for the *CZA-1* and *CZA-3*: for both the pastes, the viscosity under a share rate of 0.1 s^{-1} lies in the range 10 - 100 Pa · s and was recovered completely after applying 100 s^{-1} shear rate, during which the viscosity was in the range of 1 - 10 Pa · s. This made the *CZA-1* and *CZA-3* pastes suitable for coating by hand. Further testing via screen printing should clarify whether the fluids are viscous enough to avoid undesired passage of the paste through the screen before squeegeeing and to obtain a proper levelling of the layer, as in literature higher viscosity at low shear rate is reported necessary for succesful printing [106, 110].

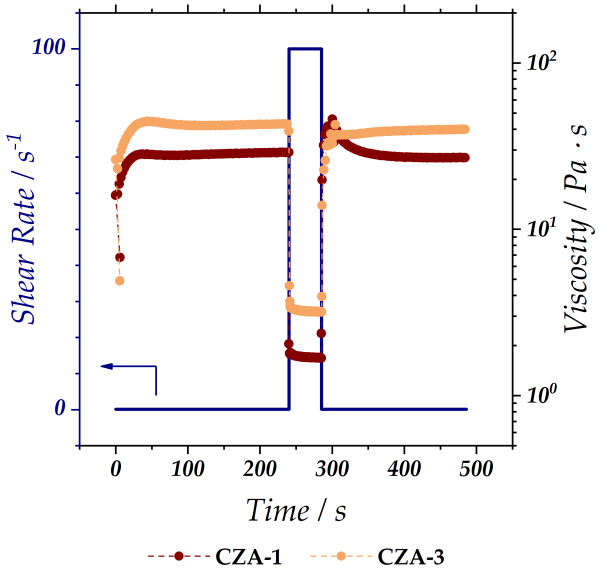


Figure 5.20: Thixotropic behaviour of the *CZA-1* and *CZA-3* pastes.

The pastes *CZA-1* and *CZA-3* were characterized, then either tested for the STM in the μ-CR (*CZA-1*) or used for preparation of the CZA//Z system (*CZA-3*), respectively.

H-ZSM-5 layer

As Table 4.3 shows, all the zeolite based pastes were synthesized using water as solvent, similar powder loading and increasing the amount of the binder, methyl cellulose. The powder loading was considerably lower compared to the other pastes, as the size of the powder used here was bigger than the zeolite prepared by CRT ($d_{[4,3]10}$, $d_{[4,3]50}$ and $d_{[4,3]90}$ of 8.1, 37.1 and 106.2 μm, respectively.).

As the flowing plots of the pastes *Zeolite-1*, *Zeolite-2* and *Zeolite-3* show (see Figure 5.21), by increasing the loading of methyl cellulose, it is possible to increase the viscosity and to approach the lower limit in printability accepted in this work. The presence of the yield stress is not as marked as in all the other pastes prepared, suggesting that this is to be linked with the presence of CZA in the paste. Moreover, changing the amount of the solvent allowed to have proper rheological behaviour of the fluids without adding a dispersant. A further increase of the amount of methyl cellulose in the paste hindered the formation of a homogeneous paste. This is the reason why no pastes were prepared with a binder loading higher than 4 wt.-%.

Figure 5.22 shows the thixotropic behaviour of the pastes *Zeolite-2* and *Zeolite-3*: in both cases, the original viscosity presented at low shear rate was recovered after applying the higher shear rate, simulating the screen printing process. In his work, Sun reported the thixotropy behaviour of a zeolitic hydrocracking catalyst (Pt-ZSM-5): after the application of a shear rate of 100 s^{-1}, within 50 s a viscosity in the same order of magnitude was recovered [114]. The success of the screen printing procedure should be therefore strengthened by Sun's result. Combining the rheological and thixotropic studies of the zeolite-based pastes, the *Zeolite-3* paste was used for coating the upper layer of the CZA//Z system.

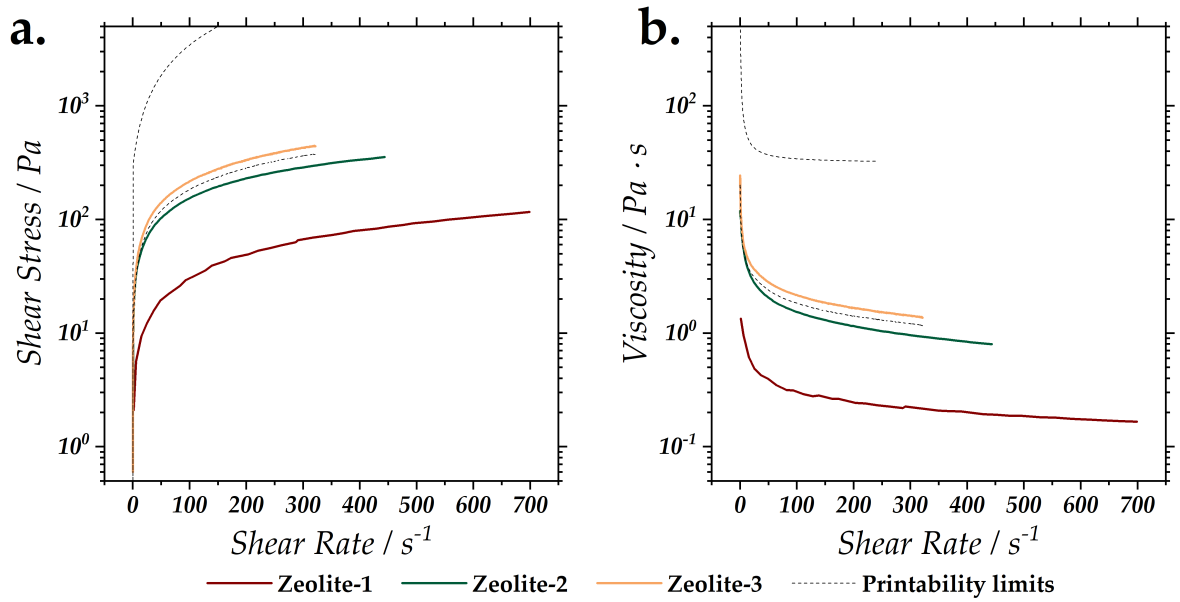


Figure 5.21: Rheological properties of the pastes *Zeolite-1*, *Zeolite-2* and *Zeolite-3*: a) shear stress vs. shear rate and b) viscosity vs. shear rate.

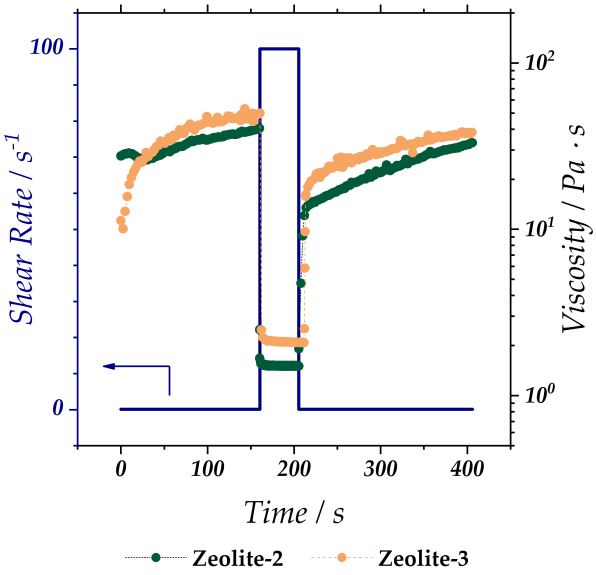


Figure 5.22: Thixotropic behaviour of the *Zeolite-2* and *Zeolite-3* pastes.

5.7 Planar catalyst configurations: structural characterization

Once suitable pastes for the coating procedure were prepared, according to the criteria accepted in this work, these were further characterized in the form of both suspension and layer. The influence of the calcination of the paste on the structural properties (specific surface area, reducibility, crystal structure) was investigated. The analysis of the layers was carried out by SE-micrographs, in order to prove the complete coverage of the micro-channel with the catalyst, the possible presence of cracks, both by EPMA/BSE and EPMA/WDX, in order to quantify the thickness of the layers and to check the metal distribution over its height. The calcination of the foils was object of study, in order to find the proper temperature for the removal of all the additives present in the paste without irreversibly affecting the catalyst. This aspect is outlined in section 5.7.1. Afterwords, further characterization of the coated systems is presented and discussed (sections 5.7.2 - 5.7.4).

5.7.1 Calcination of the coated foils

The calcination of the coated foils was necessary for removal of the solvent, the binder and the dispersant contained in the paste. Sun carried out the calcination at 500 °C, in literature temperatures up to 1900 °C are reported [83, 106, 108, 110, 111]. The temperature changes with the aim of the calcination step. This is only the removal of all the additives in case of catalysis but sintering of ceramic layered systems for preparation of rigid membranes and electrodes [106, 108, 110]. In the frame of this work, special attention had to be paid because of the known effects on the Cu-based systems at temperatures higher than 300 °C, which have already been discussed in section 5.2.4. For this reason, the pastes *Hybrid-T3* and *CZA-1* were subject to an investigation on the choice of a proper calcination temperature.

The evaporation temperature of terpineol and the autoignition point of ethyl cellulose are 219 °C and 370 °C [158], respectively, while the dispersant KD-1 is supposed to burn out well below 200 °C [159]. Therefore, a calcination temperature lower than 400 °C is not recommended. Thermal gravimetric analy-

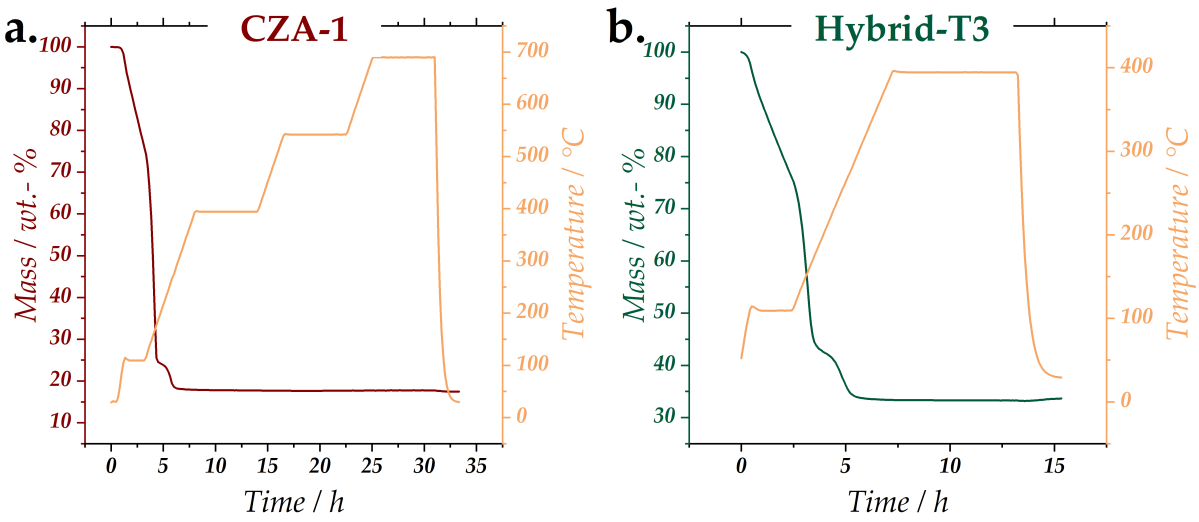


Figure 5.23: Mass loss with respect to the temperature during the TG-analysis of the a) *CZA-1* and b) *Hybrid-T3* pastes.

sis of the pastes *CZA-1* and *Hybrid-T3* up to 700 °C and 400 °C, respectively, were carried out, applying a heating rate of 2 K/min. For the sample *CZA-1*, temperatures of 400 °C, 540 °C and 690 °C were held for 6 h, in order to understand clearly the correlation between the loss in mass of the sample and the temperature. From the result, which is shown in Figure 5.23a, it can be concluded that the mass loss takes place up to 400 °C, at higher temperature the sample maintains a constant weight. The paste *Hybrid-T3* was investigated in the same way up to 400 °C: as Figure 5.23b shows, no further mass loss was detected above 300 °C. At the end of the TG-analysis, the remaining mass was of 17.5 and 33.7 wt.-% for the *CZA-1* and the *Hybrid-T3* pastes, respectively, which is in accordance with the original powder loading in the pastes of 17.9 and 29.1 wt.-%, respectively (see Table 4.3). The loss in mass is close to the values expected and no

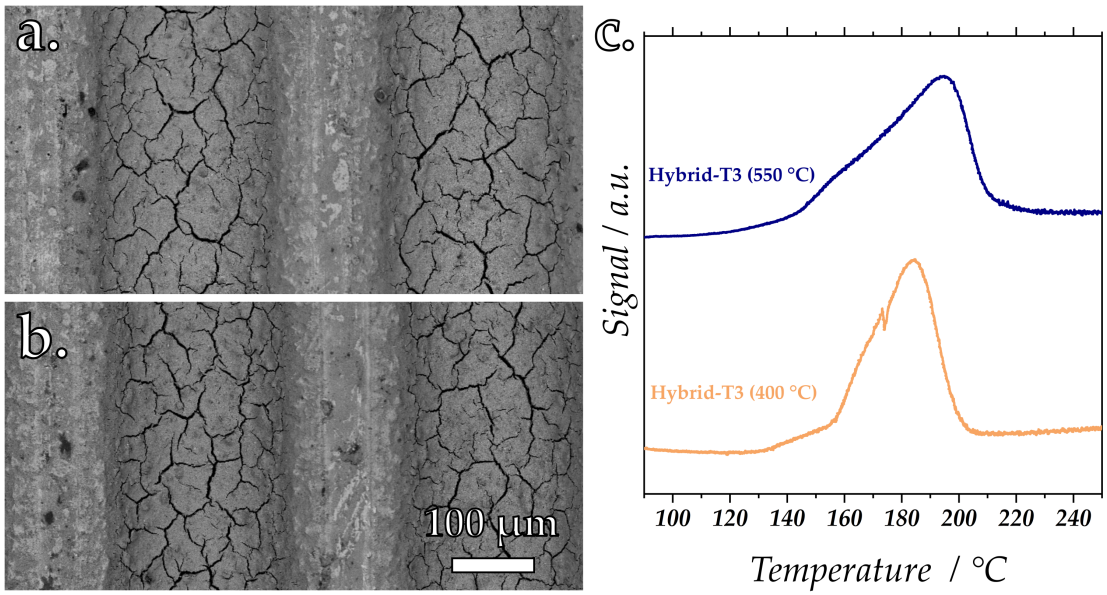


Figure 5.24: SE-micrograph of two coated micro-channels (*Hybrid-T3*) after calcination at a) 400 °C and b) 550 °C. c) TPR profiles of the *Hybrid-T3* paste after calcination.

further removal of additives present in the paste could occur at temperatures above 400 °C. Even if the analysis was applied only to terpineol-based pastes, the same calcination temperature was also applied to the water-based ones, as the solvent has a much lower boiling point (100 °C). In the open literature it is reported that a sudden exposure of the coated layers to high temperatures could damage the layer itself [83]. For this reason, SE-micrographs of the micro-channels coated with the *Hybrid-T3* paste after calcination at 400 °C and 550 °C were obtained for comparison and are shown in Figure 5.24a-b. Both layers, regardless of the calcination temperature, present some cracks. Figure 5.24c represents the TPR-profiles of the powder obtained after calcining the paste *Hybrid-T3* at 400 °C and 550 °C. The increase of the calcination temperature lets the peak of reduction shift from 185 °C to 195 °C, which is in agreement with the values reported in section 5.2.4.
In conclusion, in order to ensure complete removal of all the additives present in the paste and to reduce the effect on the CZA catalytic performance, the calcination temperature of the coated foils was fixed at 400 °C for all systems.

5.7.2 Hybrid planar catalyst of medium proximity (CZA#Z)

In this section, the characterization of the hybrid planar configuration of medium proximity CZA#Z with respect to the catalyst systems obtained from the *Hybrid-T3* and *Hybrid-W* pastes is presented and discussed.
The calcined *Hybrid-T3* paste ($\omega_{CZA}/\omega_{Zeo} = 1$) resulted in a specific surface area of 150 $m^2\ g^{-1}$. The value deviates from the average of the two starting catalysts, namely the H-ZSM-5 ($a_{BET} = 346\ m^2\ g^{-1}$) and the FSP-CZA ($a_{BET} = 84\ m^2\ g^{-1}$), but the deviation decreases if compared to the CZA-1-f_c ($a_{BET} = 16\ m^2\ g^{-1}$).
Figure 5.25 shows the XRD patterns of the *Hybrid-T3* paste after calcination as well as of the nanosized zeolite and of the CZA-1-f_c for comparison. The presence of both the MFI and the CZA structures are ensured by comparing the pattern of the sample to the references. In general, the considerations laid out in section 5.2.4 about the influence of the calcination on the crystalline structure of CZA can be accepted

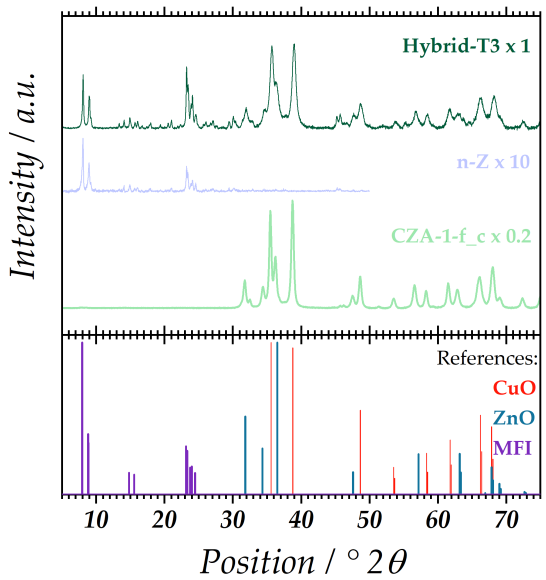


Figure 5.25: XRD patterns of the calcined *Hybrid-T3* paste, the nano-zeolite (n-Z), the CZA-1-f_c (with adjusted intensities) and the reference data for the CuO, ZnO and MFI-structures International Center for Diffraction Data (ICDD).

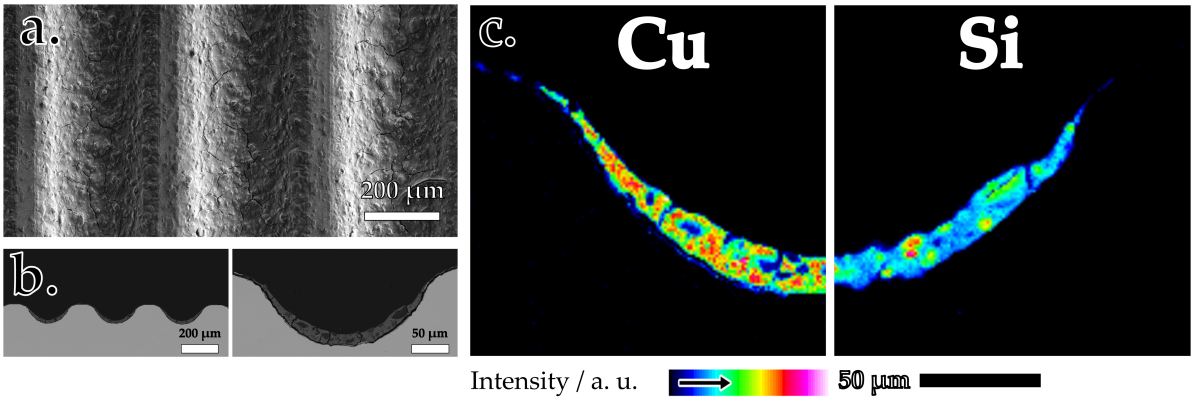


Figure 5.26: a) SE-micrographs, b) cross-sectional analysis of the layer via EPMA/BSE and c) elemental map via EPMA/WDX for Cu and Si of the CZA#Z obtained from the paste *Hybrid-T3*.

also in this case. Based on the CuO[111] reflection at 2Θ = 38.8°, CuO crystallite size in the *CZA-1* material was determined by using the Scherrer equation to be 13 nm (see Figure 5.25).

Each foil was coated, on average, with 0.039 g of hybrid catalyst, and no measurable loss in weight was detected before and after letting them drop from a height of 2 m: the adhesion between catalyst and substrate was ensured. Figure 5.26 shows the results concerning the structure of the layer and provides information about its surface (Figure 5.26a), its thickness (Figure 5.26b), and the elemental distribution of Cu and Si (Figure 5.26c), the signals of which are correlated to the presence of the CZA and H-ZSM-5, respectively. As already discussed in section 5.7.1, some cracks at the surface of the layer were detected: this fact is confirmed by the cross-sectional pictures (Figure 5.26b). Due to the coating method, the catalyst is also detected among the micro-channels, where the gas is not supposed to flow and the reaction cannot take place: this is unavoidable when the foils are coated by hand, but this challenge can be overcome by automated screen printing. However, the thickness in different micro-channels is comparable, and this is crucial for assuming that each micro-channel is containing the same amount of catalyst, namely the reaction rate is the same in each micro-channel. Moreover, a homogeneous distribution of the catalyst along the foils and within each micro-channel allows to assume that the µ-CR behaves as a system of parallel plug-flow-reactors with as many reactors as there are micro-channels on the foils. From Figure 5.26b it is possible to estimate the layer thickness of the CZA#Z system, which is

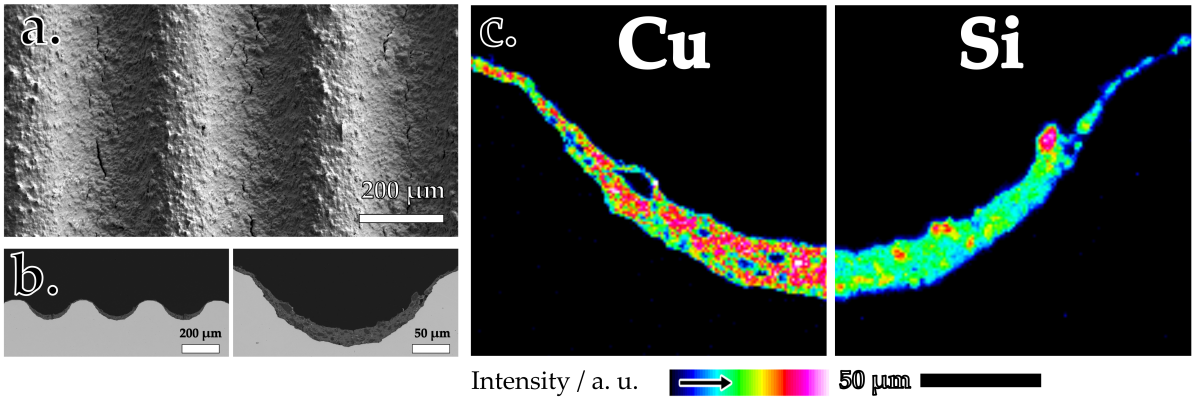


Figure 5.27: a) SE-micrographs, b) cross-sectional analysis of the layer via EPMA/BSE and c) elemental map via EPMA/WDX for Cu and Si of the CZA#Z obtained from the paste *Hybrid-W*.

approximatively 16 µm. The elemental distribution of Cu and Si confirms the homogeneity of the two catalysts within the layer and, therefore, the success in the synthesis of the CZA#Z system starting from the *Hybrid-T3* paste.

The CZA#Z system was also prepared starting from the water-based paste *Hybrid-W*. Each foil was coated, on average, with 0.04 g, which is in agreement with the amount obtained by the *Hybrid-T3*. The coating results with respect to the surface, the cross-section as well as the elemental distribution of Cu and Si are presented in Figure 5.27.
Analysing the SE-micrograph of the surface (Figure 5.27a) as well as the cross-sectional images (Figure 5.27b), it can be observed that, unlike the layer obtained by the *Hybrid-T3* paste (see Figure 5.26), here the surface is almost crack-free and a higher amount of catalyst is present between the micro-channels. Moreover, a thicker (21 µm) and rougher (estimated by observing the SE-micrographs at the surface and the cross section) layer was prepared starting from the *Hybrid-W* paste. This fact may be ascribed to the larger size of the commercial zeolite ($d_{[4,3]50}$ = 37.1 µm) compared to the powder synthesized at CRT ($d_{[4,3]50}$ = 21 µm); the *Hybrid-W* contains bigger particles than the mean layer thickness, resulting in a rougher CZA#Z layer. Finally, the elemental distribution confirms the homogeneity of the layer in the CZA and the H-ZSM-5 catalysts (Figure 5.27c).

In summary, both the *Hybrid-T3* and the *Hybrid-W* pastes were successfully used for preparation of the CZA#Z layered catalytic system. The fulfilment of the coating was proved and a dependence of both thickness and roughness of the final layers on the zeolite crystallite size in the starting material used was found.

5.7.3 CZA planar catalyst system

Two different CZA-based pastes were used for coating: the *CZA-1*, used for testing the STM only reaction, and the *CZA-3*, used for preparation of the CZA//Z system. The physico-chemical properties of the calcined *CZA-1*, which were compared to the pristine CZA-1-f material (see section 5.2) and the morphology of the final layer obtained from the *CZA-3*, are shown here.

The calcined *CZA-1* paste has a specific surface area of 17 $m^2\ g^{-1}$, which is in agreement with the respective value of the CZA-1-f_c (see section 5.2.4). The influence of the calcination treatment on the CZA catalytic system has already been discussed in section 5.2.4. The calcination step applied during the preparation of the layer was necessary in order to remove completely the solvent, the binder and the dispersant. Therefore, the effect of this synthesis step on the CZA structure is supposed to take place during this procedure, even if the coated foils were calcined at a lower temperature (400 °C) compared to the calcination temperature of 550 °C applied during the core@shell catalyst synthesis (section 5.2.4). The crystal structure as well as the reducibility of the *CZA-1* were evaluated by XRD and TPR analysis, respectively, and the results are shown in Figure 5.28. As mentioned for the CZA#Z, also in this case no change in the crystallinity of the CZA when applied as a layer could be detected by observing the XRD pattern and comparing it with the result obtained for the CZA-1-f_c. Based on the CuO[111] reflection at $2\Theta = 38.8°$, the CuO crystallite size in the *CZA-1* material was determined by using the Scherrer equation to be 15.8 nm (see Figure 5.28a). This value is in agreement with the crystallite size in the *Hybrid-T3*

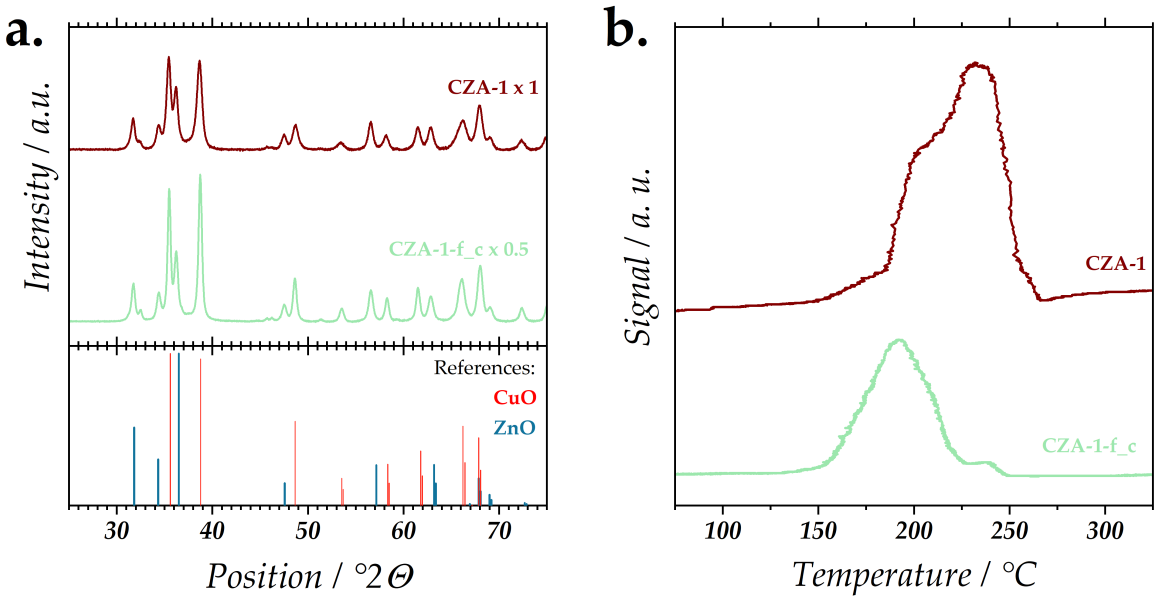


Figure 5.28: *CZA-1* paste characterization in comparison with the CZA-1-f_c: a) XRD patterns (with adjusted intensities) and the reference data for the CuO and ZnO; b) TPR profiles.

sample (see section 5.7.2). However, some discrepancy in the reducibility of the calcined *CZA-1* paste in comparison to the CZA-1-f_c and the calcined *Hybrid-T3* paste were detected. As Figure 5.28b shows, the reduction of the calcined *CZA-1* paste starts at about 150 °C, is completed at 275 °C and presents a peak at 230 °C with a shoulder at 200 °C. Reduction peaks for the CZA-1-f_c and the *Hybrid-T3* paste were detected at 190 °C and 185 °C, respectively. The order of appearance of the shoulder and the main reduction peak is inverted for the calcined *CZA-1* paste and the CZA-1-f_c: for the former, the shoulder is followed by the reduction peak, for the latter the opposite is occurring. In the open literature, different reasons for the presence of a shoulder with respect to the main reduction peak for Cu-based catalyst are reported, as already discussed in section 5.4. Further studies about the dispersion of the Cu in the *CZA-1* sample are necessary to investigate in detail the reason of the shift of the reduction peak to higher temperature.

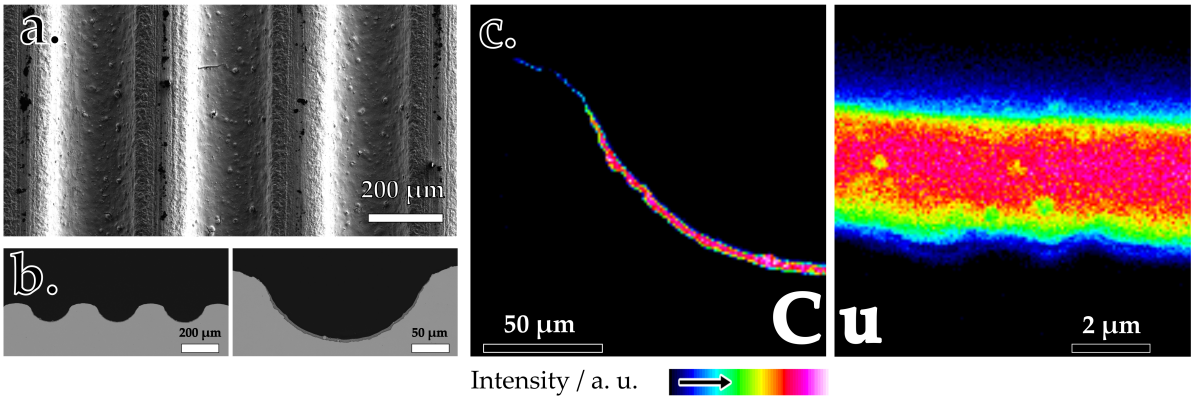


Figure 5.29: a) SE-micrographs, b) cross-sectional analysis of the layer via EPMA/BSE and c) elemental map via EPMA/WDX for Cu of the CZA layer obtained from the paste *CZA-3*.

Due to the similarity of the two CZA layers obtained, only the SE-micrographs (EPMA/BSE and EPMA/WDX) for the coating prepared from the *CZA-3* are shown in Figure 5.29. From their analysis, the presence of a homogeneous and crack-free layer is confirmed (Figure 5.29a-b); moreover, a uniform distribution of Cu in the final film was reached (Figure 5.29c). By coating the *CZA-1* and *CZA-3* pastes each coated foil contained, on average, 0.013 g and 0.017 g of powder, respectively; this corresponds to a much lower amount compared to the hybrid layered systems described in section 5.7.2 and to a much thinner resulting layer (the thickness of the *CZA-3* layer was estimated to be 3.5 µm). As observed for the hybrid CZA#Z system, also in this case, the particle size of the starting material rather than the powder loading in the paste determined the thickness of the layer ($d_{[4,3]50}$ of the CZA-1-f nanopowder is equal to 4.7 µm).
Over the CZA-layer, the zeolitic one was prepared . The characterization of which is presented in the next section.

5.7.4 Structured planar double layer catalyst system (CZA//Z)

The zeolitic layer atop the CZA layer for the CZA//Z system was prepared using a water-based paste (*Zeolite-3*). The SE-micrograph is shown in Figure 5.30. The surface of the layer is quite irregular, as shown in Figure 5.30a and confirmed by the cross sectional analysis (Figure 5.30b). As for the preparation of the *Hybrid-W* paste, the commercial zeolite was used as starting material. The strong roughness of the layer makes it challenging to estimate its thickness, which was approximately 22 µm. During the coating of the *Hybrid-W* paste, the CZA, smaller in size, could level the hybrid layer decreasing the final roughness of the CZA#Z catalyst. In the case of CZA//Z, the paste contained only the zeolite, which has a larger $d_{[4,3]50}$ compared to the layer thickness is hardly feasible for hand-coating. As a consequence of the absence of the CZA, the zeolite crystals are randomly oriented along the channel and the voids cannot be filled with CZA nanoparticles. This challenge could be overtaken by automated screen printing instead of hand coating, as the repetition of the screen printing procedure increases the layer thickness; in this way the levelling of the layer would occur more uniformly.

In summary, the CZA#Z, the pure CZA, and the CZA//Z planar catalyst configurations were successfully prepared and characterized with respect to the structure of the layer itself (homogeneity, presence

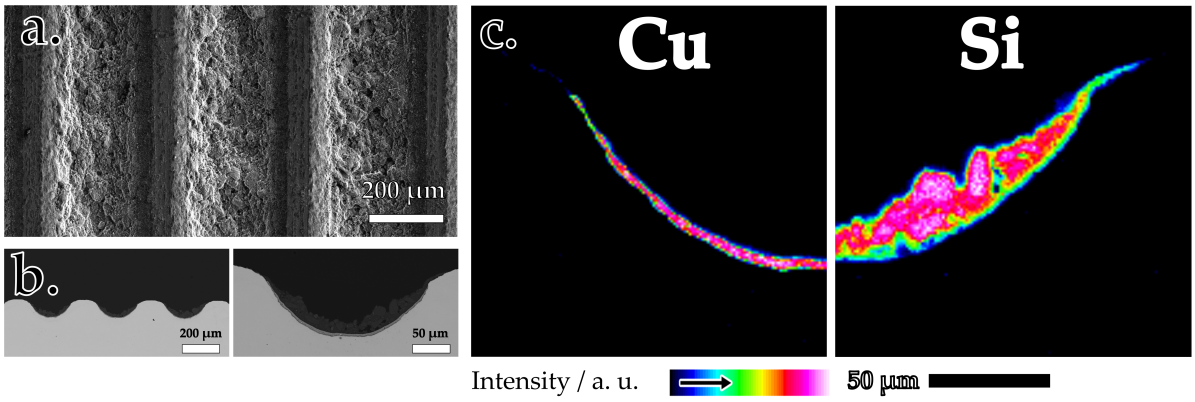


Figure 5.30: a) SE-micrographs, b) cross-sectional analysis of the layer via EPMA/BSE and c) elemental map via EPMA/WDX for Cu and Si of the CZA//Z system.

Table 5.4: $d_{[4,3]50}$ of the powders used for the synthesis of the three coated systems and the correspondent layer thickness obtained.

Paste	$d_{[4,3]50}$ / μm	*Thickness* / μm
CZA-3	4.7	3.5
Zeolite-3	37.1	22
Hybrid-W	4.7 // 37.1	21

of cracks, layer thickness and elemental distribution), and the possible effects of the calcination on the final catalyst were investigated.
The calcination up to 400 °C affects the CZA in terms of a decrease of the specific surface area and a shift to higher reduction temperature, in agreement with the results presented in section 5.2.4. The homogeneity of the surface of the layer as well as the roughness are to be associated with the size of the powder to be coated. However, layers with homogeneous catalyst distribution were successfully prepared. A correlation between the size of the starting material and the roughness of the final layer was found. The CZA nanopowder, the zeolite H-ZSM-5 prepared at CRT, and the commercial H-ZSM-5 have a $d_{[4,3]50}$ of 4.7, 21 and 37.1 µ, respectively. Table 5.4 summarizes the $d_{[4,3]50}$ of the *CZA-3*, *Zeolite-3* and the *Hybrid-W* and the thickness of the corresponding layers obtained, which appears to be in the same order of magnitude as the $d_{[4,3]50}$ of the starting material. When the catalyst powder is larger in size, the resulting layer show higher roughness. Mixing the CZA and the H-ZSM-5 (during the preparation of the *Hybrid-W* paste), the uniformity of the layer thickness improves, because the particles smaller in size, namely CZA nanopowder, are able to act as levelling agents, which is missing during the coating of the zeolitic layer in the CZA//Z.

5.8 Planar catalyst configurations: reaction tests

The sole CZA layer, the hybrid planar system of medium proximity CZA#Z and the structured double layer system CZA//Z were tested in the µ-CR, as described in section 5.1. In the following the results are displayed and discussed.

5.8.1 Hybrid planar catalyst of medium proximity (CZA#Z)

The µ-CR was filled with 30 foils coated with the *Hybrid-T3* system in order to get a total CZA#Z catalyst loading of 1.17 g. The measurement was carried out under a $(F/W)^*$ of 9700 $mL_{Reagents}\ h^{-1}\ mg_{CAT}^{-1}$; p = 45 bar; 220 °C $\leq T \leq$ 290 °C. An unexpected activity behaviour was detected: no conversion was measured up to 240 °C; in the temperature range of 260 - 280 °C, $X_{CO} < 1$ % was registered and only MeOH (no DME) was produced. In order to investigate the reasons for the low activity, the calcined *Hybrid-T3* paste was pressed into pellets, crushed, and sieved into the fraction 50 - 100 µm and tested in the µ-Berty reactor. The same conditions as used for the measurement of the CZA+Z_1 sample (see section 5.5.1) were applied for comparison, and the results are shown in Figure 5.31. In comparison with the CZA+Z_1 catalyst system, a lower X_{CO} was detected (at T = 280 °C, $X_{CO,Hybrid-T3}$ = 11.9 % and $X_{CO,CZA+Z_1}$ = 26.4 %), but the strongest discrepancy was found in the product distribution: while on the CZA+Z_1 catalyst the STM equilibrium was shifted and almost all the MeOH produced was further

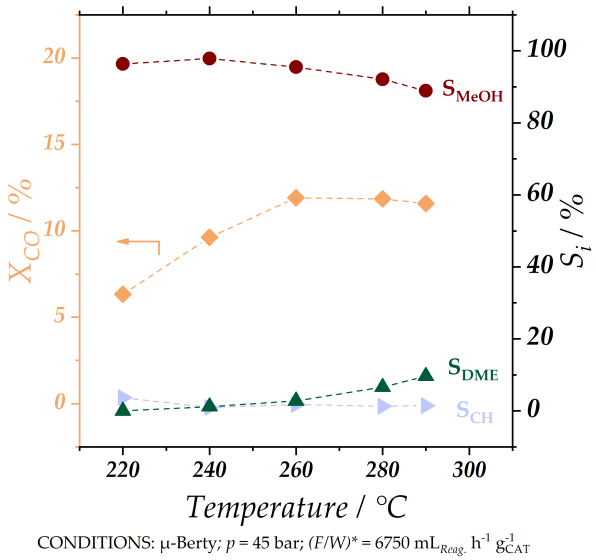


Figure 5.31: Activity of the *Hybrid-T3* pelletized catalyst in terms of X_{CO} and S_i for the STD reaction in the μ-Berty reactor as function of the temperature (at T = 220 °C: $X_{CO}^{eq.,out}$ = 57.5 %; at T = 290 °C: $X_{CO}^{eq.,out}$ = 13.6 %).

dehydrated to DME, the pelletized *Hybrid-T3* catalyst revealed only slight activity of the zeolite. DME was detected from the temperature of 240 °C (S_{DME} = 1.2 %) onwards and, increasing the temperature up to 290 °C, S_{DME} reached 9.7 %. At the same time, S_{MeOH} was in the range 88.9 - 97.9 % and, in general, decreased with increasing temperature. Hydrocarbons up to C_3 were detected, and their selectivity (S_{HC}) reached 3.7 % at T = 220 °C and below 2 % at higher temperatures. X_{CO} is only slightly changing in the temperature range 260 °C $\leq T \leq$ 290 °C, which is due to the fact that $X_{CO}^{eq.,out}$ is close to the measured X_{CO} (see caption of Figure 5.31). In general, a lower activity of the CZA due to the calcination of the foils is expected (see section 5.2.4), which should make the CZA only catalyst layer comparable in activity with the P-CZA_c. The lower X_{CO} performance of the *Hybrid-T3* catalyst in particle form compared to the P-CZA_c (see Figures 5.31 and 5.16, respectively) has to be ascribed to the different composition of the catalysts (ω_{CZA} = 50 wt.-% and ω_{CZA} = 100 wt.-% for the *Hybrid-T3* and the P-CZA_c, respectively), which means that the $(F/W)^*$ for the CZA only catalyst was twice as big during the STD reaction over the *Hybrid-T3* pelletized catalyst.

For better understanding of possible effects of the paste preparation procedure on the zeolitic material, a suspension of the commercial H-ZSM-5 and terpineol was prepared. After few hours, the suspension became orange, after one day the colour was even stronger (see Figure A.12). The same result was detected for the zeolite prepared by CRT (not shown). As shown in section 5.7.2, no change in the crystal structure could be observed comparing the XRD patterns in the reflection range of the MFI (2Θ = 5° - 35°) of the pristine hydrothermally synthesized zeolite and the calcined paste *Hybrid-T3*. Further research in the open literature was therefore necessary: the synthesis of 1,8-cineole and 1,4-cineole by isomerization of the α-terpineol apparently takes place on Brönsted acids at 25 - 60 °C [160, 161, 162]. Observing the scheme of the reaction (see Figure A.13), it can be concluded that the protons in the H-ZSM-5 structure take part in this reaction with the consequent loss in acidity resp. activity for MeOH dehydration. Therefore, the degradation of the acid catalyst explains its scarce activity as well as the difference between the performance of the CZA+Z_1 and the *Hybrid-T3* catalyst as particles in the μ-Berty reactor. Because of the inactivity of the zeolite, the *Hybrid-T3* catalyst was not able to shift the thermodynamic equilibrium

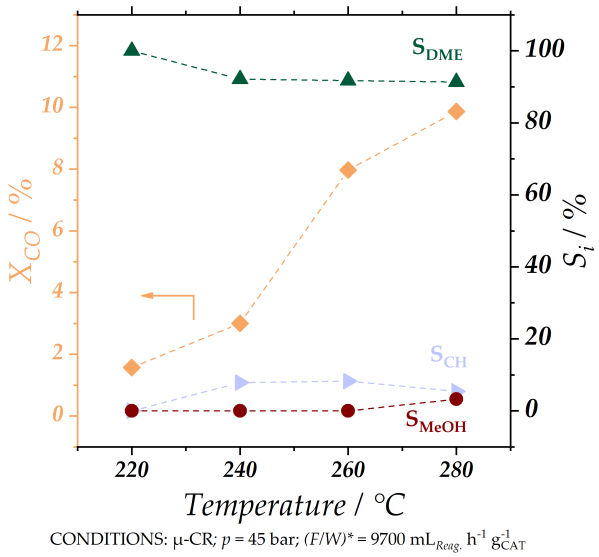


Figure 5.32: Activity of the CZA#Z catalyst system from *Hybrid-W* paste in terms of X_{CO} and S_i in the STD reaction in the μ-CR.

and to increase X_{CO} via the MTD reaction. This caused the gas composition to remain limited by the STM equilibrium, namely MeOH was the major product.

Because of the reaction between the zeolite and the terpineol, a further water-based paste was prepared (see section 5.6.1). 30 foils coated with the *Hybrid-W* catalyst were inserted into the μ-CR, in order to reach a total CZA#Z catalyst loading of 1.2 g. The measurement was carried out at the same conditions as those used for the *Hybrid-T3* CZA#Z system ($(F/W)^* = 9700\,\mathrm{mL_{Reagents}\,h^{-1}\,mg_{CAT}^{-1}}$; $p = 45\,\mathrm{bar}$; $220\,^\circ\mathrm{C} \leq T \leq 280\,^\circ\mathrm{C}$). The results of the measurement concerning X_{CO} and the product selectivity S_i are shown in Figure 5.32. Unlike the previous case, here the desired trend in the product distribution was observed: DME was the major product ($S_{DME} > 90$ % at each temperature investigated), with a low detection of by-products. MeOH was observed only at T = 280 °C ($S_{MeOH,280\,^\circ\mathrm{C}} = 3.2$ %), while hydrocarbons (mostly C_4 - C_6) were already detected at 240 °C ($S_{HC,240\,^\circ\mathrm{C}} = 7.9$ %). X_{CO} lies in the range of 1 - 10 %. In the frame of this work, it was not possible to operate at lower $(F/W)^*$. The coating via screen printing permits the preparation of thicker layers with a consequently higher amount of catalyst on each foil, namely the reaction would take place at lower *(F/W)**. This is crucial in order to let the X_{CO} increase during the STD process, as well as to approach the optimal (F/W) of $2000\,\mathrm{mL\,h^{-1}\,mg_{CAT}^{-1}}$ (corresponding to *(F/W)** of $1800\,\mathrm{mL\,h^{-1}\,mg_{CAT}^{-1}}$), according to the modelling results (see chapter 3).

5.8.2 CZA planar system

The activity of the sole CZA coated system was measured over a *(F/W)** of $6330\,\mathrm{mL_{Reagents}\,h^{-1}\,mg_{CAT}^{-1}}$, (CZA loading in the reactor of 0.83 g); $p = 45\,\mathrm{bar}$; $220\,^\circ\mathrm{C} \leq T \leq 280\,^\circ\mathrm{C}$. The result concerning X_{CO} is shown in Figure 5.33. The values of X_{CO} reached were higher compared to the CZA#Z system (*Hybrid-W*, see section 5.8.1) and, at the same time, lower than for the CZA//Z system (see section 5.8.3). The strong dependence of X_{CO} on the temperature suggests that the system is not limited by the thermodynamic equilibrium. The CZA coated system is active for the STM process, even if the catalyst is supposed to be negatively affected by the calcination step (see section 5.2.4). Terpineol is confirmed as a proper

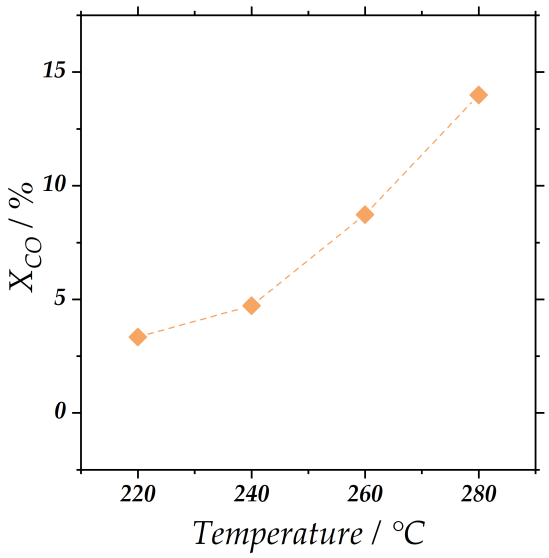


Figure 5.33: Activity of the *CZA-1* catalyst system in terms of X_{CO} in the STM reaction in the μ-CR.

solvent for the preparation of the CZA-based pastes, as the catalyst is still active after the coating procedure. Confirming the activity of the pure CZA-layer was helpful for a better interpretation of the STD performance of the CZA//Z system, which will be presented in section 5.8.3.

5.8.3 Structured planar double layer catalyst (CZA//Z)

The activity test of the CZA//Z system was operated at $(F/W)^* = 9700\,\mathrm{mL_{Reagents}\ h^{-1}\ mg^{-1}_{CAT}}$; $p = 45\,\mathrm{bar}$; $220\,^{\circ}\mathrm{C} \leq T \leq 280\,^{\circ}\mathrm{C}$, which are the same conditions as those used for the activity tests on the CZA#Z system. It is noteworthy to remark that different values of ω_{Zeo} were applied in the two catalyst configurations, namely 50 wt.-% for the CZA#Z and 60 wt.-% for the CZA//Z. As shown in chapter 3, these catalyst compositions are close to the values of ω_{Zeo} able to maximize X_{CO} in the respective configurations. The results concerning X_{CO} and S_i of the double layered system are shown in Figure 5.34. The CZA//Z system showed higher X_{CO} compared to the CZA#Z at each temperature measured, and DME was the major product ($S_{DME} \geq 73$ % at each temperature measured); at the same time, the intermediate and the hydrocarbons were also detected. MeOH was present in the outlet gas starting from 240 °C, and its selectivity remained under 4 %; the selectivity towards hydrocarbons (C_3 - C_6) was in the range of 9 - 23 %. The higher X_{CO} reached with this catalyst compared to CZA#Z leads to an increase of the formation of MeOH and of the side-products.

In section 2.3.3 the co-production of hydrocarbons during the STD reaction reported in the open literature has been summarized. In this work, a significant amount of hydrocarbons during the STD reaction was detected on the coated systems, especially on the CZA//Z system (S_{HC} up to 22.9 %), while on the CZA#Z system a maximal S_{HC} of 8.3 % was registered. At the same time, the lowest S_{HC} was detected on the CZA+Z catalytic system. The distribution of the hydrocarbons produced on the CZA+Z_1 (in the μ-Berty reactor) as well as the CZA#Z and CZA//Z (in the μ-CR) systems at $T = 280\,^{\circ}\mathrm{C}$ and the respective X_{CO} reached by the catalysts are summarized in Table 5.5. In general, longer hydrocarbons

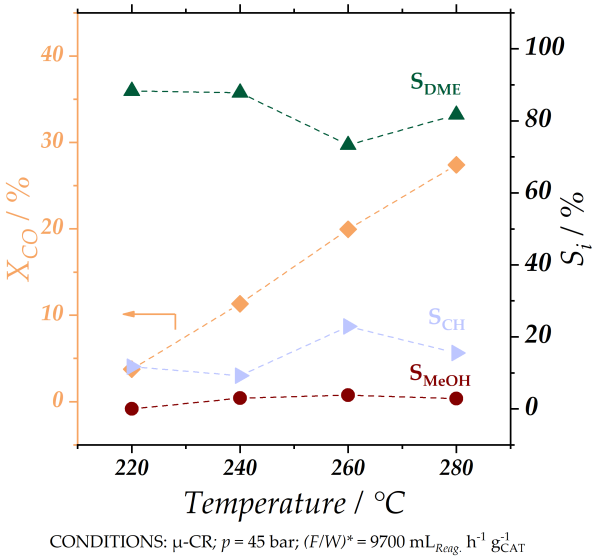


Figure 5.34: Activity of the CZA//Z catalyst system in terms of X_{CO} and S_i in the STD reaction in the μ-CR.

were produced by the coated systems and, increasing the S_{HC}, the length of the hydrocarbons produced is getting longer, which suggests that the hydrocarbons are growing on the catalyst by reacting jointly. As Table 5.5 presents, an analysis of the results of the present work confirms that, in general, the coated structures (both CZA#Z and CZA//Z) favour the formation of hydrocarbons compared to the particulate catalyst. The CZA+Z_1 and the CZA//Z catalysts, in the μ-Berty and the μ-CR, respectively, obtained at T = 280 °C, a conversion of $X_{CO,CZA+Z_1}$ = 26.4 % and a conversion of $X_{CO,CZA//Z}$ = 27.4 %, respectively, but selectivities of $S_{HC,CZA+Z_1}$ = 1.5 % and $S_{HC,CZA//Z}$ = 15.5 % were detected.

Table 5.5: X_{CO} and selectivity towards hydrocarbons (in %) of the CZA#Z, CZA//Z and CZA+_1 systems.

Catalyst System	X_{CO}	S_{CH_4}	S_{C_2}	S_{C_3}	S_{C_4}	S_{C_5}	S_{C_6}
CZA#Z	9.8	0	0	0	3.1	0.7	1.6
CZA//Z	27.4	0	0	11.5	1.9	0.7	1.3
CZA+Z_1	26.4	0.9	0.2	0.2	0.2	0	0

Conditions: p = 45 bar; T = 280 °C

The CZA//Z system prepared and tested here is comparable to a similar one synthesized in the work of Lee, where the CZA//Z configuration was prepared via inkjet printing of the FSP-CZA and hydrothermally synthesizing H-ZSM-5. The coating procedure dealt with the formulation of the ink, comparable to the paste preparation for the screen printing, and the final calcination of the foil at T = 550 °C. A previous ball-milling of both catalysts was necessary to get a succesful ink, even if it changed the crystal structure of the catalysts [100], which was not the case for the triple roll milling carried out in this work. The resulting layers in the work of Lee had a thickness in the range of 1 - 10 μm [100]. The activity tests of the inkjet printed CZA//Z system were operated in the μ-CR at similar conditions (p = 40 bar; T = 200 - 290 °C; $(F/W)^*$ = 2000 - 18 000 mL$_{Reagents}$ h^{-1} mg$_{CAT}^{-1}$; gas composition H_2 : CO : CO_2 equal to 16 : 8 : 1, with 10 vol.-% of N_2), but a different product distribution was observed: regardless of the conditions, the major products were the hydrocarbons, while MeOH and DME were subordinate byproducts.

Moreover, comparing the results in the two works at similar *(F/W)**, pressure and temperature, in the present work the CZA//Z reached a $X_{CO,260\,°C}$ = 19.9 %, while in the work of Lee $X_{CO,260\,°C}$ was limited approximatively 5 %. The discrepancy in the activity could be due to the change in the crystal structure taking place during the ink preparation [100]. Therefore, the synthesis of the paste as carried out in the frame of this work is more suitable for the coating of micro-channels, as this procedure maintains the original activity of the catalysts.

5.9 Kinetic study of the STM reaction

It is well known that the mechanism and the reaction rate of the STM reaction is strongly depending on the features of the catalyst itself, such as the Cu-surface area and the proximity between the Cu and ZnO nanoparticles [28]. Many kinetic studies reported in literature are based on commercial catalysts, even if the composition and physico-chemical properties thereof are often not well known and therefore hard to reproduce experimentally [26, 27, 30]. For this reason, it was important to get the kinetics of the catalysts actually used in the synthesis and preparation in the frame of this work. The STM kinetics was obtained started from the study of Seidel et al. (see chapter 2 and Ref. [30]). According to this work, Equations 5.4 - 5.7 describe the reaction rates of the CO-hydrogenation, CO_2-hydrogenation and r-WGS, respectively. In these Equations, A and B are either β_1 and β_2, or β_3 and β_4, or β_5 and β_6 for k_1, k_2 and k_3, respectively, p_i is the partial pressure of the component i, K_{Pj} is the equilibrium constant of the reaction j, $\Theta^{\odot}$, Θ^{*} and $\Theta^{\otimes}$ are the surface coverage relative to the active sites for the CO- and the CO_2-hydrogenation and the decomposition of H_2, respectively, and T_{ref} = 523.15 K. The model contains further 8 parameters (β_7, ..., β_{14}) which are used for the calculation of the surface coverages $\Theta^{\odot}$, Θ^{*} and $\Theta^{\otimes}$ (see Ref. [30] for equations). As only the β_1, ..., β_6 parameters are directly linked to the reaction rate constants, in this thesis, these were fitted to 34 experiments ruled by the sole kinetics. The equilibrium constants were calculated according to Winkelman et al. [163]. The experimental tests were carried out in the μ-Berty reactor at 200 °C $\leq T \leq$ 260 °C, p = 40 bar and 45 bar, 15 000 $mL_{Reagents}\,h^{-1}\,g_{CAT}^{-1} \leq (F/W)^{*} \leq$ 80 000 $mL_{Reagents}\,h^{-1}\,g_{CAT}^{-1}$, feed gas composition: $H_2/CO/CO_2$ = 16/8/1, 10 vol.-% N_2 (for procedure see section 5.1).

$$r_{CO} = k_1\, p_{CO}\, p_{H_2}^2 \left(1 - \frac{1}{K_{P1}}\,\frac{p_{MeOH}}{p_{CO}\, p_{H_2}^2}\right) \Theta^{\odot}\Theta^{\otimes 4} \tag{5.4}$$

$$r_{CO_2} = k_2\, p_{CO_2}\, p_{H_2}^2 \left(1 - \frac{1}{K_{P2}}\,\frac{p_{MeOH}\, p_{H_2O}}{p_{CO_2}\, p_{H_2}^3}\right) \Theta^{*^2}\Theta^{\otimes 4} \tag{5.5}$$

$$r_{r-WGS} = k_3\, p_{CO_2} \left(1 - \frac{1}{K_{P3}}\,\frac{p_{CO}\, p_{H_2O}}{p_{CO_2}\, p_{H_2}}\right) \Theta^{*}\Theta^{\odot} \tag{5.6}$$

$$k_i = \exp\left(A\ - B\ \left(\frac{T_{ref}}{T} - 1\right)\right) \tag{5.7}$$

Starting from initial guesses for β_1, ..., β_6, by using a CSTR balance, the outlet concentrations were calculated and compared with the experimental ones. The six parameters β_1, ..., β_6 were fitted with a least-square method. The results of the fitting of the six parameters β_1, ..., β_6 are summarized in Table 5.6. Table A.2 shows the k_i values at different temperatures for both commercial (values taken from Seidel et

Table 5.6: Resulting estimates of the dimensionless parameters $\beta_1, ..., \beta_6$ obtained by fitting of the STM-kinetic model proposed by Seidel et al. [30] to the data from 34 experiments from the μ-Berty reactor ruled out by the sole kinetics of the STM reaction.

β_i	*Value*	β_i	*Value*
β_1	-6.007	β_4	6.147
β_2	2.184	β_5	5.065
β_3	-4.508	β_6	5.668

al. [30]) and self made CZA catalysts. Moreover, parity diagrams showing modelled and experimental concentrations for each gas species as well as the effect of temperature on y_{CO} for experiments and kinetic model are shown in Figure A.14 - A.15, respectively. Only few analysed samples show a deviation from the bisector higher than 20 %, while at most the deviation is lower than 10 % (see Figure A.14). As Figure A.15 shows, similar trends of experimental and modelled y_{CO} were observed by changing the reaction temperature at both pressures of 40 and 45 bar.

5.9.1 Further modelling results

Implementing the STM-kinetics obtained as described above and maintaining all the other modelling parameters as reported in section 3.2.2, the influence of the catalyst configuration and its composition on X_{CO} was investigated. Here, the aim was to compare the results obtained starting from the STM kinetics of a commercial catalyst from open literature to those of the FSP-CZA catalyst synthesized in the context of this work.

The results summarized in Figure 5.35 show X_{CO} for all catalyst configurations investigated. In general, X_{CO} presents lower absolute values as compared to the results showed in section 3.2.2. This is due to the fact that the commercial STM catalyst shows higher activity: for the same conditions and amount of catalyst, over the self-made FSP-CZA the first reaction step (STM) is slowed down and, consequently, X_{CO} of the whole process is affected. However, the qualitative behaviour of the catalyst systems for both reactor systems can be confirmed: for the particulate catalysts, the activity follows the sequence CZA@Z < CZA+Z < CZA&Z, within the set of planar systems CZA//Z and the CZA&/Z perform similar in terms of X_{CO}, while CZA#Z shows lower activity. Each structure shows a maximum in X_{CO} depending on ω_{Zeo}; for the CZA@Z this maximum is not as marked as for the other configurations. Maximum X_{CO} is given at 20 and 15 wt.-% for particulate systems CZA&Z and CZA+Z and 15 wt.-% for all the three planar systems. Regarding the structured CZA@Z catalyst, the modelling did not reveal a strong dependence of X_{CO} on ω_{Zeo} in the range investigated, as the presence of the shell is limiting the overall reaction system. As discussed in section 3.2.2, the diffusion limitation introduced by the shell leads to a decrease of the X_{CO} in comparison to the other systems.

The shift of the maximum in X_{CO} towards lower ω_{Zeo} was explained with a more pronounced limitation of transport among the different structures (see section 3.2.2). This is further supported by comparing Figure 5.35a and the accordant results shown in section 3.2.2 (Figure 3.4a - 3.6a): each structure presents the maximum in X_{CO} at higher ω_{Zeo} when the commercial STM catalyst is considered because of the more efficient MeOH synthesis. Thus, a lower amount of CZA is necessary in order to reach the maximum in X_{CO} at given process conditions.

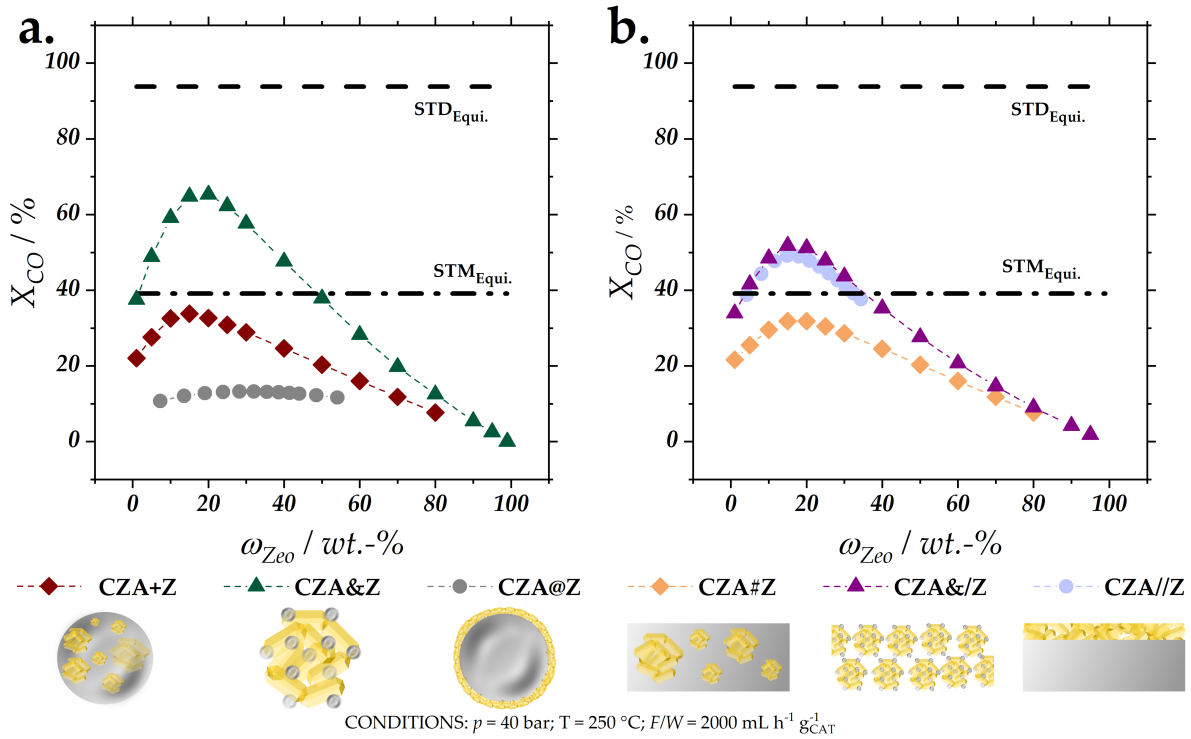


Figure 5.35: Predicting X_{CO} in the a) PBR and b) µ-CR over the bifunctional catalysts implementing the STM-kinetics relative to the CZA obtained in this work.

The product selectivity (not shown) predicted for varying ω_{Zeo} in the two reactors presents values next to the thermodynamic equilibrium of the STD, once the proper ω_{Zeo} is applied (at about 20 wt.-%): the MeOH formed in the CZA can at most be dehydrated to DME, enhancing the selectivity to the desired product with low selectivity to the intermediate. Once the STM rate slows down, less MeOH is produced regardless of the ω_{Zeo} applied. In summary, the STM kinetics for the CZA-catalyst prepared in the frame of this work was obtained and used for revised modelling of the catalyst configurations at the same operation conditions as presented in chapter 3. The STM rate was obtained by fitting the parameters of the equations proposed in the study of Seidel et al. [30] to experimental data obtained on the self-made made CZA catalyst. The modelling results showed in general a slower MeOH formation, which affects the absolute values of the X_{CO}, but still leads to the same trends among the structures investigated. Combining these results from the modelling with the synthesis and characterization proposed in the frame of this work, both hybrid particulate system with medium proximity (CZA+Z) and structured double layer catalyst configuration (CZA//Z) are promising configurations for the direct synthesis of DME from synthesis gas: both modelling results and their practical feasibility recommend the system for of further investigations.

5.10 Summary

The catalysts considered and prepared in the frame of this work starting from $CuO/ZnO/Al_2O_3$ (CZA) and zeolite H-ZSM-5 (Z) for the synthesis gas to methanol (STM) and methanol dehydration (MTD) reactions, respectively, were characterized with the aim of demonstrating their successful synthesis and

their activity.
At first, the FSP-CZA catalysts were investigated, finding out that:

- The final FSP-CZA is barely influenced by the collection system (either batch or semi-continuously in a bag-house filter); however, using the bag-house filter, the final fulfils a better performance in the STM reaction, according to several studies reported in literature, due to the higher specific surface area, lower reduction temperature and smaller Cu-crystallite size.
- Starting from a solution with higher combustion enthalpy leads to an increase of the surface area and improves the uniformity of the primary particle size; on the other hand, the reduction shifted to higher temperatures and the activity in the STM reaction decreased. This behaviour could be ascribed to a higher formation of carbonates at the surface of the nanopowder during the pyrolysis, even if this hypothesis should be confirmed by more detailed investigations.

The results of the characterization of the particulate catalyst configurations for the STD reaction, namely the hybrid systems of both medium (CZA+Z) and close (CZA&Z) proximity as well as the structured core@shell CZA@Z, let conclude that:

- The hybrid particles of medium proximity CZA+Z are a feasible solution for carrying out the STD; both the CZA+Z_1 ($\omega_{CZA}/\omega_{Zeo}$ = 1/1) and CZA+Z_5 ($\omega_{CZA}/\omega_{Zeo}$ = 5/1) outperformed the bare CZA catalyst in terms of X_{CO}, while the share of zeolite predetermines whether the STD reaction is limited by MeOH formation (CZA+Z_1) or by its dehydration (CZA+Z_5).
- The hybrid particles of close proximity CZA&Z are not suitable for being tested in the STD so far, due to a too low value of $\omega_{CZA}/\omega_{Zeo}$, the small size of the final particles and the expected degradation the CZA catalyst during the steam assisted crystallization procedure (which was demonstrated for the core@shell system).
- Along the core@shell CZA@Z synthesis, the CZA is altered irreversibly; the physico-chemical structure is affected and a consequent decrease of the activity in the STD can be ascribed to the calcination and to the exposure of the CZA catalyst to the hydrothermal zeolite synthesis conditions (Cu is partially dissolved). Moreover, diffusion limitations caused by the dense microporous zeolite shell also lower the obtainable X_{CO}.

The characterization of the planar (coated) systems, both as hybrid layer of medium proximity (CZA#Z) and as structured double layer (CZA//Z), dealt with the demonstration of the printability of the respective pastes based on rheological investigations, the structural characterization of the coated layers as well as their activity tests for the STD reaction, with the following main conclusions:

- Correspondence between the starting particle size and features of the final layer were found: thicker layers could be achieved coating particles bigger in size; on the other hand, when the $d_{[4,3]50}$ of the powder to be coated is bigger than the mean layer thickness, its roughness increases.
- Degradation on the CZA catalyst due to the final calcination of the coated systems should be considered, even if the required temperature of 400 °C is lower than applied during the CZA@Z synthesis at 550 °C.

- Using a proper solvent, both the CZA#Z and the CZA//Z were found active for the STD reaction; higher X_{CO} was obtained for the double layer CZA//Z, even if a higher amount of hydrocarbons was detected. However, DME was the main product for both systems.

6 CO_2 activation for MeOH synthesis

6.1 State of the Art

In the frame of the P2X technology, besides combining the r-WGS step of H_2, obtained by electrolysis, and CO_2, e.g. from carbon capture technologies, in order to obtain the CO necessary for traditional synthesis gas and its further conversion into valuable molecules (see chapter 1), the possibility of direct activation of CO_2 with H_2 is nowadays in focus of plenty of scientific studies [164, 165]. There are various challenges linked to the activation of CO_2: first, the thermodynamic stability of this molecule, which constrains the development of new *ad hoc* methods and catalysts able to reduce the energy demand of the process [166]. The scientific community has been strongly involved in this field and different solutions have been proposed. The photo- and electro-catalytic CO_2 activation is reported in studies by Maina et al. and Chai et al.: the former group immobilized metal organic frameworks on the surface of a reactor with tunable selectivity to either MeOH or CO switching between photo- and electro-catalysis [164]; the latter converted the CO_2 photo-catalytically to CO and CH_4 using a Zn-Ti-Ge based catalyst [165]. The Ozin group at the University of Toronto of could demonstrate that photocatalytic CO_2 reduction can be tailored either to CO or CH_4 by varying the size of the Pd nanocrystals supported on Nb_2O_5 [167]. Plasma-assisted CO_2 conversion, either by its reduction to CO [168], or by methanation [169, 170, 171] also has been investigated in recent years.
On the other hand, established processes, such as Fischer-Tropsch or MeOH synthesis, carried out industrially for decades starting from CO-rich feeds, could be switched to CO_2-rich feed gas. This involves the lower adsorption rate compared to CO, with consequently lower activity of the catalyst and higher selectivity to undesired CH_4, in case of hydrocarbon production [172, 173]. The CO_2 hydrogenation to hydrocarbons via the formation of CO (r-WGS) and the Fischer-Tropsch reaction, if performed on Fe-based catalysts, has been optimized for high selectivity towards the C_{5+} fraction as well as low selectivity towards the undesired CH_4 [173, 174]. Wei et al. report the benefit of combining the metallic catalyst with zeolites, preferably H-ZSM-5, in order to increase the selectivity to the C_5 - C_{11} hydrocarbon fraction [173]. The possibility of obtaining liquid fuel from CO_2 with MeOH as an intermediate is reported in literature in the work of Gao et al., who propose a bifunctional catalyst combining In_2O_3, for the formation of MeOH, with the zeolite H-ZSM-5, on which the MeOH further reacts to hydrocarbons at p = 30 bar and T = 340 °C [172]. Wang et al. propose the combination of an In_2O_3/ZrO_2 catalyst combined with SAPO-5, which could maximize the selectivity to the lower hydrocarbon fraction (C_2 - C_4) and suppress the production of CH_4 at p = 30 bar and T = 300 °C [175]. In section 6.1.1 the catalysis of MeOH synthesis from CO_2 as the focus of several studies is presented.

6.1.1 Catalysts for CO_2-to-MeOH reaction

CO_2-hydrogenation to MeOH has been studied in recent years, in order to identity the mechanism of the reaction on different catalysts as well as to find the best performing materials in terms of conversi-

on and selectivity. The so few only example for production of MeOH from CO_2 on a commercial scale (4000 ton $year^{-1}$) takes place in Grindavik (Iceland) by *Carbon Recycling International*, obtaining CO_2 by processing the gas emissions from a geothermal power plant and using renewable energy [176]. Notwithstanding this, the interest of the scientific community in this topic is high, and many works deal with the catalysis of this new process [33, 34, 177, 178, 179, 180].

Grabow et al. propose a microkinetic model for MeOH synthesis from CO_2 on Cu[111], including the WGS reaction and taking into account the formation of byproducts (formaldehyde (CH_2O), formic acid (HCOOH) and methyl formate ($HCOOCH_3$)) [33]. The *Density Functional Theory* calculations carried out by the authors resulted in a CO_2-hydrogenation path via the formate as an intermediate, namely $CO_2^\star \rightarrow HCOO^\star \rightarrow HCOOH^\star \rightarrow CH_3O_2^\star \rightarrow CH_2O^\star \rightarrow CH_3O^\star \rightarrow CH_3OH^\star$ [33]. This reaction mechanism is well known and reported in several works for polycrystalline Cu[111] as well as for the single crystal Cu[110] and Cu[100] phases [34, 181]. In the works of Frei et al. and Gao et al., the formate-route is reported also for In-based catalysts, where the presence of oxygen vacancies enables CO_2 adsorption [172, 182].

Many works are focused on the choice of the proper catalyst for the CO_2-hydrogenation reaction by experimental investigations. Cu-based catalysts have been reported and the influence of the addition of diverse oxides has been studied already in the 90s, when Nitta et al. showed the advantage of supporting the Cu either on ZnO, getting a benefit regarding higher Cu-dispersion, which is in accordance with the findings with respect to the CZA catalysts, or on ZrO_2, getting a benefit in the selectivity to MeOH instead of CO [183]. Angelo et al. prepared $Cu/ZnO/MO_x$ catalysts via both sol-gel and co-precipitation and performed the CO_2-to-MeOH reaction, suggesting $Cu/ZnO/ZrO_2$ (CZZ) containing 30 wt.-% of Cu and prepared via co-precipitation as the most promising catalyst (reaction conditions: $p = 50$ bar, 240 °C $\leq T \leq$ 280 °C, gas composition: $H_2/CO_2 = 3.89/1$) [184]. According to the same study, the substitution of ZrO_2 with ceria results in a lower Cu dispersion [184]. Arena et al. co-precipitated CZZ catalysts with different compositions and compared them to a commercial CZA for the CO_2-to-MeOH synthesis; the authors concluded that the CZA system is negatively affected by the water produced during the reaction, the desorption of which is hindered by its chemical affinity to the Al_2O_3; therefore, the CZZ system with a weight ratio Cu : ZnO : ZrO_2 = 45 : 11.8 : 43.2 was claimed as the most suitable one for CO_2-hydrogenation (reaction conditions: p = 10 and 30 bar, 200 °C $\leq T \leq$ 240 °C, gas composition: $H_2/CO_2 = 3/1$) [185]. In a further contribution, the same group mentions the promotion of both ZnO and ZrO_2 during the formation of the formate ($HCOO^\star$), which is, together with its hydration, the rate determining step of MeOH synthesis from CO_2: the proximity of the basic sites of the two oxides, necessary for CO_2 adsorption, with the metallic Cu, namely the hydrogenation site, makes this step more efficient [186]. Frei et al. investigated the influence of the synthesis conditions of a CZZ catalyst prepared via co-precipitation with the composition of $Cu/ZnO/ZrO_2 = 4.2/2/1$ [177]. The authors found out that the crystallinity, the volume and size of the pores as well as the specific surface area are affected by the precipitation conditions and confirmed a better catalytic performance in terms of MeOH productivity of the CZZ when compared to a commercial CZA catalyst (reaction conditions: p = 40 bar, T = 240 °C, $H_2/CO_2 = 3/1$) [177]. Cu/ZrO_2 catalysts were prepared via two-nozzle-FSP by Tada et al. with CuO different in size [187]. The performance of the samples in the CO_2-to-MeOH reaction was compared to a physical mixture of CuO and ZrO_2 as well as to a commercial CZA: at the same X_{CO_2}, the FSP-Cu/ZrO_2 catalyst with a Cu loading of 14 wt.-% and with CuO particles smaller

in size enabled a higher selectivity to MeOH compared to the FSP-Cu/ZrO_2 system with larger Cu particles, the physical mixture of the two oxides and the commercial CZA catalyst (reaction conditions: $p = 20\,\text{bar}$, $T = 230\,^\circ\text{C}$, $H_2/CO_2 = 3/1$) [187]. Cu/Zn/Al/Zr-based catalysts (CZAZ) have been investigated by several research groups [188, 189, 190]. Dong et al. showed that the benefit in CO_2-hydrogenation on the CZZ catalyst with a molar ratio of Cu/Zn/Zr = 6/3/1 synthesized via liquid reduction is higher compared to the co-precipitated material, and that it can even increase if CZAZ with a molar ratio of Cu/Zn/Al/Zr = 6/3/0.5/0.5 is prepared by the same technique (reaction conditions: $p = 50\,\text{bar}$, $230\,^\circ\text{C} \leq T \leq 270\,^\circ\text{C}$, $H_2/CO_2 = 3/1$) [188, 191]. The ultrasonic spray precipitation technique for synthesis of a similar catalyst with the molar ratio Cu/Zn/Al/Zr = 4/3/1/2 was investigated by Ramli et al., who proved the superiority of this preparation procedure compared to only spraying and sonication as well as to the conventional precipitation method for performing the CO_2-to-MeOH reaction (conditions: $p = 30\,\text{bar}$, $T = 230\,^\circ\text{C}$, $H_2/CO_2 = 3/1$); however, the authors report CO as main product instead of MeOH for the catalysts prepared ($S_{CO} > 70\,\%$) [189]. Gao et al. co-precipitated several CZAZ catalysts with different amount of Al, concluding that the molar ratio of Cu/Zn/Al/Zr = 2/1/1.2/0.1 optimizes the CO_2-to-MeOH reaction in terms of X_{CO_2} and S_{MeOH} (conditions: $p = 50\,\text{bar}$, $T = 250\,^\circ\text{C}$, $H_2/CO_2 = 3/1$) [190]. At higher temperatures, even if an increase of the X_{CO_2} was measured, S_{MeOH} was negatively affected [190]. More recently, the same research group proposed a core@shell system, where either the Cu or the Cu/ZnO were enwrapped in mesoporous SiO_2: the authors show the advantage of this catalyst geometry compared to the impregnation of the Cu-precursor on the SiO_2 regarding activity, selectivity and stability [192]. By comparing the two studies of Gao et al., where the experimental tests were carried out at the same reaction conditions, the Cu/ZnO@SiO_2 reached lower X_{CO_2} but higher S_{MeOH} than the CZAZ system [190, 192].

Novel catalysts, obtained by substitution of Cu with noble metals, have been investigated: Pd/In-, supported Pd/Zn and Pt-based catalyst were found promising [193, 194, 195]. Vidal et al. synthesized Au- and Cu-based catalysts supported on TiC [196]. Here, the authors show that TiC as the sole support is even more active compared to the pure metallic Cu, detecting MeOH as main product and CH_4 only in traces, but not as active as the Cu/ZnO catalyst (reaction conditions: $p = 5\,\text{bar}$, $230\,^\circ\text{C} \leq T \leq 330\,^\circ\text{C}$, $H_2/CO_2 = 9/1$) [196]. The authors found the reason of the selective activation of CO_2 for the MeOH synthesis in the capability of the catalyst of adsorbing the CO_2 without breaking the C−O bonds before the hydrogenation takes place [196]. The addition of Au, which in the metallic form is not active in MeOH synthesis, on the TiC support enhances X_{CO_2}, even though the Cu/TiC system is reported as more active [196]. The same group also shows the benefit of a $Cu/CeO_x/TiO_2$ catalyst prepared by vapor-deposition compared to a Cu surface covered with ceria (CeO_x/Cu), a Cu/ZnO catalyst and the pure Cu at the same conditions reported above [178]. The authors propose by theoretical calculations that the $Cu/CeO_x/TiO_2$ catalyst favours CO_2 adsorption and MeOH formation via the carboxyl (OCOH*) path instead of the formate (HCOO*) route [178]. All these considerations are well summarized in the contribution of Rodriguez et al., where metal-oxides and metal-carbide materials have been compared to each other and to metallic Cu [179]. In this latter contribution, the authors declare that the optimization of the overall catalyst should concern separately the metallic (or bimetallic) system and the support: the former should be synthesized with controlled particle size or using alloy and needs to be promoted; the latter, either an oxide or a carbide, is influenced by the morphology, the composition, and

the chemical state and should contain more than one metal for the catalytic performance to improve, as the authors have shown for the $Cu/CeO_x/TiO_2$ system [179].

6.2 Synthesis

In the frame of this work it was chosen to synthesize a $CuO/ZnO/ZrO_2$ catalyst (CZZ) using the FSP technique, as described for the CZA catalyst in chapter 4. Before preparing the final catalysts, the sole ZrO_2 was synthesized via batch-FSP and characterized (via XRD, N_2-physisorption, TGA), in order to prove the success of the procedure. The precursor was chosen after analysing several works reported in the open literature with respect to the ZrO_2 synthesis via FSP: zirconium acetyl-acetonate [197, 198], zirconium (IV) n-propoxide [149, 199, 200], $Zr(OH)_2CO_3$ [201] and zirconium n-butoxide [202] are reported as suitable. For this work, the zirconium (IV) n-propoxide (70 wt.-% in n-propanol, ThermoFisher GmbH) was chosen. Copper and zinc nitrates (see section 4.2) were used.
The ZrO_2 as well as the CZZ systems were prepared by dissolving either only zirconium (IV) n-propoxide or all the metal precursors in the molar ratio of Cu : Zn : Zr equal to 6 : 3 : 1 into pure EtOH (*solution 1*) or into a solution composed of EtOH : X : DEGBE : EHA in a volume ratio equal to 1 : 1 : 1 : 1 (*solution 2*), with a molarity of 0.5 M. The solution obtained was stirred and the pyrolysis took place as described for the CZA system in section 4.2.
The batch collection system was used for the synthesis of the ZrO_2 powders, denoted as ZrO_2-1 and ZrO_2-2 for the oxide powder obtained from the solution 1 and 2, respectively. The nanopowder was scratched from the glass fiber filter and sieved under 200 µm. A part of both samples was calcined up to 550 °C as described in section 4.2, and the resulted samples are denoted as ZrO_2-1_c and ZrO_2-2_c, respectively.

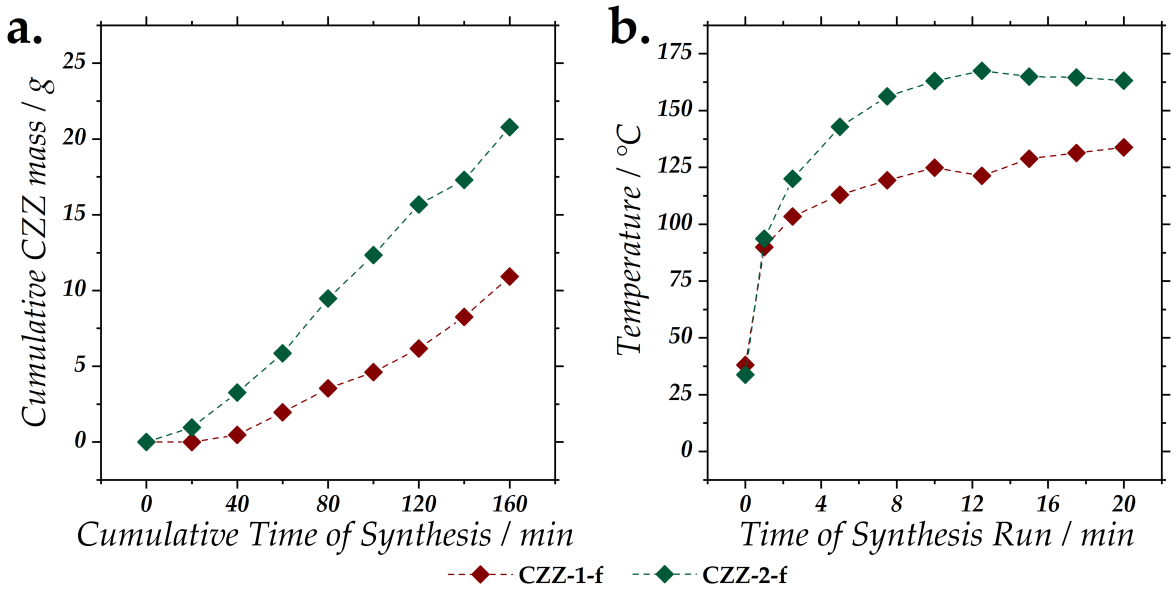


Figure 6.1: a) Cumulative mass of the CZZ-1-f and CZZ-2-f collected using the bag-house filter and b) temperature at the entrance of the bag-house filter over synthesis time. *Cumulative time of synthesis*: sum of time of several single synthesis runs. *Time of synthesis run*: time of a single run.

Both the batch and the semi-continuous collection systems were used for the preparation of the CZZ catalysts. The resulting materials are denoted as CZZ-*i*-*x*, where *i* indicates the precursor solvent and *x* denotes the batch, when *b*, or the semi-continuous, when *f*, collection system. The CZZ-*i*-b samples were sieved under 200 µm. The filters in the bag-house system were changed for these syntheses, in order to avoid contamination due to the presence of the CZA nanopowder synthesized before.
A part of the CZZ-1-f and CZZ-2-f was pressed into tablets, crushed and sieved to obtain particles in the sieve fraction of 50 - 100 µm, which are denoted as P-CZZ-1 and P-CZZ-2, respectively, and were used for the CO_2-to-MeOH synthesis in the µ-Berty reactor.

Figure 6.1 shows the cumulative collected mass of the CZZ-1-f and CZZ-2-f over the cumulative time of synthesis (Figure 6.1a) and the rise of the temperature at the bag-house filter entrance during 20 min of synthesis (Figure 6.1b), after which the pyrolysis was stopped for cooling down the filter (see also section 4.2.1). From Figure 6.1a, the productivity of both catalysts after the induction period can be extrapolated: 0.09 g min^{-1} and 0.14 g min^{-1} for the CZZ-1-f and CZZ-2-f, respectively. The values are in agreement with the productivity calculated for the FSP-CZA samples reported in chapter 4 (0.1 g min^{-1} 0.13 g min^{-1} for the CZA-1-f and CZA-2-f, respectively). This can prove that the productivity of the flame spray pyrolysis is mostly depending on the efficiency of the combustion of the solvent, namely of its enthalpy content. As in case of the CZA catalyst, the increase of the temperature is stronger during the first five minutes of synthesis and after approximatively 10 min a constant temperature is maintained, which corresponds to 130 °C and 165 °C for the CZZ-1-f and CZZ-2-f, respectively, in accordance with the temperatures detected during FSP-CZA synthesis (see chapter 4). Solution 2, with higher enthalpy of combustion, reaches a higher temperature of the flame as well as of the solid-gas medium at the entrance of the bag-house filter.

6.3 Characterization

The ZrO_2 only powder was characterized in order to prove the success of the synthesis of the oxide starting from zirconium (IV) n-propoxide as precursor. Afterwards, the CZZ-*i*-*x* samples were characterized in terms of physico-chemical structure, analysing the eventual differences due to the collection system and to the precursor solution used. This analysis was done analogous to what already was presented and discussed in chapter 5 for the FSP-CZA materials. The measurements were carried out as described in section 5.1. Finally, the P-CZZ catalysts were used for the CO_2-to-MeOH synthesis in the µ-Berty reactor for comparison to other materials regarding X_{CO_2} and S_{MeOH} (see section 5.1 for the procedure and Equations 6.1 - 6.2).

6.3.1 ZrO_2: physico-chemical characterization

ZrO_2-1 and ZrO_2-2, obtained as described in section 6.2, were characterized before and after calcination via N_2-physisorption, XRD and TGA.
Table 6.1 shows the specific surface area (SSA) of ZrO_2-1 and ZrO_2-2 before and after thermal treatment, which is denoted by the addition of the letter _*c*. In general, the sample prepared with pure EtOH showed a lower specific surface area, which is compliant with the results obtained for the FSP-CZA (see section 5.2). The loss in specific surface area due to the calcination is 29 % and 20 % for ZrO_2-1 and

Table 6.1: Specific surface area of the ZrO_2 samples before and after calcination.

Sample	*SSA / m^2 g^{-1}*
ZrO_2-1	85
ZrO_2-2	105
ZrO_2-1_c	60
ZrO_2-1_c	84

SSA = specific surface area

ZrO_2-2, respectively. Stark et al. prepared Ce-Zr systems (Ce content of of 0.1 - 0.9) and reported specific surface areas in the range of 130 - 170 m^2 g^{-1} and 65 - 85 m^2 g^{-1} for the pristine and the calcined (up to 900 °C) material, respectively [198]. Tok et al. reported specific surface areas of 20 - 70 m^2 g^{-1} for different ZrO_2 samples prepared via FSP and using solvents containing water and EtOH with different compositions [201]. Higher specific surface areas were measured increasing the ratio of EtOH in the solvent, confirming what presented in section 2.2, namely the use of water leads to an increase of the size of the final nanopowder as well as to a decrease in the specific surface area [201]. Theo et al. reported a specific surface area of 73 m^2 g^{-1} for ZrO_2 prepared via FSP [149]. In summary, the ZrO_2 obtained in this work presents a specific surface area in line with what is reported in literature for similar systems.
Figure 6.2 shows the XRD patterns of ZrO_2-1 and ZrO_2-2 before and after calcination. In general, no effect of the thermal treatment could be observed for both samples, as the position and the intensity of each reflection are maintained. By comparing the patterns to the reference for ZrO_2 in [149] and [201] (not shown), the presence of all characteristic reflections of the monoclinic and tetragonal structures of the oxide is confirmed. Small deviations between ZrO_2-1 (Figure 6.2a) and ZrO_2-2 (Figure 6.2b) can be noticed: the sample ZrO_2-1 reveals sharper reflections at 2Θ = 28° and 32°, which, according to [199] and [201], should be attributed to monoclinic ZrO_2. The crystallite size in ZrO_2-1 and ZrO_2-2 was calculated

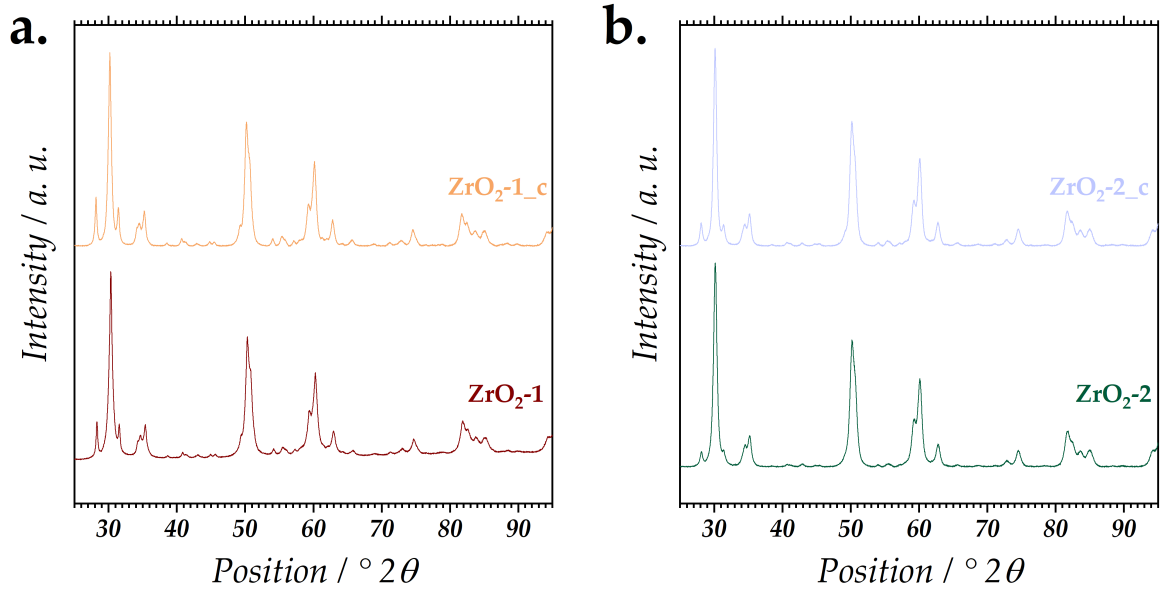


Figure 6.2: XRD patterns of the samples a) ZrO_2-1 and a) ZrO_2-2 before and after calcination, denoted with _c.

to be 12.5 nm and 17 nm, respectively, by using the Scherrer equation for the reflection at 2Θ = 30.2°. Thermal gravimetric analysis was applied to ZrO_2-1 and ZrO_2-2 to understand whether impurities coming from the solution or pyrolysis side-products are present in the final nanopowder. The results are shown in Figure A.16. The final weight corresponded to 98 wt.-% and 98.4 wt.-% for ZrO_2-1 and ZrO_2-2, respectively, and both samples lost about 0.7 wt.-% up to T = 100 °C, correlated to the presence of adsorbed water on the surface of the powder. Thus, it can be concluded that the ZrO_2 prepared via FSP did not contain remaining fragments of the solvents and/or pyrolysis side-products in the final product.

In summary, the synthesis of ZrO_2 starting from a liquid precursor and two different solvents was carried out, in order to ensure the success of the synthesis of CZZ catalysts. The samples were characterized in terms of specific surface area, crystallinity and presence of organic impurities. The results obtained prove that the powders were synthesized properly and showed comparable features to similar materials reported in the open literature.

6.3.2 CZZ catalysts: physico-chemical characterization

The same characterization methods applied to the FSP-CZA materials, presented in chapter 5, were used for finding out the physico-chemical structure of the FSP-CZZ powder. The specific surface area of the CZZ samples and the metal composition measured by ICP-OES of P-CZZ-1 and P-CZZ-2 are listed in Table 6.2. When comparing these results with those obtained for the CZA catalysts (see chapter 5), the same trend is confirmed, with lower absolute values of the specific surface area for FSP-CZA-1 and CZZ-1 compared to FSP-CZA-2 and CZZ-2, respectively. The semi-continuous collected nanopowder showed a higher specific surface area compared to the batch-collected one. As discussed for the CZA system, this should be caused by the quenching of the powder on the glass fiber filter occurring during the batch synthesis (see section 5.2.1). In the open literature, Jeong and Suh reported a specific surface area of 30 - 100 $m^2\ g^{-1}$ for CZZ materials with a Zr-molar loading in the range of 0 - 40 % [203]; Arena et al. reported a specific surface area in the range of 125 - 175 $m^2\ g^{-1}$ for CZZ catalysts [185]; Angelo et al. measured 61 $m^2\ g^{-1}$ for CZZ catalyst (19 wt.-% of ZrO_2) [184]. For all the cases mentioned, the catalysts were prepared via precipitation methods [54, 184, 185]. From Table 6.2, the reproducibility of the FSP technique for synthesis of nanopowders with the same composition but different precursor solutions is

Table 6.2: Specific surface area and metal content of the CZZ samples synthesized via FSP.

		Metal content / wt.-%		
Sample	***SSA / $m^2\ g^{-1}$***	***Cu***	***Zn***	***Zr***
CZZ-1-b	58	N/A	N/A	N/A
CZZ-2-b	100	N/A	N/A	N/A
CZZ-1-f	70	N/A	N/A	N/A
CZZ-2-f	111	N/A	N/A	N/A
P-CZZ-1	46	61.6	35.1	3.3
P-CZZ-2	68	62.3	33.7	4.0

SSA = specific surface area

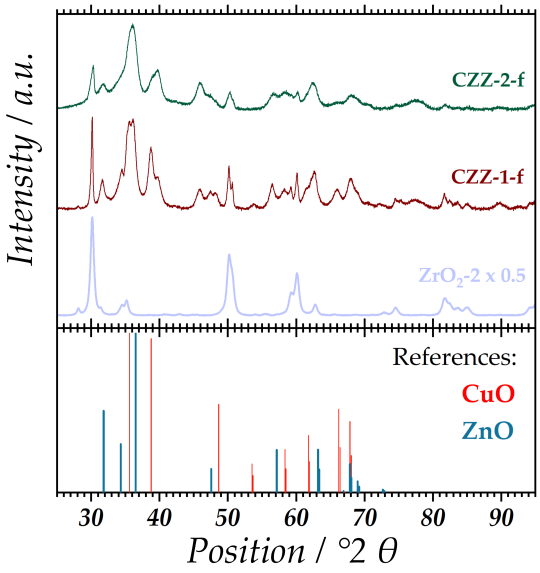


Figure 6.3: XRD patterns of the samples CZZ-1-f, CZZ-2-f and the references for ZrO_2 (sample ZrO_2-2, with adjusted intensity), for CuO and ZnO structures (International Center for Diffraction Data (ICDD)).

proved (see the metal content in Table 6.2). The crystallinity of the nanopowder was proved with XRD, and the obtained patterns are shown in Figure 6.3. As references for the CuO and ZnO phases were used the data from the ICDD, while the presence of the ZrO_2 was referred to the pattern of the ZrO_2-2 synthesized in this work. In general, the presence of the three phases is confirmed. Unlike for CZA catalysts, where due to overlapping patterns no reflections could be attributed to the crystalline Al_2O_3 phase, for the CZZ systems, the ZrO_2 phase is confirmed (see reflections at $2\Theta = 30°$, 50.2° and 60.2°). The reflection at $2\Theta = 45.9°$ is present in both the samples considered and, according to the ICDD (pdf No. 00-013-0311, not shown), it could be attributed to the ZrO_2 crystal phase. Furthermore, observing

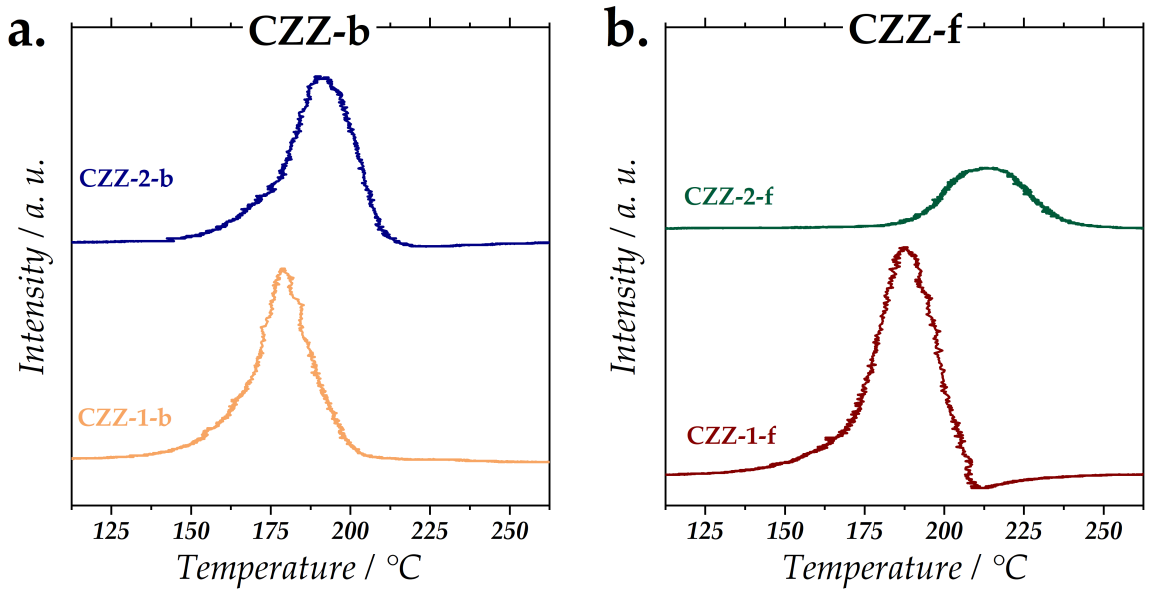


Figure 6.4: TPR profiles of the a) CZZ-*i*-b and b) CZZ-*i*-f nanopowder.

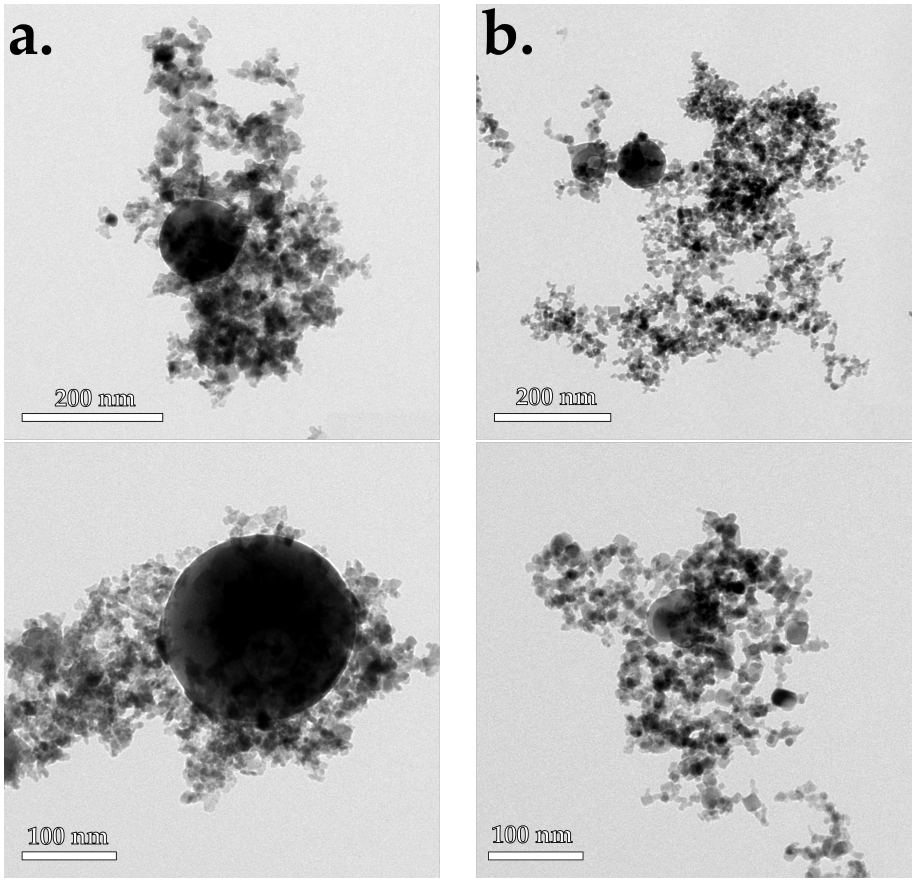


Figure 6.5: TE-micrographs of the a) CZZ-1-f and b) CZZ-2-f samples.

the range of 2Θ = 30° - 45°, the sample CZZ-2-f shows broader and less intense reflections compared to CZZ-1-f, namely the crystallinity of the CZZ-1-f sample is higher. Due to the overlapping of the reflections of the three oxides, it was not possible to apply the Scherrer equation and determine the Cu-crystal size in the two samples.

The reducibility of the prepared nanopowder was evaluated with TPR; these results are shown in Figure 6.4. CZZ-1-b and CZZ-2-b present the reduction peak at T = 179 °C and 189 °C, while the CZZ-1-f and CZZ-2-f at T = 188 °C and 215 °C, respectively. Similar reduction temperatures ($T_{red.}$) are reported in literature in the works of Arena et al., who measured $T_{red.}$ in the range of 210 - 248 °C, changing the composition of the CZZ catalyst [185], of Frei et al., who measured $T_{red.}$ in the range of 115 - 215 °C, changing the precipitation temperature during the preparation of diverse CZZ catalysts [177] and of Ramli et al., who measured $T_{red.}$ in the range of 190 - 240 °C for CZAZ catalysts via two different precipitation procedures [189]. In the frame of this work the reduction peak is shifted to higher temperatures when *solution 2* is used as solvent, which is in agreement with what was reported here for the FSP-CZA nanopowder (see section 5.2.2). TEM-micrographs of CZZ-*i*-f are shown in Figure 6.5. In general, both CZZ-1-f (Figure 6.5a) and CZZ-2-f (Figure 6.5b) present primary particles in the range of 10 - 30 nm; the size of these particles is rather uniform except for some bigger clusters, the size of which strongly depends on the precursor solution used. In case of CZZ-1-f, the size of the bigger clusters is around 200 nm, while for CZZ-2-f it is below 100 nm. These are probably to be be ascribed to ZrO_2-particles. The different size of the primary particles obtained with the different precursor solutions is in accordance with the difference

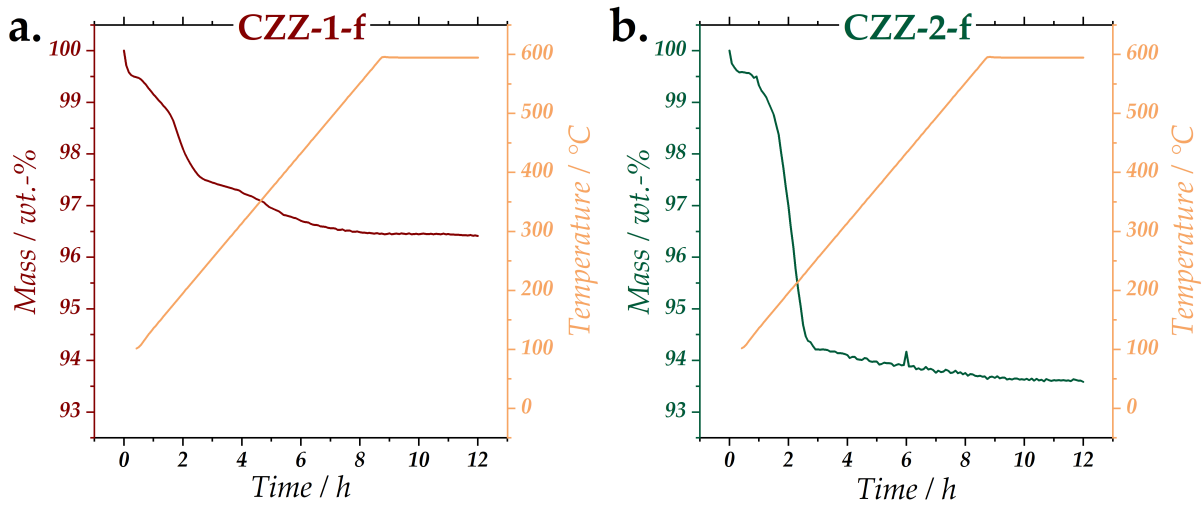


Figure 6.6: Mass loss over temperature during the TG-analysis of a) CZZ-1-f and b) CZZ-2-f samples.

in the specific surface area of the two samples as well as with the results obtained with the FSP-CZA system, as discussed in section 5.2.2. The higher temperature in the flame during the pyrolysis leads to faster evaporation of the droplets and the formation of smaller particles. Figure 6.6 shows the result of the thermal gravimetric analysis applied to the CZZ-1-f and CZZ-2-f nanopowders. As for the FSP-CZA, the mass loss over temperature occurs more strongly for the powder synthesized by *solution 2* compared to the sample prepared by *solution 1*. This aspect has been already discussed in section 5.2.2: the high partial pressure of CO_2 above the flame zone favours the formation of carbonates [31, 147]. Furthermore, as the loss in mass could not be observed for the sole ZrO_2, this should be ascribed to the presence of the CuO and/or the ZnO.

6.3.3 CZZ catalysts: reaction tests in the CO_2-to-MeOH reaction

The P-CZZ-1 and P-CZZ-2 catalysts were tested for the CO_2-to-MeOH reaction in the μ-Berty reactor. The equipment used, namely the feeding system, the plant and the on-line chromatograph as well as the pre-treatment of the catalyst (purging, reduction) prior to the reaction have been carried out as explained in section 5.1. The catalytic tests were carried out at $p = 45\,\text{bar}$, $200\,°\text{C} \leq T \leq 260\,°\text{C}$, $H_2/CO_2 = 3/1$ with 10 vol.-% N_2 as internal standard, $(F/W)^* = 5250\,\text{mL}_{\text{Reagents}}\,\text{h}^{-1}\,\text{g}_{\text{CAT}}^{-1}$. The CO_2-conversion (X_{CO_2}) and the product selectivity (S_i) were calculated according to the Equations 6.1 - 6.2 (for the definition of Z and ν_i see Equation 5.1). To make a comparison, the P-CZA-1 catalyst was tested for the CO_2-to-MeOH reaction at $p = 45\,\text{bar}$, $200\,°\text{C} \leq T \leq 280\,°\text{C}$, $(F/W)^* = 6000\,\text{mL}_{\text{Reagents}}\text{h}^{-1}\,\text{g}_{\text{CAT}}^{-1}$.

$$X_{CO_2} = \left(1 - Z \cdot \frac{y_{CO_2}}{y^0_{CO_2}}\right) \cdot 100\,\% \tag{6.1}$$

$$S_i = \frac{\nu_i \left(Z \cdot y_i - y_i^0\right)}{y^0_{CO_2} - Z \cdot y_{CO_2}} \cdot 100\,\% \tag{6.2}$$

Figure 6.7 shows the results of the catalytic tests of the P-CZZ-*i*. In general, X_{CO_2} is increasing with temperature, namely the system is kinetically limited. The P-CZZ-1 catalyst (Figure 6.7a) is less active than the P-CZZ-2 (Figure 6.7b). On both catalysts, S_{CO} increases with higher temperature, while

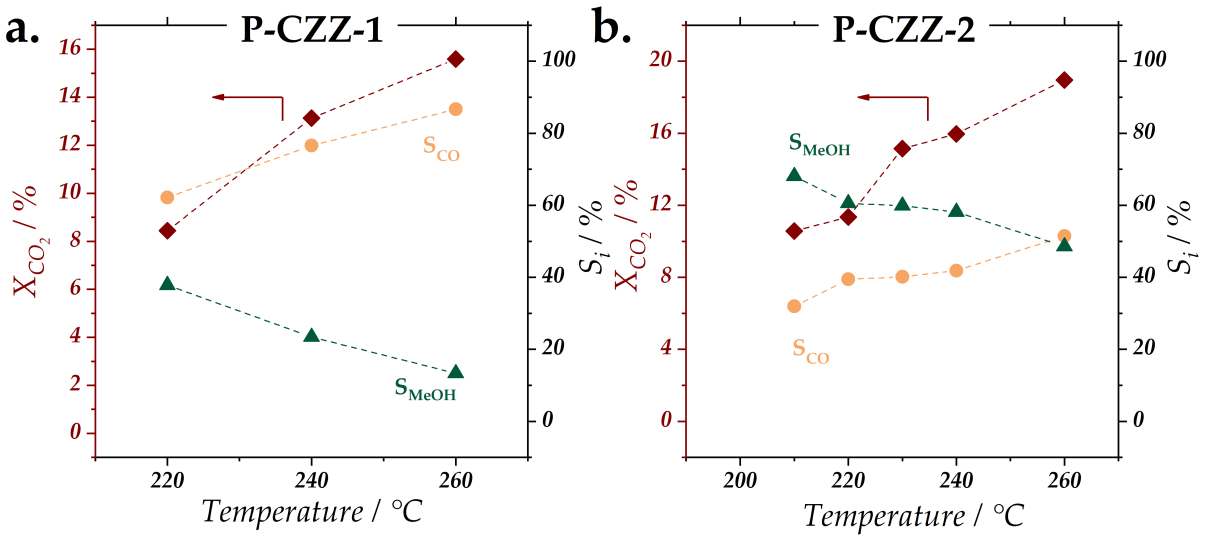


Figure 6.7: Activity of a) the P-CZZ-1 and b) the P-CZZ-2 catalysts in terms of X_{CO_2} and S_i as a function of temperature for the CO_2-to-MeOH reaction in the μ-Berty reactor.

S_{MeOH} is favoured at lower temperatures; no further products were detected at the measured conditions. The product distribution is strongly affected by the catalyst used: on P-CZZ-1 mostly CO was produced, while on P-CZZ-2 MeOH was the main product for each temperature except T = 260 °C ($S_{CO,T=260\,°C,P-CZZ-2}$ = 51.4 %). The dependence of the selectivity on the temperature is related to the endothermic r-WGS reaction: the feed gas is not containing CO, the r-WGS reaction is favoured at higher temperatures and, at the same time, the exothermic MeOH formation from CO_2 is thermodynamically favoured at lower temperatures. This behaviour is well known and reported in literature in several contributions [184, 185, 190]. Furthermore, comparing the S_{MeOH} values at similar X_{CO_2}, the results obtained here for the P-CZZ-2 catalyst are, for some cases, even better than what is reported in literature: Angelo et al. measured $S_{MeOH,X_{CO_2}=14.3\%}$ = 45 % at p = 50 bar, T = 240 °C [184]; Arena et al. measured $S_{MeOH,X_{CO_2}=15.9\%}$ = 48.4 % at p = 30 bar, T = 240 °C (for comparison, in this work: $S_{MeOH,X_{CO_2}=15.9\%}$ = 58.1 % at T = 240 °C) [185]; Ramli et al. measured $S_{MeOH,X_{CO_2}=18.3\%}$ = 22.1 % at p = 30 bar, T = 230 °C [189] (for comparison, in this work: $S_{MeOH,X_{CO_2}=18.9\%}$ = 48.5 % at T = 260 °C); Gao et al. measured higher X_{CO_2}, in the range of 23 - 26 %, at p = 50 bar, T = 250 °C and, over the proper CZZ catalyst, S_{MeOH} = 61.3 % [190] (here: S_{MeOH} = 60.5 % has been obtained for X_{CO_2} = 11.3 % at T = 220 °C). The P-CZA-1 catalyst was tested at similar conditions and reached slightly lower X_{CO_2} compared to the P-CZZ-1, but a similar capability to allow the r-WGS reaction to take place instead of MeOH formation, as shown in Figure 6.8. These measurements suggest that the solvent in the precursor solution for the FSP synthesis affects the selectivity more strongly than the metal used, either the Al_2O_3 or the ZrO_2. The influence of the precursor solution during the formation of the nanopowder via FSP has been already presented in section 2.2. Those considerations, together with the characterization carried out in this work, could explain the difference in the activity and in the product distribution during the CO_2-to-MeOH reaction. The CZZ-2-f sample showed smaller primary particle size and consequent higher specific surface area as well as broader reflections in the XRD pattern and higher $T_{red.}$ (see section 6.3.2). All these features could prove the enhanced synergy of the three oxides present in this catalyst, as their

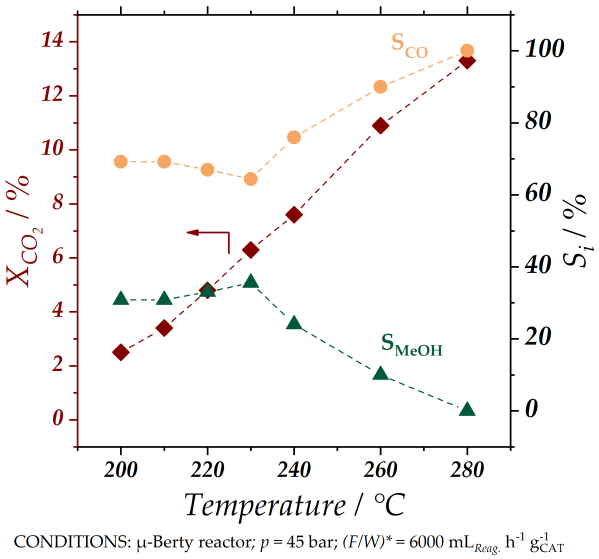


Figure 6.8: Activity of the P-CZA-1 catalyst in terms of X_{CO_2} and S_i for the CO_2-to-MeOH reaction in the μ-Berty reactor.

more intimate contact results in the better performance during the reaction compared to CZZ-1. Besides, the hypothesis of the formation of copper carbonates at the surface during the FSP synthesis, reported as difficult to avoid in the open literature [147, 148] and supported by the TGA results in this work, should be also taken into account. The presence of copper carbonate species on the catalytic surface could enhance the CO_2-to-MeOH reaction mechanism into the formation of MeOH instead of CO (see section 6.1.1). This hypothesis is supported by the reaction mechanisms of both CO-hydrogenation and the WGS reaction, which proceed through the carboxyl route rather than a formate, as a characteristic intermediate during CO_2-hydrogenation [31]. In the P-CZZ-2, synthesized from a solvent containing more carbon, the amount of carbonates at the surface should be higher compared to P-CZZ-1 and P-CZA-1, with a consequent additional advantage in the CO_2-to-MeOH reaction. However, these hypotheses should be confirmed by further investigations, such as reaction measurements at longer time on stream.

6.4 Summary

The direct activation of CO_2 with H_2 into valuable molecules instead of the r-WGS step for getting the synthesis gas is challenging from the catalytic point of view, due to the high thermodynamic stability of CO_2 [166]. In the frame of this work, two $CuO/ZnO/ZrO_2$-based catalysts (CZZ) were synthesized via flame spray pyrolysis (FSP), characterized and tested for the CO_2-to-MeOH reaction. At first, in order to ensure the success of the synthesis of the final catalysts, the sole ZrO_2 nanopowder was prepared and characterized, starting from two different solvents. The CZZ catalysts were then synthesized with the metallic molar ratio Cu/Zn/Zr = 6/3/1. The most important findings related to this study can be summarized as follows:

- The succesful synthesis of ZrO_2 using a liquid precursor was proved with XRD. Furthermore, different specific surface area was obtained, depending on the solvent used in the precursor solution; no loss in mass was observed over thermal treatment of the powder.

- In accordance with the study carried out for the FSP-CZA, also for the FSP-CZZ catalysts, the solvent in the precursor solution was found to affect the productivity and the temperature reached during the synthesis: the enthalpy of the solvent affects the mechanism of the powder formation and, as a consequence, the physico-chemical properties (specific surface area, crystallinity, reducibility and primary particle size) of the final product.
- The eventual formation of copper carbonates during the pyrolysis, supported by studies reported in literature as well as by the TG-analyses carried out in this work, could be facilitated when the solvent in the precursor solution contains more carbon and higher enthalpy of combustion. Such formation could be the reason of an appreciable influence on the activity of the final catalyst and, even more strongly, in the product distribution, favouring the formation of MeOH instead of CO.
- A promising catalyst for the CO_2-to-MeOH reaction has been successfully synthesized, and results comparable to studies reported in literature regarding X_{CO_2} and S_{MeOH} have been obtained.

In future work, the combination of CZZ with a proper dehydration catalyst for the CO_2-to-DME direct synthesis could be carried out in order to enhance the per-pass conversion, necessary for e.g. decentralized plants in the frame of the Power-to-X technology. Furthermore, the activity of the material as planar catalyst system in a μ-CR could be investigated.

7 Conclusion & Outlook

In the present work, the direct synthesis of dimethyl ether (DME) from synthesis gas (STD reaction) over several catalyst configurations for application in decentralized compact plants in the frame of the Power-to-X concept has been discussed. Both particulate and planar (coated) catalyst systems have been investigated by combining the $CuO/ZnO/Al_2O_3$ (CZA) with zeolite H-ZSM-5 (Z) for methanol synthesis and its dehydration, respectively. Thus, hybrid particulate systems of medium (CZA+Z) and close (CZA&Z) proximity (proximity of the two catalysts in the micrometer- and sub-micrometer-scale, respectively) and the structured core@shell configuration (CZA@Z) for application in a packed-bed-reactor (PBR) as well as their coated counterparts, namely hybrid planar systems of medium (CZA#Z) and close (CZA&/Z) proximity and the structured double layer configuration (CZA//Z) for application in a micro-channel-reactor (μ-CR), were considered. In order to understand how CO-conversion (X_{CO}) and DME-selectivity (S_{DME}) are influenced by the configuration of the catalyst, modelling, synthesis and characterization tools were brought into connection.

Aim of the **Modelling** was to foresee how the catalytic structure (investigated via characterization) together with the synthesis parameters influence both X_{CO} and product distribution in both reactors considered. Regarding the particulate catalysts modelled for the PBR, it was found out that the structured CZA@Z is limited by mass transport of the reactants to the CZA core through the zeolite shell; at the same time, due to its hierarchical structure, the CZA@Z system allows the highest S_{DME}. Among the particulate structures, the best performance was found for the CZA&Z: absence of diffusion limitation and close proximity between CZA and zeolite permit the achievement of the highest X_{CO} and similar S_{DME} as compared to the CZA@Z. The capability of overcoming the STM equilibrium at the operational conditions investigated was confirmed for the CZA+Z system: the segregation of the two catalysts within the particle, namely medium proximity, is the reason of a lower X_{CO} and S_{DME} compared to the CZA&Z structure. Regarding the planar catalyst configurations, the best STD-performances were predicted for the coated hybrid system of close proximity CZA&/Z and the structured double layer CZA//Z; both configurations reached similar X_{CO} and S_{DME}. Besides, for each structure, the mass ratio STM-/MTD-catalysts (expressed as the zeolite mass fraction, ω_{Zeo}) influences the performance: in general, when the mass transport within the catalyst is enhanced, the maximum in X_{CO} is detected at higher ω_{Zeo}, while the S_{DME} is barely affected by the catalyst composition.

Aim of the **Synthesis** was to achieve a reproducible preparation of the desired catalyst configurations: it was possible to apply the most suitable techniques for a succesful synthesis of all the catalyst structures proposed, also within cooperation with the Institute of Particle Technology (MVT) (TU Clausthal) and the Chair of Chemical Reaction Engineering (CRT) (Friedrich-Alexander-University of Erlangen-Nürnberg, FAU). In particular, the CZA was was synthesized via flame spray pyrolysis (FSP): the semi-continuous collecting system using a bag-house filter allows a productivity of up to 20 g per day (for

comparison: using a batch collection, only 5 g per day could be synthesized). The pristine FSP-CZA was either pelletized together with the nanosized zeolite or suspended in the zeolite mother liquor, then spray dried at MVT and crystallized by steam assisted crystallisation at CRT, in order to obtain CZA+Z or CZA&Z hybrid particulate configurations, respectively; furthermore, the CZA core, obtained either by pelletization or spray drying the FSP-CZA, was enwrapped with a zeolite shell via a two-step hydrothermal synthesis (*in-situ* seeding followed by secondary growth) at CRT (FAU). For the planar systems, pastes containing the nanopowder (FSP-CZA and/or the Z) were prepared and their printability was evaluated by investigations on their rheological behaviour, in order to ensure the success of the coating procedure via by screen printing.

Aim of the of the **Characterization** was the demonstration of the synthesis and accomplishment of the parameters to be implemented in the modelling (e.g. crystallite particle size, porosity, ...). The CZA as well as the STD- catalyst configurations were analysed in terms of the physico-chemical properties and their activity for the STM/STD reaction. The synthesis of the CZA catalyst via FSP can be considered as promising, as it fulfils the requirements reported in the open literature with respect to the structure of the nanoparticles, the specific surface area and the reducibility. Regarding the particulate catalyst structures, the hybrid pellets CZA+Z showed activity for the STD at the conditions measured (p = 45 bar; 220 °C $\leq T \leq$ 280 °C); both the CZA+Z_1 ($\omega_{CZA}/\omega_{Zeo}$ = 1/1) and CZA+Z_5 ($\omega_{CZA}/\omega_{Zeo}$ = 5/1) outperformed the bare CZA catalyst in terms of X_{CO}, while the share of zeolite predetermines whether the STD reaction is limited by MeOH formation (CZA+Z_1) or by its dehydration (CZA+Z_5), in accordance with the modelling results. With respect to the CZA&Z, it was found that this catalyst system presents practical challenges, which could not be overcome in the frame of this work and make it unsuitable for the STD reaction so far: besides the unfeasible ω_{Zeo} beyond 92 wt.-% (according to the modelling, this catalyst composition is far from its optimum at the conditions considered (p = 40 bar; T = 250 °C)), irreversible alterations of the CZA catalyst should occur during steam assisted crystallisation. This latter aspect was investigated in detail for the core@shell system and, due to the similar synthesis conditions, should be expected also for the CZA&Z catalyst. Regarding the planar systems, both the CZA#Z and the CZA//Z were found active for the STD reaction and DME was detected as the main product (p = 45 bar; 220 °C $\leq T \leq$ 280 °C).

Combining Modelling, Synthesis and Characterization tools, from the whole study the following can be concluded:

- The hybrid particulate and planar configurations of close proximity (CZA&Z and CZA&/Z), from a theoretical point of view, correspond to the most promising catalyst systems for the STD reaction among those investigated; the particulate configuration CZA&Z was successfully synthesized but, due to practical challenges, is not suitable for a reaction test so far and the planar counterpart CZA&/Z was not included in the scope of the investigation into the synthesis.
- The **hybrid particulate configuration of medium proximity** (**CZA+Z**) was found to be the most promising catalyst in the form of particulate system for the STD, due to its feasible synthesis and activity under reaction conditions.

- The structured core@shell system (CZA@Z) synthesized via a two-step approach, namely *in-situ* seeding followed by secondary growth, is limited by the mass transport of the reactants to the CZA core catalyst through the zeolite shell; furthermore, irreversible changes of the CZA core during the shell synthesis make this configuration even less active compared to the predictions made in the frame of the modelling.
- The hybrid planar configuration of medium proximity (CZA#Z) was found a feasible system, active and selective for the STD reaction in the μ-CR.
- The **double layer planar configuration** (**CZA//Z**) was successfully synthesized and, both from modelling and characterization results, was found to be the most promising system for the STD reaction in the μ-CR in terms of X_{CO} and S_{DME}.

In the frame of this work, the CO_2-to-MeOH reaction was investigated, in order to find a proper catalyst for the reaction. $Cu/ZnO/ZrO_2$ prepared via FSP was found active and, using the proper precursor solution, MeOH was the main product instead of CO.

This work could pave the way for future investigations, which should deal with a detailed study about the stability of the catalyst over long time on stream and on the co-production of hydrocarbons. As also summarized in this work, in literature several deactivation effects are reported for such catalyst configurations. It is generally agreed, that in hybrid systems, where the two constituents are in close proximity, deactivation effects are to be expected by the interplay of the two constituents, especially under STD reaction conditions. These aspects should be investigated theoretically by modelling as well as evaluated by experimental studies.

List of Abbreviations and Symbols

$\mathbf{A_{cat}^{cell}}$	catalyst area of the cell; $[m^2]$
Bo	Bodenstein number; $[-]$
C	connectivity; $[-]$
CZA	$Cu/ZnO/Al_2O_3$
CZAZ	$Cu/ZnO/Al_2O_3/ZrO_2$
CZA+Z	hybrid particulate catalyst of medium proximity
CZA&Z	hybrid particulate catalyst of close proximity
CZA@Z	structured core@shell catalyst configuration
CZA#Z	hybrid coated catalyst of medium proximity
CZA&/Z	hybrid coated catalyst of close proximity
CZA//Z	structured double layer catalyst configuration
_c	calcined
CZZ	$Cu/ZnO/ZrO_2$
DEGBE	diethylene glycol monobutyl ether
DME	dimethyl ether
EC	ethyl cellulose
EFAl	extra framework aluminum
EHA	2-ethyl hexanoic acid
EtOH	ethanol
$\mathbf{f_a}$	form factor; $[-]$
FID	flame ionization detector
FSP	flame spray pyrolysis
FSP-CZA	CZA synthetized via FSP
F/W	molar flow per mass of catalyst; $\left[mL\ h^{-1}\ g_{CAT}^{-1}\right]$

(F/W)* reagents molar flow per mass of catalyst; $\left[\mathrm{mL_{Reagents}\ h^{-1}\ g_{CAT}^{-1}}\right]$

HC hydrocarbons

$\mathbf{\dot{j}_{i,tr}}$ molar flux from/to the catalyst within cell *i*; $\left[\mathrm{mol\ m^{-2}\ s^{-1}}\right]$

$\mathbf{K_{Pi}}$ equilibrium constant of the reaction *i*; [−]

ICP/OES inductively coupled plasma optical emission spectrometry

isS_P-CZA *in-situ* seeded P-CZA

isS_SD-CZA *in-situ* seeded SD-CZA

lam laminar

$\mathbf{L_{Reac}}$ reactor length; [m]

ME methyl cellulose

MeOH methanol

MTD methanol to DME

MTG methanol to gasoline

MTO methanol to olefins

$\mathbf{\dot{N}_{i,in}}$ inlet molar flow of component *i*; $\left[\mathrm{mol\,s^{-1}}\right]$

$\mathbf{\dot{N}_{i,out}}$ outlet molar flow of component *i*; $\left[\mathrm{mol\,s^{-1}}\right]$

$\mathbf{n_{Rea}}$ number of cells; [−]

n-Z nanosized zeolite

PBR packed-bed-reactor

$\mathbf{P_{Conn}}$ connection probability; [%]

P-CZA CZA pellet

P-CZA_c calcined P-CZA

P-CZA@Z CZA@Z with P-CZA as core

$\mathbf{P_{DME}}$ DME productivity; $\left[\mathrm{mol\ g^{-1}}\right]$

$\mathbf{p_i}$ partial pressure of the component i; [−]

PP polypropylene

PTFE polytetrafluoroethylene

P2X Power-to-X

$\mathbf{r_i}$ rate of the reaction i; $\left[\mathrm{mol\ kg_{CAT}^{-1}\ s^{-1}}\right]$

Re Reynolds number; [−]

s' dimensionless radius; [−]

SAC steam assisted crystallization

Sc Schmidt number; [−]

SD-CZA spray dried CZA

SD-CZA_core SD-CZA after modified shell synthesis without shell

SD-CZA@Z CZA@CZA with SD-CZA as core

SEM scanning electron microscopy

Sh Sherwood number; [−]

$\mathbf{S_i}$ selectivity to component *i*; [%]

SLS static light scattering

SSA specific surface area

STD synthesis gas to DME

STM synthesis gas to MeOH

T terpineol

TCD thermal conductivity detector

TEOS tetraethyl orthosilicate

TGA thermal gravimetric analysis

$\mathbf{T_{IN}}$ inlet temperature; [°C]

TPAOH tetrapropylammonium hydroxide

TPR temperature programmed reduction

tr transfer

$\mathbf{T_{red.}}$ reduction temperature; [°C]

turb turbolent

X xylene mixture

$\mathbf{X_i}$ conversion of component *i*; [%]

$\mathbf{X_{CO}^{eq.}}$ X_{CO} at the equilibrium; [%]

$\mathbf{X_{CO}^{eq.,out}}$ $X_{CO}^{eq.}$ of the gas composition at the reactor outlet; [%]

$\mathbf{w_{cell}}$ cell width; [m]

WGS	water-gas-shift
$\mathbf{y'_{CO}}$	dimensionless concentration of CO; $[-]$
$\mathbf{Y_i}$	yield to component *i*; [%]
$\mathbf{y_i}$	molar fraction of molecule *i*; $[-]$
Z	zeolite H-ZSM-5
$\mathbf{\Delta x}$	length of cell; [m]
$\boldsymbol{\eta}$	dynamic viscosity; $[\mathrm{Pa \cdot s}]$
$\boldsymbol{\gamma}$	shear strain; $[-]$
$\dot{\boldsymbol{\gamma}}$	shear rate; $[\mathrm{s}^{-1}]$
μ**-CR**	micro-channel-reactor
$\boldsymbol{\sigma}$	shear stress; [Pa]
$\boldsymbol{\omega_{CZA}}$	weight fraction of CZA; $[wt. - \%]$
$\boldsymbol{\omega_{STM}}$	weight fraction of STM-catalyst; $[wt. - \%]$
$\boldsymbol{\omega_{MTD}}$	weight fraction of MTD-catalyst; $[wt. - \%]$
$\boldsymbol{\omega_{Zeo}}$	weight fraction of zeolite; $[wt. - \%]$
3D-CPNM	3D-crystallite pore network model

List of Figures

1.1 Scheme of the Power-to-X concept. 1
1.2 CO-conversion (X_{CO}) at the thermodynamic equilibrium for synthesis gas to methanol (STM) and direct synthesis of DME (STD). 2
1.3 Illustration of the catalyst configurations investigated in the frame of this thesis. 3
1.4 Knowledge-based circular work flow pursued in this thesis. 4

2.1 Shear stress (σ) vs. shear rate ($\dot{\gamma}$) plot for diverse kinds of fluids. 17
2.2 a) Schematic representation and b) viscosity and shear rate vs. time (adapted from [113]) of the different phases of the coating via screen printing. 18
2.3 Thixotropic behaviour of a printable paste during coating via screen printing and levelling. . 19
2.4 Printability range of a paste respectively the criteria of the a) yield stress and b) viscosity. . . 19

3.1 Illustration of the catalyst configurations investigated. a) Hybrid configurations on the pellet/layer level with close proximity of the two catalysts in micrometer scale, b) hybrid configurations with medium proximity of the two catalysts in sub-micrometer scale and c) structured catalysts core@shell and double layer configurations. Simplified, the range of ω_{Zeo} investigated and the model of a cell used for the simulation thereof in the accordant reactor are shown. 22
3.2 Flowchart of the model implemented in MatLab®. $TolFun = 10^{-30}$ (termination tolerance). . . 28
3.3 X_{CO} as a function of the relative reactor length (L_{Reac}) and ω_{Zeo} for the particulate systems a) of close proximity CZA&Z and b) of medium proximity CZA+Z in a PBR, for the layered systems c) of close proximity CZA&/Z and d) structured CZA//Z in a µ-CR. 29
3.4 a) X_{CO}, b) S_{DME}, c) S_{MeOH} for the particulate catalyst systems CZA&Z, CZA+Z and CZA@Z in a PBR. 31
3.5 Dimensionless CO concentration (y'_{CO}) versus the dimensionless coordinate (s') of the CZA&Z and the zeolite shell of the CZA@Z system in a PBR. 33
3.6 a) X_{CO}, b) S_{DME}, c) S_{MeOH} for the layered catalyst systems CZA&/Z, CZA#Z and CZA//Z in a µ-CR. 34
3.7 Y_{DME} as a function of catalyst composition in a) particulate configurations in a PBR and b) coated configurations in a µ-CR. 35
3.8 X_{CO} as a function of temperature for all catalyst structures considered: a) particulate configurations in a PBR (ω_{Zeo}(CZA+Z) = 30 wt.%, ω_{Zeo}(CZA&Z) = 40 wt.%, ω_{Zeo}(CZA@Z) = 17 wt.%) and b) coated configurations in a µ-CR (ω_{Zeo}(CZA+Z) = 40 wt.-%, ω_{Zeo}(CZA&/Z) = 40 wt.%, ω_{Zeo}(CZA//Z) = 43 wt.%). 36

3.9 Y_{DME} as a function of temperature for all catalyst structures considered: a) particulate configurations in a PBR (ω_{Zeo}(CZA+Z) = 30 wt.%, ω_{Zeo}(CZA&Z) = 40 wt.%, ω_{Zeo}(CZA@Z) = 17 wt.%) and b) coated configurations in a μ-CR (ω_{Zeo}(CZA+Z) = 40 wt.-%, ω_{Zeo}(CZA&/Z) = 40 wt.%, ω_{Zeo}(CZA//Z) = 43 wt.%). 37
3.10 X_{CO} as a function of temperature and ω_{Zeo} for a) the particulate configuration CZA&Z in a PBR and b) the coated configuration CZA//Z in a μ-CR. 38
3.11 X_{CO} as a function of *F/W* for all catalyst structures considered: a) particulate configurations in a PBR (ω_{Zeo}(CZA+Z) = 30 wt.%, ω_{Zeo}(CZA&Z) = 40 wt.%, ω_{Zeo}(CZA@Z) = 17 wt.%) and b) coated configurations in a μ-CR (ω_{Zeo}(CZA+Z) = 40 wt.-%, ω_{Zeo}(CZA&/Z) = 40 wt.%, ω_{Zeo}(CZA//Z) = 43 wt.%). 39
3.12 Influence of the feed composition for the particulate CZA&Z system on X_{CO_x} and a) Y_{DME} as a function of y_{CO_2}/y_{CO} (H_2 = 57.6 vol.-% = const.) b) P_{DME} as a function of $y_{H_2}/\left(y_{CO}+y_{CO_2}\right)$ (y_{CO_2}/y_{CO}= 1/8 = const.) in a PBR. (ω_{Zeo} = 40 wt.-%). 41

4.1 Illustration of the FSP-nozzle: a) top- and b) lateral-view. 44
4.2 Scheme of the a) batch and b) semi-continuous powder collection systems for the FSP synthesis. 45
4.3 Cumulative mass of a) CZA-1-f for different precursor flow rates and b) CZA-2-f for the precursor flow rate equal to 5 mL min^{-1} synthesized via FSP and collected using the bag-house filter. *Cumulative time of synthesis*: sum of time of several single synthesis runs. 46
4.4 Temperature at the entrance of the bag-house filter over synthesis time for the CZA-1-f and CZA-2-f systems. *Time of synthesis run*: time of a single run. 47
4.5 Illustration of a spray dryer equipment (Figure adapted from [134]). 49
4.6 Microscope picture of the coated foil obtained by screen printing the paste *Hybrid-T1*. 54
4.7 Rheology of the paste *Hybrid-T1*: shear stress/shear rate plot. 55

5.1 a) XRD patterns of the CZA-1-b, CZA-1-f (with adjusted intensity) and the references for CuO and ZnO structures (International Center for Diffraction Data (ICDD)); b) TPR profiles of the CZA-1-b and CZA-1-f nanopowder. 59
5.2 Transmission electron micrograph of the a) CZA-1-b and b) CZA-1-f. 60
5.3 a) XRD patterns of the CZA-1-f, CZA-2-f and the references for CuO and ZnO structures (International Center for Diffraction Data (ICDD)); b) TPR profiles of the CZA-1-f and CZA-2-f nanopowder. 61
5.4 Transmission electron micrograph of the a) CZA-1-f and b) CZA-2-f. 62
5.5 Mass loss over temperature during the TG-analysis of the CZA-1-f, CZA-2-f and, for comparison, of the CZA-1-f_c. 63
5.6 a) XRD patterns of the CZA-2-f_c, CZA-1-f_c, P-CZA_c (with adjusted intensities) and the references for CuO and ZnO structures (International Center for Diffraction Data (ICDD)); b) TPR profiles of the CZA-2-f_c, CZA-1-f_c and P-CZA_c samples. 65
5.7 Transmission electron micrograph of the a) CZA-1-f_c and b) CZA-2-f_c. 66
5.8 SD-CZA characterization: a) SEM image and b) influence of the sonication on the particle size distribution for the evaluation of the mechanical stability. 67
5.9 Activity for the STM reaction in the μ-Berty reactor of P-CZA-1 and P-CZA-2 in terms of X_{CO} as function of the temperature. 68

5.10 Activity for the STM reaction in the μ-Berty reactor of the a) SD-CZA and P-CZA-1 as function of the temperature at different pressure (at $p = 45$ bar: $X_{CO;220\,^{\circ}C}^{eq.,out} = 53.4\,\%$; $X_{CO;260\,^{\circ}C}^{eq.,out} = 23.7\,\%$); b) P-CZA-1 as function of the temperature over different $(F/W)^*$. 69
5.11 Morphological analysis of the CZA&Z: a) TE-micrograph after spray drying; b) SEM-micrograph and details of the outer surface (inset) after the steam assisted crystallization and calcination. 71
5.12 a) XRD patterns of the samples after each step of the shell synthesis (with adjusted intensities), as well as of n-Z for comparison and the references for CuO, ZnO and zeolite MFI structures (International Center for Diffraction Data (ICDD)); b) TPR profiles of the different (intermediate) materials obtained during the shell synthesis procedure. 72
5.13 Morphological analysis of the P-CZA@Z catalyst. a) SE-micrographs of a P-CZA@Z and details of the shell outer surface (inset), b) cross-section analysis of distinct core@shell particles via EPMA/BSE and c) elemental map (EPMA/WDX) for the representative elements for the core (Cu, Zn, Al) and shell (Si, Al). 73
5.14 a) SEM image and b) Si-EPMA/WDX signal of the SD-CZA@Z. 75
5.15 Influence of the zeolite amount in the CZA+Z catalyst on the performance in the STD-reaction. X_{CO}, S_{DME} and S_{MeOH} of a) CZA+Z_1 and b) CZA+Z_5 hybrid catalysts in the μ-Berty reactor as a function of temperature. 76
5.16 Activity for the STM reaction in the μ-Berty reactor after individual steps of the shell synthesis procedure in terms of X_{CO} as a function of the temperature. 77
5.17 Rheological properties of the pastes *Hybrid-T2*, *Hybrid-T3*, *Hybrid-T4*: a) shear stress vs. shear rate and b) viscosity vs. shear rate. 79
5.18 a) Rheological properties of the paste *Hybrid-W*: shear stress vs. shear rate and viscosity vs. shear rate. b) Thixotropy behaviour of the *Hybrid-W* paste. 79
5.19 Rheological properties of the pastes *CZA-1*, *CZA-2* and *CZA-3*: a) shear stress vs. shear rate and b) viscosity vs. shear rate. 81
5.20 Thixotropic behaviour of the *CZA-1* and *CZA-3* pastes. 81
5.21 Rheological properties of the pastes *Zeolite-1*, *Zeolite-2* and *Zeolite-3*: a) shear stress vs. shear rate and b) viscosity vs. shear rate. 82
5.22 Thixotropic behaviour of the *Zeolite-2* and *Zeolite-3* pastes. 83
5.23 Mass loss with respect to the temperature during the TG-analysis of the a) *CZA-1* and b) *Hybrid-T3* pastes. 84
5.24 SE-micrograph of two coated micro-channels (*Hybrid-T3*) after calcination at a) 400 °C and b) 550 °C. c) TPR profiles of the *Hybrid-T3* paste after calcination. 84
5.25 XRD patterns of the calcined *Hybrid-T3* paste, the nano-zeolite (n-Z), the CZA-1-f_c (with adjusted intensities) and the reference data for the CuO, ZnO and MFI-structures International Center for Diffraction Data (ICDD). 85
5.26 a) SE-micrographs, b) cross-sectional analysis of the layer via EPMA/BSE and c) elemental map via EPMA/WDX for Cu and Si of the CZA#Z obtained from the paste *Hybrid-T3*. 86
5.27 a) SE-micrographs, b) cross-sectional analysis of the layer via EPMA/BSE and c) elemental map via EPMA/WDX for Cu and Si of the CZA#Z obtained from the paste *Hybrid-W*. 86
5.28 *CZA-1* paste characterization in comparison with the CZA-1-f_c: a) XRD patterns (with adjusted intensities) and the reference data for the CuO and ZnO; b) TPR profiles. 88

5.29 a) SE-micrographs, b) cross-sectional analysis of the layer via EPMA/BSE and c) elemental map via EPMA/WDX for Cu of the CZA layer obtained from the paste *CZA-3*. 88
5.30 a) SE-micrographs, b) cross-sectional analysis of the layer via EPMA/BSE and c) elemental map via EPMA/WDX for Cu and Si of the CZA//Z system. 89
5.31 Activity of the *Hybrid-T3* pelletized catalyst in terms of X_{CO} and S_i for the STD reaction in the μ-Berty reactor as function of the temperature (at T = 220 °C: $X_{CO}^{eq.,out}$ = 57.5 %; at T = 290 °C: $X_{CO}^{eq.,out}$ = 13.6 %). 91
5.32 Activity of the CZA#Z catalyst system from *Hybrid-W* paste in terms of X_{CO} and S_i in the STD reaction in the μ-CR. 92
5.33 Activity of the *CZA-1* catalyst system in terms of X_{CO} in the STM reaction in the μ-CR. 93
5.34 Activity of the CZA//Z catalyst system in terms of X_{CO} and S_i in the STD reaction in the μ-CR. 94
5.35 Predicting X_{CO} in the a) PBR and b) μ-CR over the bifunctional catalysts implementing the STM-kinetics relative to the CZA obtained in this work. 97

6.1 a) Cumulative mass of the CZZ-1-f and CZZ-2-f collected using the bag-house filter and b) temperature at the entrance of the bag-house filter over synthesis time. *Cumulative time of synthesis*: sum of time of several single synthesis runs. *Time of synthesis run*: time of a single run.104
6.2 XRD patterns of the samples a) ZrO_2-1 and a) ZrO_2-2 before and after calcination, denoted with _c. 106
6.3 XRD patterns of the samples CZZ-1-f, CZZ-2-f and the references for ZrO_2 (sample ZrO_2-2, with adjusted intensity), for CuO and ZnO structures (International Center for Diffraction Data (ICDD)). 108
6.4 TPR profiles of the a) CZZ-*i*-b and b) CZZ-*i*-f nanopowder. 108
6.5 TE-micrographs of the a) CZZ-1-f and b) CZZ-2-f samples. 109
6.6 Mass loss over temperature during the TG-analysis of a) CZZ-1-f and b) CZZ-2-f samples. . . 110
6.7 Activity of a) the P-CZZ-1 and b) the P-CZZ-2 catalysts in terms of X_{CO_2} and S_i as a function of temperature for the CO_2-to-MeOH reaction in the μ-Berty reactor. 111
6.8 Activity of the P-CZA-1 catalyst in terms of X_{CO_2} and S_i for the CO_2-to-MeOH reaction in the μ-Berty reactor. 112

A.1 S_{DME} as a function of X_{CO} (combined simulation data from Figures 3.4 and 3.6) of hybrid catalyst structures of a) close proximity (CZA&Z and CZA&/Z) and b) medium proximity (CZA+Z and CZA#Z). Reaction conditions: p = 40 bar, T = 250 °C, F/W = 2000 mL h^{-1} g_{CAT}^{-1}. . 147
A.2 Scheme of the foils used in the μ-CR. 148
A.3 Scheme of the screen used for the coating via screen printing. 149
A.4 Scheme of the μ-CR. 150
A.5 XRD patterns of the P-CZA-1, P-CZA-2 and the references for CuO and ZnO structures (International Center for Diffraction Data (ICDD)). 151
A.6 SD-CZA characterization: Cu- and Zn-distribution from EPMA/WDX a) before and b) after calcination. 152
A.7 Activity of the P-CZA-1 and a reference catalyst in terms of X_{CO} in the STM reaction in the μ-Berty reactor. 152
A.8 TPR profile of the CZA+Z_5 sample. 153

A.9 Morphological analysis of the CZA+Z_5 catalyst. a) cross-sectional analysis via EPMA/BSE and b) elemental map (EPMA/WDX) for the representative elements for the core (Cu, Zn, Al) and shell (Si, Al). 153
A.10 XRD patterns of the CZA-1-f (with adjusted intensity), CZA&Z and the references for CuO, ZnO and MFI structures (International Center for Diffraction Data (ICDD)). 154
A.11 a) SE-micrograph image and b) Si-EPMA/WDX-images of the SD-CZA_core sample. 154
A.12 Resulting red-coloured suspension obtained mixing the H-ZSM-5 with terpineol. 155
A.13 Reaction scheme of the isomerization of the α-terpineol to 1,8-cineole and 1,4-cineole [161]. . 155
A.14 Parity diagrams of modelled ($y_i^{mod.}$) and experimental ($y_i^{exp.}$) molar fraction of a) CO, b) CO_2, c) H_2 and d) MeOH. 156
A.15 Effect of temperature on y_{CO} for experiments and kinetic model at a) $p = 45$ bar and b) $p = 40$ bar. 157
A.16 Mass loss over temperature during the TG-analysis of the a) ZrO_2-1 and b) ZrO_2-2 samples. . 157

List of Tables

3.1 Parameters used for the modelling of each catalyst configuration. . . . 23
3.2 Parameters used for the modelling of the hybrid catalyst configurations of medium proximity (CZA+Z and CZA#Z). . . . 24
3.3 Parameters used for the modelling of the hybrid catalyst configurations of close proximity (CZA&Z and CZA&/Z). . . . 24
3.4 Parameters used for the modelling of the structured core@shell (CZA@Z) and double layer (CZA//Z) configurations. . . . 25
3.5 Dimensions of the PBR and μ-CR. . . . 27

4.1 Investigation range of the process parameters for the preliminary study and optimized values used during the spray drying. . . . 50
4.2 Preliminary study of the spray drying on commercial particles: process conditions and product properties. . . . 51
4.3 Composition of the pastes prepared in this work. . . . 53

5.1 Summary about the physico-chemical characterization of FSP-CZA samples. . . . 64
5.2 Impurities (K and Na) in the STD-catalysts based on ICP/OES. . . . 74
5.3 X_{CO} over P-CZA-1 and CZA+Z_5 at different reaction temperatures. . . . 76
5.4 $d_{[4,3]50}$ of the powders used for the synthesis of the three coated systems and the correspondent layer thickness obtained. . . . 90
5.5 X_{CO} and selectivity towards hydrocarbons (in %) of the CZA#Z, CZA//Z and CZA+_1 systems. . . . 94
5.6 Resulting estimates of the dimensionless parameters $\beta_1, ..., \beta_6$ obtained by fitting of the STM-kinetic model proposed by Seidel et al. [30] to the data from 34 experiments from the μ-Berty reactor ruled out by the sole kinetics of the STM reaction. . . . 96

6.1 Specific surface area of the ZrO_2 samples before and after calcination. . . . 106
6.2 Specific surface area and metal content of the CZZ samples synthesized via FSP. . . . 107

A.1 X_{CO} (data shown are mean values within 4 h TOS each) v.s. time on stream of P-CZA catalyst for different reaction temperatures. . . . 151
A.2 k_i values at different temperatures for commercial CZA (calculated according to Ref. [30]) and self-made CZA. . . . 155

Bibliography

[1] J. Cook, N. Oreskes, P.T. Doran, W.R.L. Anderegg, B. Verheggen, E. W. Maibach, J.S. Carlton, S. Lewandowsky, A.G. Skuce, S.A. Green, D. Nuccitelli, P. Jacobs, M. Richardson, B. Winkler, R. Painting, and K. Rice. *Consensus on consensus: a synthesis of consensus estimates on human-caused global warming*. Environ. Res. Lett., Vol. 11, pp. 1-7, 2016.

[2] NASA Global Climate Change. *Scientific Consensus: Earth's Climate is Warming*. 2019, Available Online: https://climate.nasa.gov/scientific-consensus/, Accessed: 27.10.2019.

[3] United Nations. *Paris Agreement*. 2015, Available Online: https://unfccc.int/sites/default/files/english_paris_agreement.pdf, Accessed: 27.10.2019.

[4] V. Masson-Delmotte, P. Zhai, H. O. Pörtner, D. Roberts, J. Skea, P.R. Shukla, A. Pirani, W. Moufouma-Okia, C. Péan, R. Pidcock, S. Connors, J.B.R. Matthews, Y. Chen, M.I. Zhou, X. adn Gomis, E. Lonnoy, T. Maycock, M. Tignor, and T. Waterfield. *Global Warming of* 1.5 °C. *An IPCC Special Report on the impacts of global warming of* 1.5 °C *above pre-industrial levels and related global greenhouse gas emission pathways, in the context of strengthening the global response to the threat of climate change, sustainable development, and efforts to eradicate poverty*. Intergovernmental Panel on Climate Change, IPCC, 2019.

[5] United Nations Framework Convention on Climate Change. *Summary of GHG Emissions for European Union (KP)*. 2018, Available Online: https://di.unfccc.int/ghg_profiles/annexOne/EUC/EUC_ghg_profile.pdf, Accessed: 27.10.2019.

[6] Official Journal of the European Union. *DIRECTIVE 2009/28/EC OF THE EUROPEAN PARLIAMENT AND OF THE COUNCIL of 23 April 2009 on the promotion of the use of energy from renewable sources and amending and subsequently repealing Directives 2001/77/EC and 2003/30/EC (Text with EEA relevance)*. 05.06.2009, Available Online: https://eur-lex.europa.eu/eli/dir/2009/28/oj, Accessed: 25.10.2019.

[7] Official Journal of the European Union. *DIRECTIVE (EU) 2018/2001 OF THE EUROPEAN PARLIAMENT AND OF THE COUNCIL of 11 December 2018 on the promotion of the use of energy from renewable sources (recast) (Text with EEA relevance)*. 05.06.2009, Available Online: https://eur-lex.europa.eu/eli/dir/2009/28/oj, Accessed: 25.10.2019.

[8] E. I. Koytsoumpa, C. Bergins, and E. Kakaras. *The CO_2 economy: Review of CO_2 capture and reuse technologies*. J. Supercrit. Fluids, Vol. 132, pp. 3-16, 2018.

[9] German Federal Ministry od Eucation and Research. *The P2X Kopernikus project*. 2019, Available Online: https://www.kopernikus-projekte.de/en/projects/power2x, Accessed: 27.10.2019.

[10] R.U. Dietrich, F. Albrecht, and T. Pregger. *Erzeugung von Strom und flüssigen Kraftstoffen mit geringem Carbon Footprint*. Chem. Ing. Tech., Vol. 90, pp. 212-225, 2018.

[11] P. Schmidt, V. Batteiger, A. Roth, W. Weindorf, and T. Raksha. *Power-to-Liquids as Renewable Fuel Option for Aviation: A Review*. Chem. Ing. Tech., Vol. 90, pp. 127-140, 2018.

[12] M. Müller and U. Hübsch. *Dimethyl Ether*. Ullmann's Encyclopedia of Industrial Chemistry, Vol. 11, 2012.

[13] C. Arcoumanis, C. Bae, R. Crookes, and E. Kinoshita. *The potential of di-methyl ether (DME) as an alternative fuel for compression-ignition engines: A review*. Fuel, Vol. 87, pp. 1014-1030, 2008.

[14] S.H. Park and S.H. Yoon. *Injection strategy for simultaneous reduction of NO_x and soot emissions using two-stage injection in DME fueled engine*. Appl. Energy, Vol. 143, pp. 262-270, 2015.

[15] D. Sheldon. *Methanol Production - A Technical History*. Johnson Matthey Technol. Rev., Vol. 61, pp. 172-182, 2017.

[16] M. Bertau, H. Offermanns, L. Plass, F. Schmidt, and H. J. Wernicke. *Methanol: The Basic Chemical and Energy Feedstock of the Future*. Springer-Verlag, Heidelberg, 2014.

[17] J.B. Hansen and P.E.H. Nielsen. *Methanol Synthesis*, chapter chpt. 13.13, pages pp. 2920–2949. Wiley-VCH Verlag GmbH and Co., 2008.

[18] M. Gentzen, D. E. Doronkin, T.L. Sheppard, J.D. Grunwaldt, J. Sauer, and S. Behrens. *An intermetallic Pd_2Ga nanoparticle catalyst for the single-step conversion of CO-rich synthesis gas to dimethyl ether*. Appl. Catal., A, Vol. 562, pp. 206-214, 2018.

[19] J. Xu, X. Su, X. Liu, X. Pan, G. Pei, Y. Huang, X. Wang, T. Zhang, and H. Geng. *Methanol synthesis from CO_2 and H_2 over $Pd/ZnO/Al_2O_3$: Catalyst structure dependence of methanol selectivity*. Appl. Catal., A, Vol. 514, pp. 51-59, 2016.

[20] H. Sakurai and M. Haruta. *Synergism in methanol synthesis from carbon dioxide over gold catalysts supported on metal oxides*. Catal. Today, Vol. 29, pp. 361-365, 1996.

[21] B. Kniep, M. Hieke, P. Kurr, M. Behrens, and R. Schlgel. *Methanolsynthesekatalysaotr auf Basis von Kupfer, Zink und Auminium*. Sd Chemie IP GmgH & Co, DE102011086451A1, 16.05.2013.

[22] G.C. Chichen and J.R. Jennings. *Copper catalyst for carbon oxide conversion*. Imperial Chemical Industry PLC, EP0296734A1, 28.12.1988.

[23] M. Behrens, D. Brennecke, F. Girgsdies, S. Kiner, A: Trunschke, N. Nasrudin, S. Zakaria, N. F. Idris, S.B.A. Hamid, B. Kniep, R. Fischer, W. Busser, W. Muhler, and R. Schlgl. *Understanding the complexity of a catalyst synthesis: Co-precipitation of mixed Cu,Zn,Al hydroxycarbonate precursors for $Cu/ZnO/Al_2O_3$ catalysts investigated by titration experiments*. Appl. Catal., A, Vol. 392, pp. 93-102, 2011.

[24] Z. Chu, H. Chen, Y. Yu, Q. Wang, and D. Fang. *Surfactant-assisted preparation of $Cu/ZnO/Al_2O_3$ catalyst for methanol synthesis from syngas*. J. Mol. Catal. A: Chem., Vol. 366, pp. 48-53, 2013.

[25] X. Zhang, L. Zhong, Q. Guo, H. Fan, H. Zheng, and K. Xie. *Influence of the calcination on the activity and stability of the $Cu/ZnO/Al_2O_3$ catalyst in liquid phase methanol synthesis*. Fuel, Vol. 89, pp. 1348-1352, 2010.

[26] G.H. Graaf, E.J. Stamhuis, and A.A.C.M. Beenackers. *Kinetics of low-pressure Methanol Synthesis*. Chem. Eng. Sci., Vol. 43, pp. 3185-3195, 1988.

[27] K.M. Vanden Bussche and G.F. Froment. *A Steady-State Kinetic Model for Methanol Synthesis and the Water Gas Shift Reaction on a Commercial Cu/ZnO/Al_2O_3 Catalyst*. J. Catal., Vol. 161, pp. 1-10, 1996.

[28] M. Behrens, F. Studt, I. Kasatkin, S. Kühl, M. Hävecker, F. Abild-Pedersen, S. Zander, F. Girgsdies, P. Kurr, B.L. Kniep, M. Tovar, R. W. Fischer, J.K. Nørskov, and R. Schlögl. *The Active Site of Methanol Synthesis over Cu/ZnO/Al_2O_3 Industrial Catalysts*. Science, Vol. 336, pp. 893-897, 2012.

[29] M. Behrens, S. Zander, P. Kurr, N. Jacobsen, G. Senker, J.and Koch, T. Ressler, R. W. Fischer, and R. Schlgl. *Performance Improvement of Nanocatalysts by Promoter-Induced Defects in the Support Material: Methanol Synthesis over Cu/ZnO:Al*. J. Am. Chem. Soc., Vol. 135, pp. 6061-6068, 2013.

[30] C. Seidel, A. Jörke, B. Vollbrecht, A. Seidel-Morgenstern, and A. Knienle. *Kinetic modeling of methanol synthesis from renewable resources*. Chem. Eng. Sci., Vol. 175, pp. 130-138, 2018.

[31] Y. Yang, C.A. Mims, D. H. Mei, C.H.F. Peden, and C.T. Campbell. *Mechanistic studies of methanol synthesis over Cu from CO/CO_2/H_2/H_2O mixtures: The source of C in methanol and the role of water*. J. Catal., Vol. 298, pp. 10-17, 2013.

[32] E.L. Kunkes, F. Studt, F. Abild-Pedersen, R. Schlgl, and M. Behrens. *Hydrogenation of CO_2 to methanol and CO on Cu/ZnO/Al_2O_3: Is there a common intermediate or not?* J. Catal., Vol. 328, pp. 43-48, 2015.

[33] L.C. Grabow and M. Mavrikakis. *Mechanism of Methanol Synthesis on Cu through CO_2 and CO Hydrogenation*. ACS Catal., Vol. 1, pp. 365-384, 2011.

[34] F. Studt, M. Behrens, N. Kunkes, E.L. Thomas, S. Zander, A. Tarasov, J. Schumann, E. Frei, J.B. Varley, F. Abild-Pedersen, J.J. Norskov, and R. Schlögl. *The Mechanism of CO and CO_2 Hydrogenation to Methanol over Cu-Based Catalysts*. Chem. Cat. Chem., Vol. 7, pp. 1105-1111, 2015.

[35] S. Kuld, M. Thorhauge, H. Falsig, C. F. Elkjr, S. Helveg, I. Chorkendorff, and J. Sehested. *Quantifying the promotion of Cu catalysts by ZnO for methanol synthesis*. Science, Vol. 352, pp. 969-974, 2016.

[36] I. Kasatkin, P. Kurr, B. Kniep, A. Trunschke, and R. Schlgl. *Role of Lattice Strain and Defects in Copper Particles on the Activity of Cu/ZnO/Al_2O_3 Catalysts for Methanol Synthesis*. Angew. Chem. Int. Ed., Vol. 46, pp. 7324-7327, 2007.

[37] M.M. Gnter, T. Ressler, B. Bems, C. Bscher, T. Genger, O. Hinrichsen, M. Muhler, and R. Schlgl. *Implication of the microstructure of binary Cu/ZnO catalysts for their catalytic activity in methanol synthesis*. Catal. Lett., Vol. 71, pp. 37-44, 2001.

[38] R. Ahmad, M. Hellinger, M. Buchholz, H. Sezen, L. Gharnati, C. Wöll, J. Sauer, M. Döring, J.D. Grunwaldt, and U. Arnold. *Flame-made Cu/ZnO/Al_2O_3 catalyst for dimethyl ether production*. Catal. Commun., Vol. 43, pp. 52-56, 2014.

[39] J.R. Jensen, T. Johannessen, S. Wedel, and H. Livbjerg. *A study of Cu/ZnO/Al_2O_3 methanol catalysts prepared by flame combustion synthesis*. J. Catal., Vol. 218, pp. 67-77, 2003.

[40] S.E. Pratsinis. *Flame aerolos synthesis of ceramic powders*. Prog. Energy Combust. Sc., Vol. 24, pp. 197-219, 1998.

[41] R. Strobel and S.E. Pratsinis. *Effect of solvent composition on oxide morphology during flame spray pyrolysis of metal nitrates*. Phys. Chem. Chem. Phys., Vol. 13, pp. 9246-9252, 2011.

[42] R. Strobel, A. Baiker, and S.E. Pratsinis. *Aerosol flame synthesis of catalysts*. Adv. Powder Technol., Vol. 17, pp. 457-480, 2006.

[43] C.Y. Chiang and S.H. Aroh, K. Ehrman. *Copper oxide nanoparticle made by flame spray pyrolysis for photoelectrochemical water splitting e Part I. CuO nanoparticle preparation*. Int. J. Hydrogen Energy, Vol. 37, pp. 4871-4879, 2012.

[44] J.H. Kim, V.I. Babushok, T.A. Germer, G.W. Mullholland, and S.H. Ehrman. *Cosolvent-assisted spray pyrolysis for the generation of metal particles*. J. Mater. Res., Vol. 18, pp. 1614-1622, 2003.

[45] R.K. Pati, I.C. Lee, S. Hou, O. Akhuemonkhan, K.J. Gaskell, Q. Wang, A.I. Frenkel, D. Chu, L. G. Salamanca-Riba, and S.H. Ehrman. *Flame Synthesis of Nanosized Cu-Ce-O, Ni-Ce-O, and Fe-Ce-O Catalysts for the Water-Gas Shift (WGS) Reaction*. ACS Appl. Mater. Interfaces, Vol. 1, pp. 2624-2635, 2009.

[46] R. Dadgar, F. anf Myrstad, P. Pfeifer, A. Holmen, and H.J. Venvik. *Direct dimethyl ether synthesis from synthesis gas: The influence of methanol dehydration on methanol synthesis reaction*. Catal. Today 270, Vol. 270, pp. 76-84, 2016.

[47] F. S. Ramos, D. de Farias, L. E. P. Borges, J. L. Monteiro, M. A. Fraga, E. F. Sousa-Aguiar, and L. G. Appel. *Role of dehydration catalyst acid properties on one-step DME synthesis over physical mixtures*. Catal. Today, Vol. 101, pp. 39-44, 2005.

[48] K. Saravanan, N. Ham, H.and Tsubaki, and J.W. Bae. *Recent progress for direct synthesis of dimethyl ether from syngas on the heterogeneous bifunctional hybrid catalysts*. Appl. Catal., B, Vol.217, pp. 494-522, 2017.

[49] A. García-Trenco and A. Martínez. *A rational strategy for preparing Cu-ZnO/H-ZSM-5 hybrid catalystswith enhanced stability during the one-step conversion of syngas todimethyl ether (DME)*. Appl. Catal., A, Vol. 493, pp. 40-49, 2015.

[50] M. Cai, V. Subramanian, V.V. Sushkevich, V.V. Ordomsky, and A.Y. Khodakov. *Effect of Sn additives on the CuZnAl-HZSM-5 hybrid catalysts for thedirect DME synthesis from syngas*. Appl. Catal., A, Vol. 502, pp. 370-379, 2015.

[51] H. Jiang, H. Bongard, W Schmidt, and F. Schüth. *One-pot synthesis of mesoporous Cu-γ-Al_2O_3 as bifunctional catalyst for direct dimethyl ether synthesis*. Microporous Mesoporous Mater., Vol. 164, pp. 3-8, 2012.

[52] J. Ereña, R. Garona, J.M. Arandes, and J. Bilbao. *Direct Synthesis of Dimethyl Ether From (H_2+CO) and (H_2+CO_2) Feeds. Effect of Feed Composition*. Int. J. Chem. Reactor Eng., Vol. 3, Article A44, 2005.

[53] F. Frusteri, M. Cordaro, C. Cannilla, and G. Bonura. *Multifunctionality of Cu-ZnO-ZrO_2/H-ZSM5 catalysts for the one-stepCO_2-to-DME hydrogenation reaction*. Appl. Catal., B, Vol. 162, pp. 57-65, 2015.

[54] J.W. Jeong, C. Ahn, D.H. Lee, S.H. Um, and J.W. Bae. *Effects of Cu-ZnO Content on Reaction Rate for Direct Synthesis of DME from Syngas with Bifunctional Cu-ZnO/gamma-Al_2O_3 Catalyst*. J. Mol. Catal. A: Chem., Vol. 261, pp. 104-111, 2013.

[55] Ateka.A., I. Sierra, J. Ereña, J. Bilbao, and A.T. Aguayo. *Performance of CuO-ZnO-ZrO_2 and CuO-ZnO-MnO asmetallic functions and SAPO-18 as acid function of the catalyst for the synthesis of DME co-feeding CO_2*. Fuel Process. Technol., Vol. 152, pp. 34-45, 2016.

[56] M. Gentzen, W. Habicht, D.E. Doronkin, J.D. Grunwaldt, J. Sauer, and S. Behrens. *Bifunctional hybrid catalysts derived from Cu/Zn-based nanoparticles for single-step dimethyl ether synthesis*. Catal. Sci. Technol., Vol. 6, pp. 1054-1063, 2016.

[57] G. Yang, N. Tsubaki, J. Shamoto, Y. Yoneyama, and Y. Zhang. *Confinement Effect and Synergistic Function of H-ZSM-5/Cu-ZnO-Al_2O_3 Capsule Catalyst for One-Step Controlled Synthesis*. J. Am. Chem. Soc., Vol. 132, pp. 8129-8136, 2010.

[58] R. Phienluphon, K. Pinkaew, G. Yang, J. li, Q. Wei, Y. Yoneyama, T. Vitidsant, and N. Tsubaki. *Designing core (Cu/ZnO/Al_2O_3)-shell (SAPO-11) zeolite capsule catalyst with a facile physical way for dimethyl ether direct synthesis from syngas*. Chem. Eng. J.,Vol. 270, pp. 605-611, 2015.

[59] Y. Wang, W. Wang, Y. Chen, J. Ma, and R. Li. *Synthesis of dimethyl ether from syngas over core-shell structure catalyst CuO-ZnO-Al_2O_3@SiO_2-Al_2O_3*. Chem. Eng. J., Vol. 250, pp. 248-256, 2014.

[60] K. Pinkaew, G. Yang, T. Vitidsant, Y. Jin, C. Zeng, Y. Yoneyama, and N. Tsubaki. *A new core-shell-like capsule catalyst with SAPO-46 zeolite shell encapsulated Cr/ZnO for the controlled tandem synthesis of dimethyl ether from syngas*. Fuel, Vol. 111, pp. 727-732, 2013.

[61] M. Sánchez-Contador, A. Ateka, and J. Aguayo, A.T. Bilbao. *Direct synthesis of dimethyl ether from CO and CO_2 over a core-shell structured CuO-ZnO-ZrO_2@SAPO-11 catalyst*. Fuel Process. Technol., Vol. 179, pp. 285-268, 2018.

[62] R. Nie, H. Lei, S. Pan, L. Wang, J. Fei, and Z. Hou. *Core-shell structured CuO-ZnO@H-ZSM-5 catalysts for CO hydrogenation to dimethyl ether*. Fuel, Vol., Vol. 96, pp. 419-425, 2012.

[63] R. Ahmad, D. Schrempp, S. Behrens, J. Sauer, M. Döring, and U. Arnold. *Zeolite-based bifunctional catalysts for the single step synthesis of dimethyl ether from CO-rich synthesis gas*. Fuel Process. Technol., Vol. 121, pp. 38-46, 2014.

[64] A. García-Trenco and A. Martínez. *Study of the interaction between components in hybrid CuZnAl/HZSM-5 catalysts and its impact in the syngas-to-DME reaction*. Catal. Today, Vol. 179, pp. 43-51, 2012.

[65] A. García-Trenco and A. Martínez. *Direct synthesis of DME from syngas on hybrid CuZnAl/ZSM-5 catalysts: New insights into the role of zeolite acidity*. Appl. Catal., A, Vol. 411-412, pp. 170-179, 2012.

[66] A. García-Trenco, S. Valencia, and A. Martínez. *The impact of zeolite pore structure on the catalytic behaviorof CuZnAl/zeolite hybrid catalysts for the direct DME synthesis*. Appl. Catal., A, Vol. 468, pp. 102-111, 2013.

[67] A. García-Trenco and A. Martínez. *The influence of zeolite surface-aluminum species on the deactivationof CuZnAl/zeolite hybrid catalysts for the direct DME synthesis*. Catal. Today, Vol. 227, pp. 144-153, 2014.

[68] R. Peláez, P. Marín, and S. Ordóñez. *Direct synthesis of dimethyl ether from syngas over mechanical mixtures of CuO/ZnO/Al_2O_3 and γ-Al_2O_3: Process optimization and kinetic modelling*. Fuel Process. Technol., Vol. 168, pp. 40-49, 2017.

[69] J. Erena, I. Sierra, M. Olazar, A.G. Gayubo, and A.T. Aguayo. *Deactivation of a CuO-ZnO-Al_2O_3/γ-Al_2O_3 Catalyst in the Synthesis of Dimethyl Ether*. Ind. Eng. Chem. Res., Vol. 47, pp. 2238-2247, 2008.

[70] A. T. Aguayo, J. Ereña, D. Mier, M. Arandes, M. Olazar, and J. Bilbao. *Kinetic Modeling of Dimethyl Ether Synthesis in a Single Step on a CuO-ZnO-Al_2O_3/γ-Al_2O_3 Catalyst*. Ind. Eng. Chem. Res., Vol. 46, pp. 5522-5530, 2007.

[71] E. Lorenz, P. Wehling, M. Schlereth, and B. Kraushaar-Czarnetzki. *Influence of the spatial arrangement of catalyst components in thesingle-stage conversion of synthesis gas to gasoline*. Catal. Today, Vol. 275, pp. 183-190, 2016.

[72] M. Bjørgen, S. Svelle, F. Joensen, J. Nerlov, S. Kolboe, F. Bonino, L. Palumbo, S. Bordiga, and U. Olsbye. *Conversion of methanol to hydrocarbons over zeolite H-ZSM-5: On the origin of the olefinic species*. J. Catal., Vol. 249, pp. 195-207, 2007.

[73] J. Ereña, R. Garona, J. M. Arandes, A.T. Aguayo, and J. Bilbao. *Effect of operating conditions on the synthesis of dimethyl ether over a CuO-ZnO-Al_2O_3/NaHZSM-5 bifunctional catalyst*. Catal. Today, Vol. 107-108, pp. 467-473, 2005.

[74] M. Cai, V. Subramanian, S. Moldovan, O. Ersen, V. Valtchev, V.V. Ordomsky, and A.Y. Khodakov. *Direct dimethyl ether synthesis from syngas on copper-zeolite hybrid catalysts with a wide range of zeolite particle sizes*. J. Catal., Vol. 338, pp. 227-238, 2016.

[75] G. Bercic and J. Levec. *Catalytic Dehydration of Methanol to Dimethyl Ether. Kinetic Investigation and Reactor Simulation*. Ind. Eng. Chem. Res., No. 32, pp. 2478-2484, 1993.

[76] Y. Tavan, S.H. Hosseini, M. Ghavipour, M.R.K. Nikou, and A. Shariati. *From laboratory experiments to simulation studies of methanol dehydration to produce dimethyl ether-Part I: Reaction kinetic study*. Chem. Eng. Process., Vol. 73, pp. 144-150, 2013.

[77] A. Hadipour and M. Sohrabi. *Kinetic Parameters and Dynamic Modeling of a Reactor for Direct Conversion of Synthesis Gas to Dimethyl Ether*. J. Ind. Eng. Chem., Vol. 13, pp. 558-565, 2007.

[78] W.Z. Lu, L.H. Teng, and W.D. Xiao. *Simulation and experiment study of dimethyl ether synthesis from syngas in a fluidized-bed reactor*. Chem. Eng. Sci., Vol. 59, pp. 5455-5464, 2004.

[79] R. Peláez, P. Marín, F. V. Díez, and S. Ordóñez. *Direct synthesis of dimethyl ether in multi-tubular fixed-bed reactors: 2D multi-scale modelling and optimum design*. Fuel Process. Technol., Vol. 174, pp. 149-157, 2018.

[80] G.H. Graaf, H. Scholtens, E.J. Stamhius, and A.A.C.M. Beenackers. *Intra-particle diffusion limitations in the low-pressure Methanol Synthesis*. Chem. Eng. Sci., Vol. 45, pp. 773-783, 1990.

[81] B.J. Lommerts, G.H. Graaf, and A.A.C.M. Beenackers. *Mathematical modeling of internal mass transport limitations in methanol synthesis*. Chem. Eng. Sci., Vol. 55, pp. 5589-5598, 2000.

[82] Y.I. Pyatnitskii, P.E. Strizhak, and N. K. Lunev. *Kinetic modeling for the conversion of synthesis gas to dimethyl ether on a mixed Cu-ZnO-Al_2O_3 catalyst with γ-Al_2O_3*. Theor. Exp. Chem., Vol. 45, pp. 325-330, 2009.

[83] H. Pennemann, M Dobra, M. Wichert, and G. Kolb. *Optimization of Wash-Coating Slurries as Catalyst Carrier for Screen Printing into Microstructured Reactors*. Chem. Eng. Technol, Vol. 36, pp. 1033-1041, 2013.

[84] V. Meille. *Review on methods to deposit catalysts on structured surfaces*. Appl. Catal., A, Vol. 315, pp. 1-17, 2006.

[85] O. K. Echendu, S.Z. Werta, F.B. Dejene, and V. Craciun. *Electrochemical deposition and characterization of ZnOS thin films for photovoltaic and photocatalysis applications*. J. Alloys Compd., Vol. 769, pp. 201-209, 2018.

[86] C.H. Leu, C.C. Chen, S.C. King, J.M. Huang, S.S. Tzeng, and W.C. Chang. *Influence of CuO/ZnO/Al_2O_3 wash-coating slurries on the steam reforming reaction of methanol*. Int. J. Hydrogen Energy, Vol. 36, pp. 12231-12237, 2011.

[87] N.R. Peela, A. Mubayi, and D. Kunzru. *Washcoating of γ-alumina on stainless steel microchannels*. Catal. Today, Vol. 147S, pp. S17-S23, 2009.

[88] P. Pfeifer, K. Schubert, M.A. Liauw, and G. Emig. *PdZn catalysts prepared by washcoating microstructured reactors*. Appl. Catal., A, Vol. 270, pp. 165-175, 2004.

[89] R. Zapf, C. Becker-Willinger, K. Berresheim, H. Bolz, H. Gnaser, V. Hessel, G. Kolb, P. Löb, A.K. Pannwitt, and A. Ziogas. *Detailed characterization of various porous alumina-based catalyst coatings within microchannels and their testingfor methanol steam reforming*. Trans. IChemE, Vol. 81, Part A, pp. 721-729, 2003.

[90] V. Meille, S. Pallier, G.V. Santa Cruz Bustamante, M. Roumanie, and J.P. Revmond. *Deposition of γ-Al_2O_3 layers on structured supports for the design of new catalytic reactors*. Appl. Catal., A, Vol. 286, pp. 232-238, 2005.

[91] M.S. Sharifiyan, A. Shanaghi, and P.K. Moradi, H. Chu. *Effects of high concentration of Benzotriazole on corrosion behavior of nanostructured titania-alumina composite coating deposited on Al 2024 by sol-gel method*. Surf. Coat. Technol. , Vol. 321, pp. 36-44, 2017.

[92] W.A. Thompson, C. Perier, and M.M. Maroto-Valer. *Systematic study of sol-gel parameters on TiO_2 coating for CO_2 photoreduction*. Appl. Catal., B, Vol. 238, pp. 136-146, 2018.

[93] N. Sahu, B. Parija, and S. Panigrahi. *Fundamental understanding and modeling of spin coating process : A review*. Indian J. Phys., Vol. 83, pp. 493-502, 2009.

[94] B. Derby. *Inkjet Printing of Functional and Structural Materials: Fluid Property Requirements, Feature Stability, and Resolution*. Annu. Rev. Mater. Res. 2010, Vol. 40, pp. 395-414, 2010.

[95] H. Wijshoff. *Drop dynamics in the inkjet printing process*. Curr. Opin. Colloid Interface Sci., Vol. 36, pp.20-27, 2018.

[96] S.K. Eshkalak, W.A.D.A.M. Chinnappan, A. Javathilaka, E. Khatibzadeh, M. Kowsari, and S. Ramakrishna. *A review on inkjet printing of CNT composites for smart applications*. Appl. Mater. Today , Vol. 9, pp. 372-386, 2017.

[97] S. Lee, T. Boeltken, A.K. Mogalicherla, U. Gerhards, P. Pfeifer, and R. Dittmeyer. *Inkjet printing of porous nanoparticle-based catalyst layers in microchannel reactors*. Appl. Catal., A, Vol. 467, pp. 69-75, 2013.

[98] M. Siebert, R.R. Zimmermann, M. Armbrüster, and R. Dittmeyer. *Inkjet Printing of GaPd2 into Micro-Channels for the Selective Hydrogenation of Acetylene*. ChemCatChem, Vol. 9, pp. 3733-3742, 2017.

[99] X. Liu, T. J. Tarn, F. Huang, and J. Fan. *Recent advances in inkjet printing synthesis of functional metal oxides*. Particuology, Vol. 19, pp. 1-13, 2015.

[100] S. Lee. *Novel bifunctional double-layer catalyst for application in microreactor for direct DME synthesis*. Dissertation. Karlsruhe Institute of Technology, Karlsruhe, 2016.

[101] W. Li, J. Yang, Q. Jiang, R. Li, and L. Zhao. *Electrochemical deposition of PbI_2 for perovskite solar cells*. Sol. Energy, Vol. 159, pp. 300-305, 2018.

[102] S. Morelli, R. Pérez, A. Querejeta, L Muñoz, J. Lusvarghi, M. Lassinantti Gualtieri, and H.J. Bolelli, G. Grande. *Photocatalytic enamel/TiO_2 coatings developed by electrophoretic deposition for methyl orange decomposition*. Ceram. Int., Vol. 44, pp. 16199-16208, 2018.

[103] J.H. Park. *Chemical vapor deposition*. ASM International, Materials Park, U.S.A., 2001.

[104] K. Seshan. *Handbook of thin-film deposition processes and techniques. Principles, Methods, Equipment and Applications*. Noyes Publications; William Andrew Publishing, Norwich, New York, U.S.A., 2002.

[105] D.R. Sahu, S.Y. Lin, and J.L. Huang. *Improved properties of Al-doped ZnO film by electron beam evaporation technique*. Microelectron. J., Vol. 38, pp. 245-250, 2008.

[106] S. Stolz. *Siebdruck von elektrisch leitfaehigen Keramiken zur Entwicklung heizbarer keramischer Mikrokomponenten*. Dissertation. Forschungszentrum Karlsruhe, Eggenstein-Leopoldshafen, 2004.

[107] H.W. Lin, C.P. Chang, W.H. Hwu, and M.D. Ger. *The rheological behaviors of screen-printing pastes*. J. Mater. Process. Technol., Vol. 197, pp. 284-291, 2008.

[108] M. R. Somalu, A. Muchtar, Daud. W. R. W., and N. P. Brandon. *Screen-printing inks for the fabrication of solid oxide fuel cell films: A review*. Renewable Sustainable Energy Rev., Vol. 75, pp. 426-439, 2017.

[109] E. Ramasamy, W.J. Lee, D.Y. Lee, and J.S. Song. *Portable, parallel grid dye-sensitized solar cell module prepared by screen printing*. J. Power Sources, Vol. 165, pp. 446-449, 2007.

[110] M. Gromada, D. Gardini, P. Galizia, and C. Galassi. *Processing and characterization of screen printing $Ba_{0.5}Sr_{0.5}Co_{0.8}Fe_{0.2}O_{3-\delta}$ inks*. Bull. Mater. Sci., Vol. 39, pp. 559-567, 2016.

[111] C. Sun, M. Klumpp, P. Binder, J. Pfeifer, and R. Dittmeyer. *Einstufige Treibstoffsynthese mittels gedruckter Katalysatorschichten in mikrostrukturierten Reaktoren*. Chem. Ing. Tech., Vol. 89, pp. 894-902, 2017.

[112] Malvern Instruments Limited. *A Basic Introduction to Rheology*. Malvern, Worcestershire, UK, 2016.

[113] R.E. Trease and R.L. Dietz. *Rheology of Pastes in Thick-Film Printing*. Solid State Technol., pp. 39-43, 1972.

[114] C. Sun. *Direct syngas-to-fuel: integration of Fischer-Tropsch synthesis and hydrocracking in micro-structured reactors*. Karlsruhe Institute of Technoogy, Karlsruhe, 2017.

[115] P. Ried, C. Lorenz, T. Bronstrup, A. Graule, N.H. Menzler, W. Sitte, and P. Holtappels. *Processing of YSZ screen printing pastes and the characterization of the electrolyte layers for anode supported SOFC*. J. Eur. Cerm. Soc., Vol. 28, pp. 1801-1808, 2008.

[116] A. Sanson, E. Roncari, S. Boldrini, P. Mangifesta, and L. Doubova. *Eco-Friendly Screen-Printing Inks of Gadolinia Doped Ceria*. J. Fuel Cell Sci. Technol., Vol. 7, pp. 1-5, 2010.

[117] S. P. Wu, L.Q. Zheng, Q.Y. Zhao, and X.H. Ding. *Preparation and characterization of high-temperature silver thick film and its application in multilayer chip inductances*. Colloids Surf., A: Physicochem. Eng. Aspects, Vol. 372, pp. 120-126, 2010.

[118] W. Ding. *Simulation-Assisted Design of Polycrystalline ZeoliteCatalysts*. Dissertation. Karlsruhe Institute of Technology. KIT Scientific Publishing, Karlsruhe, 2016.

[119] W. Ding, M. Klumpp, S. Lee, S. Reuß, S. A. Al-Thabaiti, P. Pfeifer, W. Schwieger, and R. Dittmeyer. *Simulation of One-Stage Dimethyl Ether Synthesis over a Core-Shell Catalyst*. Chem. Ing. Tech., Vol. 87, pp. 702-712, 2016.

[120] C. Baerlocher, L.B. McCusker, and D.H. Olson. *Atlas of Zelte Frameworks Types*. Elsevier B. V., Amsterdam, 2007.

[121] W. He, Lv Weiqiang, and J. Dickerson. *Gas Transport in Solid Oxide Fuel Cells, Chap. 2*. Springer, Heidelberg, 2014.

[122] S. Tauro. *One-Step Synthesis of Dimethyl Ether Using Microreactors*. Dissertation. Karlsruhe Institute of Technology. Shaker, Aachen, 2014.

[123] VDI-Gesellschaft Verfahrenstechnik und Chemieingenieurwesen-Herausgeber. *VDI-Wärmeatlas*. Springer-Verlag, Berlin Heidelberg, 2013.

[124] W. Ding, H. Li, P. Pfeifer, and R. Dittmeyer. *Crystallite-pore network model of transport and reaction of multicomponent gas mixtures in polycrystalline microporous media*. Chem. Eng. J., Vol. 254, pp. 545-558, 2014.

[125] L. Li, D. Mao, J. Xiao, X. Guo, and J. Yu. *Facile preparation of highly efficient CuO-ZnO-ZrO_2/HZSM-5 bifunctional catalyst for one-step CO_2 hydrogenation to dimethyl ether: Influence of calcination temperature*. Chem. Eng. Res. Des., Vol. 11, pp. 100-108, 2016.

[126] S. Lee and K.J. Gogate. *Methanol-to -Gasoline vs. DME-to-Gasoline II. Process comparison and analysis*. Fuel Sci. Technol. Int., Vol. 13, pp. 1039-1057, 2007.

[127] K.L. Ng, D. Chadwick, and B.A. Toseland. *Kinetics and modelling of dimethyl ether synthesis from synthesis gas*. Chem. Eng. Sci., Vol. 54, pp. 3587-3592, 1999.

[128] A. T. Aguayo, J. Ereña, I. Sierra, M. Olazar, and J. Bilbao. *Deactivation and regeneration of hybrid catalysts in the single-step synthesis of dimethyl ether from syngas and CO_2*. Catal. Today, Vol. 106, pp. 265-270, 2005.

[129] S. Lee, K. Schneider, J. Schumann, A.K. Mogalicherla, P. Pfeifer, and R. Dittmeyer. *Effect of metal precursor on $Cu/ZnO/Al_2O_3$ synthesized by flame spray pyrolysis for direct DME production*. Chem. Eng. Sci., Vol. 138, pp. 194-202, 2015.

[130] J.T. Sun, I.S. Metcalfe, and M. Sahibzada. *Deactivation of Cu/ZnO/Al2O3 Methanol Synthesis Catalyst by Sintering*. Ind. Eng. Chem. Res., Vol. 38, pp. 3868-3872, 1999.

[131] B.H. Park, S.B. Kim, Z.M. Jo, and M.H. Lee. *Filtration Characteristics of Fine Particulate Matters in a PTFE/GlassComposite Bag Filter*. Aerosol Air Qual. Res., Vol. 12, pp. 1030-1036, 2012.

[132] L. Zeng and A.P. Weber. *Aerosol synthesis of nanoporous silica particles with controlled pore size distribution*. J. Aerosol Sci., Vol. 76, pp. 1-12, 2014.

[133] M. Klumpp. *Neue Materialien für die Prozessintensivierung: Herstellung und Charakterisierung hierarchisch strukturierter Katalysatoren und Katalysatorträger*. Dissertation. Friedrich-Alexander-Universität Erlangen-Nürnberg (FAU), Shaker Verlag, 2017.

[134] Büchi Labortechnik AG. *Operation Manual Mini SPray Dryer B-290*. www.buchi.com, Flawil, Switzerland, 2010.

[135] K. Okuyama, M. Abfullah, Q.W. Lenggoro, and F. Iskandar. *Preparation of functional nanostructured particles by spray drying*. Adv. Powder Technol., Vol. 17, pp. 587-611, 2006.

[136] R. Vehring, W.R. Foss, and D. Lechuga-Ballesteros. *Particle formation in spray drying*. Aerosol Sci., Vol. 38, pp. 728-746, 2007.

[137] J. Vicente, J. Pinto, J. Menezes, and F. Gaspar. *Fundamental analysis of particle formation in spray drying*. Powder Technol., Vol. 247, pp. 1-7, 2013.

[138] R. Zhao, J. G. Goodwin, K. Jothimurugesan, S. K. Gangwal, and J.J. Spivey. *Spray-Dried Iron Fischer-Tropsch Catalysts. 1. Effect of Structure on the Attrition Resistance of the Catalysts in the Calcined State*. Ind. Eng. Chem. Res., Vol. 40, pp. 1065-1075, 2001.

[139] Q.L. Hao, F.X. Liu, H. Wang, J. Chang, L. Bai, H. W. Xiang, Y.W. Li, F. Yi, and B.F. Xu. *Effect of reduction temperature on a spray dried iron-based catalyst for slurry Fischer Tropsch synthesis*. J. Mol. Catal. A: Chem., Vol. 261, pp. 104-111, 2007.

[140] A.B.D. Nandiyanto and K. Okuyama. *Progress in developing spray-drying methods for the production of controlled morphology particles: From the nanometer to submicrometer size ranges*. Adv. Powder Technol., Vol. 22, pp. 1-19, 2011.

[141] L. Zhang, H. Yang, X. Qiao, T. Zhou, Z. Wang, J. Zhang, D. Tang, D. Shen, and Q. Zhang. *Systematic optimization of spray drying for YAG transparent ceramics*. J. Eur. Ceram. Soc., Vol. 35, pp. 2391-2401, 2015.

[142] S. Brunauer, P.H. Emmett, and E. Teller. *Adsorption of Gases in Multimolecular Layers*. Bureau of Chemistry and Soils and George Washington University, pp. 309-319, 1938.

[143] R. Müller, L. Mädler, and S.E. Pratsinis. *Nanoparticle synthesis at high production rates by flame spray pyrolysis*. Chem. Eng. Sci., Vol. 58, pp. 1969-1976, 2003.

[144] Q. Zhu, Q. Zhang, and L. Wen. *Anti-sintering silica-coating CuZnAlZr catalyst for methanol synthesis from CO hydrogenation*. Fuel Process. Technol., Vol. 156, pp. 280-289, 2017.

[145] M. Huber, W.J. Stark, S. Loher, M. Maciejewski, F. Krumeich, and A. Baiker. *Flame synthesis of calcium carbonate nanoparticles*. Chem. Commun., pp. 648-650, 2005.

[146] D.S. Jung, S.K. Hong, J.S. Cho, and Y.C. Kang. *Morphologies and crystal structures of nano-sized $Ba_{1-x}Sr_xTiO_3$ primary particles prepared by flame spray pyrolysis*. Mater. Res. Bull., Vol. 43, pp. 1789-1799, 2008.

[147] P. Haider and A. Baiker. *Gold supported on Cu-Mg-Al-mixed oxides: Strong enhancement of activity in aerobic alcohol oxidation by concerted effect of copper and magnesium*. J. Catal., Vol. 248, pp. 175-187, 2007.

[148] X. Chen, Z. Xu, F. Yang, and H. Zhao. *Flame spray pyrolysis synthesized CuO-TiO_2 nanoparticles for catalytic combustion of lean CO*. Proc. Combust. Inst. , Vol. 37, pp. 5499-5506, 2019.

[149] W.Y. Teoh, R. Setiawan, L. Mädler, J.D. Grunwaldt, R. Amal, and S.E. Pratsinis. *Ru-Doped Cobalt-Zirconia Nanocomposites by Flame Synthesis: Physicochemical and Catalytic Properties*. Chem. Mater., Vol. 20, pp. 4069-4079, 2008.

[150] W.Y. Teoh, R. Amal, and L. Mädler. *Flame spray pyrolysis: An enabling technology for nanoparticles design and fabrication*. Nanoscale, Vol. 2, pp. 1324-1347, 2010.

[151] I.W.M. Brown, K.J.D. Mackenzie, and G.J. Gainsford. *Thermal decomposition of the basic copper carbonates mlachite and azurite*. Thermochim. Acta, Vol. 74, pp. 23-32, 1984.

[152] W. Gao, H. Wang, Y. Wang, W. Guo, and M. Jia. *Dimethyl ether synthesis from CO_2 hydrogenation on La-modified CuO-ZnO-Al_2O_3/HZSM-5 bifunctional catalysts*. J. Rare Earths, Vol. 31, pp. 470-476, 2013.

[153] J.D. Grunwaldt, A.M. Molenbroek, N.Y. Topse, H. Topse, and B.S. Clausen. *In Situ Investigations of Structural Changes in Cu/ZnO Catalysts*. J. Catal., Vol. 194, pp. 452-460, 2000.

[154] T. Fujitani and J. Nakamura. *The effect of ZnO in methanol synthesis catalysts on Cu dispersion and the specific activity*. Catal. Lett., Vol. 56, pp. 119-124, 1998.

[155] N.Y. Topse and H. Topse. *On the nature of surface structural changes in Cu/ZnO methanol synthesis catalysts*. Top. Catal., Vol. 8, pp. 267-270, 1999.

[156] B. Lindström, L.J. Pettersson, and P.G. Menon. *Activity and characterization of Cu/Zn, Cu/Cr and Cu-Zr on γ-Al_2O_3 for methanol reforming for fuel cell vehicles*. Appl. Catal., A, Vol. 234, pp. 111-125, 2002.

[157] M. Shimokawabe, H. Asakawa, and N. Takezawa. *Characterization of Copper/Zirconia Catalysts Prepared by an Impregnation Method*. Appl. Catal., Vol. 59, pp. 45-58, 1990.

[158] R.H. Perry and D.W. Green. *Perry's Chemical Engineers' Handbook-7th Edition*. Mc Graw Hill, USA, 1999.

[159] E. Maines, N. Bell, L. Evans, M. Roach, L. Tsui, J. Lavin, and D. Keicher. *Material Properties of Ceramic Slurries for Applications in Additive Manufacturing Using Stereolithography*. Solid Freeform Fabrication 2018, pp. 932-946, 2018.

[160] M. Kaur and P.M.S. Sharma, S. ans Bedi. *Silica supported Brönsted acids as catalyst in organic transformations: A comprehensive review*. Chin. J. Catal., Vol. 36, pp. 520-549, 2015.

[161] E.J.L. Lana, K.L. da Silva Rocha, I.V. Kozhevnikov, and E.V. Gusevskaya. *Synthesis of 1,8-cineole and 1,4-cineole by isomerization ofα-terpineol catalyzed by heteropoly acid*. J. Mol. Catal. A, Vol. 259, pp. 99-102, 2006.

[162] B. Piechulla, R. Bartelt, A. Brosemann, U. Effmert, H. Bouwmeester, F. Hippauf, and W. Brandt. *The α-Terpineol to 1,8-Cineole Cyclization Reaction of Tobacco Terpene Synthases*. Plant Physiol., Vol. 172, pp. 2120-2131, 2016.

[163] G.H. Graaf and J.G.M. Winkelman. *Chemical Equilibria in Methanol Synthesis Including the Water-Gas Shift Reaction: A Critical Reassessment*. Ind. Eng. Chem. Res., Vol. 55, pp. 5854-5864, 2016.

[164] J. Maina, C. Pozp-Gonzalo, J. Schütz, J. Wang, and L.F. Dumée. *Tuning CO_2 conversion product selectivity of metal organic frameworks derived hybrid carbon photoelectrocatalytic reactors*. Carbon, Vol. 148, pp. 80-90, 2019.

[165] Y. Chai, L. Li, J. Lu, D. Li, J. Shen, Y. Zhang, J. Liang, and X. Wang. *Germanium-substituted Zn_2TiO_4 solid solution photocatalyst for conversion of CO_2 into fuels*. J. Catal., Vol. 371, pp. 144-152, 2019.

[166] A. Behr and R. Kuhlmann. *Chemische Umsetzung von Kohlendioxid*. Chem. Ing. Tech., Vol. 90, pp. 593-601, 2018.

[167] J. Jia, H. Wang, Z. Lu, P.G. O'Brien, M. Ghoussoub, P. Duchesne, Z. Zheng, P. Li, Q. Qiao, L. Wang, A. Gu, A.A. Jelle, Y. Dong, Q. Wang, K. K. Ghuman, T. Wood, C. Qian, Y. Shao, C. Qiu, M. Ye, Y. Zhu, Z. H. Lu, P. Zhang, A.S. Helmy, C.V. Singh, N.P. Kherani, D.D. Perovic, and G.A. Ozin. *Photothermal Catalyst Engineering: Hydrogenation of Gaseous CO_2 with High Activity and Tailored Selectivity*. Adv. Sci., Vol. 4, pp. 1-13, 2017.

[168] L. Li, H. Zhang, X. Li, X. Kong, R. Xu, K. Tay, and X. Tu. *Plasma-assisted CO_2 conversion in a gliding arc discharge: Improving performance by optimizing the reactor design*. J. CO_2 Util., Vol. 29, pp. 196-303, 2019.

[169] M. Biset-Peiró, J. Guilera, J. Zhang, T.and Arbiol, and T. Andreu. *On the role of ceria in Ni-Al_2O_3 catalyst for CO_2 plasma methanation*. Appl. Catal., A, Vol. 575, pp. 223-229, 2019.

[170] F. Azzolina-Jury. *Novel boehmite transformation into γ-alumina and preparation of efficient nickel base alumina porous extrudates for plasma-assisted CO_2 methanation*. J. Ind. Eng. Chem., Vol. 71, pp. 410-424, 2019.

[171] F. Dębek, R. nd Azzolina-Jury, A. Travert, F. Maugé, and F. Thibault-Starzyk. *Low-pressure glow discharge plasma-assisted catalytic CO_2 hydrogenation-The effect of metal oxide support on the performance of the Ni-based catalyst*. Catal. Today, Vol. 337, pp. 182-194, 2019.

[172] P. Gao, S. Li, X. Bu, S. Dng, Z. Liu, H. Wang, L. Zhong, M. Qiu, C. Yang, J. Cai, W. Wei, and Y. Sun. *Direct conversion of CO_2 into liquid fuels with high selectivity over a bifunctional catalyst*. Nat. Chem., Vol. 9, pp. 1019-1024, 2017.

[173] J. Wei, Q. Ge, Z. Wen, C. Fang, L. Guo, H. Xu, and J. Sun. *Directly converting CO_2 into a gasoline fuel*. Nat. Commun., Vol. 8, pp. 1-8, 2017.

[174] N. Boreriboon, X. Jiang, C. Song, and P. Prasassarakich. *Fe-based bimetallic catalysts supported on TiO_2 for selective CO_2 hydrogenation to hydrocarbons*. J. CO_2 Util., Vol. 25, pp. 330-337, 2018.

[175] J. Wang, A. Zhang, X. Jiang, C. Song, and X. Guo. *Highly selective conversion of CO_2 to lower hydrocarbons (C_2-C_4) over bifunctional catalysts composed of In_2O_3-ZrO_2 and zeolite*. J. CO_2 Util., Vol. 27, pp. 81-88, 2018.

[176] Carbon Recycling International (CRI). *Products: Renewable Methanol*. 2019, Available Online: https://www.carbonrecycling.is/vulcanol, Accessed: 27.10.2019.

[177] E. Frei, A. Schaadt, T. Ludwig, H. Hillebrecht, and I. Krossing. *The Influence of the Precipitation/Ageing Temperature on a Cu/ZnO/ZrO_2 Catalyst for Methanol Synthesis from H_2 and CO_2*. Chem. Cat. Chem., Vol. 6, pp. 1721-1730, 2014.

[178] J. Graciani, K. Mudiyanselage, F. Xu, A. E. Baber, J. Evans, S.D. Senanayake, D.J. Stacchiola, P. Liu, J. Hrbek, J.F. Sanz, and J.A. Rodriguez. *Highly active copper-ceria and copper-ceria-titania catalysts for methanol synthesis from CO_2*. Science, Vol. 345, pp. 546-550, 2014.

[179] J.A. Rodriguez, P. Liu, D. Stacchiola, S.D. Senanayake, M. G. White, and J.G. Chen. *Hydrogenation of CO_2 to Methanol: Importance of Metal-Oxide and Metal-Carbide Interfaces in the Activation of CO_2*. ACS Catal., Vol. 5, pp. 6696-6706, 2015.

[180] J. Weigel, R.A. Koeppel, and A. Baiker, A. abd Wokaun. *Surface Species in CO and CO_2 Hydrogenation over Copper/Zirconia: On the Methanol Synthesis Mechanism*. Langmuir, Vol. 12, pp. 5319-5329, 1996.

[181] A. Karelovic, G. Galdames, J.C. Medina, C. Yévenes, and R. Barra, Y. Jiménez. *Mechanism and structure sensitivity of methanol synthesis from CO_2 over SiO_2-supported Cu nanoparticles*. J. Catal.,Vol. 369, pp. 415-426, 2019.

[182] M.S. Frei, M. Capdevilla-Cortada, R. García-Muelas, C. Mondelli, N. López, J.A. Stewart, D. Curulla Ferré, and J. Pérez-Ramírez. *Mechanism and microkinetics of methanol synthesis via CO_2 hydrogenation on indium oxide*. J. Catal., Vol. 361, pp. 313-321, 2018.

[183] Y. Nitta, O. Sueata, Y. Ikeda, Y. Okamoto, and T. Imanaka. *Copper-zirconia catalysts for methanol synthesis from carbon dioxide: effect of ZnO addition to Cu-ZrO_2 catalysts*. Catal. Lett., Vol. 26, pp. 345-354, 1994.

[184] L. Angelo, L.M.M. Kolb, K. andTejada, Y. Zimmermannm, K. Parkhomenko, and A.C. Roger. *Study of $CuZnMO_x$ oxides (M = Al, Zr, Ce, CeZr) for the catalytic hydrogenation of CO_2 into methanol*. C.R. Chim., Vol. 18, pp. 250-260, 2015.

[185] F. Arena, K. Barbera, G. Italiano, G. Bonura, L. Spadaro, and F. Frusteri. *Synthesis, characterization and activity pattern of Cu-ZnO/ZrO_2 catalysts in the hydrogenation of carbon dioxide to methanol*. J. Catal., Vol. 249, pp. 185-194, 2007.

[186] F. Arena, G. Italiano, K. Barbera, S. Bordiga, G. Bonura, L. Spadaro, and F. Frusteri. *Solid-state interactions, adsorption sites and functionality of Cu-ZnO/ZrO_2 catalysts in the CO_2 hydrogenation to CH_3OH*. Appl. Catal., A, Vol. 350, pp. 16-23, 2008.

[187] S. Tada, K. Larmier, and C. Büchel, R.and Copéret. *Methanol synthesis via CO_2 hydrogenation over CuO-ZrO_2 prepared by two-nozzle flame spray pyrolysis*. Catal. Sci. Technol., Vol. 8, pp. 2056-2060, 2018.

[188] X. Dong, F. Li, N. Zhao, Y. Tan, J. Wang, and F. Xiao. *CO_2 hydrogenation to methanol over Cu/Zn/Al/Zr catalysts prepared by liquid reduction*. Chin. J. Catal., Vol.38, pp. 717-725, 2017.

[189] M.Z. Ramli, S.S.A. Szed-Hassan, and A. Hadi. *Performance of Cu-Zn-Al-Zr catalyst prepared by ultrasonic spray precipitation technique in the synthesis of methanol via CO_2 hydrogenation*. Fuel Process. Technol., Vol 169, pp. 191-198, 2018.

[190] P. Gao, R. Xie, H. Wang, L. Zhong, L. Xia, Z. Zhang, W. Wei, and Y. Sun. *Cu/Zn/Al/Zr catalysts via phase-pure hydrotalcite-like compounds for methanol synthesis from carbon dioxide*. J. CO_2 Util., Vol. 11, pp. 41-48, 2015.

[191] X. Dong, F. Li, N. Zhao, F. Xiao, J. Wang, and Y. Tan. *CO_2 hydrogenation to methanol over $Cu/ZnO/ZrO_2$ catalysts preparedby precipitation-reduction method*. Appl. Catal., B, Vol. 191, pp. 8-17, 2016.

[192] H. Yang, O. Gao, C. Thang, L. Zhong, X. Li, S. Wang, H. Wang, W. Wei, and Y. Sun. *Core-shell structured Cu@m-SiO_2 and Cu/ZnO@m-SiO_2 catalysts for methanol synthesis from CO_2 hydrogenation*. Catal. Commun., Vol. 84, pp. 56-60, 2016.

[193] A. García-Trenco, A. Regoutz, E.R. White, D.J. Payne, .M.S.P. Shaffer, and C.K. Williams. *PdIn intermetallic nanoparticles for the Hydrogenation of CO_2 to Methanol*. Appl. Catal., B, Vol. 220, pp. 9-18, 2018.

[194] A. S: Malik, A. F. Zaman, A. A. Al-Zahrani, M. A. Daous, H. Driss, and L. A. Petriv. *Development of highly selective $PdZn/CeO_2$ and Ca-doped $PdZn/CeO_2$ catalysts for methanol synthesis from CO_2 hydrogenation*. Appl. Catal., A, Vol. 560, pp. 42-53, 2018.

[195] Y. L. Men, Y. Liu, Q. Wang, Z.H. Luo, S. Shao, Y.B. Li, and Y.X. Pan. *Highly dispersed Pt-based catalysts for selective CO_2 hydrogenation to methanol at atmospheric pressure*. Chem. Eng. Sci., Vol. 200, pp. 167-175, 2019.

[196] A.B. Vidal, L. Feria, J. Evans, Y. Takahashi, P. Liu, K. Nakamura, F. Illas, and J.A. Rodriguez. *CO_2 Activation and Methanol Synthesis on Novel Au/TiC and Cu/TiC Catalysts*. J. Phys. Chem. Lett., Vol. 3, pp. 2275-2280, 2012.

[197] M. Compagnoni, A. Tripodi, A. Di Michele, P. Sassi, M. Signoretto, and I. Rossetti. *Low temperature ethanol steam reforming for process intensification: New Ni/M_xO-ZrO_2 active and stable catalysts prepared by flame spray pyrolysis*. Int. J. Hydrogen Energy, Vol. 42, pp. 28193-28213, 2017.

[198] W.J. Stark, L. Mädler, M. Maciejewski, S. E. Pratsinis, and A. Baiker. *Flame synthesis of nanocrystalline ceria-zirconia: effect of carrier liquid*. Chem. Commun., pp. 588-589, 2003.

[199] F.L. Yuan, C.H. Chen, and J. Kelder, E.M.and Schoonman. *Preparation of zirconia and yttria-stabilized zirconia (YSZ) fine powders by flame-assisted ultrasonic spray pyrolysis (FAUSP)*. Solid State Ionics, Vol. 109, pp. 119-123, 1998.

[200] R. Müller, R. Jossen, H.K. Kammler, and S.E. Pratsinis. *Growth of Zirconia Particles Made by Flame Spray Pyrolysis*. AlChE J., Vol. 50, pp. 3085-3094, 2004.

[201] A.I.Y. Tok, F.Y. C. Boey, S.W. Du, and B.K. Wong. *Flame spray synthesis of ZrO_2 nano-particles using liquid precursors*. Mater. Sci. Eng., B, Vol. 130, pp. 114-119, 2006.

[202] C. Chaisuk, P. Boonpitak, J. Panpranot, and O. Mekasuwandumrong. *Effects of Co dopants and flame conditions on the formation of Co/ZrO_2 nanoparticles by flame spray pyrolysis and their catalytic properties in CO hydrogenation*. Catal. Commun., Vol. 12, pp. 917-922, 2011.

[203] C. Jeong and Y.W. Suh. *Role of ZrO_2 in $Cu/ZnO/ZrO_2$ catalysts prepared from the precipitated Cu/Zn/Zr precursors*. Catal. Today, Vol. 265, pp. 254-263, 2016.

A Supplementary Figures and Tables

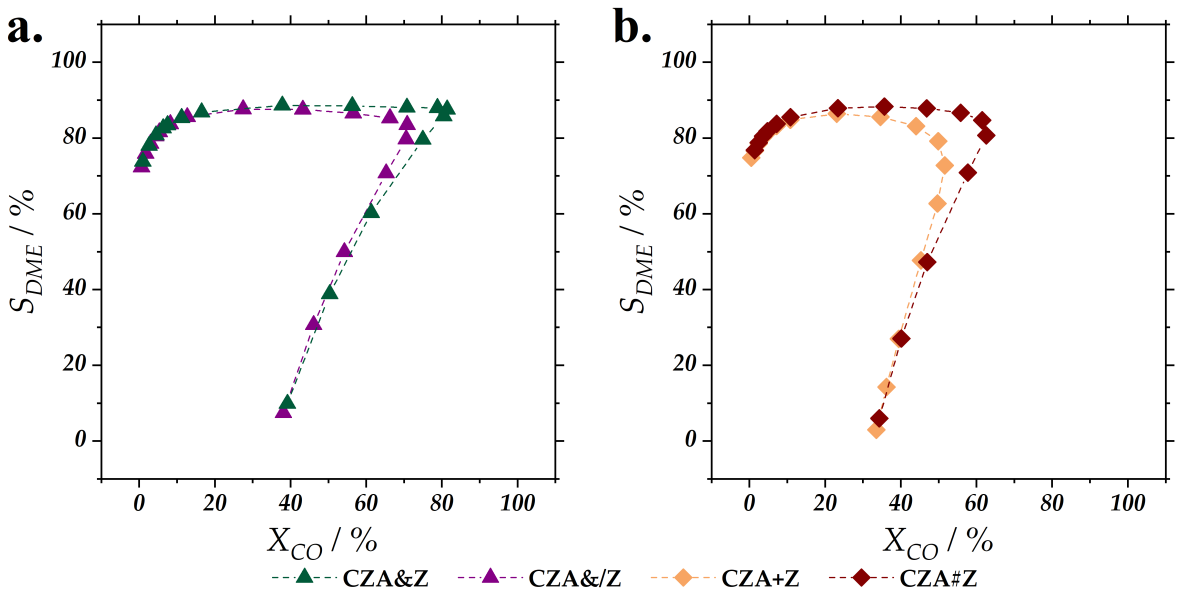


Figure A.1: S_{DME} as a function of X_{CO} (combined simulation data from Figures 3.4 and 3.6) of hybrid catalyst structures of a) close proximity (CZA&Z and CZA&/Z) and b) medium proximity (CZA+Z and CZA#Z). Reaction conditions: p = 40 bar, T = 250 °C, F/W = 2000 mL h^{-1} g_{CAT}^{-1}.

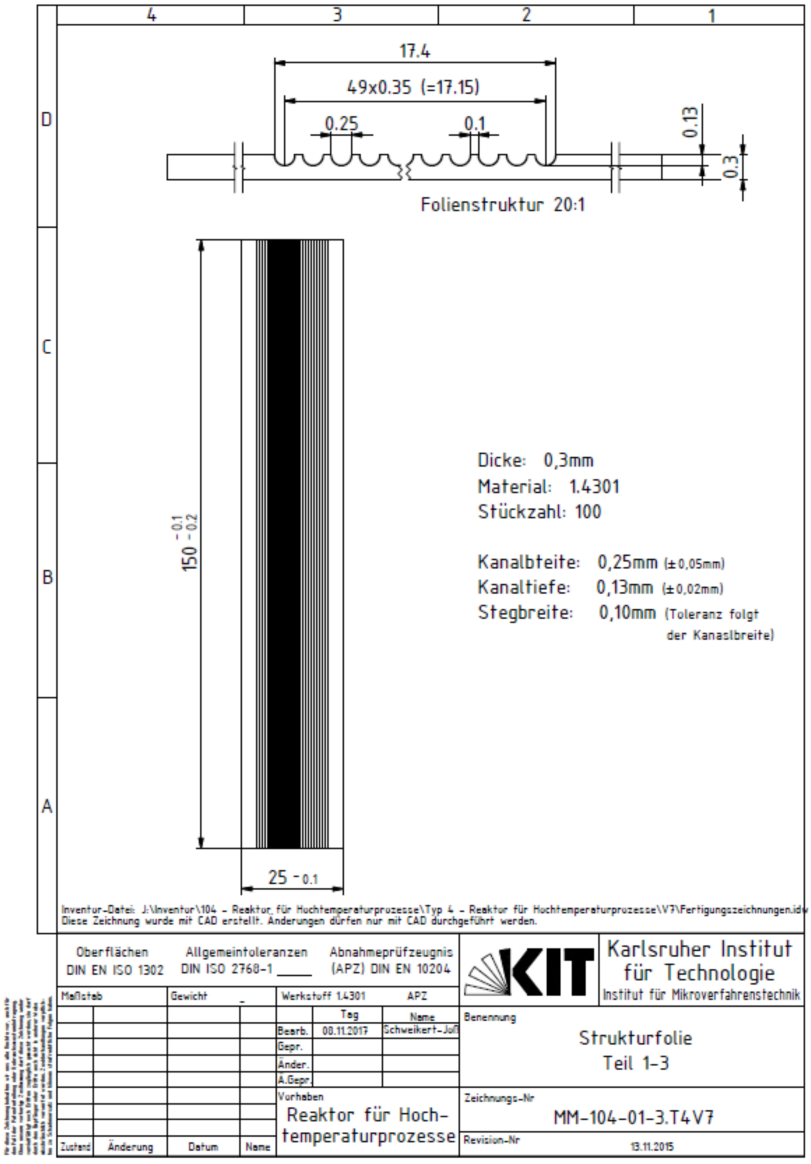


Figure A.2: Scheme of the foils used in the μ-CR.

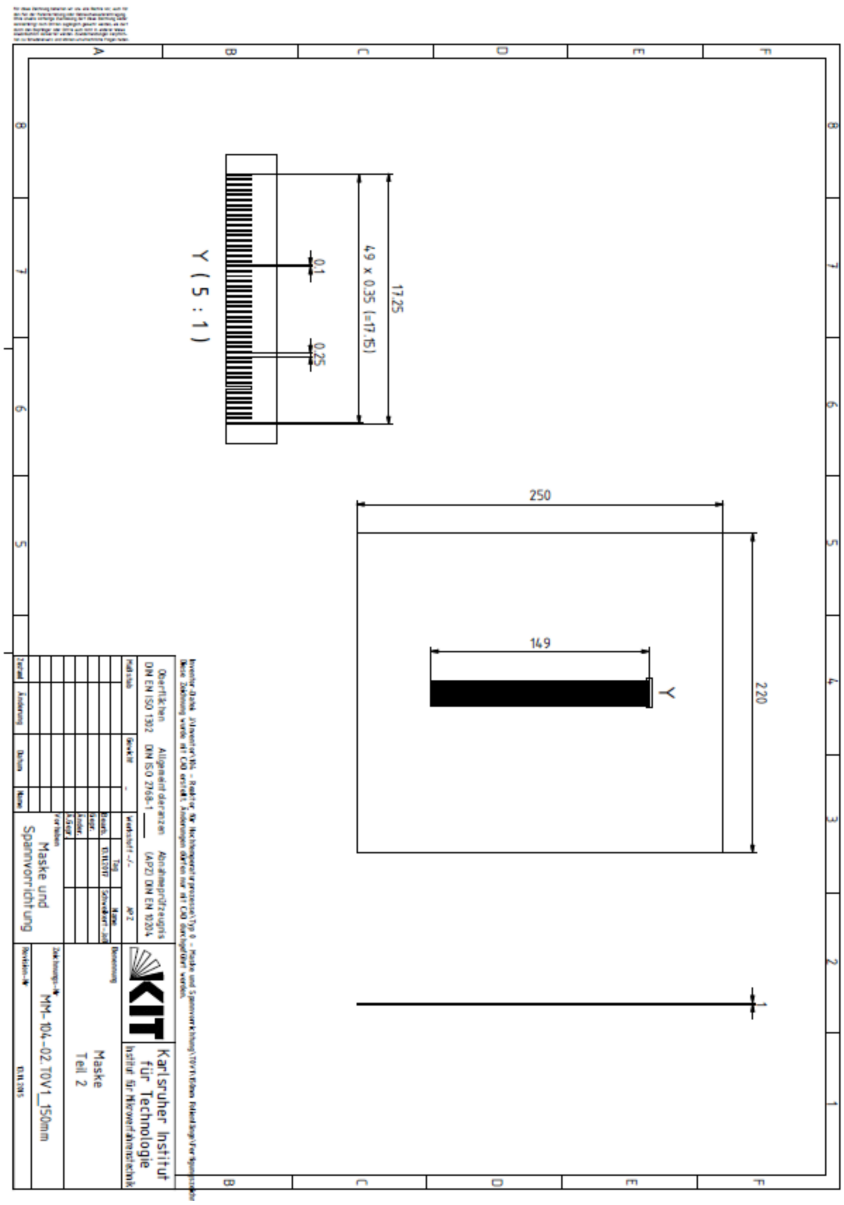


Figure A.3: Scheme of the screen used for the coating via screen printing.

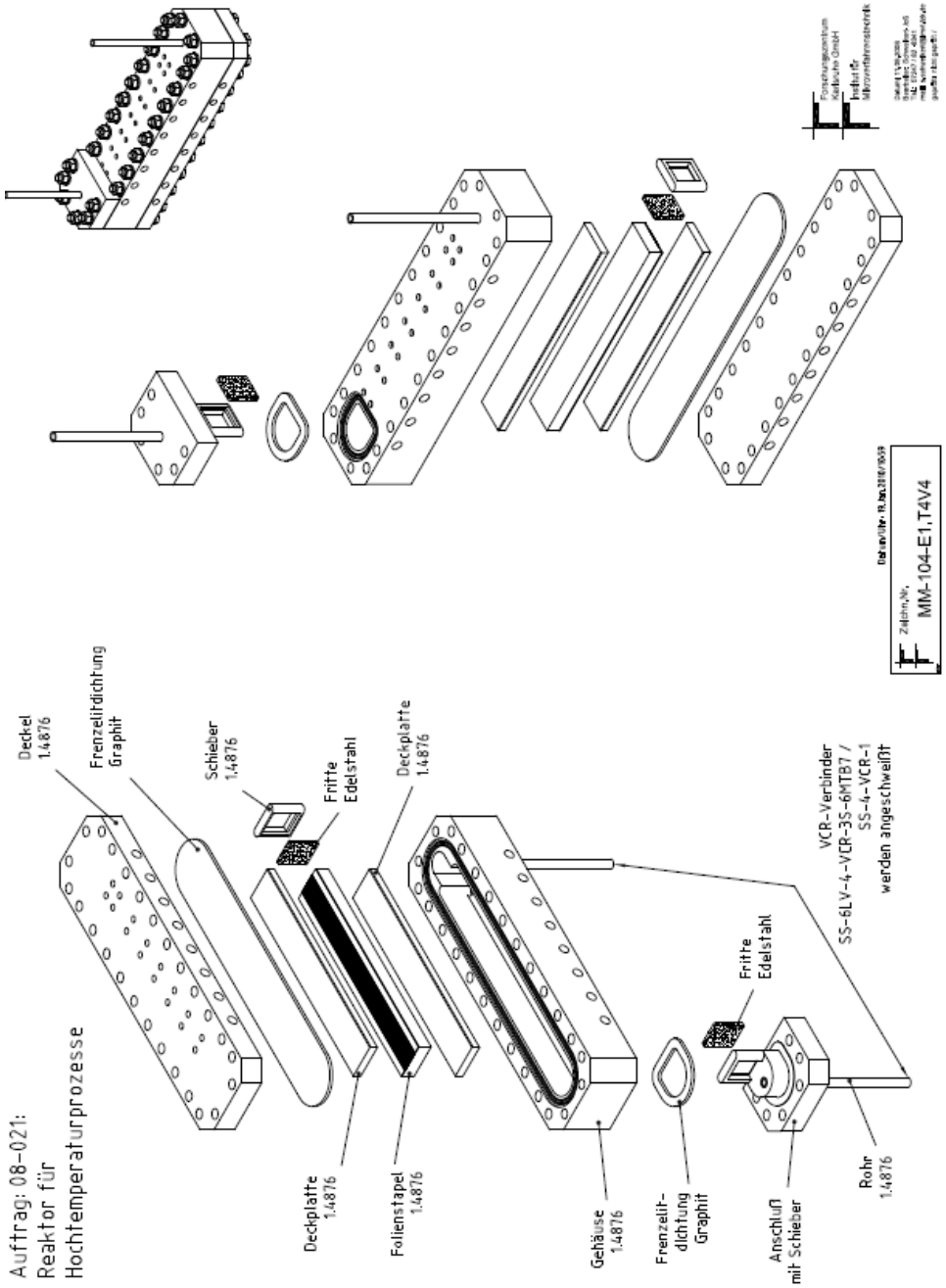


Figure A.4: Scheme of the μ-CR.

Table A.1: X_{CO} (data shown are mean values within 4 h TOS each) v.s. time on stream of P-CZA catalyst for different reaction temperatures.

Time on Stream / h	*Reaction Temperature / °C*	X_{CO} / %
0 - 4	230	3.2
4 - 8	240	5.1
8 - 12	250	6.9
12 - 16	260	8.4
	...	
142 - 146	230	3.1
146 - 150	240	5.0

Reaction conditions: μ-Berty reactor; p = 45 bar; $(F/W)^*$ = 80 000 $mL_{Reagents}$ h^{-1} g_{CAT}^{-1}

Feed composition: $H_2/CO/CO_2$ = 16/8/1 with 10 vol.-% N_2.

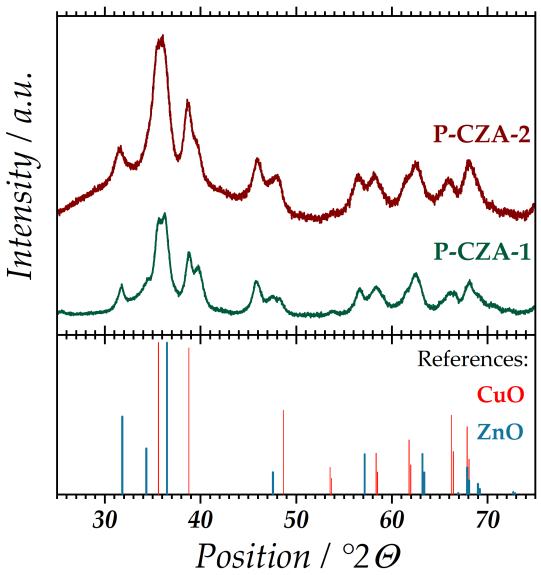


Figure A.5: XRD patterns of the P-CZA-1, P-CZA-2 and the references for CuO and ZnO structures (International Center for Diffraction Data (ICDD)).

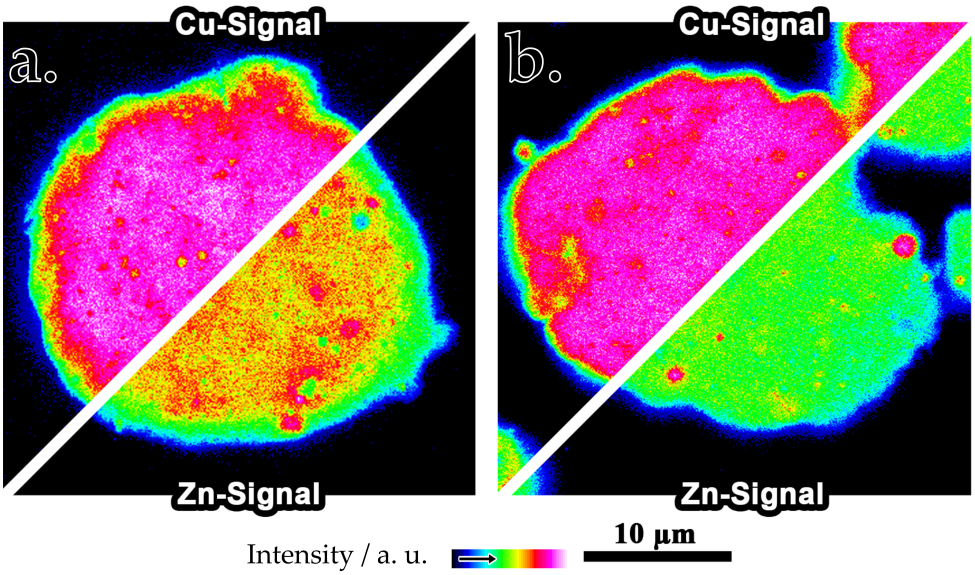
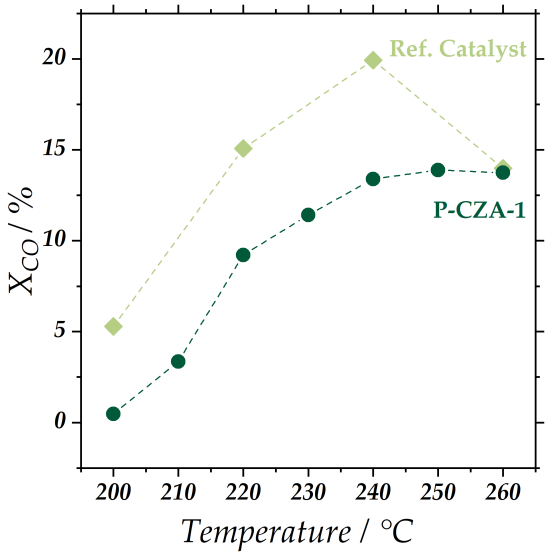


Figure A.6: SD-CZA characterization: Cu- and Zn-distribution from EPMA/WDX a) before and b) after calcination.



CONDITIONS: µ-Berty; p = 45 bar; $(F/W)^*_{.}$ = 24000 $mL_{Reag.}\ h^{-1}\ g^{-1}_{CAT}$

Figure A.7: Activity of the P-CZA-1 and a reference catalyst in terms of X_{CO} in the STM reaction in the µ-Berty reactor.

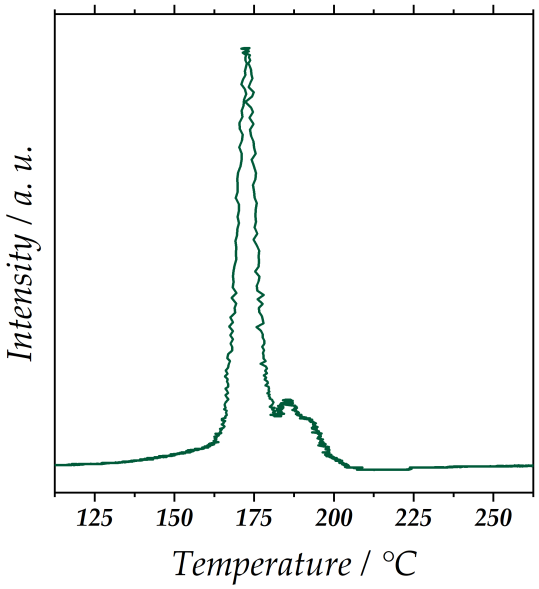


Figure A.8: TPR profile of the CZA+Z_5 sample.

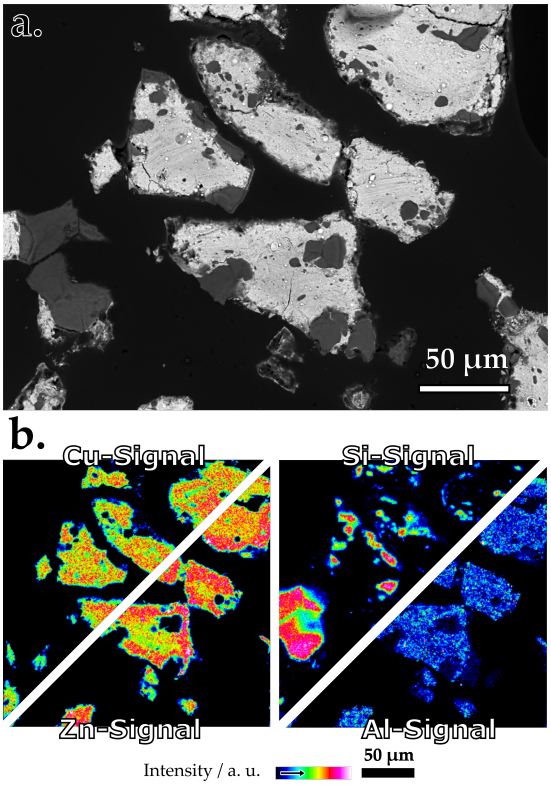


Figure A.9: Morphological analysis of the CZA+Z_5 catalyst. a) cross-sectional analysis via EPMA/BSE and b) elemental map (EPMA/WDX) for the representative elements for the core (Cu, Zn, Al) and shell (Si, Al).

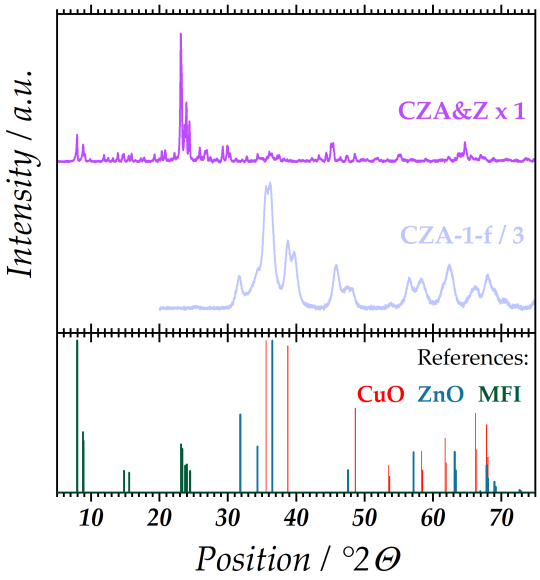


Figure A.10: XRD patterns of the CZA-1-f (with adjusted intensity), CZA&Z and the references for CuO, ZnO and MFI structures (International Center for Diffraction Data (ICDD)).

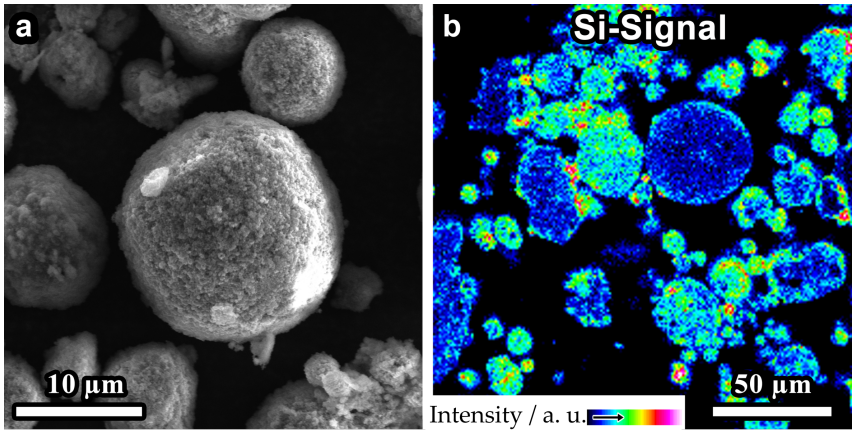


Figure A.11: a) SE-micrograph image and b) Si-EPMA/WDX-images of the SD-CZA_core sample.



Figure A.12: Resulting red-coloured suspension obtained mixing the H-ZSM-5 with terpineol.

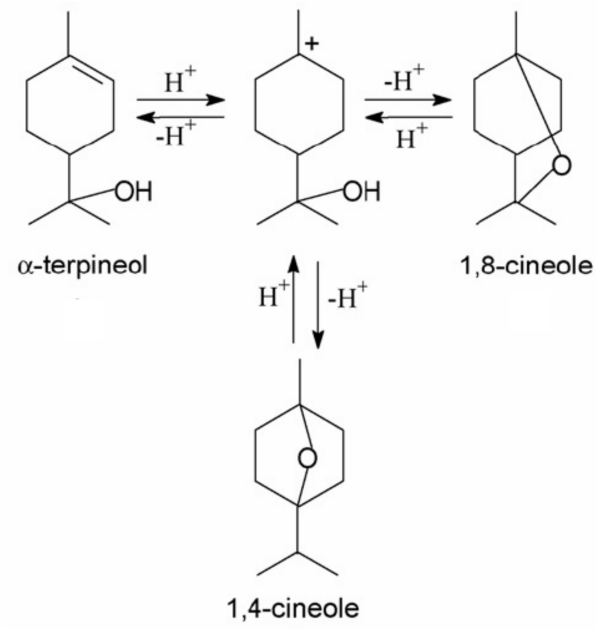


Figure A.13: Reaction scheme of the isomerization of the α-terpineol to 1,8-cineole and 1,4-cineole [161].

Table A.2: k_i values at different temperatures for commercial CZA (calculated according to Ref. [30]) and self-made CZA.

T / °C	k_1 / - *[30]*	k_1 / - *this study*	k_2 / - *[30]*	k_2 / *this study*	k_3/- *[30]*	k_3/- *this study*
230	$3.01 \cdot 10^{-3}$	$2.26 \cdot 10^{-3}$	$2.88 \cdot 10^{-2}$	$8.63 \cdot 10^{-3}$	$1.28 \cdot 10^{-3}$	$1.26 \cdot 10^{2}$
240	$5.12 \cdot 10^{-3}$	$2.36 \cdot 10^{-3}$	$3.09 \cdot 10^{-2}$	$9.77 \cdot 10^{-3}$	$2.07 \cdot 10^{-3}$	$1.42 \cdot 10^{2}$
250	$8.53 \cdot 10^{-3}$	$2.46 \cdot 10^{-3}$	$3.3 \cdot 10^{-2}$	$1.1 \cdot 10^{-2}$	$3.27 \cdot 10^{-3}$	$1.58 \cdot 10^{2}$
260	$1.39 \cdot 10^{-2}$	$2.56 \cdot 10^{-3}$	$3.52 \cdot 10^{-2}$	$1.24 \cdot 10^{-2}$	$5.07 \cdot 10^{-3}$	$1.76 \cdot 10^{2}$

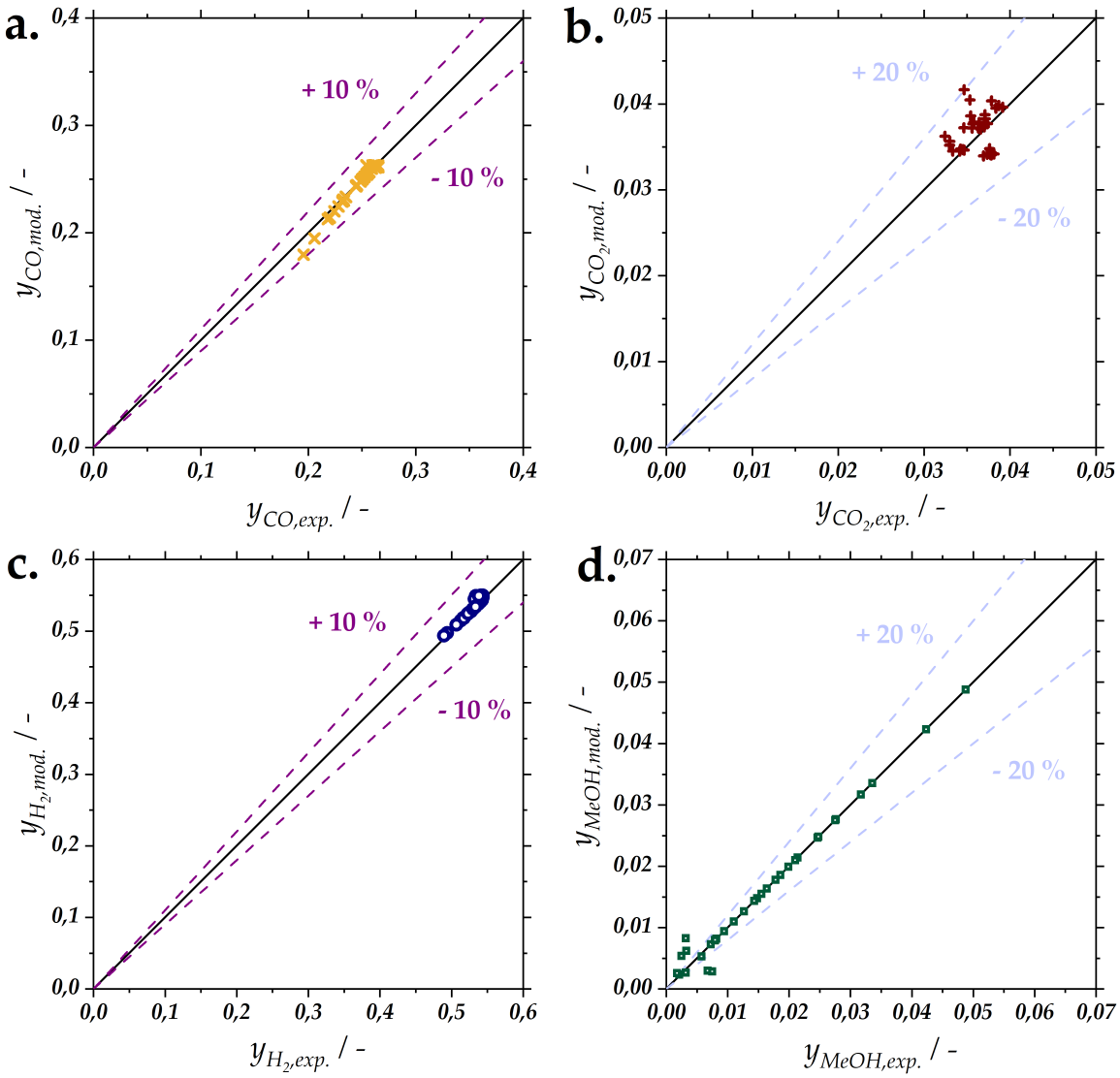


Figure A.14: Parity diagrams of modelled ($y_i^{mod.}$) and experimental ($y_i^{exp.}$) molar fraction of a) CO, b) CO_2, c) H_2 and d) MeOH.

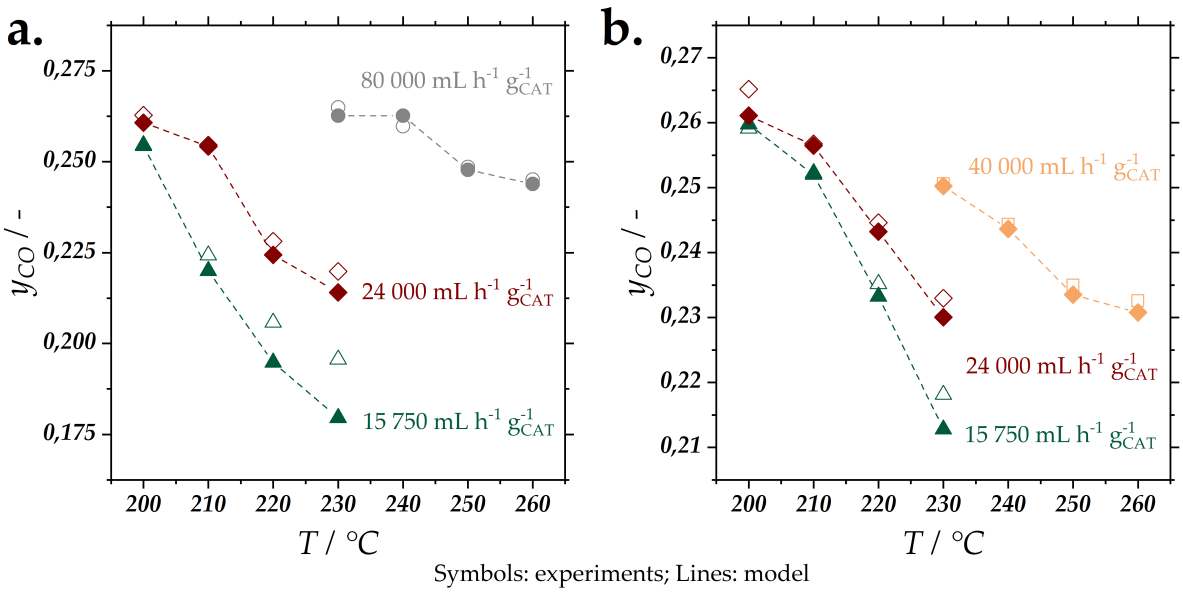


Figure A.15: Effect of temperature on y_{CO} for experiments and kinetic model at a) $p = 45$ bar and b) $p = 40$ bar.

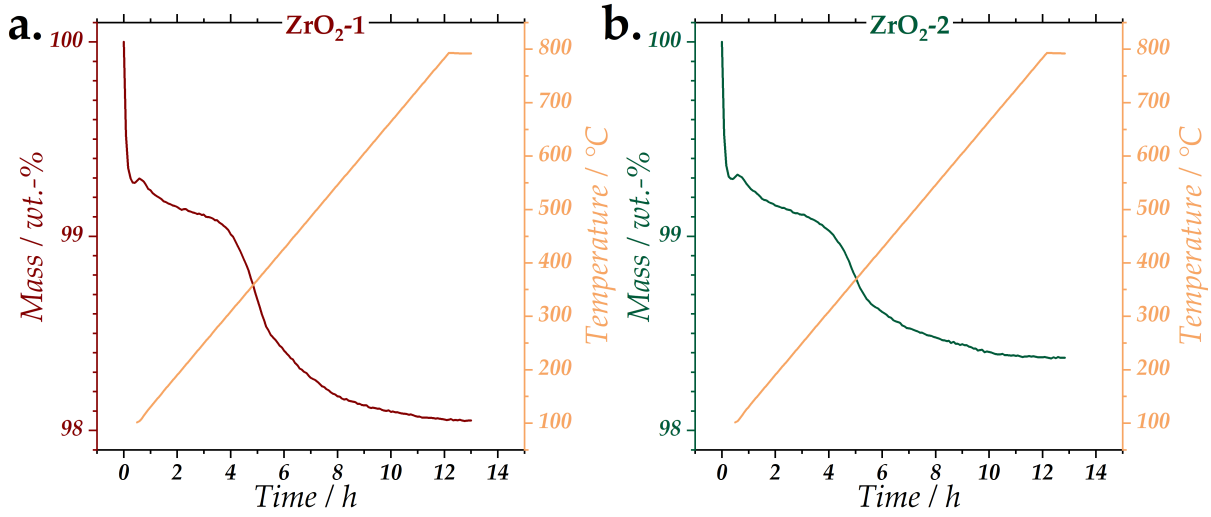


Figure A.16: Mass loss over temperature during the TG-analysis of the a) ZrO_2-1 and b) ZrO_2-2 samples.